

The CORQUENCH Code for Modeling of Ex-Vessel Corium Coolability under Top Flooding Conditions

Code Manual – Version 4.1-beta

Nuclear Science and Engineering Division

About Argonne National Laboratory

Argonne is a U.S. Department of Energy laboratory managed by UChicago Argonne, LLC under contract DE-AC02-06CH11357. The Laboratory's main facility is outside Chicago, at 9700 South Cass Avenue, Argonne, Illinois 60439. For information about Argonne and its pioneering science and technology programs, see www.anl.gov.

DOCUMENT AVAILABILITY

Online Access: U.S. Department of Energy (DOE) reports produced after 1991 and a growing number of pre-1991 documents are available free at OSTI.GOV (<http://www.osti.gov/>), a service of the US Dept. of Energy's Office of Scientific and Technical Information.

Reports not in digital format may be purchased by the public from the National Technical Information Service (NTIS):

U.S. Department of Commerce
National Technical Information
Service 5301 Shawnee Rd
Alexandria, VA 22312
www.ntis.gov
Phone: (800) 553-NTIS (6847) or (703) 605-6000
Fax: (703) 605-6900
Email: orders@ntis.gov

Reports not in digital format are available to DOE and DOE contractors from the Office of Scientific and Technical Information (OSTI):

U.S. Department of Energy
Office of Scientific and Technical Information
P.O. Box 62
Oak Ridge, TN 37831-0062
www.osti.gov
Phone: (865) 576-8401
Fax: (865) 576-5728
Email: reports@osti.gov

Disclaimer

This report was prepared as an account of work sponsored by an agency of the United States Government. Neither the United States Government nor any agency thereof, nor UChicago Argonne, LLC, nor any of their employees or officers, makes any warranty, express or implied, or assumes any legal liability or responsibility for the accuracy, completeness, or usefulness of any information, apparatus, product, or process disclosed, or represents that its use would not infringe privately owned rights. Reference herein to any specific commercial product, process, or service by trade name, trademark, manufacturer, or otherwise, does not necessarily constitute or imply its endorsement, recommendation, or favoring by the United States Government or any agency thereof. The views and opinions of document authors expressed herein do not necessarily state or reflect those of the United States Government or any agency thereof, Argonne National Laboratory, or UChicago Argonne, LLC.

The CORQUENCH Code for Modeling of Ex-Vessel Corium Coolability under Top Flooding Conditions

Code Manual – Version 4.1-beta

prepared by
M.T. Farmer
Nuclear Science and Engineering Division, Argonne National Laboratory

August 2018

ACKNOWLEDGEMENTS

Successful preparation of this report required input and technical support from several individuals and organizations. Mr. Jeff Gabor and Mr. David Luxat from Jensen Hughes and Mr. Richard Wachowiak from Electric Power Research Institute provided valuable input and advice on the overall modelling needs that have been implemented as part of this work. Dr. Kevin Robb from Oak Ridge National Laboratory provided critical technical support and insights regarding the approach for implementing the multi-nodal modeling capability within the current version of CORQUENCH4.1. At Argonne, Dr. Matt Bucknor provided valuable assistance in setting up the validation cases for this work. Model development activities were funded by the U.S. Department of Energy's Office of Nuclear Energy (DOE-NE) Light Water Reactor Sustainability (LWRS) Program.

Table of Contents

ACKNOWLEDGMENTS	i
1.0 INTRODUCTION.....	1
1.1 Background.....	2
1.2 Objectives and Approach.....	2
1.3 Phenomenology and Literature Review.....	3
2.0 MODELING DESCRIPTION	8
2.1 Summary of Overall Modeling Approach	8
2.2 Melt Zone Conservation of Mass and Energy Equations	10
2.3 Concrete Ablation Modeling.....	19
2.3.1 <i>Quasi-Steady Concrete Ablation Model</i>	21
2.3.2 <i>Fully Developed Concrete Dryout Model</i>	22
2.3.3 <i>Transient Concrete Dryout Model</i>	24
2.4 Melt Upper Surface Heat Transfer: Dry Cavity Conditions	31
2.4.1 <i>Crust-Free and Incipient Crust Formation Boundary Conditions</i>	31
2.4.2 <i>Stable Floating Crust Boundary Condition</i>	35
2.5 Melt Upper Surface Heat Transfer: Wet Cavity Conditions.....	36
2.5.1 <i>Crust-Free and Incipient Crust Formation Boundary Conditions</i>	37
2.5.2 <i>Stable Floating Crust Boundary Condition</i>	44
2.5.3 <i>Melt Eruption Modeling</i>	49
2.5.4 <i>Crust Water Ingression Modeling</i>	54
2.5.4.1 Water Ingression Modeling Approach.....	54
2.5.4.2 Dryout and Remelting of Crust Material Formed by Water Ingression	56
2.5.5 <i>Crust Anchoring Criterion</i>	57
2.5.6 <i>Anchored Crust Boundary Condition</i>	59
2.5.6.1 Impervious Crust Models	59
2.5.6.2 Permeable Crust Models	63
2.6 Auxiliary Relationships	65
2.6.1 <i>Melt Void Fraction Models</i>	66
2.6.2 <i>Melt Pool Sparging Gas Bubble Diameter Correlations</i>	67
2.6.3 <i>Melt-Concrete Heat Transfer Coefficient Models</i>	68
2.6.3.1 Bradley Slag Film Model.....	68

2.6.3.2 Gas Film Models	70
2.6.3.3 Gas Film - Slag Film Transition Model.....	79
2.6.3.4 Sevon Correlations	79
2.7 Water Inventory Modeling.....	80
2.8 Automated Multi-Nodal Analysis Capability	89
2.8.1 Overview of Multi-Nodal Modeling Approach	89
2.8.2 Remaining Modeling Deficiencies	91
3.0 DESCRIPTION OF CODE INPUT	92
3.1 Overview.....	92
3.2 Input Description	108
4.0 DESCRIPTION OF CODE OUTPUT	120
4.1 Text Output and Diagnostics File	120
4.2 Plotting Package Output Files.....	120
5.0 REFERENCES.....	130
APPENDIX A: MATERIAL PROPERTIES EVALUATION	138
A.1 Corium Property Evaluation	138
A.1.1 Corium Enthalpy-Temperature Relationship	138
A.1.2 Corium Phase Diagram Evaluation	142
A.1.3 Corium Thermal Conductivity Evaluation	148
A.1.4 Corium Viscosity Evaluation	151
A.1.5 Corium Emissivity Evaluation	154
A.1.6 Corium Surface Tension Evaluation	154
A.1.7 Corium Density Evaluation	154
A.1.8 Corium Mechanical Properties Evaluation	155
A.2 Concrete Property Evaluation	156
A.2.1 Concrete Enthalpy-Temperature Evaluation	158
A.2.2 Concrete Density Evaluation.....	160
A.2.3 Concrete Thermal Conductivity Evaluation	160
A.2.4 Concrete Emissivity Evaluation	159
A.3 Water Property Evaluation.....	161
A.4 Gas Properties Evaluation.....	161
APPENDIX B: BACKGROUND MODELING MATERIAL	163

B.1	Solution Method for Case 1) Anchored Impervious Crust Boundary Condition.....	163
B.2	Solution Method for Case 2) Anchored Impervious Crust Boundary Condition.....	165
B.3	Solution Method for Case 3) Anchored Impervious Crust Boundary Condition.....	166
B.4	Solution Method for Case 1) Anchored Permeable Crust Boundary Condition.....	167
APPENDIX C: VALIDATION CALCULATIONS		169
C.1	Overview	169
C.2	Summary of Modeling Assumptions	170
C.3	Dry Cavity Experiment Results.....	172
C.3.1	<i>ACE/MCCI Experiments</i>	172
C.3.1.1	ACE/MCCI Test L2.....	176
C.3.1.2	ACE/MCCI Test L4.....	176
C.3.1.3	ACE/MCCI Test L5.....	180
C.3.1.4	ACE/MCCI Test L6.....	180
C.3.1.5	ACE/MCCI Test L8.....	185
C.3.2	<i>SNL SURC Tests</i>	185
C.3.2.1	SNL SURC-1 Test.....	188
C.3.2.2	SNL SURC-2 Test.....	191
C.3.3	<i>Dry OECD/MCCI Tests</i>	194
C.3.3.1	OECD/MCCI CCI-4 Test	196
C.3.3.2	OECD/MCCI CCI-5 Test	196
C.4	Wet Cavity Experiment Results	199
C.4.1	<i>Wet OECD/MCCI Tests</i>	199
C.4.1.1	OECD/MCCI CCI-2 Test	199
C.4.1.2	OECD/MCCI CCI-3 Test	202
C.4.1.3	OECD/MCCI CCI-6 Test	202
C.5	Summary	207

List of Figures

Figure	Page
1-1 (a) Traditional View of CCI with Conduction-Limited Upper Crust at Melt-Water Interface; (b) CCI with Water Ingression and Melt Eruption Cooling Mechanisms	3
2-1 Illustration of Simplified Modeling Approach (dry cavity conditions).....	11
2-2 Reaction Heats vs. Temperature for Gas- and Condensed-Phase Chemical Reactions.....	18
2-3 Assumed Phenomenological States and Flow Diagram Governing Crust Progression Modeling	20
2-4 Illustration of Physical Situation During Phase 4 Interaction	23
2-5 Illustration of Physical Situation During Phases 1 and Phase 2a	25
2-6 Illustration of Physical Situation During Phase 2b.....	29
2-7 Illustration of Physical Situation at Core-Concrete Interface.....	30
2-8 Illustration of Physical Situation for the Wet Cavity, Floating Crust Boundary Condition.....	37
2-9 Illustration of Boiling Curve.....	46
2-10 Physical Depiction of Crust Configuration for Melt Eruption Model.....	50
2-11 Illustration of Geometry and Nomenclature for Case 1 Separated Crust Configuration	60
2-12 Illustration of Geometry and Nomenclature for Case 2 Separated Crust Configuration	62
2-13 Illustration of the Basic Features of the Gas Film Model ^[41] a) Without and b) With Crust Formation at the Melt-Film Interface	71
2-14 Illustration of Geometry and Nomenclature for Differencing of Water Spreading Equation	84
2-15 Illustration of Flow over Large Elevation Discontinuities in Substrate Surface	86
2-16 Illustration of BWR Mark I Containment	90
3-1 Illustration of Nomenclature for Water Spreading Model Nodalization Scheme	117
4-1 Typical Code Output at Print Timestep.....	122
A-1 Curve Fits to Lamberston and Mueller ^[88] Phase Diagram Data	143
A-2 Dimensionless Curve Fits to Roche <i>et al.</i> ^[78] Solidus Temperature Data for PWR Corium Containing Various Levels and Types of Concrete	144

A-3	Curve Fits to Roche <i>et al.</i> ^[78] Liquidus Temperature Data for PWR Corium Containing Various Levels and Types of Concrete	144
A-4	(U,Zr)O _{2-x} Phase Diagram Constructed from Various Data Sources.....	146
A-5	Oxide Phase Solid Fraction vs. Normalized Temperature.....	147
C-1	DEH Input Power Relative to Onset of Basemat Ablation for ACE/MCCI Test Series.....	175
C-2	Melt Temperature Prediction for ACE Test L2	176
C-3	Ablation Front Location Prediction for ACE Test L2	177
C-4	Superficial Gas Velocity Prediction for ACE Test L2.....	177
C-5	Melt-Concrete and Melt-Atmosphere Heat Flux Prediction for ACE Test L2.....	178
C-6	Melt Temperature Prediction for ACE Test L4	178
C-7	Ablation Front Location Prediction for ACE Test L4	179
C-8	Superficial Gas Velocity Prediction for ACE Test L4.....	179
C-9	Melt-Concrete and Melt-Atmosphere Heat Flux Prediction for ACE Test L4.....	180
C-10	Melt Temperature Prediction for ACE Test L5	181
C-11	Ablation Front Location Prediction for ACE Test L5	181
C-12	Superficial Gas Velocity Prediction for ACE Test L5.....	182
C-13	Melt-Concrete and Melt-Atmosphere Heat Flux Prediction for ACE Test L5.....	182
C-14	Melt Temperature Prediction for ACE Test L6	183
C-15	Ablation Front Location Prediction for ACE Test L6	183
C-16	Superficial Gas Velocity Prediction for ACE Test L6.....	184
C-17	Melt-Concrete and Melt-Atmosphere Heat Flux Prediction for ACE Test L6.....	184
C-18	Melt Temperature Prediction for ACE Test L8	185
C-19	Ablation Front Location Prediction for ACE Test L8	186
C-20	Superficial Gas Velocity Prediction for ACE Test L8.....	186
C-21	Melt-Concrete and Melt-Atmosphere Heat Flux Prediction for ACE Test L8.....	187
C-22	Input Power Relative to Onset of Basemat Ablation for SURC-1 and -2	189
C-23	Melt Temperature Prediction for SNL SURC-1 Test	189
C-24	Ablation Front Location Prediction for SNL SURC-1 Test	190
C-25	Superficial Gas Velocity Prediction for SNL SURC-1 Test.....	190
C-26	Melt- Atmosphere Heat Flux Prediction for SNL SURC-1 Test.....	191

C-27	Melt Temperature Prediction for SNL SURC-2 Test	192
C-28	Ablation Front Location Prediction for SNL SURC-2 Test	192
C-29	Superficial Gas Velocity Prediction for SNL SURC-2 Test.....	193
C-30	Melt-Atmosphere Heat Flux Prediction for SNL SURC-2 Test.....	193
C-31	Input Power for OECD/MCCI CCI Tests.....	196
C-32	Melt Temperature Prediction for OECD/MCCI CCI-4 Test	197
C-33	Ablation Front Location Prediction for OECD/MCCI CCI-4 Test	197
C-34	Melt Temperature Prediction for OECD/MCCI CCI-4 Test	198
C-35	Ablation Front Location Prediction for OECD/MCCI CCI-4 Test	198
C-36	Melt Temperature Prediction for OECD/MCCI CCI-2 Test	200
C-37	Ablation Front Location Prediction for OECD/MCCI CCI-2 Test	200
C-38	Melt-Atmosphere Heat Flux Prediction for OECD/MCCI CCI-2 Test.....	201
C-39	Surface Elevation Predictions for OECD/MCCI CCI-2 Test	201
C-40	Melt Temperature Prediction for OECD/MCCI CCI-3 Test	203
C-41	Ablation Front Location Prediction for OECD/MCCI CCI-3 Test	203
C-42	Melt-Atmosphere Heat Flux Prediction for OECD/MCCI CCI-3 Test.....	204
C-43	Surface Elevation Predictions for OECD/MCCI CCI-3 Test	204
C-44	Melt Temperature Prediction for OECD/MCCI CCI-6 Test	205
C-45	Ablation Front Location Prediction for OECD/MCCI CCI-6 Test	206
C-46	Melt-Atmosphere Heat Flux Prediction for OECD/MCCI CCI-6 Test.....	206
C-47	Surface Elevation Predictions for OECD/MCCI CCI-6 Test	207

List of Tables

<u>Table</u>	<u>Page</u>
1-1 Summary of Coolability Mechanisms Observed in MACE Integral Tests	3
2-1 Summary of Concrete and Melt Constituents Treated in CORQUENCH4.1	11
2-2 Summary of Hierarchical Oxidation Scheme Assumed in CORQUENCH4.1	16
2-3 Summary of Conversion Factors for Evaluating Chemical Reaction Heat Due to Metals Oxidation in the Melt	18
3-1 Summary Format for CORQUENCH4.1 Input File ‘quenchin.dat’	93
3-2 CORQUENCH4.1 Input Variable Descriptions for ‘quenchin.dat’	96
3-3 Summary of Indicial Scheme for Melt/Concrete Interactions	107
3-4 Default Concrete Breakdowns in Terms of Simple Oxides ^[76-77]	109
3-5 Solidus and Liquidus Temperatures for Several Concrete Types ^[78]	109
4-1 Summary of CORQUENCH4.1 Data Output Files	121
4-2 Variable Definitions in Plotting File ‘spaceplot.x’	125
4-3 Variable Definitions in Plotting File ‘bigplots.1xxx’	126
4-4 Variable Definitions in Plotting File ‘quickplots.10xxx’	128
4-5 Variable Definitions in Plotting File ‘integralplot’	129
A-1 Summary of Indicial Scheme for Corium/Concrete Interactions	139
A-2 Summary of Solidus/Liquidus Specific Enthalpy Coefficients for the Materials Treated in CORQUENCH4.1.	140
A-3 Heat of Formation from the Oxides for the Various Concrete Decomposition Reactions Treated in CORQUENCH4.1	141
A-4 Solidus and Liquidus Temperatures for Several Concrete Types ^[78]	145
A-5 Metal Phase Constituent Coefficients for Thermal Conductivity below the Solidus	149
A-6 Oxide Phase Constituent Coefficients for Thermal Conductivity Below the Solidus	150
A-7 Factors Employed in the Shaw Viscosity Methodology ^[32] for the Oxide Mixtures Containing Silica	153
A-8 Assumed Liquid and Solid Phase Densities for the Various Corium Constituents Modeled by CORQUENCH4.1	155
A-9 Database ^[101-106] for Evaluating Crust Mechanical Properties in CORQUENCH4.1	156
A-10 Mineral Composition of Default Concretes	157

A-11	The Breakdown of CaO, MgO, H ₂ O, and CO ₂ into Dolomite, Calcium Carbonate, Calcium Hydroxide, and Free Water for Default Concretes	157
A-12	Default Concrete Breakdowns in Terms of Simple Oxides.....	157
C-1	Summary of Code Validation Experiment Characteristics	169
C-2	Composition of Metal-Concrete Inserts for ACE/MCCI Tests	172
C-3	Composition of Base Concretes for ACE/MCCI Tests	173
C-4	Composition of L4 Serpentine Concrete Layer	173
C-5	Assumed Properties of Concrete-Metal Inserts and Base Concretes for ACE/MCCI Tests.....	174
C-6	Assumed Properties for ACE/MCCI Test L4 Serpentine Concrete Layer	174
C-7	Initial Melt Compositions for the ACE/MCCI Tests	174
C-8	Assumed Initial Melt and Boundary Temperatures for the ACE/MCCI Tests.....	175
C-9	SURC-1 and -2 Concrete Compositions	187
C-10	Assumed Properties of Concretes for SURC Tests.....	188
C-11	Initial Corium Compositions for SURC Tests	188
C-12	Assumed Initial Melt and Boundary Temperatures for the SURC Tests.....	188
C-13	Concrete Compositions for OECD/MCCI Tests.....	195
C-14	Assumed Properties of Concretes for OECD/MCCI CCI Tests	195
C-15	Initial Corium Compositions for OECD/MCCI CCI Tests	195
C-16	Assumed Initial Melt and Boundary Temperatures for OECD/MCCI CCI Tests	195
C-17	Summary of CORQUENCH4.1 Validation Results Against 1-D Dry Cavity Tests	208

1.0 INTRODUCTION

1.1 Background

In support of the Melt Attack and Coolability Experiment (MACE) and OECD/MCCI programs,^[1] phenomenological model development for various ex-vessel debris cooling mechanisms has been underway at Argonne National Laboratory since the early 1990's.^[2-3] These efforts have increased the basic understanding of the unique heat and mass transfer processes that occur at the interface between corium and water when an MCCI is flooded from above.

To provide an integrated framework for assessing the ability of these models to adequately capture debris cooling behavior, a simple parametric core-concrete interaction code was developed^[4] to allow model comparisons with experiment results. The capability of this CORium QUENCHing (CORQUENCH) code was subsequently extended to allow first-order analysis of plant accident scenarios in which core-debris is postulated to accumulate in simplified, single node geometries (e.g., a sump or cylindrical cavity) under either wet or dry cavity conditions.^[5]

Since that work was completed,^[1-5] the reactor accidents at Fukushima Daiichi occurred. As a result, the nuclear industry has been reevaluating accident management strategies for both PWRs and BWRs. Specific to BWRs, previous accident management guidance called for flooding the drywell to a level of approximately 1.2 m (4 feet) above the drywell floor once vessel breach has been determined. While this action can help to submerge ex-vessel core debris, it can also result in flooding the wetwell and thereby rendering the wetwell vent path unavailable. On this basis, an alternate strategy has been proposed in industry guidance^[6] for responding to the severe accident capable vent Order, EA-13-109.^[7] This alternate strategy aims to throttle the flooding rate to achieve a stable wetwell water level while preserving the wetwell vent path and keeping the core debris covered with water.

To inform the development of these Severe Accident Water Management (SAWM) strategies, it became clear that improved analytical tools would be needed in order to realistically model ex-vessel core debris spreading and debris coolability behavior. This most recent version of CORQUENCH is intended to satisfy the enhanced modeling needs related to debris coolability; a separate model (i.e., MELTSPREAD3^[8]) has been enhanced to satisfy the need for realistic evaluations of likely debris locations within containment following vessel failure. The overall focus of this work is to provide a *flexible, analytically capable, and validated* model to support development of SAWM strategies that aim to keep ex-vessel core debris covered with water while preserving the BWR wetwell vent path. Specifically, there are gaps in analysis capability for evaluating core melt relocation and cooling behavior that accounts for several important factors that include the effect of water throttling on spreading and long term debris coolability. These gaps have been identified by an industry-lab advisory group as high priority items to address.^[9]

One specific factor that can impact flooding strategy is the spatial distribution of core melt in containment following vessel failure and melt spreading. For instance, a localized accumulation of melt in the pedestal region of a BWR may require a more specific flooding approach in comparison to the situation in which core melt is spread uniformly over the pedestal and drywell floor areas. In the former case, the localized core melt accumulation could form a dam preventing adequate debris flooding and cooling if the water is not injected directly on top the core debris, whereas in the latter case, effective debris flooding is expected regardless of injection point(s) as

long as the injection flowrate is high enough to remove both sensible and decay heat from the debris. These spatial distribution questions, coupled with the overall effectiveness of the debris cooling process, impact the water injection requirements for achieving a balance between water injection flowrate versus boil-off, thereby minimizing extraneous spillover into the wetwell.

1.2 Objectives and Approach

With the above background, the overall objectives of this work are three-fold:

- 1) Document the overall modeling strategy as well as the various phenomenological models that are embedded in CORQUENCH for calculating ex-vessel core debris coolability under realistic core melt distribution and cavity flooding conditions.
- 2) Provide a user guide for the code to facilitate the utilization of the software by other organizations and individuals that may have an interest.
- 3) Summarize the validation calculations that have been carried out in order to gauge the predictive capability of the code.

To this end, a phenomenology and literature review is provided to complete this introductory section as precursor to the phenomenological model descriptions that are provided in Section 2. This is followed by instructions on how to assemble the user input file for the code in Section 3. Subsequently, a description of the output text and plotting files is provided in Section 4. Finally, validation calculations, material property subroutines, and ancillary model derivations are provided in the appendices.

1.3 Phenomenology and Literature Review

Regarding the physics of core debris cooling in the presence of overlying water, several heat transfer mechanisms have been identified through experiments that can contribute to long-term corium coolability. These mechanisms are summarized in Table 1-1, while physical illustrations are provided in Figure 1-1. The database upon which these observations are based includes low temperature simulant experiments that were conducted by Theofanous *et al.*^[10] to identify phenomena associated with melt coolability, as well as high temperature simulant experiments conducted at Sandia National Laboratories by Blose *et al.*^[11,12] to investigate coolability with concurrent concrete erosion. In terms of reactor material testing, the COTELS,^[13,14] MACE,^[15,16] and OECD/MCCI programs^[17-22] have been completed to investigate the mechanisms of coolability under prototypic MCCI conditions. The results obtained from both the simulant and reactor material test programs have been summarized by Farmer *et al.*^[1]

In general, when an MCCI is flooded from above, the question of whether or not a significant amount of the thermal energy is initially removed will depend upon whether a stable crust is able to form that inhibits heat transfer from the melt to the water over layer. For a stable crust to form, two necessary conditions must be met:^[3] (i) a thermal condition, viz., the melt/water interfacial temperature must fall below the corium freezing temperature, and (ii) a mechanical condition, viz., the incipient crust must be stable with respect to local mechanical loads imposed by the agitated melt. If either of these two conditions is violated, then stable crust formation is precluded. In this bulk cooling regime, efficient melt/water heat transfer occurs due to conduction

and, predominately, radiation heat transfer across the agitated (i.e., area enhanced) melt/water interface, in addition to entrainment of melt droplets into the water overlayer.

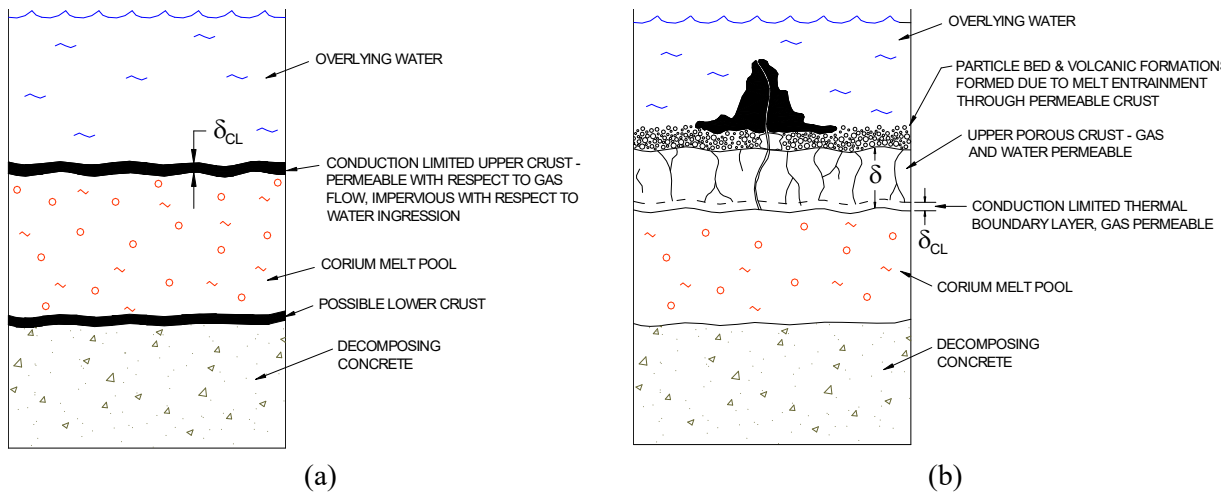


Figure 1-1. (a) Traditional View of CCI with Conduction-Limited Upper Crust at Melt-Water Interface; (b) CCI with Water Ingression and Melt Eruption Cooling Mechanisms.

Table 1-1. Summary of Coolability Mechanisms Observed in MACE Integral Tests.

Mechanism	Description	Experimental Evidence
Bulk Cooling	Melt sparging rate is initially high enough to preclude stable crust formation at melt/water interface. As a result, high heat transfer rates occur due to conduction and, predominately, radiation across the agitated (area enhanced) interface. This phase is terminated when a stable crust forms.	High heat transfer rates measured during early phase of the melt-water interaction. Data indicates that a coherent crust cannot form; rather, crust segments are broken up and mixed into melt.
Melt Eruptions	Melt dispersal mechanism by which concrete decomposition gases carry melt through defects in the crust to the overlying coolant; the dispersed material is quenched in the form of particle beds and as high surface area volcanic formations.	Eruptions observed in tests conducted with all concrete types after incipient crust formation. The particle beds are characterized by high porosity and large particle size.
Water Ingression	Corium shrinkage from an initially molten to a fully quenched state amounts to ~ 18 vol%. This causes voids/defects to appear in the frozen material. Water penetrates down through the voids/defects, augmenting what would otherwise be a conduction-limited heat transfer process.	Melt/water heat flux far exceeds that which can be transferred by conduction across the (up to 10 cm) thick crusts formed during the tests. Posttest measurements indicate that crusts are permeable to gas and water flows.
Crust Breach	Due to water ingression, thick crusts will form and bond to the reactor cavity walls. These crusts will not be stable in the typical ~ 6 m span of most plants. Thus, they will periodically fail, leading to renewed cooling by the above three mechanisms.	Partial crust failure and relocation events observed in MACE integral effects tests. Various structural - mechanical analyses have shown that crusts will not be stable at reactor scale.

As bulk cooling heat transfer continues, the melt temperature gradually declines. As the downward heat transfer rate decreases, then melt sparging arising from concrete decomposition also decreases. Thus, a point will eventually be reached at which the thermal and mechanical thresholds for interfacial crust formation are both satisfied, and an insulating crust will form between the coherent melt zone and water layer. The physical configuration at this point consists

of an ongoing MCCI at reduced temperature with a crust atop the melt (Figure 1-1(a)). The crust will be characterized by some degree of porosity, or cracks, owing to the necessity of venting concrete decomposition gases.

After incipient crust formation, completion of the quench process can only be achieved if one of two conditions is met. The first condition is that the melt depth lies below the minimum depth at which decay heat can be removed via conduction heat transfer alone (~10 cm). This case is trivial, and is not addressed in further detail. The second condition is that water is able to penetrate into the debris by some mechanism to provide sufficient augmentation to the otherwise conduction-limited heat transfer process to remove the decay heat. Three potential mechanisms have been identified through experiments that provide pathways for water to penetrate the debris.

The first mechanism is water ingress through interconnected porosity or cracks (Figure 1-1(b)). This process relies on crack propagation through the material and, as such, is highly dependent upon the mechanical properties, since thermal stress drives this process. The second mechanism is particle bed formation through “volcanic” eruptions. In this case, concrete decomposition gases entrain melt droplets into the overlying coolant as they pass through the crust. The entrained droplets then solidify in the overlying coolant and accumulate as a porous particle bed atop the crust. The third mechanism is mechanical breach of a suspended crust. In particular, the thick crusts that form from water ingress could bond to the reactor cavity walls, eventually causing the melt to separate from the crust as the MCCI continues downward. However, this configuration is not expected to be mechanically stable due to the poor mechanical strength of the crust in comparison to the applied loads (i.e., the crust weight itself, plus the weights of the overlying water pool and the accumulating, dispersed material). Eventually the suspended crust will fail, leading to rapid ingress of water beneath the crust. This sudden introduction of water will provide a pathway for renewed debris cooling by the bulk cooling, water ingress, and melt eruption cooling mechanisms.

In terms of modeling, a correlation for predicting the melt/water heat transfer rate during bulk cooling have been developed,^[2] as well as a model for predicting the critical superficial gas velocity at which stable crust formation occurs, thereby terminating the bulk cooling phase.^[3] These models have been compared with MACE test data with favorable results.^[4-5] Thus, of the four cooling mechanisms that have been identified, bulk cooling is thought to be the best understood since models exist, and limited validation of the models against test data has been performed. The test data as well as the models are deemed to be directly applicable to the reactor case since the interaction is scale independent as long as the test section lateral dimension is several times the sparging gas bubble diameter. This condition was satisfied for all reactor material tests. Aside from coolant properties, the models are dependent upon the sparging rate, gas bubble diameter, melt/crust thermophysical properties as well as the crust fracture strength. Crust strength data has been obtained as part of the MACE and MCCI programs,^[22] and this database is fairly substantial. The heat transfer coefficient during bulk cooling is linearly proportional to the gas sparging rate. Therefore, the model is sensitive to system pressure since the melt sparging rate is inversely proportional to system pressure.

For the water ingress cooling mechanism, fundamental modeling has been underway for some time in the area of geological research. In particular, Lister^[24] developed a theory for the mechanism of penetration of water into hot rock by using the concept of a cracking front which

separates a convective region in cracked porous rock from the conductive boundary layer below it. The material in the conduction boundary layer cools, and as a result, builds up horizontal tensile stress as the resistance to creep rises. Cracks within the material then propagate when the tensile stress exceeds the overburden pressure, resulting in stable downward propagation of a pattern of sub-vertical (polygonal) cracks. Further cooling and shrinkage widens the cracks to the percolation of water, so that the effective bulk permeability is a strong function of crack spacing and temperature. Equations were developed for the bulk permeability based on the above modeling approach, which permits the evaluation of the dryout heat flux.^[24] This theory has been used to explain qualitative aspects of cooling of the earth's mantle, in particular geological ridge crest heat-flow and seismic data. The attractive aspect of this modeling is that it provides a method for calculating the permeability based on the thermophysical properties (and temperatures) of the material involved, which includes the crust density, specific heat, thermal conductivity, linear expansion coefficient, fracture stress, Poisson's ratio, and the elastic modulus, in addition to properties of the coolant.

In a more recent study, Epstein^[25] developed a purely thermal, steady state model of the water ingress process. Epstein then combined the thermal model with Lister's description of the cracking front to obtain an approximate solution for the dryout heat flux, as well as the rate of downward solidification of the crust. Epstein found that the combined model is capable of predicting the field measurements obtained by watering of molten lava flow.^[26] Application of Epstein's model to the case of MCCI indicates that corium solidification by water ingress is not possible if the permeability of corium is the same as water-cooled lava (rock). However, whether the creep and cracking behavior of corium is similar to rock can only be answered through well-controlled experiments on the solidification rate of corium under a layer of water.^[25] This was one of several technical justifications for the conduct of the SSWICS water ingress tests.^[20-22] As part of the analysis efforts supporting these tests, Lomperski and Farmer^[20-21] extended the Epstein model to remove some of the empirical assumptions and make the correlation applicable to a wider range of conditions that might be expected in a plant accident. In particular, a simple analytical solution was proposed for evaluating the material temperature at onset of cracking. In addition, methods were proposed for evaluating key material mechanical properties (i.e., Young's modulus, tensile strength, and thermal expansion coefficient) as a function of melt composition. These considerations led to a correlation for the corium dryout heat flux with one empirical constant remaining, and this constant was adjusted to fit the SSWICS dryout heat flux data.^[21]

Motivated by the melt eruptions observed in the MACE Scoping Test, Bonnet and Seiler^[27] developed a parametric model of particle bed formation by means of melt entrainment during MCCI. In this model, melt dispersal is calculated by assuming that the melt entrainment rate is proportional to the gas volumetric flow rate times an entrainment coefficient. The entrained melt is assumed to accumulate on the upper surface of the crust in the form of a particle bed of specified porosity and particle diameter. The entrainment coefficient is an input parameter. Parametric calculations were performed with the model to determine if debris bed formation by the mechanism of melt entrainment is a viable means of achieving long term coolability. The results of the analysis indicated that transformation into a quenched debris bed could be achieved for entrainment coefficients as low as 0.1 to 0.01 % at atmospheric pressure. The entrainment process was found to be more efficient with concretes of higher gas content (since entrainment is proportional to gas release). The entrainment efficiency decreased with increasing system pressure (since gas volumetric flowrate from MCCI is inversely proportional to system pressure). The entrainment

coefficient was also found to be a sensitive input parameter. However, the initial melt temperature was found to have little effect on the entrainment process.

Aside from the reactor material experiments, the PERCOLA experiment program was carried out at the Commissariat à l'Energie Atomique (CEA) in Grenoble by Tourniaire *et al.*^[28] to provide fundamental insights into the eruption process under well-controlled experiment conditions. These tests utilized simulant materials with different viscosities to simulate the enrichment of corium with silica (SiO_2) during core-concrete interaction. Based on these data, Tourniaire and Seiler^[29] developed models of liquid ejection for the single-phase extrusion (or 'fountain') and two phase jetting eruption mechanisms through a floating solid layer that represented the interfacial crust that forms during core-concrete interaction. They compared their solutions with the test results and found that the principal trends in the test data were reasonably reproduced by the models. The results of their work highlighted the importance of modeling the frictional pressure drop through the solid layer, and the influence of the pressure drop on the calculation of liquid ejection for viscous fluids.

Although the models of Tourniaire and Seiler^[29] provide a sound technical basis for evaluating the entrainment rate when freezing effects are absent, these models need to be extended to include the effects of melt solidification and gas flow through the permeable crust that develops at the interface between the melt pool and overlying coolant. Other needs are the ability to predict the diameter of the vent holes through the crust, and also the eruption hole site density within the crust.^[29] On this basis, Farmer^[30] extended these existing models to include melt solidification and gas flow effects through the crust that develops at the interface between the melt pool and overlying coolant during core-concrete interaction. These efforts led to analytical solutions for the active melt eruption hole site density, as well as the average eruption hole diameter. The modeling considered the thermal hydraulic flow, pressure drop, and freezing processes involved with melt ejections through a crust that is permeable to both gas and water flows. Although significant progress was made with this modeling effort, two-phase flow effects still need to be factored into that analysis to ensure a robust treatment.

The crust breach mechanism has been postulated to be a contributor to debris coolability under prototypic conditions. Sustained anchoring and separation of a crust from the melt is not expected in a plant accident due to the large lateral span of the drywell/pedestal regions of these structures (typically 6 meters). However, the MACE test results showed that intermittent or localized crust anchoring to the pedestal walls is plausible. The thick crusts that form from water ingress may have sufficient mechanical strength to bond to the pedestal walls and temporarily separate from the ongoing MCCI. The voided region that results could take the form of an annular ring, due to potential slumping of the suspended crust in the central region. This configuration is, however, not expected to be stable due to mechanical weakness of the crust^[22] coupled with the combined loads that consist of the crust weight plus the weights of the overlying water and particle bed. Eventually the suspended crust will fail, leading to rapid ingress of water beneath the crust.

During a crust breach event, water will most likely flow down through the newly formed opening(s) and fill the intervening voided region. Depending upon the MCCI conditions at the time of breach, a renewed bulk cooling phase may occur. The introduction of water into the void will provide additional cooling of any crust material that remains attached to the pedestal sidewalls

from the initial breach event. A crust will eventually form over the underlying MCCI zone. After incipient crust formation, the potential exists for water ingression and melt dispersal cooling mechanisms to be reactivated. If this process continues, the final debris configuration could consist of layers of particles/porous lava interspersed with layers of permeable crust in a configuration reminiscent of a honeycomb.

Modeling of crust bridging is considered to be fairly straightforward; i.e., the analysis consists of utilizing correlations for stress in a flat plate as a function of plate area, thickness, and the loading which consists of the weight of the crust itself, as well as the weights of the overlying water and particle beds.^[4-5] Crust mechanical strength data from the tests^[22] is the final model input required to determine the plate (viz. crust) thickness required to be mechanically stable in the reactor cavity. This analysis indicates that crust thicknesses in the range of 20 to 30 cm would need to form before anchoring with separation would occur in a typical 6 m cavity span. This thickness is of the same order as the melt depth calculated in some accident sequences. Thus, if the crust were to anchor at this point, the core-concrete interaction would be effectively terminated since the heat removal would be sufficient to freeze and stabilize a large melt depth. The primary benefit of the modeling in this area is that for most plant simulations, one can assume a floating crust boundary condition, which greatly simplifies the modeling approach.

2.0 MODELING DESCRIPTION

2.1 Summary of Modeling Approach

The original philosophy behind the development of CORQUENCH was to build a simple, modular, MCCI analysis tool that could readily be adapted to incorporate new melt/water heat models as they become available for comparison with experiments. However, as noted in Section 1, the code has been upgraded as part of the current work to include a multi-nodal analysis capability that can treat variations in core debris distributions arising from containment geometry effects, and/or the extent of core debris spreading following vessel breach. A detailed water inventory model has also been integrated into the multi-nodal analysis capability so that realistic evaluations of cavity flooding behavior can be performed.

Regarding the general approach for MCCI modeling behavior on a node-by-node basis, the code is capable of performing either a 1-D or simplified 2-D ablation calculation (2-D geometry can be selected to be either cylindrical or rectilinear, with average axial and radial ablation depths calculated). The MCCI conservation of energy equation includes the following energy source/sink terms: i) decay heat, ii) mass flux of melt from the failed reactor pressure vessel, iii) chemical reactions between metallic melt constituents Zr, Si, Cr, Fe (in sequence) and concrete decomposition gases H₂O and CO₂, iv) condensed phase chemical reactions between Zr and SiO₂, v) downward (and sideward for 2-D case) heat transfer to concrete, including slag ingression into the melt, and vi) heat transfer to overlying atmosphere (wet or dry). The melt composition can range from fully metallic to fully oxidic; in all cases, the two phases are assumed to be well mixed (i.e., phase stratification is not modeled). The MCCI conservation of mass equations and thermophysical property subroutines consider most core and concrete metals and their corresponding oxides, so that a wide range of cases can be considered. Melt viscosity is calculated using the Andrade formula (see Nazare *et al.*^[31]) with a correction for SiO₂ as developed by Shaw.^[32] Viscosity enhancement due to buildup of solids within the melt can be calculated using either the Ishii-Zuber^[33] or Kunitz^[34] models. Melt void fraction, which is relevant in determining the melt upper surface location as well as the location where the crust anchors to the test section sidewalls in experiments, can be evaluated from one of several different correlations; i.e., those due to Brockmann *et al.*,^[35] Wallis,^[36] and Kataoka and Ishii.^[37]

In terms of heat transfer at the melt/concrete interface, CORQUENCH incorporates a transient concrete ablation/decomposition model based on integral thermal boundary layer theory (Corradini^[38]). This model has been upgraded as part of this work to account for the effects of transient concrete heatup with simultaneous crust growth following initial melt contact with the concrete. The inclusion of a concrete dryout model is considered to be important in evaluating both the early and late phases of core-concrete interaction. In the early phase, transient crust formation can affect the timing of onset of ablation, while in the late phase, heat transfer to underlying concrete can fall to low levels as the decay heat decreases, and so conduction into the concrete behind the ablation front becomes important in determining the overall ablation rate and eventual core debris stabilization. The heat transfer coefficient at the melt/concrete interface can be selected from a variety of options, including: i) Bradley's modification^[39] to the bubble agitation heat transfer model of Kutateladze and Malenkov,^[40] ii) gas film models similar to those deployed in CORCON Mod3,^[41] and iii) the empirical correlations developed by Sevón^[42] on the basis of the CCI test results.

At the melt upper surface, radiant heat transfer to overlying structure is calculated when the cavity is dry. When water is present, bulk cooling and incipient crust formation are calculated using the models developed by Farmer *et al.*^[2,3] Following incipient crust formation, crust growth is calculated by solving a growth rate equation; the crust material composition is treated separately from the melt material composition, which is important in long-term calculations where significant mass may be frozen in the crust. The melt-side convective heat transfer coefficient is calculated using the correlation of Kutateladze and Malenkov.^[40] For the case in which the crust is treated as permeable to water ingression, then the crust dryout limit can be calculated using either a user-specified permeability, or the limit can be calculated with the Lomperski and Farmer model.^[20]

For situations in which water is present and a particle bed develops over the crust, the heat flux from the crust upper surface may be limited by the particle bed dryout limit. For this case, the dryout limit is calculated with the Lipinski correlation.^[43] The heat flux from the crust upper surface is checked during the calculation to ensure that it does not exceed the effective dryout limit. If this limit is exceeded, then the heat flux from the crust surface is capped at the dryout limit.

Aside from calculating crust growth under a variety of modeling assumptions, particle bed formation by the mechanism of melt eruptions is also evaluated. In order to incorporate the basic elements of this cooling mechanism in the current analysis, the modeling approach of Bonnet and Seiler is adopted;^[27] i.e., melt dispersal is calculated by assuming that the melt entrainment rate is proportional to the gas volumetric flowrate times an entrainment coefficient. Several options are provided for evaluating the melt entrainment coefficient: i) the user may specify the coefficient directly, ii) the entrainment coefficient can be evaluated with the Ricou-Spalding model,^[44] or the coefficient can be evaluated using the model due to Farmer^[30] that also provides analytical solutions for the active melt eruption hole site density, as well as the average eruption hole diameter. Consistent with test observations, the dispersed melt is assumed to be rendered in the form of an accumulating particle bed (with specified particle diameter and porosity) on top of the crust. As noted earlier, the bed dryout heat flux limitation is evaluated with the Lipinski correlation.^[43]

The above methods provide a general framework for predicting simultaneous upper crust and particle bed growth rates during MCCI. However, the model has also been developed to mechanistically calculate the important experiment distortion of crust anchoring to the test section sidewalls, as well as the subsequent melt/crust separation phase that arises due to concrete densification upon melting. For a given cavity span, the minimum crust thickness required to be mechanically stable due to the combined weights of the overlying water pool, particle bed, and the crust itself is evaluated using a first-order plate strength equation from Roark and Young.^[45] During the calculation, the upper crust thickness is compared with that predicted from the Roark and Young equation. When the thickness exceeds the minimum required to be mechanically stable in the given test section configuration, the crust is assumed to attach to the test section sidewalls with the upper surface elevation fixed at the location at the time of anchoring. Thereafter, the voided melt upper surface location is tracked relative to the crust location so that the onset of gap formation can be predicted. When a gap does form, debris quenching by the mechanisms of crust water ingression and melt eruptions terminates, and there is a corresponding reduction in upwards heat transfer due to *solidification* (latent heat) processes. Moreover, a heat transfer resistance across the gap is introduced into the heat balance, which causes a further reduction in upwards heat

transfer. This methodology, although first order in nature, does allow the prediction of the crust anchoring time and location for comparison with test results such as those obtained in the MACE program.^[1,15,16] Moreover, the model allows the prediction of the upwards heat flux both before and after separation. This allows the model to be more rigorously validated against test data, which increases the confidence level when the model is extrapolated to plant conditions.

The above summary was intended to highlight some of the key modeling features as well as shortcomings of the CORQUENCH model. More detailed information regarding the modeling approach is provided in the following sections that lay out the overall set of equations that are used to calculate the progression of the core-concrete interaction under both wet and dry cavity conditions on a node-by-node basis. Changes made to incorporate a multi-node analysis capability as well as the detailed water inventory model are outlined at the end of this section. Aside from these physical models, the code has been developed with a fairly extensive set of property subroutines; these are described in Appendix A. Validation calculations carried out with the code against a collection of experiments are documented in Appendix C.

2.2 Melt Zone Conservation of Mass and Energy Equations

The mass conservation and material property routines within CORQUENCH consider most of the major LWR core and concrete metals, as well as their corresponding oxide forms. The materials that are treated within the code are summarized in Table 2-1, while a sketch illustrating the overall modeling approach is provided in Figure 2-1. Fission products are not currently modeled as they normally constitute a fairly small volumetric fraction of the overall corium composition. Decay heat within the debris is of course modeled, but rather than tracking fission product decay chains as a means of evaluating the overall debris heating level, the code relies on a user-specified decay heat function that can be expressed in several different forms (see Section 3.0). The melt composition can range from fully metallic to fully oxidic. However, in all cases the two phases are assumed to be well mixed (i.e., phase stratification is not modeled).

The conservation of mass equation for the i^{th} melt constituent is written in general form as:

$$\begin{aligned} \dot{m}_i = A_b \left\{ \gamma_i^{H_2O} \dot{m}_{b,H_2O} + \gamma_i^{CO_2} \dot{m}_{b,CO_2} + \gamma_i^{SiO_2} \dot{m}_{b,SiO_2} - \langle \chi \rho \rangle_{t,i} \dot{\delta}_t - \langle \chi \rho \rangle_{b,i} \dot{\delta}_b \right. \\ \left. + \chi_{con,i} \rho_{con} \dot{\eta}_b - \chi_{m,i} \dot{m}_{ent} \right\} + A_s \left\{ \gamma_i^{H_2O} \dot{m}_{s,H_2O} + \gamma_i^{CO_2} \dot{m}_{s,CO_2} + \gamma_i^{SiO_2} \dot{m}_{s,SiO_2} \right. \\ \left. - \langle \chi \rho \rangle_{s,i} \dot{\delta}_s + \chi_{con,i} \rho_{con} \dot{\eta}_s \right\} + \dot{m}_{core} - X_C \chi_{m,i} \rho_{sol,m} (\delta_b + \delta_t) \dot{\eta}_s - \langle \chi \rho \rangle_{s,i} A_C \dot{H}_m \end{aligned} \quad (2-1)$$

where superscript ‘ \cdot ’ denotes a derivative with respect to time, subscripts b , s , and t denote the basemat, sidewall, and top surfaces of the melt zone, respectively, subscripts m and con denote melt and concrete zones, subscript sol denotes solid state, and:

Table 2-1. Summary of Concrete and Melt Constituents Treated in CORQUENCH4.1.

Constituent	Notes
Na ₂ O	Concrete and/or Corium Constituents
TiO ₂	
SiO ₂	
CaO	
MgO	
Al ₂ O ₃	
FeO	
Fe ₂ O ₃	
Fe ₃ O ₄	
Fe	
Cr	
Ni	
Zr	
ZrO ₂	
B ₂ O ₃	
U	Corium Constituents
B ₄ C	
Si	
SiC	
Cr ₂ O ₃	
NiO	
UO ₂	

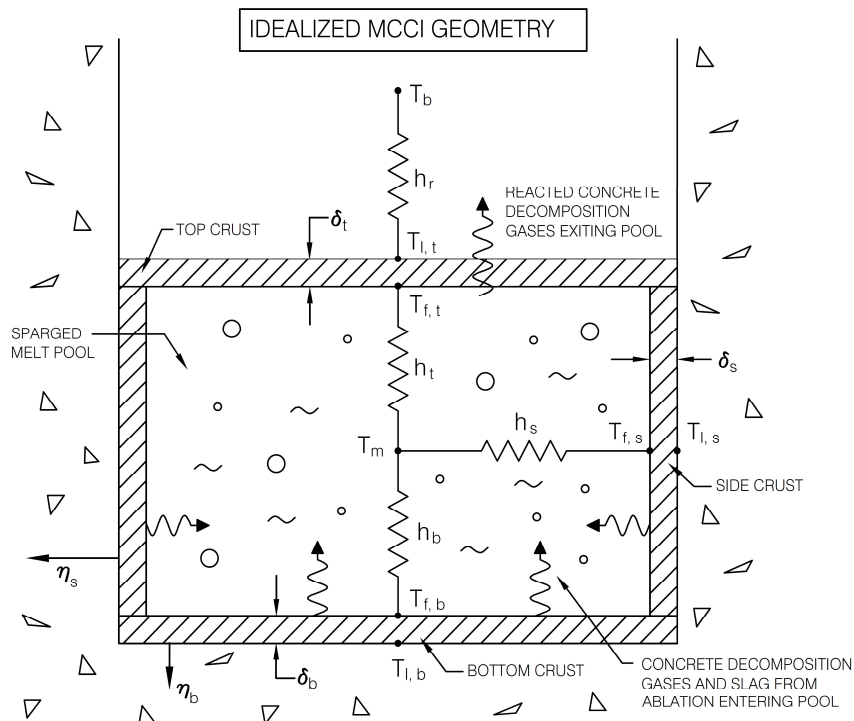


Figure 2-1. Illustration of Simplified Modeling Approach (dry cavity conditions).

m_i	=	mass of i^{th} constituent present in melt zone,
A_b	=	basemat axial surface area (assumed equal to top surface area),
A_s	=	radial surface area of melt in contact with the concrete,
\dot{m}_{H_2O}	=	local mass flux of H_2O into melt from concrete ablation,
$\gamma_i^{H_2O}$	=	factor relating the flux of H_2O into melt to the flux of metal consumed (or oxide created) due to oxidation reactions within the melt,
\dot{m}_{CO_2}	=	local mass flux of CO_2 into melt from concrete ablation,
$\gamma_i^{CO_2}$	=	factor relating the flux of CO_2 into melt to the flux of metal consumed (or oxide created) due to oxidation reactions within the melt,
\dot{m}_{SiO_2}	=	local mass flux of SiO_2 into melt from concrete erosion,
$\gamma_i^{SiO_2}$	=	factor relating the flux of SiO_2 into the melt to the flux of Zr consumed and SiO_x produced due to condensed phase chemical reactions,
\dot{m}_{ent}	=	mass flux from the melt zone to the particle bed due to volcanic eruptions,
$\dot{m}_{core,i}$	=	mass flux of i^{th} melt constituent from the RPV into the melt zone,
ρ	=	density,
χ	=	weight fraction,
X_C	=	circumference around periphery of the concrete crucible,
A_C	=	total planar area of sidewall crust material,
\dot{H}_m	=	rate of change of melt pool depth in contact with sidewall crust,
δ	=	crust depth, and
η	=	concrete ablation depth.

A melt zone conservation equation is solved for each of the 22 constituents shown in Table 2-1 (i.e., $i=1, \dots, 22$).

The signs on the crust growth rates in Eq. 2-1 are taken as positive when the crusts are thickening, while the ablation rates are taken as positive when the progression is into the concrete. Specific expressions for the crust and ablation rates, as well as the gas mass flux from concrete decomposition and the flux due to melt eruptions, are developed later in this section. When a 1-D calculation is performed, the sidewall (subscript s) components in Eq. 2-1 are set to zero within the code. The functions $\langle \chi \rho \rangle_i$ denotes the mass density of the i^{th} constituent that is being deposited in the crust from the melt when the crust is growing, or is being placed into the melt from the crust if the crust is remelting. Thus, this function is dependent upon the sign on $\dot{\delta}$, and for the top crust can be expressed as:

$$\langle \chi \rho \rangle_{t,i} = \begin{cases} \chi_{m,i} \rho_{sol,m}; & \dot{\delta}_t > 0 \\ \chi'_{cr,i} \rho_{cr,t}; & \dot{\delta}_t < 0 \end{cases} \quad (2-2)$$

where subscript *cr* denotes the crust zone. Analogous expressions apply to the additional $\langle \chi \rho \rangle_i$ functions shown in Eq. 2-1 for the side and bottom crusts. CORQUENCH has been structured to solve separate conservation of mass equations for the crusts and the particle bed that develop during the course of the interaction. This step was taken so that material properties, such as the crust densities shown in Eq. 2-2, can be evaluated on the basis of the actual compositions, as opposed to assuming that the compositions are approximately equal to that of the melt. Thus, aside from the 22 simultaneous mass conservation equations for the melt, the code solves an additional 22 mass conservation equations for each of the top, bottom, and side crusts, as well as the particle bed over the melt. Equations for these additional mass conservation equations are provided later in this subsection after additional background is provided.

Given the solutions to Eq. 2-1 for each of the constituents shown in Table 2-1, then the total time-rate of change of the mass in the *melt zone* is calculated from:

$$\dot{m} = \sum_{i=1}^{22} \dot{m}_i \quad (2-3)$$

Similarly, given the integrated mass of the melt pool constituents, then the total melt pool mass at any time is found through the expression:

$$m = \sum_{i=1}^{22} m_i \quad (2-4)$$

As noted earlier, CORQUENCH performs either a 1-D or simplified 2-D cavity erosion analysis. For the 2-D case, four simple geometries are provided as user options. The first is an idealized cylindrical geometry in which the cavity is characterized by an initial circular basemat area of $A_{b,o}$, and corresponding initial radius $R_o = \sqrt{A_{b,o} / \pi}$. The second and third options are simple notch geometries like that employed in the CCI test series.^[17,18] In particular, for the second option the basemat is initially rectangular in shape, with two diametrically opposite walls that undergo ablation, while the other two walls are treated as adiabatic. The user specifies the length L between the two ablating walls and width W between the two adiabatic walls, and the initial basemat surface area is then calculated as $A_{b,o} = L_o W$. The third option is identical to the second, but only one wall undergoes ablation while the other three are treated as adiabatic. The fourth option is a cylindrical annulus model with an inner surface of radius R_i that is treated as adiabatic. In this case the initial outer radius is given by $R_o = \sqrt{A_{b,o} / \pi + R_i^2}$. For the assumed cavity geometry, the basemat surface area in Eq. 2-1 is then evaluated through the following equation:

$$A_b = \begin{cases} \pi [(R_o + \eta_s)^2 - R_i^2], & \text{cylindrical geometries} \\ W(L_o + 2\eta_s), & \text{notch geometry with two ablatable walls} \\ W(L_o + \eta_s), & \text{notch geometry with one ablatable wall} \end{cases} \quad (2-5)$$

As noted earlier, the surface area at the top of the melt pool is assumed to be identical to the basemat surface area in this simplified scheme (i.e., $A_t = A_b$).

Given the initial basemat surface area $A_{b,o}$ for the 1-D case, or the time-dependent basemat area from Eq. 2-5 for the 2-D case, then the voided melt height in the crucible is found from:

$$H_{m,v} = \frac{m}{\rho_m A_b (1 - \alpha)} \quad (2-6)$$

where α is the melt void fraction (correlations are provided later in this section). With this result, the concrete sidewall surface area in contact with the melt is calculated from:

$$A_s = \begin{cases} 2\pi(R_o + \eta_s)H_{m,v}, & \text{cylindrical geometries} \\ 2WH_{m,v}, & \text{notch geometries} \end{cases} \quad (2-7)$$

With the above description of the idealized 2-D cavity geometry models, it is now possible to explain the last two terms on the right hand side of Eq. 2-1; i.e., $X_C \rho_{sol,m} \chi_{m,i} \dot{\eta}_s (\delta_b + \delta_t)$ and $\langle \chi \rho \rangle_{s,i} A_C \dot{H}_m$. For situations in which crust growth is calculated at the bottom and/or top surface of the melt zone, the term $X_C \rho_{sol,m} \chi_{m,i} \dot{\eta}_s (\delta_b + \delta_t)$ accounts for the extra crust area that is created as the cavity erodes laterally outwards. In a true 2-D cavity erosion model in which the local crust depth is calculated as a continuum around the full periphery of the melt surface in contact with concrete, this term would not be required. However, it is required in this simplified model in order to properly conserve mass. For the cylindrical cavity models, the circumferential distance around the cavity periphery in contact with melt is $X_C = 2\pi(R_o + \eta_s)$, whereas for the 2-D notch models, $X_C = 2W$.

For situations in which crust growth is calculated on the side surface of the melt pool, the term $\langle \chi \rho \rangle_{s,i} A_C \dot{H}_m$ in Eq. 2-1 similarly accounts for the sidewall crust mass that is created (or consumed) as the melt depth increases (or decreases). The rate of change of the melt depth is calculated through the following expression:

$$\dot{H}_m \sim \frac{(1 - \chi_{con,g}) \rho_{con}}{\rho_{slag}} \dot{\eta}_b + \frac{\dot{m}_{core}}{\rho_{core} A_b} - \left(\dot{\delta}_b + \dot{\delta}_t + j_m \right) \quad (2-8)$$

where:

$\chi_{con,g}$	=	combined mass fraction of H ₂ O and CO ₂ in concrete,
ρ_{slag}	=	density of concrete slag formed upon decomposition of concrete,
\dot{m}_{core}	=	total mass pour rate from the RPV into the melt zone,
ρ_{core}	=	density of melt issuing from the RPV, and
j_m	=	superficial gas velocity of melt entrained from pool due to eruptions.

Equation 2-8 is an approximate expression that neglects the influence of oxidation reactions and melt void fraction on the rate of change of melt depth in the cavity. Finally, the planar area A_C of the sidewall crust material in this mass transfer term is calculated through:

$$A_C = \begin{cases} \pi[(R_o + \eta_s)^2 - (R_o + \eta_s - \delta_s)^2], & \text{cylindrical geometries} \\ 2W\delta_s, & \text{notch geometries} \end{cases} \quad (2-9)$$

With the above explanations, then the conservation of mass equation for the i^{th} corium constituent in the solidified bottom crust is found from:

$$\dot{m}_{b,i} = A_b \langle \chi \rho \rangle_{b,i} \dot{\delta}_b + X_C \rho_{sol,m} \chi_{m,i} \dot{\delta}_b \dot{\eta}_s \quad (2-10)$$

From this equation, it is clear that the bulk (i.e., homogenized) composition of the crust is tracked, but the spatial variation of the composition that would arise due to variations in melt composition as the crust forms is not. The integrated conservation of mass equation for the crust is thus:

$$\dot{m}_b = \sum_{i=1}^{22} \dot{m}_{b,i} \quad (2-11)$$

Finally, given the rate equations for the crust constituents, the total mass of the bottom crust is found through the summation:

$$m_b = \sum_{i=1}^{22} m_{b,i} \quad (2-12)$$

The analogous conservation equations for the constituents in the top and side crusts are:

$$\dot{m}_{t,i} = A_t \langle \chi \rho \rangle_{t,i} \dot{\delta}_t + X_C \rho_{sol,m} \chi_{m,i} \dot{\delta}_t \dot{\eta}_s \quad (2-13)$$

$$\dot{m}_{s,i} = A_s \langle \chi \rho \rangle_{s,i} \dot{\delta}_s + \langle \chi \rho \rangle_{s,i} A_C \dot{H}_m \quad (2-14)$$

The integrated conservation of mass equations for the top and side crusts are identical in form to those given in Eqs. 2-11 and 2-12. For completeness, the final set of equations describing the mass evolution in the particle bed that forms above the top crust due to melt eruptions are:

$$\dot{m}_{bed,i} = A_b \chi_{m,i} \dot{m}_{ent} \quad (2-15)$$

$$\dot{m}_{bed} = A_b \dot{m}_{ent} \quad (2-16)$$

$$m_{bed} = \sum_{i=1}^{22} m_{bed,i} \quad (2-17)$$

As previously noted, models for $\dot{\delta}_b$, $\dot{\delta}_s$, $\dot{\delta}_t$, $\dot{\eta}_s$, and \dot{m}_{ent} are provided later in this section.

Returning to the melt conservation of mass equation, the formulation accounts for mass transfer mechanisms within the melt due to oxidation reactions between metallic melt constituents and the sparging concrete decomposition gases H₂O and CO₂, as well as condensed phase chemical reactions between unoxidized Zr cladding and SiO₂ introduced into the melt from concrete erosion. The chemical reactions that are currently modeled are summarized in Table 2-2. (Note that M in this table denotes the molecular weight of the subscripted metal or oxide). This table also provides the definitions of the various stoichiometric conversion factors (γ) that are required to relate the mass flux of oxidizing agents into the melt from concrete erosion to the rate of metal consumption (as well as the rate of oxide formation) by these reactions. For the gas phase reactions, a hierarchical oxidation scheme is employed in which Zr is assumed to oxidize first, followed by Si, Cr, and finally Fe. The condensed phase reaction between Zr and SiO₂ is assumed to proceed in parallel with the gas phase reactions, if the user invokes this modeling assumption.

Both the gas and condensed phase chemical reactions are assumed to be limited by the mass transfer rate of oxidizing agents (i.e., H₂O, CO₂, and SiO₂) brought into the melt from

concrete erosion. However, the code does check at each timestep to see if the reaction rate could be limited by the amount of metal present in the melt. This type of situation can develop, for instance, when the basemat contains a modest amount of reinforcing bar. In this case, iron could be ablated into the melt at a rate less than the amount that could be consumed by the oxidation gases produced by concrete erosion. The code checks at each timestep to see if this is the case and, if so, the reaction fraction for the chemical reaction is set equal to the value that would result in complete oxidation of the metal brought into the melt at each timestep. These reaction fractions, which range from 0 to 1, are denoted as F_{Zr} , F_{Si} , F_{Cr} , F_{Fe} , and F_{cond} in Table 2-2.

Table 2-2. Summary of Hierarchical Oxidation Scheme Assumed in CORQUENCH4.1.

Constituents	$\gamma_i^{H_2O}$	$\gamma_i^{CO_2}$	$\gamma_i^{SiO_2 *}$	Oxidation Reactions
$i = Zr$	$-\frac{F_{Zr}M_{Zr}}{2M_{H_2O}}$	$-\frac{F_{Zr}M_{Zr}}{2M_{CO_2}}$	$-\frac{F_{cond}(1+F_{Si})M_{Zr}}{2M_{SiO_2}}$	$Zr + 2H_2O \rightarrow ZrO_2 + 2H_2$ $Zr + 2CO_2 \rightarrow ZrO_2 + 2CO$
$i = ZrO_2$	$\frac{F_{Zr}M_{ZrO_2}}{2M_{H_2O}}$	$\frac{F_{Zr}M_{ZrO_2}}{2M_{CO_2}}$	$\frac{F_{cond}(1+F_{Si})M_{ZrO_2}}{2M_{SiO_2}}$	See $i = Si$ and $i = SiO_2$ below for condensed phase chemical reaction definitions
$i = Cr$	$-\frac{2F_{Cr}M_{Cr}}{3M_{H_2O}}$	$-\frac{2F_{Cr}M_{Cr}}{3M_{CO_2}}$	0	$2Cr + 3H_2O \rightarrow Cr_2O_3 + 3H_2$ $2Cr + 3CO_2 \rightarrow Cr_2O_3 + 3CO$
$i = Cr_2O_3$	$\frac{F_{Cr}M_{Cr_2O_3}}{3M_{H_2O}}$	$\frac{F_{Cr}M_{Cr_2O_3}}{3M_{CO_2}}$	0	
$i = Fe$	$-\frac{F_{Fe}M_{Fe}}{M_{H_2O}}$	$-\frac{F_{Fe}M_{Fe}}{M_{CO_2}}$	0	$Fe + H_2O \rightarrow FeO + H_2$ $Fe + CO_2 \rightarrow FeO + CO$
$i = FeO$	$\frac{F_{Fe}M_{FeO}}{M_{H_2O}}$	$\frac{F_{Fe}M_{FeO}}{M_{CO_2}}$	0	
$i = Si$	$-\frac{F_{Si}M_{Si}}{2M_{H_2O}}$	$-\frac{F_{Si}M_{Si}}{2M_{CO_2}}$	$\frac{F_{cond}F_{Si}M_{Si}}{2M_{SiO_2}}$	Gas phase: $Si + 2H_2O \rightarrow SiO_2 + 2H_2$ $Si + 2CO_2 \rightarrow SiO_2 + 2CO$
$i = SiO_2$	$\frac{F_{Si}M_{SiO_2}}{2M_{H_2O}}$	$\frac{F_{Si}M_{SiO_2}}{2M_{CO_2}}$	$-F_{cond}$	Condensed Phase: For $T_m \leq 2784$ K, $F_{Si}=1$ and: $Zr + SiO_2 \rightarrow ZrO_2 + Si(l)$ For $T_m > 2784$ K, $F_{Si}=0$ and: $Zr + 2SiO_2 \rightarrow ZrO_2 + 2SiO(g)$
All other constituents	0	0	0	-

*If condensed phase chemical reactions are modeled and Zr is present either in the melt or the concrete, then the parameter F_{cond} is set equal to one by the code. Otherwise, F_{cond} is set to zero to turn off this modeling option.

Finally, analysis of the Gibbs free energy for potential Zr-SiO₂ reactions indicates that the reaction $Zr + SiO_2 \rightarrow ZrO_2 + Si(l)$ is preferred when the melt temperature is < 2784 K, while the reaction $Zr + 2SiO_2 \rightarrow ZrO_2 + 2SiO(g)$ is preferred when the temperature is above this value. As shown in Table 2-2, the stoichiometric constants within the code are set according to this temperature in order to yield the appropriate chemical reaction. When the temperature is above 2784 K, the SiO is assumed to be liberated from the system as a gas.

The melt zone conservation of energy equation includes the usual list of energy source/sink terms, including decay heat, energy flux of melt from the failed reactor pressure vessel, chemical

reactions, downward (and sideward for 2-D case) heat transfer to concrete, including heat addition due to slag ingression into the melt, and heat transfer to overlying atmosphere (wet or dry). Specifically, the conservation of energy equation is of the form:

$$\begin{aligned}
 \dot{e} = \frac{1}{m} & \left\{ -\dot{m} e + \chi_{m,UO_2} m q_{dec} - A_b h_t (T_m - T_t) - A_b h_b (T_m - T_b) - A_s h_s (T_m - T_s) \right. \\
 & + E_{H_2O} \left(A_b \dot{m}_{b,H_2O} + A_s \dot{m}_{s,H_2O} \right) + E_{CO_2} \left(A_b \dot{m}_{b,CO_2} + A_s \dot{m}_{s,CO_2} \right) \\
 & + E_{SiO_2} \left(A_b \dot{m}_{b,SiO_2} + A_s \dot{m}_{s,SiO_2} \right) + (1 - \chi_{con,g}) \rho_{con} e_{con,d} \left(A_b \dot{\eta}_b + A_s \dot{\eta}_s \right) \\
 & - A_b \left(\langle \rho e \rangle_b \dot{\delta}_b + \langle \rho e \rangle_t \dot{\delta}_t \right) - A_s \langle \rho e \rangle_s \dot{\delta}_s - X_C \rho_{sol,m} e \dot{\eta}_s (\delta_b + \delta_t) \\
 & \left. - \langle \rho e \rangle_s A_C \dot{H}_m - A_b \dot{m}_{ent} e + \dot{m}_{core} e_{core} \right\} \quad (2-18)
 \end{aligned}$$

where:

e	=	melt zone specific enthalpy (J/kg),
e_{core}	=	specific enthalpy of corium draining from the reactor vessel,
$e_{con,d}$	=	concrete specific enthalpy at the decomposition temperature,
T_m	=	melt temperature,
E_{H_2O}	=	reaction heat for metals that are undergoing oxidation by H ₂ O,
E_{CO_2}	=	reaction heat for metals that are undergoing oxidation by CO ₂ ,
E_{SiO_2}	=	reaction heat for Zr metal undergoing oxidation by SiO ₂ ,
q_{dec}	=	melt decay heat level (expressed as W/kg fuel), and
h	=	interfacial heat transfer coefficient.

The melt zone boundary temperatures T_t , T_s , and T_b in Eq. 2-18 are functions of the particular heat transfer modeling assumption that is made at a surface, and whether or not a crust is present at that interface. Specifications for these temperatures are provided in Sections 2.3 to 2.5, while models for the interfacial heat transfer coefficients h_t , h_s , and h_b are provided in Sections 2.4 to 2.6. Similar to the definition of $\langle \chi \rho \rangle_i$ in Eq. 2-1, the functions $\langle \rho e \rangle_i$ in Eq. 2-18 denote the enthalpy per unit volume of the material that is deposited in the crust from the melt when the crust is growing, or is being placed back into the melt from the crust if the crust is remelting; e.g.,

$$\langle \rho e \rangle_t = \begin{cases} \rho_{sol,m} e(T_m); & \dot{\delta}_t > 0 \\ \rho_{t,cr} e_{t,cr}(T_{t,frz}); & \dot{\delta}_t < 0 \end{cases} \quad (2-19)$$

where $e_{t,cr}(T_{t,frz})$ is the specific enthalpy of the top crust material evaluated at the crust freezing temperature. Analogous expressions apply to the additional $\langle \rho e \rangle$ functions shown in Eq. 2-18 for the side and bottom crusts.

Finally, definitions for the conversion factors relating the mass flux of oxidizing agents into the pool to the heat liberated through chemical reactions with metallic melt constituents are provided in Table 2-3. The reaction heats (i.e., q_i^j variables in Table 2-3) have been expressed in units of MJ/kg metal reacted, and are shown graphically in Figure 2-2. These data have been computed for the various chemical reactions based on heat of formation data found in the JANAF Thermochemical Tables. [46]

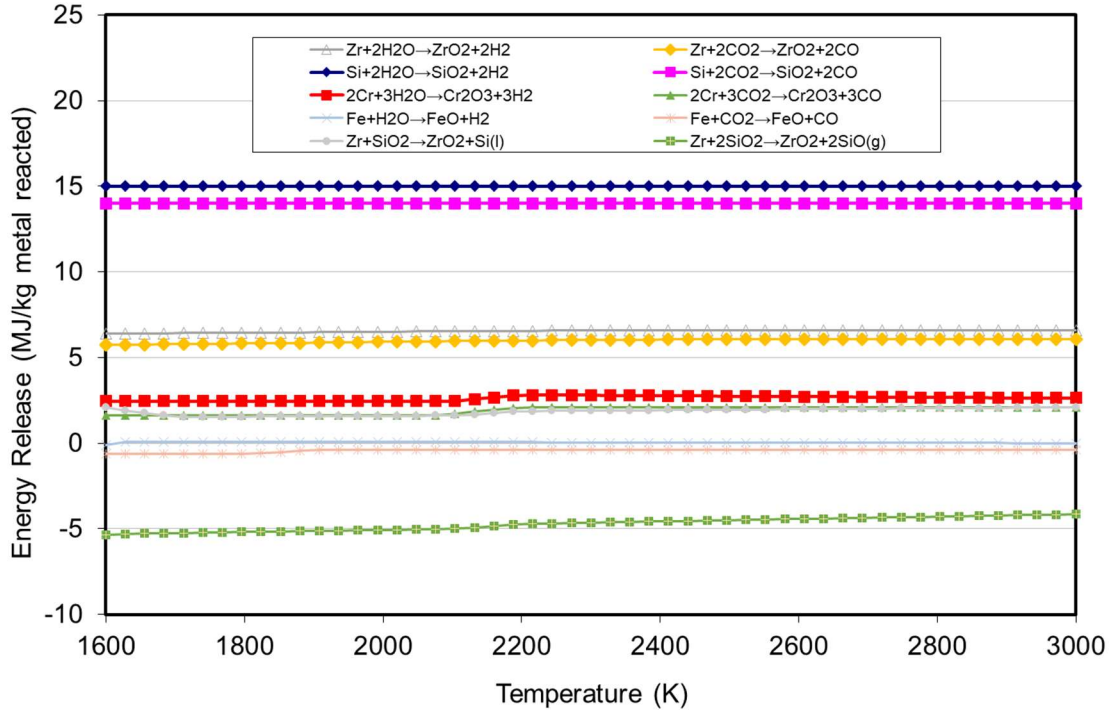


Figure 2-2. Reaction Heats vs. Temperature for Gas- and Condensed-Phase Chemical Reactions (reaction heats defined as positive for exothermic reactions).

Table 2-3. Summary of Conversion Factors for Evaluating Chemical Reaction Heat Due to Metals Oxidation in the Melt.

Constituents	E_{H_2O}	E_{CO_2}	E_{SiO_2}
$i = Zr$	$\frac{F_{Zr} M_{Zr}}{2M_{H_2O}} q_{Zr}^{H_2O}$	$\frac{F_{Zr} M_{Zr}}{2M_{CO_2}} q_{Zr}^{CO_2}$	$\frac{F_{cond} M_{Zr}}{M_{SiO_2}} \left(F_{Si} q_{Zr}^{SiO_2 \rightarrow Si} + \frac{(1-F_{Si})}{2} q_{Zr}^{SiO_2 \rightarrow SiO} \right)$
$i = Si$	$\frac{F_{Si} M_{Si}}{2M_{H_2O}} q_{Si}^{H_2O}$	$\frac{F_{Si} M_{Si}}{2M_{CO_2}} q_{Si}^{CO_2}$	0
$i = Cr$	$\frac{2F_{Cr} M_{Cr}}{3M_{H_2O}} q_{Cr}^{H_2O}$	$\frac{2F_{Cr} M_{Cr}}{3M_{CO_2}} q_{Cr}^{CO_2}$	0
$i = Fe$	$\frac{F_{Fe} M_{Fe}}{M_{H_2O}} q_{Fe}^{H_2O}$	$\frac{F_{Fe} M_{Fe}}{M_{CO_2}} q_{Fe}^{CO_2}$	0

Eqs. 2-1 through 2-4 and 2-18 constitutes the basic models that are used to calculate the evolution of the melt pool temperature and composition during the course of the core-concrete

interaction. The balance of the information provided in this section addresses the interfacial heat and mass transfer models that are currently employed in the code, as well as constitutive relationships that support the overall computational approach.

2.3 Concrete Ablation Modeling

When corium first comes into contact with concrete, there is a natural tendency for an insulating crust to form on the cold surface. However, continued heat transfer across the crust will eventually warm the underlying concrete, and the heat sink provided by this material will be reduced to the point at which the crust may begin to remelt. Moreover, continued heat transfer to the concrete will lead to the production of decomposition gases H_2O and CO_2 . As they expand, these gases will exert a mechanical force on the crust as they pass through or around the crust material. As the crust thins, a point may be reached at which the crust will no longer be mechanically stable under the combined loads applied by the melt and the expanding gases. The crust would then fail, providing the opportunity for melt to directly contact the concrete surface. At this point the system would evolve into a new state in which the ablation rate is expected to increase as a result of removing the thermal resistance provided by the crust. The CCI test results^[47-49] have shown that crusts can fail locally, which leads to a rapid period of ablation on the newly exposed concrete surface(s). Variations in the duration and location of these crust failure events led to initial asymmetries in the ablation behavior, and these asymmetries made it difficult to interpret the long-term radial-axial power split over the relatively short duration of the tests. Thus, as part of CORQUENCH development, models have been developed for calculating this transient crusting behavior in order to aid in the interpretation of the test results, as well as providing a better understanding of the progression of core-concrete interactions in general.

In terms of the modeling approach, CORQUENCH is formulated as an initial value problem in which simply cavity geometries are assumed, and the axial and radial ablation behaviors are calculated while maintaining these same basic cavity configurations (see Section 2.2). Thus, the coupled partial differential equations that govern the local crust growth and concrete temperature evolution in a given direction are first reduced to an initial value problem using boundary layer theory. These equations are then numerically integrated along with the other equations describing the core-concrete interaction that are described elsewhere in this section, thereby yielding an approximate, but coupled, solution. In order to guide the model development, the following requirements were established:

- 1) The heat sink provided by cold concrete drives crust growth, and so heat conduction into concrete needs to be modeled.
- 2) Relatively thick crusts may initially form, and so decay heat in the crust needs to be included so that the resultant models can be extrapolated to plant conditions.
- 3) Freezing temperatures are a strong function of composition, and so the crust composition needs to be tracked separately from the melt composition.
- 4) Localized crust failure has been observed in tests, and so the modeling needs to be able to simulate situations in which the crust fails locally, while crust(s) continue to protect other surfaces in contact with the melt.

With these requirements, the second step was to establish a logical progression for the crusting behavior to further guide model development. The logic flow diagram used in the code is provided in Figure 2-3. The system evolution is described in four distinct phases. These phases are outlined immediately below, while the models for each phase are described in the balance of this section.

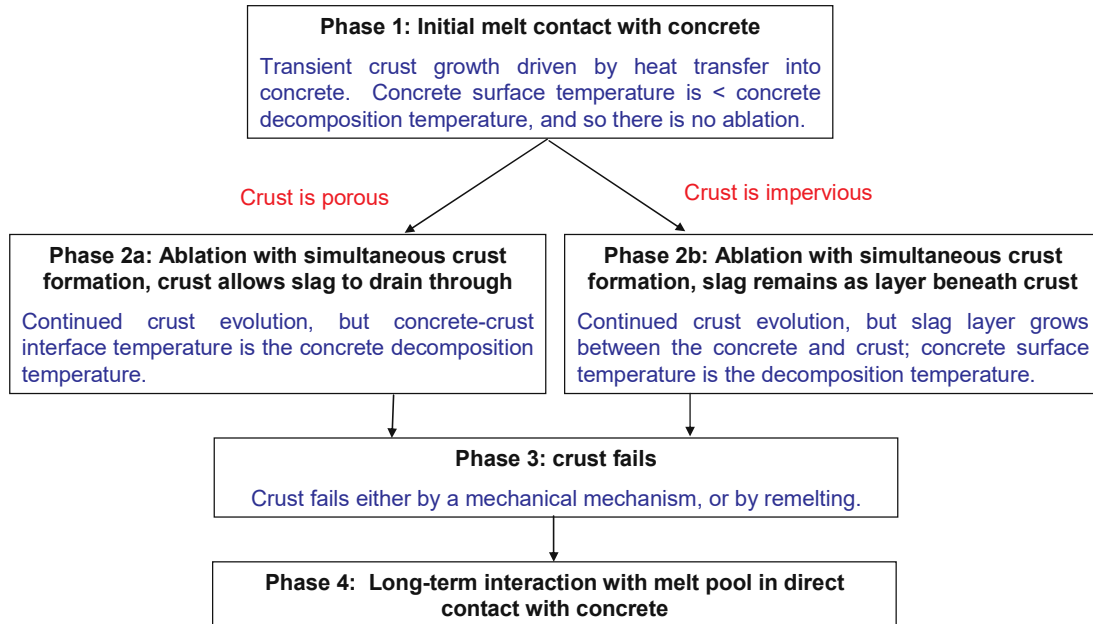


Figure 2-3. Assumed Phenomenological States and Flow Diagram Governing Crust Progression Modeling.

The first phase is the initial melt contact with the concrete. In this case, transient crust growth is driven by conduction heat transfer into concrete, and the rate of growth is slowed by convective heat transfer from the melt to the crust/melt interface. The crust/concrete interface temperature is less than the concrete decomposition (ablation) temperature, and so there is no ablation. For situations in which the initial crust/concrete contact temperature is above the concrete decomposition temperature, the corresponding high rate of gas release from the concrete is assumed to mechanically fail the crust. In this case, the calculation is initiated in Phase 4: melt pool in direct contact with concrete. This type of situation can arise for plant scenarios in which very high temperature core melt from the vessel initially contacts the concrete surface.

Once the concrete surface temperature rises to the ablation temperature, the second phase of the process is initiated in which ablation of the underlying substrate occurs. This constitutes a branch point in the modeling, depending upon whether or not the crust is assumed to be porous or impervious with respect to the slag that is produced by the ablation process. The branch denoted 2a is that in which the crust is assumed to be porous, thereby allowing slag (and concrete decomposition gases) to drain through the material into the adjacent melt. During this phase, there is continued crust evolution, but the concrete-crust interface temperature is fixed at the concrete decomposition temperature. In the second branch denoted 2b, there is ablation with simultaneous crust formation, but the slag is retained as a growing liquid film beneath the crust, and this film constitutes an additional heat transfer resistance to the underlying concrete. In this case, there is

also continued ablation with the concrete/film interface temperature fixed at the concrete decomposition temperature.

The third phase of the interaction constitutes the crust failure point. Here, modeling criteria need to be established for how and why the crust fails. A rudimentary model based on a mechanical strength argument is proposed as part of this work. User options are also provided to cover situations in which the crust fails at a specified time or thickness.

Finally, following failure, phase four of the interaction is initiated wherein long-term ablation occurs with no crust present at the core/concrete interface; i.e., the ablation is driven by convection from the melt directly to the concrete surface.

To provide flexibility, CORQUENCH offers three options for calculating the concrete heatup and ablation sequence outlined in Figure 2-3. These options are summarized as follows:

- 1) A traditional quasi-steady ablation model in which conduction heat transfer into the concrete behind the ablation front, as well as the initial surface temperature rise to the ablation point, are neglected (i.e., the calculation is initiated in Phase 4),
- 2) A dryout model in which conduction into the concrete is taken into account, but the early transient surface heatup phase is neglected (i.e., the calculation is also initiated in Phase 4, but with a more mechanistic concrete ablation model), and
- 3) A complete transient dryout model that accounts for both conduction into the concrete and the initial concrete heatup phase, along with interfacial corium crust growth (i.e., Phases 1-4 are calculated, based on user-supplied modeling options).

Descriptions of the modeling approaches for these three cases are provided sequentially below.

2.3.1 Quasi-Steady Concrete Ablation Model

As noted, this case corresponds to the situation in which conduction into the concrete behind the ablation front is neglected, so that the concrete latent heat of fusion, as well as the sensible heat required to raise the concrete to the ablation temperature, are lumped into an effective decomposition enthalpy that is used to relate the heat flux to the local ablation rate. Due to the low thermal conductivity of concrete, this is the traditional modeling approach employed in many system-level codes. For this case, the downward axial concrete erosion rate is evaluated through an equation of the form:

$$\dot{\eta}_b = \frac{h_b (T_m - T_{dc})}{\rho_{con} e_{con,d}} \quad (2-20)$$

With this relationship, the mass flux of CO₂ and H₂O gases and SiO₂ liquid into the melt from basemat erosion can be calculated through the following expressions:

$$\dot{m}_{b,H_2O} = \chi_{con,H_2O} \rho_{con} \dot{\eta}_b \quad (2-21)$$

$$\dot{m}_{b,CO_2} = \chi_{con,CO_2} \rho_{con} \dot{\eta}_b \quad (2-22)$$

$$\dot{m}_{b,SiO_2} = \chi_{con,SiO_2} \rho_{con} \dot{\eta}_b \quad (2-23)$$

These quantities are required to calculate the oxidation reaction rates in Eqs. 2-1 and 2-18. Note that an analogous set of equations apply for calculating the sidewall ablation rate as well as gas and silica release rates into the melt when the 2-D modeling options are selected.

2.3.2 Fully Developed Concrete Dryout Model

This modeling option corresponds to the situation in which conduction heat transfer into the concrete is factored into the analysis, but the early transient surface heatup phase is neglected so that the calculation begins in Phase 4. The physical situation and nomenclature are shown in Figure 2-4. For the purposes of this work, the concrete is modeled assuming constant thermo-physical properties, which includes the thermal conductivity, density, and specific heat. Thus enthalpy changes associated with the dryout of free and bound water, as well as the carbonates that release CO₂ upon decomposition, are all lumped into an effective average specific heat for the concrete. If the concept of a thermal boundary layer thickness ξ in the concrete sidewall behind the ablation front is employed, then the thermal response in this layer satisfies the transient one-dimensional heat conduction equation; i.e.,

$$\rho_{con} c_{con} \frac{dT}{dt} = k_{con} \frac{d^2T}{dx^2} , \quad (2-24)$$

This equation is subject to the boundary conditions:

$$T(x = \eta_s) = T_{dc} \quad (2-25)$$

$$T(x = \eta_s + \xi_s) = T_c \quad (2-26)$$

$$\left. \frac{dT}{dx} \right|_{x=\eta_s+\xi_s} = 0 \quad (2-27)$$

In addition, the following energy balance must be satisfied at the core-concrete interface:

$$\rho_{con} \Delta e_{con} \dot{\eta}_s = k_{con} \left. \frac{dT}{dx} \right|_{x=\eta_s} + h_s (T_m - T_{dc}) \quad (2-28)$$

Assuming a parabolic temperature profile in the concrete, then boundary layer theory can be used to derive the following simultaneous set of equations for the concrete erosion and thermal boundary layer depths:

$$\rho_{con} \Delta e_{con} \dot{\eta}_s = h_s (T_m - T_{dc}) - 2k_{con} \frac{(T_{dc} - T_o)}{\xi_s} \quad (2-29)$$

$$\dot{\xi}_s = 6 \frac{\alpha_{con}}{\xi_s} - 3 \dot{\eta}_s \quad (2-30)$$

where:

- Δe_{con} = concrete heat of fusion,
- α_{con} = concrete thermal diffusivity = $k_{con} / (\rho_{con} c_{con})$,
- k_{con} = concrete thermal conductivity, and
- c_{con} = concrete effective specific heat.

To numerically initialize the boundary layer calculation, a physically plausible but non-zero value for the thermal boundary layer depth ξ_s must be specified. For the purposes of this

analysis, this thickness is deduced by equating the ablation rate computed from the dryout model (viz. Eq. 2-29) to that calculated from the quasi-steady model (viz. Eq. 2-20) at time $t=0$, and solving for the boundary layer depth. These efforts yield:

$$\xi_s(t=0) = 2k_{con}\Delta e_{con}\left(\frac{1}{c_{con}} + \frac{(T_{dc} - T_o)}{\Delta e_{con}}\right)h_s(T_m - T_{dc}) \quad (2-31)$$

This equation is used to establish the initial condition on Eq. 2-30 at the start of the calculation.

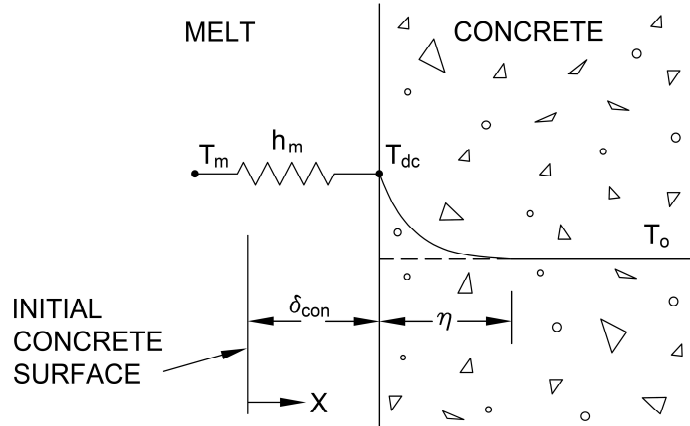


Figure 2-4. Illustration of Physical Situation During Phase 4 Interaction.

As noted above, the current model does not attempt to calculate the progression of the discrete enthalpy changes within the concrete that are associated with the decomposition of hydroxides and carbonates, resulting in gas release. However, given the assumed parabolic temperature profile in the boundary layer, the propagation rate of the isotherms at which these decomposition reactions occur can be tracked. These velocities are then used to calculate the mass flux of CO_2 and H_2O from the concrete. In particular, given the Eulerian coordinate system depicted in Figure 2-4, the location of a prescribed temperature T_j , (with $T_o \leq T_j \leq T_{dc}$) in the concrete sidewall can be expressed as:

$$\Omega_{s,j} = \eta_s + \beta_j \xi_s \quad (2-32)$$

with:

$$\beta_j = 1 - \sqrt{\frac{T_j - T_o}{T_{dc} - T_o}} \quad (2-33)$$

The isotherm propagation rate is then readily deduced from Eq. 2-32 as:

$$\dot{\Omega}_{s,j} = \dot{\eta}_s + \beta_j \dot{\xi}_s \quad (2-34)$$

As currently formulated, there are four ($j=4$) isotherms that are tracked in order to evaluate the gas release: i) free water, ii) water bound in the form of calcium hydroxide $[\text{Ca}(\text{OH})_2]$, and CO_2 bound in the form of iii) calcium carbonate $[\text{CaCO}_3]$ and iv) dolomite $[\text{MgCa}(\text{CO}_3)_2]$.¹ With this information, the mass flux of water vapor and CO_2 from the concrete sidewall due to ablation can then be evaluated as follows:

¹Decomposition points are specified as part of code input; see Section 3.0. Typical data are: i) free water: saturation temperature; ii) calcium hydroxide: 785 K, iii) calcium carbonate: 1098 K; and iv) dolomite: 1172 K.

$$\dot{m}_{s,H_2O}'' = \rho_{con} \left(\chi_{con,H_2O}^{free} \dot{\Omega}_{s,H_2O} + \frac{\chi_{con,Ca(OH)_2} M_{H_2O}}{M_{Ca(OH)_2}} \dot{\Omega}_{s,Ca(OH)_2} \right) \quad (2-35)$$

$$\dot{m}_{s,CO_2}'' = \rho_{con} \left(\frac{\chi_{con,CaCO_3} M_{CO_2}}{M_{CaCO_3}} \dot{\Omega}_{s,CaCO_3} + \frac{2\chi_{con,MgCa(CO_3)_2} M_{CO_2}}{M_{MgCa(CO_3)_2}} \dot{\Omega}_{s,MgCa(CO_3)_2} \right) \quad (2-36)$$

As a reminder, M denotes molecular weight in the above and the χ parameters denote the weight fraction of the (subscripted) compounds within the concrete.² Since silica is assumed to be released at the ablation temperature, then the mass flux of this compound into the melt is given by:

$$\dot{m}_{s,SiO_2}'' = \chi_{con,SiO_2} \rho_{con} \dot{\eta}_s \quad (2-37)$$

This equation is identical to that used for the quasi-steady ablation model (i.e., Eq. 2-23).

Equations 2-29, 2-30, and 2-33 through 2-37 constitute the simplified concrete dryout initial value problem that is integrated in conjunction with Eqs. 2-1 and 2-18 to determine the ablation and thermal boundary layer depths in the concrete sidewall, along with the flux of oxidizing agents into the melt that control the metal oxidation rates. Analogous equations apply to the basemat axial erosion case.

2.3.3 Transient Concrete Dryout Model

This section summarizes key aspects of the full transient model that accounts for conduction into the concrete, including the initial surface heatup phase, along with a model for the growth and eventual failure of an interfacial corium crust. This particular model is intended to capture (at least to first order) all phases of the interaction outlined in Figure 2-3.

A sketch outlining the physical situation soon after initial melt contact with the concrete sidewall is provided in Figure 2-5. For this study, quasi-steady heat transfer in the crust is assumed. Additionally, the volumetric decay heat in the crust, $\dot{Q}_{s,c}$ (W/m³), is assumed to be distributed uniformly. Finally, the assumption of constant thermo-physical properties used above is retained in this analysis. With these assumptions and the nomenclature depicted in Figure 2-5, the differential equation and boundary conditions governing heat transfer across the crust during Phase 1 of the interaction are given as:

$$k_{s,c} \frac{d^2 T}{dx^2} = -\dot{Q}_{s,c} \quad (2-38)$$

$$T(x=0) = T_{s,I} \quad (2-39)$$

$$T(x=-\delta_s) = T_{s,frz} \quad (2-40)$$

²As part of code input (see Section 3.0), the concrete free water, bound water, CO₂, CaO, and MgO contents are specified. With this data, the corresponding amounts of Ca(OH)₂, CaCO₃, and MgCa(CO₃)₂ present in the concrete are then calculated for use in Eqs. 2-35 and 2-36. This frees the user of this tedious task.

where subscripts c and frz denote crust zone and freezing point, respectively, and $\dot{Q}_{s,c} \equiv \chi_{s,UO_2} \rho_{s,c} q_{dec}$. The solution for the temperature distribution in the crust is thus found as:

$$T(x) = T_{s,l} - \left(\frac{T_{s,frz} - T_{s,l}}{\delta_s} + \frac{\dot{Q}_{s,c} \delta_s}{2k_{s,c}} \right) x - \frac{\dot{Q}_{s,c}}{2k_{s,c}} x^2; \quad -\delta_s \leq x \leq 0 \quad (2-41)$$

Given this expression, the heat fluxes at the melt-crust ($x = -\delta_s$) and crust-concrete ($x = 0$) interfaces are then:

$$k_{s,c} \frac{dT}{dx} \Big|_{x=-\delta_s} = -k_{s,c} \frac{(T_{s,frz} - T_{s,l})}{\delta_s} + \frac{\dot{Q}_{s,c} \delta_s}{2} \quad (2-42)$$

$$k_{s,c} \frac{dT}{dx} \Big|_{x=0} = -k_{s,c} \frac{(T_{s,frz} - T_{s,l})}{\delta_s} - \frac{\dot{Q}_{s,c} \delta_s}{2} \quad (2-43)$$

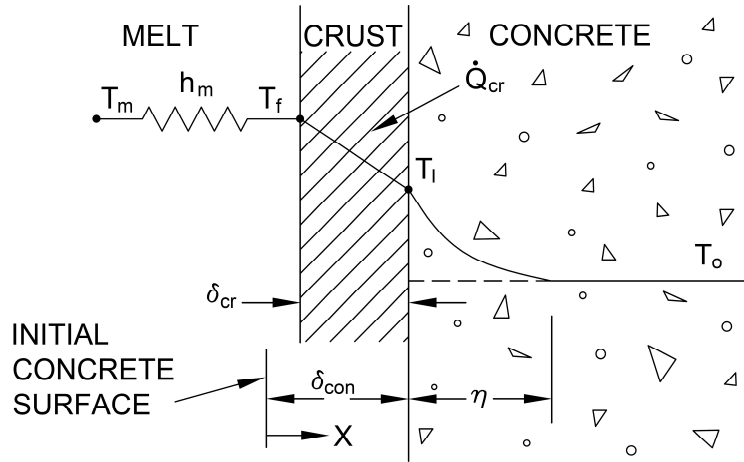


Figure 2-5. Illustration of Physical Situation During Phases 1 and Phase 2a.

With these results, and again employing the concept of a thermal boundary layer thickness ξ_s in the sidewall, then the thermal response in the boundary layer satisfies the heat conduction equation previously defined in Eq.2-24, in addition to the following boundary conditions:

$$k_{con} \frac{dT}{dx} \Big|_{x=0} = -k_{s,c} \frac{(T_{s,frz} - T_{s,l})}{\delta_s} - \frac{\dot{Q}_{s,c} \delta_s}{2} \quad (2-44)$$

$$T(x = \xi_s) = T_c \quad (2-45)$$

$$\frac{dT}{dx} \Big|_{x=\xi_s} = 0 \quad (2-46)$$

Assuming the now-familiar parabolic temperature profile in the concrete and employing boundary layer theory, the following simultaneous set of equations for the boundary layer and crust thicknesses are obtained:

$$\dot{\xi}_s = -\frac{\xi_s}{2(T_{s,I} - T_o)} \left[\frac{2k_{con}}{\xi_s} + \frac{k_{s,c}}{2\delta_s} \right]^{-1} \left[\dot{Q}_{s,c} - \frac{2k_{con}(T_{s,I} - T_o)}{\xi_s \delta_s} \right] \dot{\delta}_s \quad (2-47)$$

$$+ \frac{3}{\rho_{con} c_{con} \xi_s (T_{s,I} - T_o)} \left[\frac{2k_{con}}{\xi_s} + \frac{k_{s,c}}{2\delta_s} \right]^{-1} \left[k_{con} + \frac{k_{s,c} \xi_s}{2\delta_s} \right] \left(k_{s,c} \frac{(T_f - T_{s,I})}{\delta_s} + \frac{\dot{Q}_{s,c} \delta_s}{2} \right)$$

$$\rho_{s,c} \Delta e_{s,c} \dot{\delta}_s = k_{s,c} \frac{(T_{s,firz} - T_{s,I})}{\delta_s} - \frac{\dot{Q}_{s,c} \delta_s}{2} - h_s (T_m - T_{s,firz}) \quad (2-48)$$

These equations are integrated in conjunction with the balance of the equations describing the core-concrete interaction to find the thermal boundary layer and crust thicknesses as a function of time during the Phase 1 interaction. Given these thicknesses, then the concrete surface temperature is evaluated from the equation:

$$T_{s,I} = T_o + \frac{\xi_s}{2} \left(k_{con} + \frac{k_{s,c} \xi_s}{2\delta_s} \right)^{-1} \left(k_{cr} \frac{(T_{s,firz} - T_o)}{\delta_s} + \frac{\dot{Q}_{s,c} \delta_s}{2} \right) \quad (2-49)$$

The interface temperature evaluated through this expression is tracked relative to the concrete decomposition temperature. Once $T(x=0) = T_{s,I} \rightarrow T_{dc}$, the solution bifurcates to either Phase 2a or 2b, depending upon the user-specified modeling choice.

To numerically initialize this calculation, physically plausible but non-zero values for the thermal boundary layer and crust depths are required as $t \rightarrow 0$. In order to determine these values, the behavior of the Eqs. 2-47 and 2-48 are examined for small times. To this end, the following solution forms are assumed as $t \rightarrow 0$:

$$\xi_s(t \rightarrow 0) = C_\xi \sqrt{t} \quad (2-50)$$

$$\delta_s(t \rightarrow 0) = C_\delta \sqrt{t} \quad (2-51)$$

Substitution of these equations into Eqs. 2-47 through 2-49 and working through the algebra yields the following solutions for C_δ and C_ξ as $t \rightarrow 0$:

$$C_\delta = \sqrt{\frac{2k_{s,c}(T_{s,firz} - T_o)}{\rho_{s,c} \Delta e_{s,c}}} \quad (2-52)$$

$$C_\xi = \frac{4k_{con} \left(\frac{1}{2} C_\delta C_\xi + \frac{6\alpha_{con} C_\delta}{C_\xi} + \frac{3k_{s,c}}{\rho_{con} c_{con}} \right)}{4k_{con} C_\delta + k_{s,c} C_\xi} \quad (2-53)$$

Equation 2-52 is in closed form, but the equation for C_ξ is non-linear and requires an iterative solution. This is accomplished using the Newton-Raphson technique. In particular, Eq. 2-53 is re-written in the following form:

$$f = C_\xi - \frac{4k_{con} \left(\frac{1}{2} C_\delta C_\xi + \frac{6\alpha_{con} C_\delta}{C_\xi} + \frac{3k_{s,c}}{\rho_{con} c_{con}} \right)}{4k_{con} C_\delta + k_{s,c} C_\xi}, \quad (2-54)$$

with convergence obtained when $f \rightarrow 0$, and:

$$\frac{df}{dC_\xi} = 1 + \frac{k_{s,c} C_\xi - 2k_{con} C_\delta + \frac{24k_{con} \alpha_{con} C_\delta}{C_\xi^2}}{4k_{con} C_\delta + k_{s,c} C_\xi} \quad (2-55)$$

Given these expressions, iteration is performed in which the value of C_ξ is updated through the following expression until a convergence criterion is met:

$$C_\xi^{n+1} = C_\xi^n - \frac{f}{\frac{df}{dC_\xi}} \quad (2-56)$$

With the solutions for C_δ and C_ξ obtained through Eqs. 2-52 through 2-56, the initial values for ξ_s and δ_s are evaluated from Eqs. 2-50 and 2-51 by setting the time equal to the user-specified timestep for the quadrature; i.e. $t = \Delta t$.

Equations 2-47 through 2-49 constitute the initial value problem that is integrated in conjunction with Eqs. 2-1 and 2-18 to determine the concrete sidewall surface temperature and thermal boundary layer depth during Phase 1 of the interaction. The sidewall gas release rates are evaluated from Eqs. 2-34 through 2-36 for this case also, but with $\dot{\eta}_s = 0$. Note that analogous equations also apply to the basemat axial erosion case.

As shown in Figure 2-3, the Phase 1 solution is calculated until $T_{s,I} \rightarrow T_{dc}$, at which time a bifurcation point is reached and Phase 2 with concrete erosion is initiated. The particular form of the solution thereafter is based on a user-specified modeling assumption; i.e., the crust is assumed to be porous so that the slag produced from concrete erosion continuously drains through the crust into the melt (branch 2a), or the crust is impervious so that the slag accumulates as a growing film between the crust and concrete (branch 2b). In either branch, the initial conditions (i.e., crust and thermal boundary layer thicknesses) are determined by the results of the Phase 1 calculation at the point at which $T_{s,I} = T_{dc}$. In terms of presentation, the porous crust case is considered first, followed by the impervious crust scenario that is described later in this section.

The physical situation for this case is also shown in Figure 2-5, but with $T_{s,I} = T_{dc}$. The equations governing heat conduction in the crust are thus identical to Eqs. 2-38 through 2-40, and those governing heat conduction in the concrete thermal boundary layer are the same as Eqs. 2-24 through 2-27. The applicable energy balances for the crust and concrete ablation thicknesses on the sidewall are of the form:

$$\rho_{s,c} \Delta e_{s,c} \dot{\delta}_s = k_{s,c} \frac{(T_{s,frz} - T_{dc})}{\delta_s} - \frac{\dot{Q}_{s,c} \delta_s}{2} - h_s (T_m - T_{s,frz}) \quad (2-57)$$

$$\rho_{con} \Delta e_{con} \dot{\eta}_s = k_{con} \left. \frac{dT}{dx} \right|_{x=\eta_s} + k_{s,c} \frac{(T_{s,frz} - T_{dc})}{\delta_s} + \frac{\dot{Q}_{s,c} \delta_s}{2} \quad (2-58)$$

Assuming a parabolic temperature profile in the concrete, then the simultaneous equations governing the crust, ablation, and thermal boundary layer thicknesses are found respectively as:

$$\rho_{s,c} \Delta e_{s,c} \dot{\delta}_s = k_{s,c} \frac{(T_{s,frz} - T_{dc})}{\delta_s} - \frac{\dot{Q}_{s,c} \delta_s}{2} - h_s (T_m - T_{s,frz}) \quad (2-59)$$

$$\rho_{con} \Delta e_{con} \dot{\eta}_s = k_{s,c} \frac{(T_{s,frz} - T_{dc})}{\delta_s} + \frac{\dot{Q}_{s,c} \delta_s}{2} - 2k_{con} \frac{(T_{dc} - T_o)}{\xi_s} \quad (2-60)$$

$$\dot{\xi}_s = 6 \frac{\alpha_{con}}{\xi_s} - 3 \dot{\eta}_s \quad (2-61)$$

Equations 2-59 through 2-61 are used to calculate the crust, erosion, and thermal boundary layer depths until the selected crust failure criterion is satisfied, at which point the solution bifurcates to Phase 4, concrete ablation with no crust present. The gas release rate from the sidewall is evaluated from Eqs. 2-34 through 2-36 for this case also. Analogous equations also apply to the basemat axial erosion case.

With the models developed for the porous crust case, attention is now focused on the situation in which the crust is assumed to be impervious to the slag formed from ablation. The physical situation here is shown in Figure 2-6. The modeling considers simultaneous crust growth with an underlying slag film layer; any slag ablated from the concrete surface is deposited in the film. Thus, this case is similar to Phase 2a, with the exception that a new equation describing the slag film thickness is required, and the thermal resistance across the film must be built into the energy balance between the crust and concrete. For this case, the coupled equations governing the crust, ablation, concrete thermal boundary layer, and slag film thicknesses on the concrete sidewall are deduced respectively using boundary layer theory as:

$$\rho_{s,c} \Delta e_{s,c} \dot{\delta}_s = k_{s,c} \frac{(T_{s,frz} - T_{slag,I})}{\delta_s} - \frac{\dot{Q}_{s,c} \delta_s}{2} - h_s (T_m - T_{s,frz}) \quad (2-62)$$

$$\rho_{con} \Delta e_{con} \dot{\eta}_s = k_{s,c} \frac{(T_{s,frz} - T_{slag,I})}{\delta_s} + \frac{\dot{Q}_{s,c} \delta_s}{2} - 2k_{con} \frac{(T_{dc} - T_o)}{\xi_s} \quad (2-63)$$

$$\dot{\xi}_s = 6 \frac{\alpha_{con}}{\xi_s} - 3 \dot{\eta}_s \quad (2-64)$$

$$\rho_{slag} \dot{\delta}_{s,slag} = (1 - \chi_{con,g}) \rho_{con} \dot{\eta}_s \quad (2-65)$$

where subscript *slag* denotes the slag layer. The slag/crust interface temperature satisfies:

$$T_{slag,I} = \left[\frac{k_{slag}}{\delta_{s,slag}} + \frac{k_{s,c}}{\delta_s} \right]^{-1} \left(\frac{k_{s,c} T_{s,frz}}{\delta_s} + \frac{k_{slag} T_{dc}}{\delta_{slag}} + \frac{\dot{Q}_{s,c} \delta_{s,c}}{2} \right) \quad (2-66)$$

Equations 2-62 through 2-65 along with 2-66 constitute the initial value problem that is integrated to find the crust, slag film, erosion, and thermal boundary layer depths until the selected

crust failure criterion is satisfied and Phase 4 of the simulation is started. Gas release rates from the sidewall are also evaluated from Eqs. 2-34 through 2-36. However, the slag is retained as a molten film beneath the crust and this material is not added to the melt until after the crust fails. Analogous equations are again noted to apply to the basemat axial erosion case.

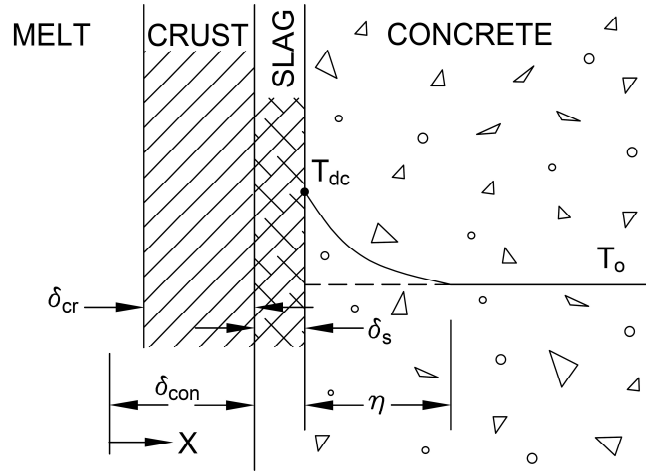


Figure 2-6. Illustration of Physical Situation During Phase 2b.

As the interaction progresses, continued heat transfer across the crust will eventually warm the underlying concrete, and the heat sink provided by this material will be reduced to the point at which the crust may begin to remelt. In theory, the crust could completely remelt, or it could be thinned to the point at which it fails under the applied loads that arise during the interaction. Crust failure is a difficult problem to analyze in and of itself, and so user options have been provided to address this issue parametrically. Specifically, the three options are summarized as follows:

- 1) The crust fails at a user-specified time,
- 2) The crust fails after the thickness falls below a user-specified thickness, or
- 3) The crust fails after the thickness falls below that required to be mechanically stable under the applied hydrostatic head applied by the melt.

Options 1) and 2) are self-explanatory. For option 3), a simple model has been developed, and that model is summarized below.

An illustration of the physical situation is provided in Figure 2-7. The concept is that at a given location, the crust is subject to the hydraulic pressure of the melt, which acts to keep the crust in place on the surface. Simultaneously, concrete decomposition gases are formed at the crust-concrete interface. These gases likely produce localized pockets at the interface that allow the melt hydrostatic pressure to act as a bending force on the crust. The crust stability criterion is then, simply, that the crust must be mechanically strong enough to withstand the hydraulic pressure applied by the melt. This concept can be expressed mathematically as:

$$F = (\rho_m - \rho_g)gH_m L_A^2 \geq C_P \sigma_{s,f} \delta_s^2 \quad (2-67)$$

where:

$$\begin{aligned} g &= \text{gravitational acceleration,} \\ L_A &= \text{characteristic lateral dimension of the crust,} \end{aligned}$$

- $\sigma_{s,f}$ = crust mechanical strength,
 ρ_g = density of sparging concrete decomposition gases, and
 C_P = $O(1)$ constant depending on the plate shape and boundary condition.

The specific criterion for crust failure is then readily deduced from the above equation as:

$$\delta_{s,min} = L_A \sqrt{\frac{(\rho_m - \rho_g)gH_m}{C_P \sigma_{s,f}}} \quad (2-68)$$

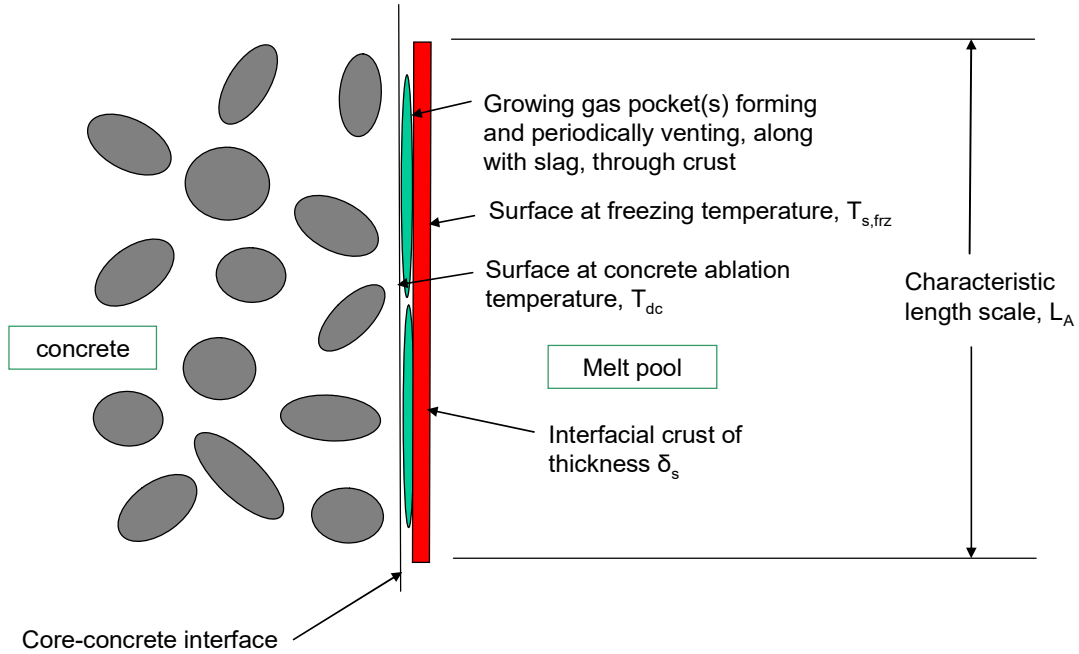


Figure 2-7. Illustration of Physical Situation at Core-Concrete Interface.

In order to utilize Eq. 2-68, the characteristic length scale L_A needs to be specified. For crusts on vertical surfaces, it would seem logical to set $L_A \sim H_m$, since the melt pool depth would be the maximum size (at least in the vertical direction) that the crust plate could obtain. For crusts on the bottom surface, several length scales could be envisioned. The first would be the diameter of the melt pool. If this were the case, then one would conclude, at least for plant accidents in which the pool diameter is much larger than the pool depth, that crusts would be very unstable on the pool bottom surface relative to those on the side surface. If this were the correct phenomenological modeling assumption, then it cannot be deduced from the CCI data base^[47-49] since the pool depth is of the same order as the cavity width for these tests. A second case would be that $L_A \sim H_m$ based on the idea that the melt depth is also a characteristic length scale in terms of controlling the stability of the bottom crust. Finally, one may argue that a characteristic length scale for the bottom crust is the gas bubble spacing on the surface, since bubbles have been postulated to form bending points for the crust. In this case, the bubble spacing is probably close to the characteristic aggregate spacing within the concrete. If this last observation were true, then crusts on the bottom surface would be very stable in comparison to sidewall crusts. Unfortunately, this trend is not completely born out in the test series.^[47-49] Given all these uncertainties, Eq. 2-68 is currently coded assuming $L_A = H_m$ for both side and bottom crusts. Also in the deployment of

Eq. 2-68, the crust tensile strength is the same as that calculated for the melt as input into the crust water ingress model. Finally, when the crust is growing (i.e., $\dot{\delta}_s > 0$) it is assumed to be mechanically stable and so even if the thickness is $< \delta_{s,min}$, the Phase 2 calculation is not terminated. This modeling decision was invoked to prevent spurious crust failures early in the transient as the crust grows to the thermal equilibrium point.

It is of interest to provide an order-of-magnitude estimate of the stable crust thickness that one would calculate from Eq. 2-68. Assuming the following typical values for an MCCI: $\rho_m \sim 5000 \text{ kg/m}^3$, $g = 9.82 \text{ m/s}^2$, $L_A = H_m \sim 0.25 \text{ m}$, $\sigma_{sf} \sim 100 \text{ MPa}$, $C \sim 1$, and $\rho_m \gg \rho_g$, then Eq. 2-68 yields $\delta_{s,min} \sim 3 \text{ mm}$.

Once the selected criterion for crust failure on a given surface has been satisfied, the solution bifurcates to Phase 4 in which no crust is present. The models governing the ablation progression and gas release for this case were previously presented as Eqs. 2-29, 2-30, 2-35 and 2-36. The boundary layer depth calculated using either the Phase 2a or 2b model is used to initialize the Phase 4 calculation. However, before that calculation is launched, any remain crust (and slag for the Phase 2b modeling choice) is first mixed with the melt, and the new melt temperature is recalculated by thermally equilibrating the melt with the crust (and slag, if applicable) material. For the sidewalls, crust mass can be thermally (as opposed to splatter) deposited above the pool height early in the transient due to high void fraction in the melt. Any solidified melt on the sidewalls that is calculated to be above the melt surface at the time of sidewall crust failure is permanently removed from the interaction. Moreover, a note to document the timing and total mass of material removed is written to the text output file generated by the code.

2.4 Melt Upper Surface Heat Transfer: Dry Cavity Conditions

In order to provide user flexibility, atmospheric heat transfer models have been implemented in the code for both wet and dry cavity conditions. This section addresses the modeling for dry cavity conditions, while details of the wet cavity models are provided in the following section. A depiction of the physical situation and nomenclature utilized in the following analysis was provided previously as Figure 2-1.

2.4.1 Crust-Free and Incipient Crust Formation Boundary Conditions

Modeling of the heat transfer from the melt to the overlying medium under dry cavity conditions considers convection from the melt to the melt-atmosphere interface, and radiation from the interface to the environment boundary. Whether or not a stable crust forms at the interface depends upon two criteria: i) a thermodynamic condition; i.e., the interface temperature falls below that at which solid crust material forms at the interface, and ii) a mechanical stability condition; i.e., the incipient crust must be mechanically stable in the presence of the sparging concrete decomposition gases that are generated from the core-concrete interaction.

Prior to crust formation, the energy balance at the melt-atmosphere interface is:

$$h_t(T_m - T_{t,l}) = h_r(T_{t,l} - T_{bound}) , \quad (2-69)$$

which can be solved for the surface interface temperature, yielding:

$$T_{t,I} = \frac{h_t T_m + h_r T_{bound}}{h_t + h_r} \quad (2-70)$$

The radiation heat transfer coefficient from the interface to the overlying cavity is given through the usual expression:

$$h_r = \frac{\sigma_{stef}}{1/\varepsilon_m + 1/\varepsilon_{bound} - 1} (T_{t,I}^2 + T_{bound}^2) (T_{t,I} + T_{bound}) \quad (2-71)$$

where:

$$\begin{aligned} \varepsilon_m &= \text{melt radiation emissivity,} \\ \varepsilon_{bound} &= \text{emissivity of surrounding cavity, and} \\ \sigma_{stef} &= \text{Stefan-Boltzman constant} = 5.67 \cdot 10^{-8} \text{ W/m}^2\text{-K}^4. \end{aligned}$$

The convective heat transfer coefficient from the bulk melt to the interface is currently evaluated using the correlation of Kutateladze and Malenkov,^[40] i.e.,

$$h_t = \begin{cases} 1.5 \cdot 10^{-3} \left(\frac{c_m P j}{k_m g} \right)^{2/3} \frac{k_m}{L_\lambda}; & j < j_{tr} \\ 1.5 \cdot 10^{-3} \left(\frac{c_m P j}{k_m g} \right)^{2/3} \left(\frac{j_{tr}}{j} \right)^{1/2} \frac{k_m}{L_\lambda}; & j \geq j_{tr} \end{cases} \quad (2-72)$$

where:

$$\begin{aligned} P &= \text{system pressure,} \\ k_m &= \text{melt thermal conductivity,} \\ c_m &= \text{melt specific heat,} \\ j_{tr} &= \text{transition velocity} = 4.3 \cdot 10^{-4} \frac{\sigma_m}{\mu_m} \\ \sigma_m &= \text{melt surface tension,} \\ \mu_m &= \text{melt viscosity,} \end{aligned}$$

and L_λ is the Laplace constant that is defined as:

$$L_\lambda = \sqrt{\frac{\sigma_m}{g(\rho_m - \rho_g)}} \quad (2-73)$$

The average melt superficial gas velocity j in Eq. 2-72 is evaluated on the basis of the gas mass flux through the pool due to concrete decomposition gases, as given by Eqs. 2-35 and 2-36. In most cases (exceptions are pointed out in the balance of this section), the velocity is evaluated as:

$$j = \frac{A_b \left(\dot{m}_{b,H_2O} + \dot{m}_{b,CO_2} \right) + A_s \left(\dot{m}_{s,H_2O} + \dot{m}_{s,CO_2} \right)}{A_b \rho_g}, \quad (2-74)$$

and the density of the sparging gas is evaluated at the melt temperature through the ideal gas law:

$$\rho_g = \frac{P \bar{M}_g}{R_{ideal} T_m}, \quad (2-75)$$

where:

$$\begin{aligned} R_{ideal} &= \text{ideal gas constant} = 8.3143 \text{ J/mol}\cdot\text{K}, \text{ and} \\ \overline{M}_g &= \text{average molecular weight of the sparging gas mixture.} \end{aligned}$$

Finally, the molecular weight of the sparging gas is calculated on the basis of the known gas content of the concrete; i.e.,

$$\overline{M}_g = F_{H_2O} M_{H_2O} + F_{CO_2} M_{CO_2}, \quad (2-76)$$

with:

$$F_{H_2O} = \frac{\chi_{con,H_2O}}{M_{H_2O}} \left(\frac{\chi_{con,H_2O}}{M_{H_2O}} + \frac{\chi_{con,CO_2}}{M_{CO_2}} \right)^{-1} \quad (2-77)$$

$$F_{CO_2} = 1 - F_{H_2O}. \quad (2-78)$$

Equations 2-69 through 2-71 constitute a non-linear set of equations for the interface temperature $T_{t,I}$. These equations are solved using the Newton-Raphson technique by first forming:

$$f = T_{t,I} - \frac{h_t T_m + h_r T_{bound}}{h_t + h_r}, \quad (2-79)$$

with convergence obtained when $f \rightarrow 0$, and:

$$\frac{df}{dT_{t,I}} = 1 + \left[\frac{h_t T_m + h_r T_{bound}}{(h_t + h_r)^2} \right] \frac{dh_r}{dT_{t,I}}. \quad (2-80)$$

where:

$$\frac{dh_r}{dT_{t,I}} = \frac{\sigma_{stef}}{1/\varepsilon_m + 1/\varepsilon_{bound} - 1} (3T_{t,I}^2 + 2T_{t,I}T_{bound} + T_{bound}^2) \quad (2-81)$$

Given these expressions, iteration is then performed to find $T_{t,I}$ using an approach identical to that outlined around Eq. 2-56. The resultant solution for $T_{t,I}$ is then compared to the melt freezing temperature $T_{m,frz}$ to determine the next step in the solution methodology. For situations in which $T_{t,I} \geq T_{m,frz}$, the solution is valid and the upwards heat transfer term $h_t(T_m - T_t)$ in the melt energy balance equation (Eq. 2-18) is evaluated by setting $T_t = T_{t,I}$.

When $T_{t,I} < T_{m,frz}$, the potential exists for crust formation to occur at the melt-atmosphere interface depending upon the thermalhydraulic conditions. In particular, the potential for sustained crust growth to occur depends upon whether the incipient crust is stable in the presence of the sparging concrete decomposition gases.^[2] During the incipient growth phase the crust will remain thin and so decay heat within the crust will be negligible. Furthermore, the crust mass will be quite small and so in this stage of the analysis the crust composition is assumed to be equal to that of the bulk melt. Under these conditions, the equation for the crust growth rate at the interface can be written as:

$$\rho_{t,c} \Delta e_{t,c} \dot{\delta}_t = k_{t,c} \frac{(T_{t,frz} - T_{t,I})}{\delta_t} - h_t (T_m - T_{s,frz}). \quad (2-82)$$

This equation can be solved in closed form for the crust thickness as a function of time subject to the initial condition $\delta_t(t=0) = 0$; i.e.,

$$C_1 h_r \delta_t + C_2 \ln \left[1 - \frac{C_1 h_r \delta_t}{C_2 - C_1 k_{t,c}} \right] + C_1^2 t = 0 \quad (2-83)$$

where:

$$C_1 = \frac{h_t h_r}{\rho_{t,c} \Delta e_{t,c}} (T_m - T_{t,frz}) \quad (2-84)$$

$$C_2 = \frac{k_{t,c} h_r^2}{\rho_{t,c} \Delta e_{t,c}} (T_{t,frz} - T_{bound}) \quad (2-85)$$

Assuming that the forming crust can be modeled as a uniform flat plate and that bubbly flow conditions exist in the pool, Farmer^[2] used a simple force balance that relates the buoyancy force of a rising bubble to the load required to fail a forming crust segment to deduce the following expression for the minimum mechanically stable crust thickness:

$$\delta_{t,min} = \sqrt{\frac{4R_{bub}^3 (\rho_m - \rho_{con,g}) g}{3C_P \sigma_{s,f}}} \quad (2-86)$$

where R_{bub} is the melt pool sparging gas bubble radius (correlations provided later in this section) and the constant $C_P = 1.5$ for a simply supported crust edge boundary condition, or $C_P = 2.814$ for a clamped edge condition. The final piece of information that is needed is an estimate of the crust growth time on the surface. Blottner^[50] developed the following correlation for the local bubble arrival time in terms of the superficial gas velocity and radius of sparging gas bubbles:

$$t_a = 0.445 \frac{R_{bub}}{j} \quad (2-87)$$

Substituting Eqs. 2-86 and 2-87 into Eq. 2-83 and rearranging yields the following correlation for the critical gas velocity to preclude stable crust formation at the melt/atmosphere interface:

$$j_{crit} = \frac{0.445 R_{bub} h_t (T_m - T_{t,frz})}{\delta_{t,min} \rho_{t,c} \Delta e_{t,c} \left\{ \frac{k_{t,c} (T_{t,frz} - T_{bound})}{\delta_{t,min} h_t (T_m - T_{t,frz})} \ln \left(\frac{1}{1 - C_3} \right) - 1 \right\}} \quad (2-88)$$

where:

$$C_3 = \frac{h_t h_r (T_m - T_{t,frz}) \delta_{t,min}}{k_{t,c} [h_r (T_{t,frz} - T_{bound}) - h_t (T_m - T_{t,frz})]} \quad (2-89)$$

Recall that this solution is only valid when $h_r (T_{t,frz} - T_{bound}) > h_t (T_m - T_{t,frz})$; i.e., the thermodynamic conditions at the interface are consistent with crust formation. Thus, when this condition is met and $j > j_{crit}$, a situation develops in which intermittent crust segments can form at the surface, but they are continuously broken up and mixed in with the bulk melt by gas sparging. Under these conditions the upwards heat transfer term $h_t (T_m - T_t)$ in the melt energy balance equation (Eq. 2-18) is evaluated by setting $T_t = T_{t,frz}$. Furthermore, the intermittent crust thickness is found from Eq. 2-83 by first setting $t = t_a$ and then solving for δ_t using the Newton Raphson technique. To this end, Eq. 2-83 is written as:

$$f = \delta_t + \frac{C_2}{C_1 h_r} \ln \left[1 - \frac{C_1 h_r \delta_t}{C_2 - C_1 k_{t,c}} \right] + \frac{C_1}{h_r} t_a = 0 \quad (2-90)$$

with convergence obtained when $f \rightarrow 0$, and:

$$\frac{df}{d\delta_t} = 1 - \frac{C_2}{C_2 - C_1 k_{t,c} - C_1 h_r \delta_t}. \quad (2-91)$$

With these expressions, iteration is then performed to find δ_t using an approach identical to that outlined around Eq. 2-56. With δ_t known through these manipulations, the interface temperature is then found from:

$$T_{t,I} = \frac{\frac{k_{t,c}}{\delta_t} T_{t,frz} + h_r T_{bound}}{\frac{k_{t,c}}{\delta_t} + h_r} \quad (2-92)$$

2.4.2 Stable Floating Crust Boundary Condition

The final phase of dry cavity modeling considers the case in which it is thermodynamically possible for the crust to form [i.e., $h_r (T_{t,frz} - T_{bound}) > h_t (T_m - T_{t,frz})$], but in addition $j < j_{crit}$ and so the incipient crust is mechanically stable in the presence of the sparging gas. A stable crust then forms and grows to the point where convective heat transfer to the underside of the crust is balanced by that conducted through the crust and dissipated to the overlying atmosphere. In this case, a crust growth rate equation is solved that includes the effect of decay heat within the crust. The same set of assumptions used in the crust modeling described in Section 2.3 are made here; i.e., i) heat transfer within the crust is quasi-steady, ii) decay heat is uniformly distributed, and iii) crust thermalphysical properties are constant. Under these dry cavity conditions, the additional assumption is made that although the crust has sufficient strength to form a coherent physical mass above the melt pool, the overall crust structure is not strong enough to bond to the cavity sidewalls and separate from the melt as the core-concrete interaction proceeds downward. Simply put: a ‘floating crust’ boundary condition is assumed to be maintained.

With this set of assumptions and the coordinate system within the crust fixed with $x = 0$ at the melt-crust interface, the differential equation and boundary conditions governing heat transfer through the crust can be written as:

$$k_{t,c} \frac{d^2 T}{dx^2} = -\dot{Q}_{t,c} \quad (2-93)$$

$$T(x = 0) = T_{t,frz} \quad (2-94)$$

$$-k_{t,c} \left. \frac{dT}{dx} \right|_{x=\delta_t} = h_r (T(x = \delta_t) - T_{bound}) \quad (2-95)$$

This set of equations has the solution:

$$T(x) = T_{t,frz} + \frac{1}{k_{t,c} + h_r \delta_t} \left(\dot{Q}_{t,c} \delta_t \left[1 + \frac{h_r \delta_t}{2k_{t,c}} \right] - h_r (T_{t,frz} - T_{bound}) \right) x - \frac{\dot{Q}_{t,c}}{2k_{t,c}} x^2 \quad (2-96)$$

With the above result, the crust growth rate equation is then readily deduced as:

$$\rho_{t,c} \Delta e_{t,c} \dot{\delta}_t = \frac{k_{t,c}}{k_{t,c} + h_r \delta_t} \left(h_r (T_{t,frz} - T_{bound}) - \dot{Q}_{t,c} \delta_t \left[1 + \frac{h_r \delta_t}{2k_{t,c}} \right] \right) - h_t (T_m - T_{t,frz}) \quad (2-97)$$

This equation is integrated using the crust thickness obtained from the intermittent crust boundary condition (i.e., Eq. 2-90) as the initial condition. The radiation heat transfer coefficient h_r in the above equation is defined through Eq. 2-71. This coefficient is a function of the crust upper surface temperature $T_{t,I}$, and that temperature is determined through the energy balance at the crust-atmosphere interface; i.e., Eq. 2-95. With Eq. 2-96, this energy balance is written explicitly as:

$$\dot{Q}_{t,c} \delta_t + \frac{k_{t,c}}{k_{t,c} + h_r \delta_t} \left(h_r (T_{t,frz} - T_{bound}) - \dot{Q}_{t,c} \delta_t \left[1 + \frac{h_r \delta_t}{2k_{t,c}} \right] \right) = h_r (T_{t,I} - T_{bound}) \quad (2-98)$$

This is a non-linear equation for $T_{t,I}$ that is solved using the Newton-Raphson technique by first forming:

$$f = T_{t,I} - T_{bound} - \frac{1}{k_{t,c} + h_r \delta_t} \left(\frac{\dot{Q}_{t,c} \delta_t^2}{2} + k_{t,c} (T_{t,frz} - T_{bound}) \right) \quad (2-99)$$

with convergence obtained when $f \rightarrow 0$, and:

$$\frac{df}{dT_{t,I}} = 1 + \frac{\delta_t \left(\frac{\dot{Q}_{t,c} \delta_t^2}{2} + k_{t,c} (T_{t,frz} - T_{bound}) \right) \frac{dh_r}{dT_{t,I}}}{(k_{t,c} + h_r \delta_t)^2} \quad (2-100)$$

with $dh_r / dT_{t,I}$ given by Eq. 2-81. These equations are solved iteratively to find $T_{t,I}$ using an approach identical to that outlined around Eq. 2-56. As noted in Section 2.2, a separate conservation of mass equation is solved for the top crust. In particular, the growth rate equation given by Eq. 2-97 allows the crust composition to be determined through Eq. 2-13.

2.5 Melt Upper Surface Heat Transfer: Wet Cavity Conditions

As for the dry cavity case outlined above, the wet cavity modeling considers crust formation and evolution at the core-coolant interface, but additional phenomenology is considered that includes melt eruption and water ingression cooling mechanisms, as well as the potential for crust anchoring to the cavity sidewalls to occur with subsequent gap formation between the crust and receding melt. An illustration of the physical situation when the crust is floating is provided in Figure 2-8. For cases in which the crust is impervious to water ingression and/or melt eruptions, a full boiling curve has been modeled on the crust surface. When one or both of these mechanisms are active, then appropriate modifications to this curve are made to reflect the differences in cooling behavior. These various modeling scenarios are described in this section.

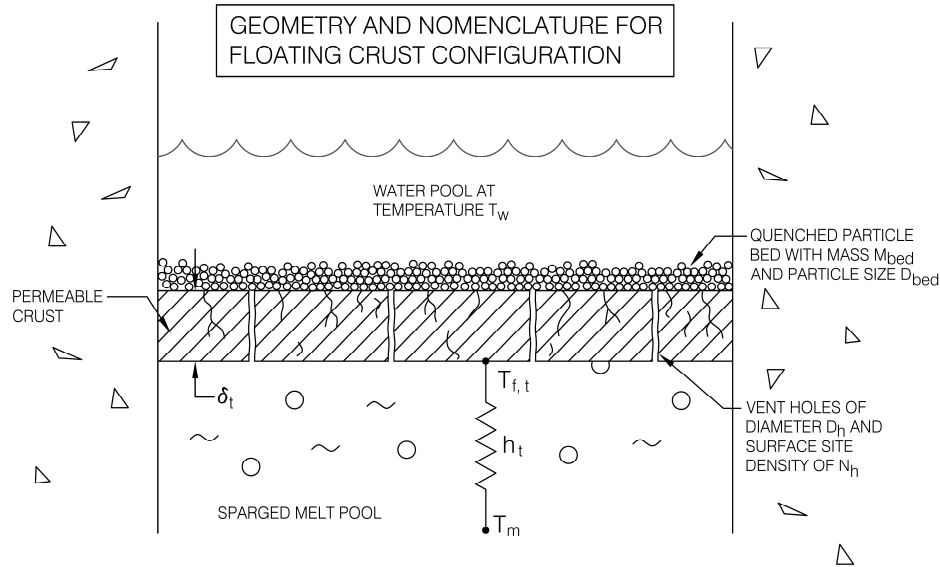


Figure 2-8. Illustration of Physical Situation for the Wet Cavity, Floating Crust Boundary Condition.

2.5.1 Crust-Free and Incipient Crust Formation Boundary Conditions

If the particular case that is being calculated includes a period of dry core-concrete interaction before cavity flooding, then the surface conditions at the end of this period constitute the initial condition for the cavity flooding phase. Otherwise, the code assumes that the surface is initially crust-free at the time of cavity flooding, and film boiling is the initial heat transfer mode. The overall methodology during this initial phase is very similar to the dry cavity case, except that the cavity boundary temperature is set to T_{sat} and the heat transfer coefficient to the atmosphere is appropriately modified to account for the presence of water. The potential for crust formation to occur is still determined through the energy balance given by Eq. 2-69, but the emissivity of the overlying coolant is assumed to be unity. Furthermore, conduction heat transfer across the gas film is also included in the evaluation of the overall heat transfer rate. Finally, gas sparging causes bulk pool mixing and area enhancement at the melt-water interface that can result in substantial augmentation in the debris-water cooling rate. In this bulk-cooling regime, the overall heat transfer rate to the coolant is written as:^[2]

$$q_{wat}'' = A_* \left[\frac{k_e \Delta T_{sat}}{\delta_{fb}} + q_r'' \right] \quad (2-101)$$

where:

- ΔT_{sat} = surface superheat relative to coolant saturation point = $(T_{t,i} - T_{sat})$
- A_* = dimensionless surface area enhancement,
- δ_{fb} = thickness of gas film containing water vapor and noncondensable gases from core-concrete interaction, and
- k_e = effective thermal conductivity of gas mixture in film.

The radiant heat flux across the film is expressed as:

$$q_r'' = h_r \Delta T_{sat} \quad (2-102)$$

Since the emissivity of water is ~ 1 and the boundary temperature presented by the overlying coolant is T_{sat} , then the radiant heat transfer coefficient takes the following form:

$$h_r = \sigma_{sef} \varepsilon_m (T_{t,l}^2 + T_{sat}^2) (T_{t,l} + T_{sat}) \quad (2-103)$$

Given a correlation for the frequency at which the bubbles arrive at the melt-water interface (Eq. 2-87), as well as a simplified model for the area enhancement as the bubbles pass through the interface, Farmer *et al.*^[2] developed the following correlation for the dimensionless surface area enhancement as a function of gas sparging rate:

$$A_* = 1 + 4.5 \frac{j}{U_T} \quad (2-104)$$

The sparging rate j in this equation is given by Eq. 2-74, and the bubble terminal rise velocity U_T is evaluated using the correlation of Peebles and Garber:^[51]

$$U_T = \begin{cases} \frac{2R_{bub}^2 (\rho_m - \rho_g) g}{9\mu_m}; & \text{Re} < 2, \\ 0.33g^{0.76} \left(\frac{\rho_m}{\mu_m} \right)^{0.52} R_{bub}^{1.28}; & 2 \leq \text{Re} < 4.02M^{-0.214}, \\ 1.35 \left(\frac{\sigma_m}{\rho_m R_{bub}} \right)^{0.5}; & 4.02M^{-0.214} \leq \text{Re} < 3.10M^{-0.25} \\ 1.18 \left(\frac{g\sigma_m}{\rho_{bub}} \right)^{0.25}; & 3.10M^{-0.25} \leq \text{Re} \end{cases} \quad (2-105)$$

where the gas bubble Morton and Reynolds numbers are defined as:

$$M = \frac{g\mu_m^4}{\rho_m \sigma_m^3} \quad (2-106)$$

$$\text{Re} = \frac{2\rho_m R_{bub} U_T}{\mu_m} \quad (2-107)$$

Finally, the gas film thickness δ_{fb} in Eq. 2-101 is calculated on the basis of a modification^[2] to Berenson's correlation^[52] for the surface heat flux in film boiling to account for the effects of coolant subcooling, radiant heat transfer across the film, and noncondensable gas injection into the film due to the concrete decomposition gases. In this analysis, Berenson made the assumption that the lateral bubble spacing over the surface was determined by Taylor instability.^[53] On this basis, the one-dimensional momentum equation governing vapor flow in the film under laminar flow conditions was solved; the pressure drop along the flow patch was equated to the buoyancy created by the growing bubbles. Heat conduction across the film vaporizes steam that feeds the gas flow within the film. These considerations led Berenson to the following equation for the vapor film thickness in film boiling,

$$\delta_{fb,B}^4 = \frac{C_B^4 \mu_v}{\rho_v \Delta e_{lv} g (\rho_l - \rho_v)} \sqrt{\frac{\sigma_l}{g (\rho_l - \rho_v)}} \left(\frac{k_v \Delta T_{sat}}{\delta_{fb,B}} \right), \quad (2-108)$$

or:

$$\delta_{fb,B} = C_B \left[\frac{k_v \mu_v \Delta T_{sat}}{\rho_v \Delta e_{lv} g(\rho_l - \rho_v)} \sqrt{\frac{\sigma_l}{g(\rho_l - \rho_v)}} \right]^{1/4} \quad (2-109)$$

where C_B is an empirical constant that was set at 2.35 in order to match experimental data,^[52] and subscripts l and v denote coolant liquid and vapor phases, respectively. Recognizing the term $k_v \Delta T_{sat} / \delta_{fb}$ in Eq. 2-108 as the heat conduction across the vapor film that drives gas production, then to first approximation this equation can be re-written to account for the effects of interfacial area enhancement, radiation heat transfer across the film, subcooling on the water-side of the film, and noncondensable gas injection into the film; i.e.,

$$\delta_{fb}^3 = \frac{C_B^4 \mu_e}{g(\rho_l - \rho_e)} \sqrt{\frac{\sigma_l}{g(\rho_l - \rho_e)}} \left(\frac{A_*}{\rho_v \Delta e_{lv}} \left[\frac{k_e \Delta T_{sat}}{\delta_{fb}} + q_r'' - q_{sub}'' \right] + j \right) \quad (2-110)$$

where subscript e denotes a property of the steam-gas mixture in the film. The radiation heat flux in this expression is given by Eqs. 2-102 and 2-103. The modeling approach for evaluating the heat flux to the subcooled water pool (q_{sub}'') that reduces the steam production rate and, thereby, the vapor film thickness is described later in this section.

It is beneficial to scale Eq. 2-110 in order to reduce the number of variable groups in the equations that follow. In particular, the following dimensionless film thickness is defined:

$$\bar{\delta} = \frac{\delta_{fb}}{\delta_{fb,B}} \quad (2-111)$$

where $\delta_{fb,B}$ is Berenson's solution for the film thickness given by Eq. 2-109. Substitution of this expression into the above equation and rearranging yields:

$$\bar{\delta}^3 = \frac{\mu_e}{\mu_v} \left(A_* \left[\frac{k_e}{k_v \bar{\delta}} - \psi \right] + \gamma \right) \quad (2-112)$$

where the fact that $[(\rho_l - \rho_v)/(\rho_l - \rho_e)]^{3/2} \sim 1$ has been utilized in order to reduce the complexity of the scaled equation, and

$$\gamma = \frac{\rho_v \Delta e_{lv} j}{q_{fb,B}''} \quad (2-113)$$

$$\psi = \frac{q_{sub}'' - q_r''}{q_{fb,B}''} \quad (2-114)$$

with $q_{fb,B}'' = k_v \Delta T_{sat} / \delta_{fb,B}$.

For the purposes of this analysis, the gas mixture thermal properties in the film are calculated on the basis of a simple volumetric weighting; i.e.,

$$k_e = F_v k_v + (1 - F_v) k_g \quad (2-115)$$

$$\mu_e = F_v \mu_v + (1 - F_v) \mu_g \quad (2-116)$$

$$\rho_e = F_v \rho_v + (1 - F_v) \rho_g \quad (2-117)$$

where F_v denotes the volume fraction of vapor in the gas mixture, which given the approach outlined above can be deduced as:

$$F_v = \frac{\frac{A_*}{\rho_v \Delta e_{lv}} \left[\frac{k_e \Delta T_{sat}}{\delta_{fb}} + q_r'' - q_{sub}'' \right]}{\frac{A_*}{\rho_v \Delta e_{lv}} \left[\frac{k_e \Delta T_{sat}}{\delta_{fb}} + q_r'' - q_{sub}'' \right] + j} = \frac{A_* \left[\frac{k_e}{k_v \delta} - \psi \right]}{A_* \left[\frac{k_e}{k_v \delta} - \psi \right] + \gamma} \quad (2-118)$$

Combining Eqs. 2-115 and 2-118 and solving yields the following solution for k_e :

$$k_e = \frac{1}{2} k_v \left\{ 1 - \bar{\delta} \left(\frac{\gamma}{A_*} - \psi \right) + \sqrt{\left[1 - \bar{\delta} \left(\frac{\gamma}{A_*} - \psi \right) \right]^2 + 4 \bar{\delta} \left[\gamma \frac{k_g}{k_v A_*} - \psi \right]} \right\} \quad (2-119)$$

This expression allows F_v to be evaluated from Eq. 2-115 as:

$$F_v = \frac{k_e - k_g}{k_v - k_g}, \quad (2-120)$$

Given this equation, the balance of the film gas mixture properties can be determined through Eqs. 2-116 and 2-117.

The final parameter requiring specification in Eqs. 2-110 and 2-114 is the effective subcooling on the water-side of the water-film interface. Bubble departure in the subcooled boiling regime is expected to stir the fluid so that the subcooled liquid adjacent to the interface is periodically replenished. Szekely^[54] developed a model based on this concept; i.e., the interfacial heat flux is evaluated using a transient heat conduction solution that is averaged over the bubble departure period. Following this same approach, then the average heat flux from the liquid-vapor interface due to subcooling can be written as:

$$q_{sub}'' = \frac{2k_l \Delta T_{sub}}{\sqrt{\pi \left(\frac{k_l}{\rho_l c_l} \right) t_{dep}}} \quad (2-121)$$

where t_{dep} is the period of bubble departure and $\Delta T_{sub} = T_{sat} - T_{wat}$ is the coolant subcooling. Consistent with the wave instability concept that underlies Berenson's film boiling model,^[52] the bubble departure period is assumed to be determined by the critical wave frequency of the Taylor instability that is given by:^[48]

$$f_{crit} = \sqrt{\frac{2\pi\sigma_l}{\lambda_{crit}^3 (\rho_l + \rho_v)}} \quad (2-122)$$

The bubble departure period is thus evaluated as $t_{dep} = 1/f_{crit}$. The parameter λ_{crit} in the above equation is the critical wavelength of the Taylor instability, and is defined as:^[53]

$$\lambda_{crit} = 2\pi \sqrt{\frac{\sigma_l}{g(\rho_l - \rho_v)}} \quad (2-123)$$

At the time this model was developed, there was considerable data available in the open literature regarding film boiling heat transfer on spheres and cylinders, but the author was unable to locate any significant data to evaluate the effect of subcooling on the film boiling heat transfer

coefficient in a pool-type geometry. On this basis, the subcooling component of the current model was adjusted according to horizontal cylinder film boiling data obtained by Sakurai *et al.*^[55] This comparison indicated that the dimensionless parameter ψ defined in Eq. 2-114 needed to be redefined in order to match the trend of the experiment data. In particular, ψ was rewritten as:

$$\psi = C_{sub} \left(\frac{q_{sub}''}{q_{fb,B}''} \right)^n - \frac{q_r''}{q_{fb,B}''}, \quad (2-124)$$

where C_{sub} and n are empirical constants. The results of the comparison indicated that the best fit was obtained with $C_{sub} \approx 2.0$ and $n \approx 0.5$. The film boiling correlation in CORQUENCH is currently coded with the constants set at these values.

The above efforts have focused on developing a general model for the film boiling heat transfer regime that includes the effects of radiant heat transfer, bulk liquid subcooling, interfacial area enhancement, and noncondensable gas injection. The overall heat flux to the water in this case is calculated through Eq. 2-101 after solving the non-linear set of equations for the film thickness given by Eq. 2-110 with Eqs. 2-111 to 2-124.

With this background, the first step in the overall solution process is to solve for the melt-coolant interfacial temperature assuming that a crust is absent. Based on the value of this temperature relative to the melt freezing temperature, decisions are then made on how to proceed with the solution. Following the general approach outlined for the dry cavity case, for situations in which the melt surface is crust-free, the *local* energy balance at the interface is of the form:

$$h_t (T_m - T_{t,I}) = h_{wat} (T_{t,I} - T_{sat}) \quad (2-125)$$

The interface temperature is thus deduced as:

$$T_{t,I} = \frac{h_t T_m + h_{wat} T_{sat}}{h_t + h_{wat}} \quad (2-126)$$

The water-side heat transfer coefficient is deduced from Eq. 2-101 as:

$$h_{wat} = A_* \left[\frac{k_e}{\delta_{fb}} + h_r \right], \quad (2-127)$$

and h_r for this case is given by Eq. 2-103. Equation 2-126 constitutes a non-linear expression for the interface temperature $T_{t,I}$. This equation is solved using the Newton-Raphson technique by first forming:

$$f = T_{t,I} - \frac{h_t T_m + h_{wat} T_{sat}}{h_t + h_{wat}}, \quad (2-128)$$

with convergence obtained when $f \rightarrow 0$, and:

$$\frac{df}{dT_{t,I}} = 1 + \left[\frac{h_t T_m + h_{wat} T_{sat}}{(h_t + h_{wat})^2} \right] \frac{dh_{wat}}{dT_{t,I}}. \quad (2-129)$$

where:

$$\frac{dh_{wat}}{dT_{t,I}} = A_* \left[\frac{dh_r}{dT_{t,I}} - \frac{k_e}{\delta_{fb}^2} \frac{d\delta_{fb}}{dT_{t,I}} \right] \quad (2-130)$$

$$\frac{d\delta_{fb}}{dT_{t,I}} = \omega A_* \left[3\delta_{fb}^2 + \frac{\omega A_* k_e \Delta T_{sat}}{\delta_{fb}^2} \right]^{-1} \left\{ \frac{k_e}{\delta_{fb}} + h_r + \Delta T_{sat} \frac{dh_r}{dT_{t,I}} - \frac{3}{8} \frac{k_v}{\delta_{fb}} \sqrt{\frac{q_{sub}''}{q_{fb,B}''}} \right\} \quad (2-131)$$

$$\omega = \frac{C_B^4 \mu_e}{\rho_v \Delta e_{lv} g(\rho_l - \rho_e)} \sqrt{\frac{\sigma_l}{g(\rho_l - \rho_e)}} \quad (2-132)$$

$$\frac{dh_r}{dT_{t,I}} = \sigma_{stef} \mathcal{E}_m (3T_{t,I}^2 + 2T_{t,I} T_{bound} + T_{bound}^2) \quad (2-133)$$

With these expressions, iteration is then performed to find $T_{t,I}$ using an approach identical to that outlined around Eq. 2-56. The iteration also provides the solution for the film boiling vapor film thickness and, thereby, the total heat flux to the overlying coolant (Eq. 2-101) that includes the various phenomena that have been previously described. The resultant solution for $T_{t,I}$ is then compared to the melt freezing temperature $T_{m,frz}$ to determine the next step in the solution methodology. For situations in which $T_{t,I} \geq T_{m,frz}$, the solution is valid and the boundary surface temperature in the melt energy balance equation (Eq. 2-18) is evaluated by setting $T_t = T_{t,I}$. However, in this case the effective melt-side heat transfer coefficient is recalculated on the basis of the total heat removal to the overlying coolant that includes the interfacial area enhancement, and the effective coefficient is used in melt energy balance equation. In particular, the coefficient is redefined as:

$$h_{t,eff} = \frac{h_{wat}(T_m - T_{sat})}{T_m - T_{t,I}} \quad (2-134)$$

When $T_{t,I} < T_{m,frz}$, the potential exists for stable crust formation to occur at the melt-atmosphere interface depending upon the thermalhydraulic conditions. As for the dry cavity case (see Section 2.4.1), the melt sparging rate at the current time is compared to the critical value required to break up the incipient crust segments that are attempting to form and bond at the melt-water interface. Following the analysis approach outlined in the Section 2.4.1, while recognizing the differences in boundary conditions due to the presence of the overlying coolant, then the following solution for the critical melt superficial gas velocity to preclude stable crust formation at the melt-water interface is obtained:^[2]

$$j_{crit} = \frac{0.445 R_{bub} h_t (T_m - T_{t,frz})}{\delta_{t,min} \rho_{t,c} \Delta e_{t,c} \left\{ \frac{k_{t,c} (T_{t,frz} - T_{sat})}{\delta_{t,min} h_t (T_m - T_{t,frz})} \ln \left(\frac{1}{1 - \hat{C}_3} \right) - 1 \right\}} \quad (2-135)$$

where:

$$\hat{C}_3 = \frac{h_t h_{wat} (T_m - T_{t,frz}) \delta_{t,min}}{k_{t,c} [h_{wat} (T_{t,frz} - T_{sat}) - h_t (T_m - T_{t,frz})]} \quad (2-136)$$

Recall that this solution is only valid when $h_{wat}(T_{t,frz} - T_{sat}) > h_t(T_m - T_{t,frz})$; i.e., the thermodynamic conditions at the interface are consistent with crust formation. Thus, when this condition is met and $j > j_{crit}$, thin crust segments form at the surface, but they are continuously broken up and mixed in with the bulk melt by gas sparging. Under these conditions the upwards heat transfer term $h_t(T_m - T_t)$ in Eq. 2-18 is evaluated by setting $T_{t,I} = T_{t,frz}$, and the melt-side

convective heat transfer coefficient is calculated through Eq. 2-134. Furthermore, the intermittent crust thickness is found from the analog of Eq. 2-83 for the wet cavity case; i.e.,

$$\hat{C}_1 h_{wat} \delta_t + \hat{C}_2 \ln \left[1 - \frac{\hat{C}_1 h_{wat} \delta_t}{\hat{C}_2 - \hat{C}_1 k_{t,c}} \right] + \hat{C}_1^2 t_a = 0 \quad (2-137)$$

where:

$$\hat{C}_1 = \frac{h_t h_{wat}}{\rho_{t,c} \Delta e_{t,c}} (T_m - T_{t,frz}) \quad (2-138)$$

$$\hat{C}_2 = \frac{k_{t,c} h_{wat}^2}{\rho_{t,c} \Delta e_{t,c}} (T_{t,frz} - T_{sat}) \quad (2-139)$$

As for the dry cavity case, Eq. 2-137 is a non-linear equation for the intermittent crust thickness that is solved using the Newton Raphson technique by first forming:

$$f = \delta_t + \frac{\hat{C}_2}{\hat{C}_1 h_{wat}} \ln \left[1 - \frac{\hat{C}_1 h_{wat} \delta_t}{\hat{C}_2 - \hat{C}_1 k_{t,c}} \right] + \frac{\hat{C}_1}{h_{wat}} t_a = 0 \quad (2-140)$$

with convergence obtained when $f \rightarrow 0$, and:

$$\frac{df}{d\delta_t} = 1 - \frac{\hat{C}_2}{\hat{C}_2 - \hat{C}_1 k_{t,c} - \hat{C}_1 h_{wat} \delta_t} \quad (2-141)$$

Iteration is then performed to find δ_t using an approach identical to that outlined around Eq. 2-56. With δ_t known through these efforts, the interface temperature is then found from:

$$T_{t,i} = \frac{\frac{k_{t,c}}{\delta_t} T_{t,frz} + h_{wat} T_{wat}}{\frac{k_{t,c}}{\delta_t} + h_{wat}} \quad (2-142)$$

The critical gas velocity given by Eq. 2-135 constitutes one criterion for onset of stable crust formation at the melt water interface. This expression has been found to reasonably predict breakdown of bulk cooling for most reactor material tests for which the model has been applied. However, in a few instances (i.e., high power density tests), the model under-predicts the critical velocity, leading to prolonged periods of bulk cooling in which the melt temperature falls far below that observed in the tests. To circumvent this shortcoming, a second criterion has been deployed in the code for determining when breakdown of bulk cooling occurs. The underlying premise is that water may begin to intermittently contact the corium surface when the heat transfer rate falls below the critical heat flux limit, and this enhanced surface cooling could lead to breakdown of bulk cooling earlier than that predicted by the critical gas velocity model (Eq. 2-135) that is based solely on area-enhanced film boiling. The specific criterion deployed in the code is that bulk cooling breaks down if the surface cooling rate falls below the following limit that is related to the critical heat flux as:

$$q_{crit,bc}'' = C_{crit} q_{CHF}'' \quad (2-143)$$

where q_{CHF}'' is the pool boiling critical heat flux and C_{crit} is a user-specified constant. The critical heat flux is evaluated using the Ivey-Morris^[56] modification to Zuber's correlation,^[57] which is presented in the next section along with the description of the overall pool boiling model that is currently deployed in the code. Equation 2-143 is used in conjunction with Eq. 2-135 for determining when bulk cooling terminates; i.e., when either criterion is met, the solution bifurcates to the stable floating crust boundary condition that is described in the next section. The user has the option of setting $C_{crit} = 0$, in which case the decision regarding whether or not bulk cooling is terminated is based solely on Eq. 2-135. Regardless of the criterion that is used, the effective corium surface area enhancement (calculated from Eq. 2-104) at termination of bulk cooling is saved, and this value is used in the evaluation of the film boiling heat transfer coefficient during the stable crust growth phase. The extent of surface area enhancement is internally limited to a value of 3.0 within the code.

2.5.2 Stable Floating Crust Boundary Condition

The final phase of the wet cavity modeling considers the case where thermodynamic conditions are correct for crust formation [i.e., $h_{wat}(T_{t,frz} - T_{sat}) > h_t(T_m - T_{t,frz})$], but in addition $j < j_{crit}$ and so the incipient crust segments can bond together to form a mechanically stable configuration, and the crust can then grow to the point where convective heat transfer to the underside of the crust balances that conducted through the crust to the overlying coolant. As noted above, the area enhancement augmentation to the debris cooling rate is set equal to the value saved at the end of the bulk cooling transient in the film boiling model for situations in which film boiling is still the applicable heat transfer mode on the crust surface.

Once stable crust formation is initiated, several different types of heat transfer mechanisms can be activated, depending upon the melt pool thermalhydraulic conditions as well as user-defined modeling assumptions. In any event, a crust growth rate equation is solved. The formulation given immediately below corresponds to the case in which the crust is impermeable to water ingress; the water ingress case is addressed later in this section.

Utilizing the same overall modeling assumptions that were employed previously for the dry cavity crust modeling case, then the equation governing crust growth at the interface with water present is deduced from Eq. 2-97 as:

$$\rho_{t,c} \Delta e_{t,c} \dot{\delta}_t = \frac{k_{t,c}}{k_{t,c} + h_{wat} \delta_t} \left(h_{wat} (T_{t,frz} - T_{sat}) - \dot{Q}_{t,c} \delta_t \left[1 + \frac{h_{wat} \delta_t}{2k_{t,c}} \right] \right) - h_t (T_m - T_{t,frz}) \quad (2-144)$$

Ideally, this equation would be integrated using the crust thickness obtained from the intermittent crust boundary condition solution (i.e., Eq. 2-137) as the initial condition. However, this thickness is usually quite small [i.e., $O(10^{-5} \text{ m})$] and is thus not compatible with a numerically stable solution for typical integration timesteps (e.g., 50-100 ms) when water is present in the cavity and the temperature gradient across the crust is initially large. For this case, the thickness is initialized by examining the form of the growth rate equation as $t \rightarrow 0$. Under this condition, the crust thickness is small and so decay heat within the crust is negligible. Furthermore, the heat conduction across the crust to the coolant that drives the growth is much larger than the convective heat transfer from the melt that is acting to retard the growth. Finally, assuming that the crust upper surface

temperature is approximately equal to the coolant saturation temperature, then the crust growth rate equation simplifies to:

$$\rho_{t,c} \Delta e_{t,c} \dot{\delta}_t \sim \frac{k_{t,c} (T_{t,frz} - T_{sat})}{\delta_t} \quad (2-145)$$

which, upon integration subject to $\delta_t(t=0) = 0$, yields:

$$\delta_t(t \rightarrow 0) = \sqrt{\frac{2k_{t,c} (T_{t,frz} - T_{bound})t}{\rho_{t,c} \Delta e_{t,c}}} \quad (2-146)$$

The initial condition on Eq. 2-144 is then evaluated from the above expression by setting the time equal to the user-specified timestep for the integration; i.e. $t = \Delta t$.

The water-side interface temperature and corresponding heat transfer coefficient in Eq. 2-144 are determined through an energy balance at the crust-coolant interface, which is deduced from the analogous dry cavity energy balance (Eq. 2-98) as:

$$\dot{Q}_{t,c} \delta_t + \frac{k_{t,c}}{k_{t,c} + h_{wat} \delta_t} \left(h_{wat} (T_{t,frz} - T_{sat}) - \dot{Q}_{t,c} \delta_t \left[1 + \frac{h_{wat} \delta_t}{2k_{t,c}} \right] \right) = h_{wat} (T_{t,I} - T_{sat}) \quad (2-147)$$

As for the dry cavity case, this energy balance is a non-linear equation for $T_{t,I}$ that can be solved using the Newton-Raphson technique by first forming:

$$f = T_{t,I} - T_{sat} - \frac{1}{k_{t,c} + h_{wat} \delta_t} \left(\frac{\dot{Q}_{t,c} \delta_t^2}{2} + k_{t,c} (T_{t,frz} - T_{sat}) \right) \quad (2-148)$$

with convergence obtained when $f \rightarrow 0$, and:

$$\frac{df}{dT_{t,I}} = 1 + \frac{\delta_t \left(\frac{\dot{Q}_{t,c} \delta_t^2}{2} + k_{t,c} (T_{t,frz} - T_{sat}) \right) \frac{dh_{wat}}{dT_{t,I}}}{(k_{t,c} + h_{wat} \delta_t)^2} \quad (2-149)$$

These equations are solved iteratively to find $T_{t,I}$ using an approach identical to that outlined around Eq. 2-56, but with h_{wat} and the corresponding derivative evaluated on the basis of the particular mode of boiling heat transfer that is applicable on the crust surface at any given time. As noted in Section 2.2, a separate conservation of mass equation is solved for the top crust. In particular, the growth rate equation given by Eq. 2-144 allows the crust constituency to be determined as a function of time through Eq. 2-13.

CORQUENCH is coded with a traditional model of the full boiling curve; a depiction is provided in Figure 2-9. This model is described below. Modifications that have been made to account for experimental observations from corium coolability and separate effect experiments are provided at the end of this general description.

After stable crust formation is initiated, film boiling heat transfer is maintained until the crust surface temperature falls below the minimum value required to maintain film boiling. In this case, the film boiling model described above is used to calculate the heat transfer coefficient to the overlying water with the area enhancement factor A^* set to the value at the end of the bulk cooling

phase. The interface temperature and heat transfer coefficient to the water pool are calculated through the energy balance given by Eq. 2-147, but with the heat transfer coefficient derivative function calculated through Eqs. 2-130 to 2-133.

After the crust surface temperature falls below the minimum point, film boiling will break down and the transition boiling regime will be entered. The surface superheat at the minimum point is calculated using Henry's correlation,^[58] which is a modification to Berenson's original expression^[52] for the minimum point to account for coolant subcooling and properties of the heating surface; i.e.,

$$\Delta T_{\min} = \Delta T_{\min,B} + 0.42(\Delta T_{\min,B} + \Delta T_{\text{sub}}) \left(\frac{\Delta e_{lv}}{c_{t,c} \Delta T_{\min,B}} \sqrt{\frac{k_l \rho_l c_l}{k_{t,c} \rho_{t,c} c_{t,c}}} \right)^{0.6} \quad (2-150)$$

where Berenson's correlation for the minimum point is given by:

$$\Delta T_{\min,B} = 0.127 \frac{\rho_v \Delta e_{lv}}{k_v} \left(\frac{g(\rho_l - \rho_v)}{\rho_l + \rho_v} \right)^{2/3} \left(\frac{\mu_v}{g(\rho_l - \rho_v)} \right)^{1/3} \sqrt{\frac{\sigma_l}{g(\rho_l - \rho_v)}} \quad (2-151)$$

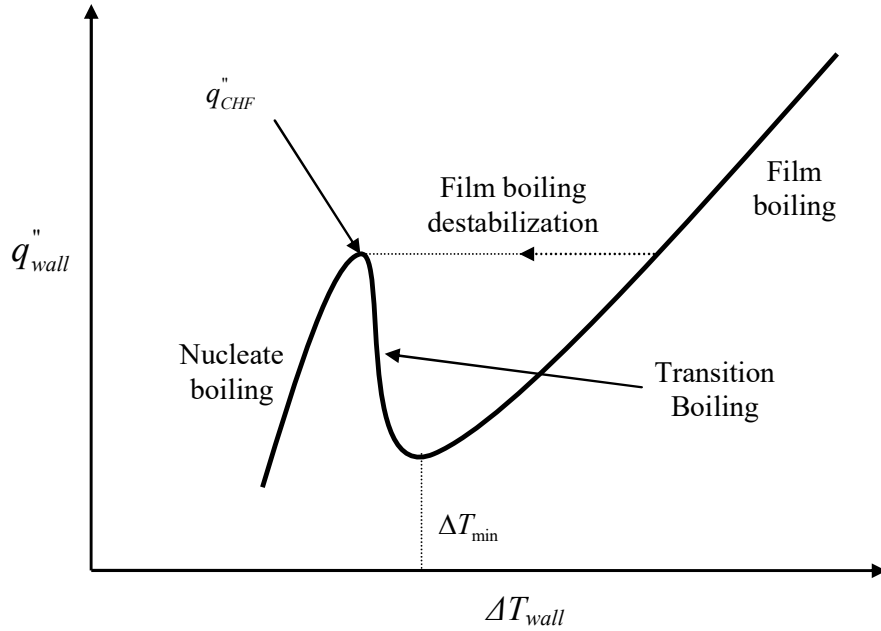


Figure 2-9. Illustration of Boiling Curve.

With the minimum film boiling temperature so specified, the heat flux at the minimum point (q''_{\min}) is calculated using the above described film boiling model evaluated at this temperature.

Correlations for the heat transfer coefficient in the transition boiling regime are sparse. Thus, the approach adopted for this work is to calculate the critical heat flux, as well as the surface superheat at this heat flux. Given this data as well as the minimum film boiling point conditions calculated as described above, the heat flux is assumed to vary linearly between these two points. The critical heat flux (CHF) is evaluated using the Ivey-Morris correlation,^[56] which is a modification to Zuber's classic model^[57] to account for the effects of coolant subcooling; i.e.,

$$q_{CHF}'' = 0.14 \rho_v \Delta e_{lv} \left(\frac{g \sigma_l (\rho_l - \rho_v)}{\rho_v^2} \right)^{1/4} \left[1 + 0.1 \left(\frac{\rho_l}{\rho_v} \right)^{3/4} \left(\frac{c_l \Delta T_{sub}}{\Delta e_{lv}} \right) \right] \quad (2-152)$$

In order to specify the surface superheat at CHF, an additional correlation is required. Working from the other side of the boiling curve (see Figure 2-9), the heat flux in the nucleate boiling regime is modeled using the Rohsenow correlation,^[59] which is of the form:

$$q_{nb}'' = C_{nb} \Delta T_{sat}^3 \quad (2-153)$$

where:

$$C_{nb} = C_{sf}^{-3} \mu_l \Delta e_{lv} \left(\frac{\sigma_l}{g (\rho_l - \rho_v)} \right)^{-1/2} \left(\frac{c_l}{\Delta e_{lv}} \right)^3 \left(\frac{c_l \mu_l}{k_l} \right)^{-5.1} \quad (2-154)$$

and C_{sf} is an empirical factor dependent upon the surface-fluid combination. Although this factor has been determined for many surfaces in contact with water, almost all are metallic. In lieu of data for a water-oxide combination, this constant is internally set at 0.02, which is indicative of a stainless steel-water system.

Given Eq. 2-153, the heat transfer coefficient and the derivative of the coefficient with respect to surface temperature in nucleate boiling are readily deduced as:

$$h_{wat,nb} = C_{nb} \Delta T_{sat}^2 \quad (2-155)$$

$$\frac{dh_{wat,nb}}{dT_{t,l}} = 2C_{nb} \Delta T_{sat} \quad (2-156)$$

These are the expressions that are required to solve the crust upper surface energy balance equation (see Eqs. 2-147 to 2-149) for the surface temperature and, thereby, the heat flux to the overlying coolant in the nucleate boiling regime. Given these results, then the surface superheat at CHF can be found by equating Eqs. 2-152 and 2-153, which yields:

$$\Delta T_{CHF} = \left(\frac{q_{CHF}''}{C_{nb}} \right)^{1/3} \quad (2-157)$$

As previously noted, in this analysis the heat flux in the transition boiling regime is assumed to vary linearly between CHF and the minimum film boiling point, and so:

$$q_{tran}'' = \left(\frac{q_{min}'' - q_{CHF}''}{\Delta T_{min} - \Delta T_{CHF}} \right) (\Delta T_{sat} - \Delta T_{CHF}) + q_{CHF}'' \quad (2-158)$$

The heat transfer coefficient and corresponding derivative in the transition boiling regime are then deduced as:

$$h_{tran} = \left(\frac{q_{min}'' - q_{CHF}''}{\Delta T_{min} - \Delta T_{CHF}} \right) \left(1 - \frac{\Delta T_{CHF}}{\Delta T_{sat}} \right) + \frac{q_{CHF}''}{\Delta T_{sat}} \quad (2-159)$$

$$\frac{dh_{tran}}{dT_{t,l}} = \frac{\Delta T_{CHF}}{\Delta T_{sat}^2} \left(\frac{q_{min}'' - q_{CHF}''}{\Delta T_{min} - \Delta T_{CHF}} \right) - \frac{q_{CHF}''}{\Delta T_{sat}^2} \quad (2-160)$$

These are the expressions that are needed to solve the crust energy balance equation for the upper surface temperature and heat flux in the transition boiling regime.

The above description has outlined the general pool boiling model that was originally implemented in CORQUENCH. A brief discussion is now provided on practical applications of

this model, including modifications that were made to account for experimental observations in core coolability experiments.

During initial trials of this model, numerical difficulties were encountered in attempting to resolve the heat flux variation as the crust surface temperature passed through the minimum film boiling point and on into transition boiling; see Figure 2-9. This is due to the fact that for a given heat flux just above the minimum point, there are two valid solutions for the surface temperature: one in the film boiling regime, while the second is in the nucleate boiling regime (see Figure 2-9). This fact caused numerical oscillations during the iteration between the film and transition boiling solutions that were difficult to resolve rationally. On this basis, the logic of the code was modified so that once the surface heat flux fell below the minimum point, film boiling was assumed to break down and the nucleate boiling regime was permanently (i.e., for the balance of the calculation) entered. This change produced numerically stable solutions, and was also not deemed to be significant, as there is a wealth of experiment data that indicates that transition boiling is highly unstable, and once coolant begins to wet the surface, rapid transition to nucleate boiling occurs.

The second significant change that was made was based on the fact that the traditional pool boiling model outlined in Figure 2-9 did not yield cooling behavior that was consistent with both separate effect and reactor material experiments conducted with oxide materials. In particular, the model predicted long periods (i.e., hours) of film boiling heat transfer from the crust upper surface following cavity flooding when applied to MACE coolability experiments.^[15,16] This is due to the fact that the minimum film boiling heat flux predicted by the models described above for water are quite low; i.e., $O[100 \text{ kW/m}^2]$ at a surface superheat of $\Delta T_{sat} = 100 \text{ }^\circ\text{C}$. Conversely, the code predicted heat fluxes to the overlying coolant well in excess of this level for extended periods of time, based on the input power levels used in the tests. This prediction can be contrasted with physical observations, which indicated that the corium surface completely darkened a few minutes after cavity flooding, most likely indicating surface quench to the saturation temperature. This observation is further supported by the results of insertable thermocouple measurements that were used to measure the crust upper surface temperature after cavity flooding. This data also indicated that the surface temperature was near T_{sat} .

Other data has been obtained in separate effects tests that are relevant in this application. For example, Moreaux, Chevrier, and Beck^[60] investigated the effect of the introduction of an insulating material (such as a low thermal conductivity oxide) at the interface between the heated surface and coolant, and found that the thermal resistance acted to destabilize film boiling. In addition, film boiling experiments were conducted by Farmer and Spencer^[61] with UO_2 and ZrO_2 surfaces, along with a variety of metals. The results of these tests indicated that surface thermal conductivity and roughness have a pronounced effect on film boiling behavior. In particular, breakdown of film boiling occurred at much higher temperatures for porous (i.e., rough) UO_2 and ZrO_2 relative to metal surfaces. In fact, with UO_2 film boiling broke down immediately upon contact with saturated water for initial surface temperatures as high as $600 \text{ }^\circ\text{C}$. Although Henry's correlation^[58] (viz. Eq. 2-150) predicts the correct trend of increasing minimum film boiling temperature with decreasing surface thermal properties, the correction is not large enough to account for the experimental observations with UO_2 and ZrO_2 surfaces.^[61]

Based on these various data sources, the pool boiling model in CORQUENCH was modified to reflect early breakdown in film boiling. As noted, available correlations do not

accurately predict the observed boiling behavior for oxidic reactor materials. The conceptual modification that has been made to the boiling curve is shown in Figure 2-9. When the surface heat flux in film boiling falls below CHF, film boiling is assumed to break down and the water contacts the corium surface, leading to an immediate transition to nucleate boiling. The specific criterion used in the code is that film boiling breaks down if the surface cooling rate falls below a limit that is related to CHF as:

$$q''_{crit,fb} = C_{CHF} q''_{CHF} \quad (2-161)$$

where C_{CHF} is a user-specified constant. Although somewhat adhoc, this change in the modeling approach has been found to do a much better job in capturing the debris quenching behavior observed in experiments. The user has the option of setting $C_{CHF} = 0$, in which case the classical film boiling model is recovered. In particular, the code compares the heat flux from the crust to the coolant to both q''_{min} and $q''_{crit,fb}$, and if either criterion is met, film boiling is assumed to break down and nucleate boiling is initiated.

2.5.3 Melt Eruption Modeling

Following stable crust formation, the potential exists for additional melt cooling mechanisms to come into play that can augment the debris cooling rate over and above that predicted on the basis of the stable impervious crust model described above. This section addresses the melt eruption cooling mechanism that has been observed in reactor material melt cooling experiments conducted with both limestone/common sand and siliceous concrete types.^[66]

To this end, the code has been configured to model melt entrainment through the crust by sparging concrete decomposition gases. The entrained melt is assumed to be quenched in the form of a particle bed that accumulates above the crust. In general, melt dispersal during eruptions is calculated by assuming that the melt entrainment rate is proportional to the gas volumetric flowrate times an entrainment coefficient; i.e.,^[27]

$$j_m = K_{ent} J \quad (2-162)$$

where j_m is again noted to be the superficial gas velocity of entrained melt into the overlying water pool, and K_{ent} is the melt entrainment coefficient. The code has been structured to allow the user to choose between three different modeling options for evaluating K_{ent} . The first is that the entrainment coefficient is defined as a user-specified input constant, which requires no further explanation.

The second option is that the entrainment coefficient can be calculated using the Ricou-Spalding correlation,^[44] which has been found to predict the entrainment rate for a wide variety of fluid systems in different flow geometries. This correlation is of the form:

$$K_{ent} = E \left(\frac{\rho_g}{\rho_m} \right)^{1/2} \quad (2-163)$$

where E is a proportionality constant which ranges from 0.06 to 0.12.^[44] Based on a literature review and comparison of this correlation with data, a mid-range value of $E = 0.08$ has been recommended for analysis of melt eruption behavior during core-concrete interaction for the case of limestone/common sand concrete.^[47] As noted in Reference [66], spontaneous eruptions are less pronounced for tests conducted with siliceous concrete. As is evident from Eq. 2-162, the entrainment rate is proportional to the melt sparging rate. Thus, the reduced gas content that is

characteristic of siliceous concrete is consistent with the reduced level of eruptions observed in tests with this concrete type.

The third option for evaluating melt eruption behavior is the model due to Farmer.^[30] In this work, existing models developed by Tourniaire and Seiler^[29] for the melt entrainment process were extended to include melt solidification and gas flow effects through the crust that develops at the interface between the melt pool and overlying coolant. The physical characteristics associated with this model are outlined in Figure 2-10. The modeling addressed the thermal hydraulic flow, pressure drop, and freezing processes involved with melt ejections through a crust that is permeable to both gas and water flows. These efforts led to analytical solutions for the active melt eruption hole site density through the crust, as well as the average eruption hole diameter and melt mass flowrate through each hole. Given the hole site density and mass entrainment rate through the holes, then the average melt entrainment coefficient through the crust is correlated as:

$$K_{ent} = \frac{\dot{m}_h N_h''}{\rho_m j} \quad (2-164)$$

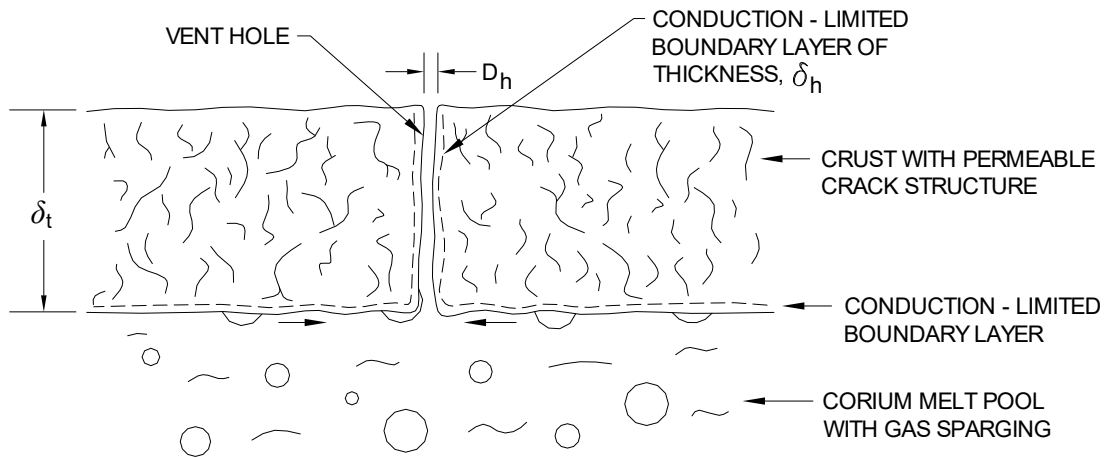


Figure 2-10. Physical Depiction of Crust Configuration for Melt Eruption Model.

where \dot{m}_h is the mass flowrate through an individual vent hole and N_h'' is the crust hole site density. The one-dimensional momentum equation was solved for a given vent hole to relate the mass flowrate through the hole to the applied hydrostatic head applied by the overlying crust, which yielded the following solution for the hole mass flowrate:

$$\dot{m}_h = \rho_m u_m \frac{\pi D_h^2}{4} = \frac{\pi \rho_m (\rho_{t,c} - \rho_m) g D_h^4}{128 \mu_m} \quad (2-165)$$

where D_h is the diameter of the vent holes through the crust. Two solutions were developed for the vent hole diameter, depending upon whether or not the crust is permeable to water ingress. For the impermeable crust case, the minimum vent hole diameter to support eruptions is found as:

$$D_h = \left(\frac{64 \mu_m k_{t,c} (T_{m,frz} - T_{sat})}{c_m (T_m - T_{m,frz}) \rho_m (\rho_{t,c} - \rho_m) g} \right)^{1/3} \quad (2-166)$$

Note that the above expression is independent of crust thickness.

The second solution is for the case in which the crust is permeable to water ingress. In this case the solution for the hole diameter is of the form:

$$D_h = \left(\frac{128\mu_m q_{sf}'' \delta_t}{c_m (T_m - T_{m,frz}) \rho_m (\rho_{t,c} - \rho_m) g} \right)^{1/3} \quad (2-167)$$

where q_{sf}'' is the heat flux at the inner surface of the vent hole that acts to cool the melt as it passes through the hole. For this case, the crust is assumed to be characterized by a permeability κ and, therefore, a dryout heat flux limit that is denoted $q_{c,dry}''$. The heat flux at the inner surface of the tube is then found to be related to the crust dryout limit^[30] through the expression:

$$q_{sf}'' = \left(1 + \frac{2\delta_h}{D_h} \right) q_{c,dry}'' \quad (2-168)$$

where δ_h is the dry thermal boundary layer thickness around the vent hole; see Figure 2-10. An energy balance was then carried out that related the heat loss from the melt flowing through the vent hole to the heat sink provided by the permeable crust. These considerations yielded the following transcendental equation for δ_h in terms of the crust dryout limit:

$$\varphi = \xi^{4/3} \ln(\xi) \quad (2-169)$$

where:

$$\xi \equiv 1 + \frac{2\delta_h}{D_h}, \quad (2-170)$$

and φ is a dimensionless parameter given by:

$$\varphi = \frac{k_{t,c} (T_{t,frz} - T_{sat})}{(q_{c,dry}'')^{4/3}} \left(\frac{c_m (T_m - T_{m,frz}) \rho_m (\rho_{t,c} - \rho_m) g}{16\mu_m \delta_t} \right)^{1/3}. \quad (2-171)$$

Equation 2-169 is solved using the Newton Raphson method by first forming:

$$f = \varphi - \xi^{4/3} \ln(\xi) \quad (2-172)$$

with convergence obtained when $f \rightarrow 0$, and:

$$\frac{df}{d\xi} = -\xi^{1/3} \left(1 + \frac{4}{3} \ln(\xi) \right). \quad (2-173)$$

Iteration is then performed to find ξ using an approach identical to that outlined around Eq. 2-56. With the thermal boundary layer known through Eq. 2-170, the minimum vent hole diameter to support eruptions for the permeable crust case is evaluated through Eqs. 2-167 and 2-168.

Finally, additional modeling was performed to develop an expression for the melt eruption hole site density through the crust. This analysis considered the thermal hydraulic flow and pressure drop through the parallel flow paths provided by the vent holes and permeable crust structure. These efforts led to the following solution for the hole site density, as well as the fraction of gas flow through the holes that drives the entrainment process:

$$N_h'' = \left(\frac{4}{\pi D_h^2} \right) \left(\frac{j - \frac{(\rho_{t,c} - \rho_m)g\kappa}{\mu_g}}{\sqrt{\frac{2(\rho_{t,c} - \rho_m)g\delta_t}{K_L \rho_g} - \frac{(\rho_{t,c} - \rho_m)g\kappa}{\mu_g}}} \right) \quad (2-174)$$

$$F_h = \frac{\pi D_h^2 N_h''}{4} \sqrt{\frac{2(\rho_{t,c} - \rho_m)g\delta_t}{K_L \rho_g j^2}} \quad (2-175)$$

where K_L is the sum of the form and friction flow loss coefficients through the vent hole; see Reference [30] for details on the evaluation of this parameter using standard methods. Examination of Eq. 2-174 indicates that there is a minimum gas velocity required to maintain active vent holes on the crust surface; i.e.,

$$j_{\min} = \frac{\kappa(\rho_{t,c} - \rho_m)g}{\mu_g} \quad (2-176)$$

Physically, the model indicates that if the crust has sufficient permeability to vent the gas flow from core-concrete interaction through the permeable structure under the applied pressure head due to the overlying crust, then there is no need to open additional flow area through the crust (i.e., eruption hole sites) to vent the gas.

The analytical solutions for the crust hole site density and flow partitioning fraction are functions of the crust permeability, κ . Crust permeabilities were measured using percolation tests in the MACE^[15,16,62] and OECD/MCCI test series.^[19,20] In addition, previous studies with porous beds have related the dryout limit to the bed permeability. In particular, Jones *et al.*^[63] derived the following correlation that has been found to provide a reasonable relationship between the permeability and dryout limit:

$$q_{c,dry}'' = \frac{\kappa \rho_v \Delta e_{lv} (\rho_l - \rho_v) g}{2 \mu_v} \quad (2-177)$$

and so:

$$\kappa = \frac{2 \mu_v q_{c,dry}''}{\rho_v \Delta e_{lv} (\rho_l - \rho_v) g} \quad (2-178)$$

This expression is used to evaluate the crust permeability from the dryout limit for use in Eqs. 2-174 and 2-176. Analytical solutions for the dryout limit that are required to complete the modeling for the permeable crust case are provided in the next section.

Equations 2-165 and 2-174 provide the models that are required to evaluate the melt entrainment coefficient through Eq. 2-164. Clearly, if the crust anchors to the cavity sidewalls and separates from the melt pool, then melt eruptions will terminate. The model is set up within the code in this manner. Farmer^[30] also performed additional studies to determine the effect of crust anchoring and melt separation on the eruption process. The results indicate that if the melt recontacts the crust after separation, as occurred in several integral debris cooling tests,^[1] then the eruption hole site density may be reduced to as little as 5% of that predicted under the floating crust boundary condition that is expected at plant scale. However, this particular feature of the modeling is currently not implemented in the code.

Data from reactor material debris cooling tests^[1,47,66] also indicates that the erupted material is rapidly quenched in the form of a discrete layer that gradually accumulates over the crust. Given this rapid quenching process, then the augmentation of the heat flux to the overlying water due to melt eruptions can be evaluated through the following equation:

$$q_{ent}'' = j_m \rho_m \Delta e_{m,sat} \quad (2-179)$$

where $\Delta e_{m,sat}$ is the enthalpy change upon complete quench of the erupted material from the melt pool temperature down to the coolant saturation temperature. The test data further indicates that the erupted material is rendered in the form of particle bed and lava-type structures with a high degree of porosity. Analysis of these structures^[62] indicates that they have extremely high dryout limits that are readily amendable to long-term cooling. Given the assumption that the erupted particulate is distributed as a layer with uniform thickness across the crust, then the overall heat flux to the water as a result of melt solidification and quench as well as decay heat within the bed is evaluated from the equation:

$$q_{bed}'' = j_m \rho_m \Delta e_{m,sat} + \frac{\chi_{bed,UO_2} m_{bed} q_{dec}}{A_b} \quad (2-180)$$

where χ_{bed,UO_2} is the mass fraction of fuel in the bed, A_b is evaluated from Eq. 2-5, and m_{bed} is given by Eq. 2-17. Given the mass of the particle bed and a user-specified bed porosity α_{bed} , then the bed height is evaluated through the expression,

$$H_b = \frac{m_{bed}}{A_b \rho_{bed} (1 - \alpha_{bed})} \quad (2-181)$$

where ρ_{bed} is the theoretical density of the material in the bed and α_{bed} is the bed porosity.

As noted earlier, the code currently solves a separate conservation of mass equation for the erupted material that is deposited in the bed so that key parameters such as the mass fraction of fuel within the bed can be calculated. Due to the high dryout limits associated with these formations,^[62] decay heat within the bed is assumed to be fully transferred to the overlying coolant. However, the code does perform an additional check to determine if the bed dryout limit could restrict the heat transfer rate from the crust upper surface. Accounting for counter-current flow of noncondensable gases from the core-concrete interaction and the decay heat within the bed itself, then the effective dryout limit evaluated at *the particle bed-crust interface* is of the form,

$$q_{eff}'' = q_{bed,dry}'' - \frac{\chi_{bed,UO_2} m_{bed} q_{dec}}{A_b} - \rho_v \Delta e_{lv} j|_{T=T_{sat}} \quad (2-182)$$

In this equation, note that the flowrate of noncondensable gases through the bed from concrete erosion is evaluated at the coolant saturation temperature, which is based on the assumption that the debris bed is maintained at saturation temperature at all times.

Test data^[15,62] indicates that the particle beds formed as a result of melt eruptions are characterized by large particle sizes (i.e., several mm \rightarrow cm). Thus, the bed dryout limit in the above equation is evaluated using the following correlation developed by Lipinski^[43] that is valid for particle sizes ≥ 1 mm,

$$q_{bed,dry}'' = \frac{0.756 \Delta e_{lv}}{\left[1 + \left(\frac{\rho_v}{\rho_l}\right)^{1/4}\right]^2} \sqrt{\frac{\rho_v \rho_l g D_{bed} \alpha_{bed}^3}{(1 - \alpha_{bed}) \left[1 + \frac{6 \sigma_l (1 - \alpha_{bed})}{D_{bed} \rho_l g H_{bed} \alpha_{bed}}\right]}} \quad (2-183)$$

where D_{bed} is the (user-specified) average particle size in the bed.

For situations in which the crust is modeled as impervious to water ingression, onset of bed formation by eruptions is assumed to not affect the current boiling regime (i.e., film vs. nucleate) that is applicable on the crust upper surface at the current time. However, the (conduction limited) heat flux from the crust upper surface is checked to see if it exceeds the effective bed dryout limit evaluated through Eqs. 2-182 and 2-183. If this situation develops, the code caps the heat flux from the crust surface at this value. However, analysis shows that even for very deep beds, the bed dryout limit does not inhibit heat removal from the crust. Again, this is due to the fact that the dryout limits predicted by Eq. 2-183 are large (e.g., typically on the order of 1 MW/m² or greater) given the physical characteristics of the particle beds observed in tests.^[62] The effect of bed formation on crust cooling for the case in which the crust is permeable to water ingression is described in the next section.

2.5.4 Crust Water Ingression Modeling

After the crust forms, the potential exists for additional cooling to occur by the mechanism of water ingression into the crust that can augment what would otherwise be a conduction-limited heat transfer process. When water ingression occurs, the possibility exists for much thicker crust accumulations to form in comparison to situations in which heat transfer across the crust is conduction-limited. Furthermore, in water-limited scenarios, crust material formed by water ingression may dry out at some point and remelt. Under these conditions, and due to the thickness of the crust accumulations, then heat capacity within the crust needs to be modeled in order to reasonably estimate the crust remelting rate.

This section addresses the modeling options implemented in CORQUENCH to evaluate the water ingression cooling mechanism, as well as the modeling approach to capture heat capacity effects when the crust dries out and remelts.

2.5.4.1 Water Ingression Modeling Approach

The criterion for onset of water ingression into the crust is that the total heat flux from the crust upper surface must fall below the crust dryout limit. Accounting for decay heat within the crust as has been done in the previous sections, then the specific criterion is of the form:

$$q_{c,dry}'' \geq k_{t,c} \frac{(T_{t,frz} - T_{sat})}{\delta_t} + \frac{\dot{Q}_{t,c} \delta_t}{2} + \rho_v h_{lv} j \Big|_{T_{sat}} \quad (2-184)$$

where, as a reminder, $\dot{Q}_{t,c} \equiv \chi_{t,UO_2} \rho_{t,c} q_{dec}$. In this equation, the assumption has been made that the noncondensable gas flow from core-concrete interaction is vented uniformly across the extent of the crust. However, note that test data^[62] indicates that at least part of these gases are vented at discrete locations through the crust. Thus, the above equation is based on the conservative assumption that the gases can act as a counter-current flow limitation if the flow rate is sufficiently

high. Consistent with the particle bed modeling described above, the gas flow rate is evaluated at coolant saturation temperature.

Equation 2-184 defines the conditions for onset of water ingression. After ingression begins, the physical picture becomes one in which the heat transfer between the remaining melt pool and coolant is controlled by a relatively thin (and dry) thermal boundary layer within the crust at the crust-melt interface, while the upper regions of the crust are maintained near the coolant saturation point. The rate of crust growth in this domain can then be expressed as:

$$\rho_{t,c} \Delta e_{m,sat} \dot{\delta}_t = q_{c,dry}'' - \dot{Q}_{t,c} \delta_t - \rho_v h_{lv} j_{nc} \Big|_{T_{sat}} - h_t (T_m - T_{t,frz}) \quad (2-185)$$

where again $\Delta e_{m,sat}$ is the corium specific enthalpy change upon quench from T_m to T_{sat} . Under these conditions, the boundary condition on the melt zone energy balance (Eq. 2-18) remains the same (i.e., the melt is cooled by convective heat transfer to an overlying crust that is maintained at a constant temperature, $T_{t,frz}$). However, the heat flux to the overlying water pool approaches a constant that corresponds to the crust dryout limit, $q_{c,dry}''$.

In terms of methods for evaluating $q_{c,dry}''$, two options are provided. The first is that the user can specify the crust permeability. In this case, the dryout heat flux is evaluated using the Jones *et al.*^[63] model that is provided in Eq. 2-177. The second option is to use the correlation for the crust dryout limit that was developed as part of the OECD/MCCI SSWICS test series.^[20,21] This correlation is of the form:

$$q_{c,dry}'' = C_{dry} \left(\frac{\Delta e_{lv} (\rho_l - \rho_v) g}{\nu_v} \right)^{5/13} \left(\frac{N k_{t,c}^2 (\Delta e_{sat})^2}{c_{t,c} \Delta e_{crack}} \right)^{4/13} \left(\alpha_{c,exp} \left[T_{t,frz} - \left(T_{sat} + \frac{\sigma_{t,f}}{\alpha_{t,ex} E_{t,y}} \right) \right] \right)^{15/13} \quad (2-186)$$

where:

- C_{dry} = empirical constant (user-specified),
- Δe_{sat} = crust specific enthalpy change upon quench from the $T_{t,frz}$ to T_{sat} ,
- Δe_{crack} = crust specific enthalpy change upon cooldown from $T_{t,frz}$ to T_{crack} ,
- $\sigma_{t,f}$ = crust tensile strength,
- $\alpha_{t,ex}$ = crust linear expansion coefficient,
- $E_{t,y}$ = crust elastic modulus, and
- N = numerical constant=0.1 K-m^{1/2},

In this model, the crust temperature at onset of cracking is evaluated through the expression:^[20,21]

$$T_{crack} = T_{t,frz} - \frac{\sigma_{t,f}}{\alpha_{t,ex} E_{t,y}} \quad (2-187)$$

As is evident from this correlation, the crust mechanical properties (tensile strength, elastic modulus, and linear expansion coefficient) are required to evaluate the crust dryout limit. The property subroutines in the code (described in Appendix A) have been set up to calculate these properties based upon the time-dependent crust composition using a volume-weighting method.

Based on the results of the SSWICS test series, this correlation was found to best fit the experimentally measured dryout limits with the empirical constant C_{dry} set at 5.5 given the crust

properties calculated by the code. Note however that the SSWICS tests upon which the correlation is based were conducted without gas sparging. Application of the code to integral debris cooling tests^[47] indicates that this value must be set to a higher value (i.e., to 9.0) in order to predict the melt-water heat flux and posttest debris morphologies observed in the experiments.

For integrated analyses, water ingression-driven crust growth will proceed until the dryout limit of the material forming the crust falls below that which can support additional crust growth. At this time, the crust will cease to grow. Thereafter, the crust will act as an interstitial heat transfer medium, with the upper portion of the material quenched and stabilized. A thin thermal boundary layer at the crust/melt interface will control the heat transfer from the melt zone to the overlying water pool. The possibility exists for additional water-ingression driven crust growth to occur later in the accident sequence as the decay heat level and concrete erosion rates decrease. Onset of this late phase cooling behavior is detected by tracking Eq. 2-184 during the course of the calculation.

2.5.4.2 Dryout and Remelting of Crust Material Formed by Water Ingression

If local dryout occurs, then crust material previously quenched and cooled by water ingression will gradually heat up due to ongoing decay heat within the material, as well as heat transfer from the underlying melt. Due to the thickness of accumulations that can form by this cooling mechanism, sensible heat (i.e. heat capacity) effects need to be modeled in the remelting material. To illustrate this point, note that based on an adiabatic heat transfer analysis, the internal heating rate of BWR core debris a few days after accident initiation is estimated to be of the order of 5 K/minute. Thus, it would take several hours for this material to reheat to the melting point. This section outlines a simple approach that has been implemented in CORQUENCH to capture heat capacity effects during heatup and remelting of material that has been previously quenched to the water saturation temperature T_{sat} .

As noted, there are two heat sources that will contribute to debris reheating: i) heat transfer from the underlying melt into the crust within which heat transfer is now limited by conduction since the water has dried out, and ii) decay heat. With respect to evaluating the first item, it is assumed that the crust is a uniform slab initially at a temperature of T_{sat} . Upon dryout at time $t=0$, the lower surface is subject to a step change in temperature that corresponds to the crust freezing temperature, $T_{t,frz}$. The conduction-limited heat flux into the crust is then given by the equation:³

$$q'' = \frac{k_{t,c}(T_{t,frz} - T_{sat})}{\sqrt{\pi\alpha_t t}} \quad (2-188)$$

Combining this heat source with decay heat within the crust, then to first approximation the rate of change of the average crust temperature, \bar{T}_c , is governed by

$$\rho_t c_t \delta_t \frac{d\bar{T}_c}{dt} = \frac{k_{t,c}(T_{t,frz} - T_{sat})}{\sqrt{\pi\alpha_t t}} + \dot{Q}_{t,c} \delta_t \quad (2-189)$$

Integration of this equation subject to the initial condition of $\bar{T}_c(t = 0) = T_{sat}$ yields:

³ H. S. Carslaw and J. C. Jaeger, Conduction of Heat in Solids, Oxford University, Oxford, UK (1959).

$$\bar{T}_c = T_{sat} + \frac{\dot{Q}_{t,c}}{\rho_t c_t} t + \frac{2(T_{t,frz} - T_{sat})}{\delta_t} \sqrt{\frac{\alpha_t t}{\pi}} \quad (2-190)$$

Conversely, once the crust has reheated to the point where a steady state condition has been reached, then the average crust temperature is given by:

$$\bar{T}_c(t = t_{QS}) = \frac{T_{t,frz} + T_{t,I}}{2} + \frac{\dot{Q}_{t,c} \delta_t^2}{12k_{t,c}} \quad (2-191)$$

The above equations are implemented within CORQUENCH as follows. Once the coolant dries out, the time is marked within the code, and the average temperature within the crust during the subsequent heatup phase is evaluated through Eq. 2-190. Once the temperature reaches that given by the quasi-steady solution, Eq. 2-191, the heatup calculation is terminated and after that point, the average temperature is evaluated through Eq. 2-191. During both the reheating and steady state heat transfer phases, the specific enthalpy change in the crust during phase change in Eq. 2-144 is evaluated as:

$$\Delta e_{t,c} = e_t(T_{t,frz}) - e_t(\bar{T}_c) \quad (2-192)$$

Thus, at the start of the dryout phase, the specific enthalpy change upon melting corresponds to heatup of the crust from the coolant saturation temperature to the crust melting temperature. However, as the crust heats up, the enthalpy change is continuously reduced due to the higher average temperature, resulting in a faster remelting rate. If the crust is reflooded, then the water ingress calculation is restarted using the current crust thickness according to the methods described in Section 2.5.4.1.

2.5.5 Crust Anchoring Criterion

After intermittent crust segments forming at the melt-water interface begin to bond together to form a coherent structural assembly, the potential exists for this assembly to anchor to the cavity sidewalls. As observed in various reactor and simulant material coolability tests,^[1] an intervening gap can then form between the melt and crust as the interaction proceeds downward if the crust is mechanically stable in the given cavity configuration. In terms of debris coolability, crust anchoring is an important phenomenon to model since melt-crust separation will deactivate the water ingress and melt eruption cooling mechanisms due to the fact that both require melt feedstock to proceed. On this basis, the code has been structured with models capable of evaluating:

- 1) whether or not a structurally stable anchored crust configuration develops in the given cavity configuration, and if so,
- 2) the follow-on heat transfer process that occurs between the melt and overlying coolant across the intervening gap.

Models for the crust anchoring aspect of the problem are described in this section, while the heat transfer models are presented in the next section.

For a given cavity span, the minimum crust thickness required for mechanical stability under the combined weights of the overlying water pool, particle bed, and the crust itself is calculated from the following first-order equation given by Roark and Young:^[45]

$$\underbrace{g(m_{bed} + \rho_{t,c} A_b \delta_{t,\min} + m_{wat})}_{\text{applied load on crust}} \leq \underbrace{C_{geom} \hat{\sigma}_{t,f} \delta_{t,\min}^2}_{\text{crust mechanical strength}} \quad (2-193)$$

where, as a reminder, m_{bed} is the particle bed mass (see Eq. 2-17). In addition, m_{wat} is the coolant mass over the crust (water inventory modeling is discussed in Section 2.7), and C_{geom} is a user-defined constant that is determined by the cavity geometry, crust edge boundary condition, and crust failure model (e.g., $C_{geom} = 2.53$ for the case of brittle failure of a circular plate with simply supported edges^[45]). Finally, $\hat{\sigma}_{t,f}$ is the user-defined effective macroscopic crust strength including the effects of crack structure that forms during quench. As discussed by Lomperski *et al.*,^[21] the MACE and OECD/MCCI test results indicate that the mechanical strength of a corium crust formed by water quench is in range of 1-3 MPa regardless of the concrete content of the material. This value is approximately two orders of magnitude smaller than that calculated for fully dense, crack free material (viz. $\sigma_{t,f}$ in Eq. 2-186). Given Eq. 2-193, then the solution for the minimum crust thickness for mechanical stability in the cavity is found as:

$$\delta_{t,\min} = \frac{\rho_{t,c} A_b g}{2 C_{geom} \hat{\sigma}_{t,f}} + \frac{1}{2} \sqrt{\left(\frac{\rho_{t,c} A_b g}{C_{geom} \hat{\sigma}_{t,f}} \right)^2 + \frac{4g(m_{bed} + m_l)}{C_{geom} \hat{\sigma}_{t,f}}} \quad (2-194)$$

As the calculation evolves, the top crust thickness δ_t evaluated via integration of Eq. 2-97 and/or Eq. 2-185 is compared with the value predicted by Eq. 2-194. If the following condition develops:

$$\delta_t \geq \delta_{t,\min}, \quad (2-195)$$

then the crust upper surface elevation is fixed at the position at which this occurs. Thereafter, the location of the upper surface of the melt pool is tracked relative to that at the time crust anchoring to determine if melt-crust separation has occurred. The expression for determining the voided melt pool depth was previously provided as Eq. 2-6. If the initial concrete surface elevation is taken as zero and the effects of axial ablation and bottom surface crust formation are taken into account, then the upper surface elevation of the voided melt pool is found as:

$$EL_{m,v}(t) = \frac{m}{\rho_m A_b (1 - \alpha)} - \eta_b + \delta_b. \quad (2-196)$$

If during the course of the calculation the crust anchoring criterion defined by Eq. 2-195 is met at, say, time $t = t_{anchor}$, then the code saves the melt upper surface elevation (which is the same as the anchored crust lower surface elevation) from Eq. 2-196 as $EL_{anchor} = EL_{m,v}(t = t_{anchor})$, as well as the top crust thickness from the integration of Eq. 2-97 or 2-185 as $\delta_{t,anchor} = \delta_t(t = t_{anchor})$. With these definitions, and additionally factoring in the possibility that the crust could remelt due to radiation across the gap when the crust is separated, then the equation for the time-dependent gap thickness can be written as:

$$D_{gap} = \langle EL_{anchor} - EL_{m,v}(t) + \delta_{t,anchor} - \delta_t(t), 0 \rangle \quad (2-197)$$

where the operator $\langle \bullet, \bullet \rangle$ denotes the larger of the two arguments.

Once the crust is declared to be anchored, it remains that way unless the thickness falls below the minimum value predicted by Eq. 2-194. If this occurs, the crust is declared to float again, and the crust material along with overlying particle bed (if applicable) is repositioned on top of the melt pool. Floating crust boundary conditions are then applied at the melt/crust interface, and tracking is resumed to determine if crust anchoring occurs at some later point in the calculation. Conversely, if the crust remains anchored and the gap thickness given by Eq. 2-197 falls to zero (as might occur due to increased pool swelling), then floating crust boundary conditions are applied at the melt-crust interface as long as contact is maintained.

2.5.6 Anchored Crust Boundary Condition

This section describes the heat transfer modeling between the melt pool and overlying coolant after the crust has separated from the melt to form an intervening gap. The test data^[1] indicates that when this occurs, water does not flood down below the anchored crust to fill the intervening gap. Rather, the concrete decomposition gases appear to continuously purge the gap, preventing water from infiltrating into this region. Thus, gap formation essentially terminates quenching processes by: i) removing the melt feedstock that is required for continuation of the water ingression and melt eruption cooling mechanisms, and ii) introducing an additional radiation heat transfer resistance between the melt and crust that does not normally exist when the melt is in direct contact with the crust.

In terms of modeling the heat transfer from the melt pool to the overlying coolant across the gap, three plausible physical cases have been identified, as outlined below:

- 1) No lower crust exists over the melt pool, and the upper bridge crust acts as a thermal insulator.
- 2) A secondary crust forms over the melt pool, while the upper bridge crust acts as a thermal insulator.
- 3) No lower crust exists over the melt pool, while the upper bridge crust is remelting.

Aside from these three cases, the situation is further complicated by the fact that water ingression into the crust may be occurring, which requires a modification in the solution methodology relative to that used when the crust is treated as impervious. The impervious crust case is therefore addressed first, followed by a discussion in a subsequent section regarding the modeling changes that are required for the permeable crust case.

2.5.6.1 Impervious Crust Models

In terms of the solution methodology, Case 1) outlined above is solved first. Based on these results, a decision is then made as to whether or not that solution is valid, or if one of the other two cases is appropriate. In particular, if the temperature at the lower surface of the bridge crust is less than the crust freezing temperature, and the melt pool surface temperature is above the melt freezing temperature, then that solution is physically correct. However, if the melt surface temperature is found to be below the freezing point, then the second case is valid and the solution is recalculated accordingly. Finally, if the bridge crust lower surface temperature is above the freezing point, then Case 3) is valid and that case is recalculated. The specific models for each of these three cases are outlined below.

A simplified sketch of the Case 1) impervious crust configuration is provided in Figure 2-11, along with the nomenclature that is used in the following model development. The same simplifying assumptions used above⁴ regarding the crust heat transfer characteristics are also used in this stage of the analysis. The quasi-steady heat transfer balances across the melt-gap, gap-crust, and crust-atmosphere interfaces are then of the form:

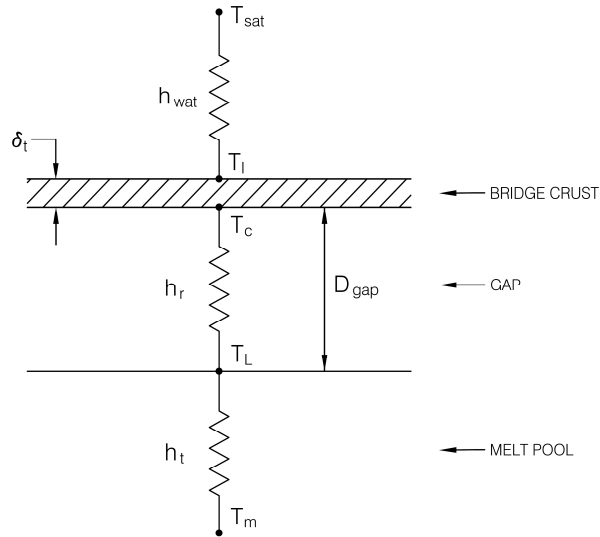


Figure 2-11. Illustration of Geometry and Nomenclature for Case 1 Separated Crust Configuration.

$$h_t(T_m - T_L) = h_r(T_L - T_C) \quad (2-198)$$

$$h_r(T_L - T_C) = k_{t,c} \frac{(T_C - T_I)}{\delta_t} - \frac{\dot{Q}_{t,c} \delta_t}{2} \quad (2-199)$$

$$k_{t,c} \frac{(T_C - T_I)}{\delta_t} + \frac{\dot{Q}_{t,c} \delta_t}{2} = h_{wat}(T_I - T_{sat}) \quad (2-200)$$

where, in this particular application,

$$h_r = \frac{\sigma_{stef} F_{view}}{1/\epsilon_m + 1/\epsilon_{t,c} - 1} (T_L^2 + T_C^2)(T_L + T_C), \quad (2-201)$$

and F_{view} is the radiation view factor between the lower melt pool and bridge crust. Under plant conditions where the aspect ratio (viz. crust lateral dimension divided by gap height) $\rightarrow \infty$, then $F_{view} \rightarrow 1$. However, in many experiments the aspect ratio is $O(1)$, and so a correction for the view factor between the melt and bridge crust is included in the model to account for this potential

⁴These assumptions were: i) quasi-steady heat transfer, ii) spatially independent thermal properties, and iii) and uniform decay heat distribution.

experimental distortion. If the cavity cross section is modeled as a square, then the length of the side is $\sqrt{A_b}$ and the cavity aspect ratio can be defined as:

$$\hat{H} = \frac{\sqrt{A_b}}{D_{gap}} \quad (2-202)$$

The radiation view factor for the assumed geometry is of the form:^[64]

$$F_{view} = \frac{2}{\pi \hat{H}^2} \left\{ \ln \left(\sqrt{\frac{1 + \hat{H}^2}{1 + 2\hat{H}}} \right) + 2 \left[\hat{H} \sqrt{1 + \hat{H}^2} \tan \left(\frac{\hat{H}}{\sqrt{1 + \hat{H}^2}} \right) - \hat{H} \tan \left(\hat{H} \right) \right] \right\} \quad (2-203)$$

Combining Eqs. 2-198 through 2-200 and solving for the crust lower surface temperature yields:

$$T_c = \frac{1}{C_\alpha + C_\beta} \left\{ C_\alpha T_m + C_\beta T_{sat} + \frac{\dot{Q}_{t,c} \delta_t}{2} \left(1 + \frac{C_\beta}{h_{wat}} \right) \right\} \quad (2-204)$$

where:

$$C_\alpha = \frac{h_r h_t}{h_r + h_t} \quad (2-205)$$

$$C_\beta = \frac{k_{t,c} h_{wat}}{\delta_t h_{wat} + k_{t,c}} \quad (2-206)$$

Equation 2-204 is a nonlinear expression that can be solved through iteration for the bridge crust lower surface temperature, T_c . The solution technique is straightforward but tedious; details are provided in Appendix B, Section B.1. Once the solution for T_c is obtained, the full temperature distribution and heat flux across the boundaries from the melt pool to overlying coolant can be determined through Eqs. 2-198 through 2-200. With this data, the solution is then checked to ensure that $T_L \geq T_{m,frz}$ and $T_c \leq T_{t,frz}$. If these criteria are met, then the solution is declared to be valid and the top boundary temperature T_t in the melt zone energy balance Eq. 2-18 is set to T_L . However, if one of the temperature criteria is violated, then additional work is required. The models for the other cases are described below.

Case 2) corresponds to the situation where a secondary crust forms over the melt pool, while the upper bridge crust acts as a thermal insulator. Based on the results of the Case 1) analysis, this case occurs when $T_L < T_{m,frz}$ and $T_c \leq T_{t,frz}$. A sketch of the geometry and nomenclature used for this case is provided in Figure 2-12. The same basic modeling assumptions used in the Case 1) analysis are invoked here, but a few additional simplifications are made in terms of treating the secondary crust that forms over the melt pool. First, the crust thickness is calculated assuming quasi-steady heat transfer, and so a rate equation is not solved. Second, the composition of the crust is assumed to be identical to that of the melt pool. Finally, decay heat in this secondary crust is neglected in the evaluation of the equilibrium crust thickness. The first assumption is motivated by the fact that this secondary crust would develop in the late phase of the accident sequence when

the system is evolving slowly, while the latter two assumptions are motivated by the fact that the crust is expected to remain relatively thin as it is interstitially located between the melt pool and overlying bridge crust in the cavity which is assumed to be devoid of coolant.

With this background, the quasi-steady heat transfer balances across the melt-lower crust, lower crust-gap, gap-upper crust, and upper crust-coolant interfaces are then of the form:

$$h_t(T_m - T_{m,frz}) = k_m \frac{(T_{m,frz} - T_L)}{\delta_L} \quad (2-207)$$

$$k_m \frac{(T_{m,frz} - T_L)}{\delta_L} = h_r(T_L - T_C) \quad (2-208)$$

$$h_r(T_L - T_C) = k_{t,c} \frac{(T_C - T_I)}{\delta_t} - \frac{\dot{Q}_{t,c} \delta_t}{2} \quad (2-209)$$

$$k_{t,c} \frac{(T_C - T_I)}{\delta_t} + \frac{\dot{Q}_{t,c} \delta_t}{2} = h_{wat}(T_I - T_{sat}) \quad (2-210)$$

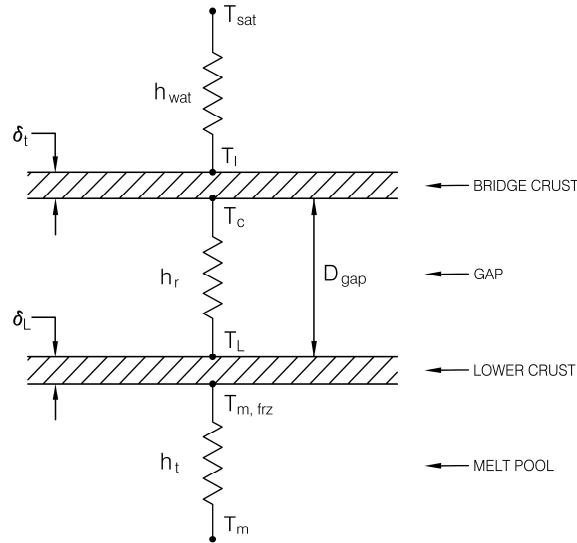


Figure 2-12. Illustration of Geometry and Nomenclature for Case 2 Separated Crust Configuration.

where h_r is still defined through Eqs. 2-201 and 2-203. Combining the above set of equations and working through the algebra yields the following equation for the crust lower surface temperature:

$$T_c = \frac{1}{h_r + C_\beta} \left\{ h_r T_L + C_\beta \left(T_{sat} + \frac{\dot{Q}_{t,c} \delta_t}{2 h_{wat}} \right) + \frac{\dot{Q}_{t,c} \delta_t}{2} \right\} \quad (2-211)$$

where C_β is given by Eq. 2-206. This equation is also a nonlinear expression that can be solved through iteration for the bridge crust lower surface temperature, T_c . The solution technique is provided in Appendix B, Section B.2. Once the solution for T_c is obtained, the full temperature

distribution and heat flux across the boundaries can be determined through Eqs. 2-207 through 2-210. With this data, the solution for the lower crust thickness is deduced from Eq. 2-207 as:

$$\delta_L = \frac{k_m (T_{m,frz} - T_L)}{h_t (T_m - T_{m,frz})} \quad (2-212)$$

Finally, the top boundary temperature T_t in the melt zone energy balance Eq. 2-18 is set to $T_{m,frz}$, which completes the specifications for the Case 2) anchored crust boundary condition.

Case 3) corresponds to the situation where the melt pool surface is devoid of a crust, while the lower surface temperature of the bridge crust has risen to the point where it is remelting. Based on the Case 1) analysis results, this case corresponds to the situation in which $T_L > T_{m,frz}$ and $T_C > T_{t,frz}$. The geometry and nomenclature used here is the same as that provided in Figure 2-11, with the exception that $T_C = T_{t,frz}$. The same basic modeling assumptions used in the Case 1) analysis are also utilized. Under these conditions, the quasi-steady heat transfer balances across the melt-gap and crust-coolant interfaces are then:

$$h_t (T_m - T_L) = h_r (T_L - T_{t,frz}) \quad (2-213)$$

$$k_{t,c} \frac{(T_{t,frz} - T_I)}{\delta_t} + \frac{\dot{Q}_{t,c} \delta_t}{2} = h_{wat} (T_I - T_{sat}) \quad (2-214)$$

where h_r is given by Eqs. 2-201 and 2-203. From Eq. 2-214, the following expression for the crust upper surface temperature can be obtained:

$$T_I = \left(\frac{k_{t,c}}{\delta_t} + h_{wat} \right)^{-1} \left[h_{wat} T_{sat} + \frac{k_{t,c}}{\delta_t} T_{t,frz} + \frac{\dot{Q}_{t,c} \delta_t}{2} \right] \quad (2-215)$$

This non-linear equation is solved using an iterative technique; details are provided in Appendix B, Section B.3. Once the solution for T_I is obtained, the heat removal to the overlying water pool from the crust upper surface can be determined. Since the crust bottom surface temperature is fixed at the melting point, the energy balance from the melt pool to the lower surface of the crust is solved as a separate problem (see Appendix B, Section B.3) to obtain T_L and thereby the heat flux across the gap to the underside of the crust. The top boundary surface temperature in the melt zone energy balance equation (i.e., T_t in Eq. 2-18) is then set equal to T_L . Finally, the crust thermal loading term in Eq. 2-144 that drives the remelting process is redefined from $h_t (T_m - T_{m,frz})$, which is the applicable boundary condition when the melt is in contact with the crust, to $h_t (T_m - T_L) = h_r (T_L - T_{t,frz})$, which is the applicable condition across the intervening gap.

2.5.6.2 Permeable Crust Models

The above section has outlined the methods used to evaluate the heat transfer to the overlying coolant in the case of an anchored impervious crust boundary condition. This section provides details of the modeling changes that are needed when the crust is not only anchored but also cooled by water ingress.

The equation governing crust growth under floating crust boundary conditions when the crust is permeable to both gas and water flows was previously defined in Eq. 2-185. Based on this

expression, then the effective heat removal rate from the bottom surface of the crust due to water ingress is deduced as:

$$q''_{eff} = q''_{c,dry} - \dot{Q}_{t,c} \delta_t - \rho_v h_{lv} j_{nc} \big|_{T_{sat}} \quad (2-216)$$

Note that this equation accounts for the effects of both decay heat within the crust as well as the counter-current flow of non-condensable gases from concrete erosion on the net surface cooling rate. Once the crust separates from the melt, this expression defines the effective limit on the heat sink that the permeable crust can provide for removing the heat that is radiated across the gap without remelting. In order to evaluate the heat transfer across the gap in a manner that is consistent with the logic structure developed for the impervious crust case, the permeable heat sink is assumed to be characterized by an effective heat transfer coefficient that is defined as:

$$h_{eff} = \frac{q''_{eff}}{T_{t,frz} - T_{sat}} \quad (2-217)$$

Thus, for a given surface temperature at the bottom of the crust, the heat removal rate to the overlying coolant is evaluated as:

$$q'' = h_{eff}(T_C - T_{sat}); \quad T_{sat} \leq T_C \leq T_{t,frz} \quad (2-218)$$

Using this approach, then as $T_C \rightarrow T_{t,frz}$, $q'' \rightarrow q''_{eff}$ and so the correct form of the heat sink is recovered for the permeable crust boundary condition.

Using this basic idea, then the overall solution methodology for the permeable crust case is basically identical to that described in Section 2.5.6.1, but with the heat sink provided by the permeable crust defined as in Eq. 2-218. In particular, for Case 1) the heat balances across the melt-gap and gap-crust interfaces simplify to:

$$h_t(T_m - T_L) = h_r(T_L - T_C) \quad (2-219)$$

$$h_r(T_L - T_C) = h_{eff}(T_C - T_{sat}) \quad (2-220)$$

These two expressions can be combined to yield the following equation for the crust lower surface temperature:

$$T_C = \frac{C_\alpha T_m + h_{eff} T_{sat}}{C_\alpha + h_{eff}} \quad (2-221)$$

where C_α is defined in Eq. 2-205. This nonlinear equation is solved for the crust lower surface temperature using an iterative technique; details are provided in Appendix B, Section B.4. Once the solution for T_C is obtained, the full temperature distribution and heat flux across the boundaries can be determined from Eqs. 2-219 and 2-220. As for the impervious crust case, the solution is then checked to ensure that $T_L \geq T_{m,frz}$ and $T_C \leq T_{t,frz}$. If these criteria are met, then the solution is valid and the top boundary temperature T_t in the melt zone energy balance Eq. 2-18 is set to T_L . However, if one of the temperature criteria is violated, then additional work is required. The models for the other two cases are described below.

Case 2) corresponds to the situation where a secondary crust forms over the melt pool, while the upper bridge crust acts as a permeable heat sink. Employing the same assumptions as used in the impervious crust case for the lower crust modeling, then the heat flux balances across the melt-lower crust, lower crust-gap, and gap-upper crust interfaces are of the form:

$$h_t(T_m - T_{m,frz}) = k_m \frac{(T_{m,frz} - T_L)}{\delta_L} \quad (2-222)$$

$$k_m \frac{(T_{m,frz} - T_L)}{\delta_L} = h_r(T_L - T_C) \quad (2-223)$$

$$h_r(T_L - T_C) = h_{eff}(T_C - T_{sat}) \quad (2-224)$$

These equations can be solved in closed form; i.e.,

$$T_C = T_{sat} + \frac{h_t(T_m - T_{m,frz})}{h_{eff}} \quad (2-225)$$

$$T_L = \left(\frac{h_t(T_m - T_{m,frz})}{\Omega_r} + T_C^4 \right)^{1/4} \quad (2-226)$$

where:

$$\Omega_r = \frac{\sigma_{sef} F_{view}}{1/\varepsilon_m + 1/\varepsilon_{t,c} - 1} \quad (2-227)$$

and the solution for δ_L was previously given as Eq. 2-212. With these expressions, the top boundary temperature T_t in the melt zone energy balance Eq. 2-18 is set to $T_{m,frz}$, which completes the specifications for the Case 2) anchored permeable crust boundary condition.

Case 3) corresponds to the situation where the melt pool surface is devoid of a crust, while the lower surface temperature of the permeable bridge crust has risen to the point where it is remelting. Based on the Case 1) results, this situation arises when $T_L > T_{m,frz}$ and $T_C > T_{t,frz}$. The heat transfer balances across the melt-gap interface are then of the form:

$$h_t(T_m - T_L) = h_r(T_L - T_{t,frz}) = \Omega_r(T_L^4 - T_{t,frz}^4) \quad (2-228)$$

This is a quartic equation for T_L which has a closed form solution that is provided as Eqs. B-17 to B-21 in Appendix B. To utilize that result in the current application, the temperature scaling variable (Eq. B-18) is redefined as:

$$T_o = \left(\frac{h_t T_m}{\Omega_r} + T_{t,frz}^4 \right)^{1/4} \quad (2-229)$$

Given this solution, the upper surface temperature T_t in the melt zone energy balance (Eq. 2-18) is set to T_L , and the heat flux across the gap is calculated from Eq. 2-228. Finally, the crust thermal loading term in the permeable crust growth rate equation (Eq. 2-185) is redefined from $h_t(T_m - T_{m,frz})$, which is applicable when the melt is in contact with the crust, to $h_t(T_m - T_L) = h_r(T_L - T_{t,frz})$, which is the applicable boundary condition across the gap.

2.6 Auxiliary Relationships

This section documents various ancillary correlations and models that are utilized within CORQUENCH for calculating core debris coolability under ex-vessel accident conditions.

2.6.1 Melt Void Fraction Models

Melt void fraction is important in terms of evaluating the overall cavity erosion profile in 2-D cavity configurations. Moreover, for 1-D experiments the extent of melt voiding is also important in determining the location where the crust anchors to the test section sidewalls. On this basis, several correlations have been implemented in the code for calculating melt void fraction to provide user flexibility. These correlations include those due to Brockmann *et al.*,^[35] Wallis,^[36] and Kataoka and Ishii.^[37] However, it is of interest to note that Tourniaire, Dufour, and Spindler^[65] have developed a mechanistic model for foam formation due to gas sparging in an effort to explain large melt void fractions observed in reactor material tests conducted with limestone/common sand concrete.^[12,66] This model was published late in the OECD/MCCI-2 program and so there was insufficient time to implement that model in the version of the code that is described in this report.

The model of Brockmann *et al.*^[35] is based on pool swell data obtained with sparged stainless steel melts. This correlation is of the form:

$$\alpha = 0.128 \left(\frac{g\mu_m^4}{\rho_m \sigma_m^3} \right)^{-0.0207} \left(\left[\frac{\rho_m}{g\sigma_m} \right]^{0.25} j \right)^{0.584} \quad (2-230)$$

The correlation due to Wallis^[36] is written in terms of a dimensionless gas flow velocity that is defined as:

$$\hat{j} = \frac{j}{j_o}; \quad j_o = 1.18 \left[\frac{g\sigma_m(\rho_m - \rho_g)}{\rho_m^2} \right]^{0.25} \quad (2-231)$$

The correlation for the pool void fraction is then of the form:^[36]

$$\alpha = \frac{1}{2} \left(1 - \sqrt{1 - 4\hat{j}} \right) \quad (2-232)$$

This correlation is only valid for bubbly flow conditions, and so \hat{j} is capped at 0.24 in the code, which limits the peak void fraction predicted by this model to 40 %. For assumed corium properties of $\sigma_m = 0.6$ N/m and $\rho_m = 6000$ kg/m³, j_o is evaluated as 20 cm/sec from Eq. 2-231, and so the 40 % void fraction limit is reached at a melt superficial gas velocity of ~ 5 cm/sec.

The correlation of Kataoka and Ishii^[37] is also based on the definition of a dimensionless gas flow velocity that is defined slightly differently in comparison to the Wallis definition; i.e.,

$$\hat{j} = \frac{j}{j_o}; \quad j_o = \left[\frac{g\sigma_m(\rho_m - \rho_g)}{\rho_m^2} \right]^{0.25} \quad (2-233)$$

For $\hat{j} \leq 0.5$, the flow regime is bubbly and the correlation for the void fraction is of the form:

$$\alpha = \frac{\hat{j}}{C_o \hat{j} + \sqrt{2}} \quad (2-234)$$

where:

$$C_o = 1.2 - 0.2 \sqrt{\frac{\rho_g}{\rho_m}} \quad (2-235)$$

For $\hat{j} > 0.5$, the flow regime is churn turbulent, and the particular form of the void fraction correlation depends upon a viscosity number that is defined as:

$$N_\mu = \frac{\mu_m}{\rho_m \sigma_m \sqrt{\frac{\sigma_m}{g(\rho_m - \rho_g)}}} \quad (2-236)$$

Thus, for $N_\mu < 2.25 \cdot 10^{-3}$, the void fraction correlation is:

$$\alpha = \frac{1}{C_o + \frac{0.03}{C_1 C_2 \hat{j}}} \quad (2-237)$$

where:

$$C_1 = \left(\frac{\rho_g}{\rho_m} \right)^{0.157} \quad (2-238)$$

$$C_2 = N_\mu^{0.562} \quad (2-239)$$

Conversely, for $N_\mu \geq 2.25 \cdot 10^{-3}$, the correlation is written as:

$$\alpha = \frac{1}{C_o + \frac{0.92}{C_1 \hat{j}}} \quad (2-240)$$

2.6.2 Melt Pool Sparging Gas Bubble Diameter Correlations

Two options have been provided for evaluating the radius of gas bubbles sparging through the melt pool. The bubbles are generated at the core-concrete interface as a result of concrete decomposition and erosion. The first model is thus based on the concept that the gas bubble size is limited by Taylor instability^[53] as the gas pockets form and grow beneath the dense, overlying core material at the interface. The critical wavelength of the Taylor instability was defined earlier in Eq. 2-123. Since two bubbles grow in an area of the surface defined by λ_{crit}^2 at any given time, the bubble radius is taken equal to $\frac{1}{4}$ the wavelength; i.e.,

$$R_{bub} = \frac{\lambda_{crit}}{4}; \quad \lambda_{crit} \equiv 2\pi \sqrt{\frac{\sigma_m}{g(\rho_m - \rho_g)}} \quad (2-241)$$

The second method for calculating the gas bubble radius is based on an unpublished model developed by the author. In this work, the effect of local gas release at the melt-concrete interface on bubble formation, growth and departure in a viscous fluid is examined. The bubble spacing on the interface is again assumed to be controlled by Taylor instability, with two bubbles growing in an area of the surface equal to λ_{crit}^2 at any given time. Local gas release is treated as the source term driving bubble growth; the ideal gas law is used to calculate the gas pressure in the expanding

bubble, and the Rayleigh equation^[67] is then solved to find the bubble radius as a function of time under the assumption that viscous forces control the radial expansion rate. A second momentum equation^[68,69] is then solved for the bubble center-of-mass elevation above the concrete surface under a quasi-steady assumption in which the bubble buoyancy force is balanced by viscous drag force as the bubble lifts away from the interface. The bubble departure time is then determined by setting the equation for the center-of-mass height above the surface equal to the bubble radius equation. These considerations yield the following solution for the bubble radius at departure from the core-concrete interface:

$$R_{bub} = \left(\frac{21}{g(\rho_m - \rho_g)} \right)^{2/5} \left(\frac{9\mu_m \rho_g R_{ideal} T_{dc} j \lambda_{crit}^2}{64\pi \bar{M}_g} \right)^{1/5} \quad (2-242)$$

The bubble radius given by this equation is then assumed to equal that sparging through the bulk of the melt pool. The model predicts that the departure radius increases with increasing melt superficial gas velocity (j) and melt viscosity (μ_m). To maintain a physically plausible solution as $j \rightarrow 0$, the bubble radius predicted by this correlation is compared with that given by Eq. 2-241, and the larger of the two values is used as the solution for the radius at any time. In practice, for a melt sparging rate of a few centimeters per second, Eq. 2-242 can predict a departure radius that is approximately an order of magnitude larger than that predicted by Eq. 2-241 (i.e., centimeters vs. millimeters) for viscous melt conditions.

2.6.3 Melt-Concrete Heat Transfer Coefficient Models

The heat transfer coefficient at the melt/concrete interface can be selected from a variety of options, including: i) the Bradley bubble agitation heat transfer model developed for core-concrete interactions,^[39] ii) gas film models similar to those deployed in CORCON Mod3,^[41] and iii) empirical correlations by Sevón^[42] developed on the basis of the CCI test results. Additional details regarding each of these models, as well as how the models are implemented in the code, are provided below.

2.6.3.1 Bradley Slag Film Model

Bradley^[39] modified the bubble agitation heat transfer model of Kutateladze and Malenkov^[40] to account for the thermal resistance of the slag film produced at the core-concrete interface as a result of the ablation process. Although Bradley's analysis was fairly detailed, he found the presence of the slag layer at the interface effectively reduced the convective heat transfer coefficient predicted by the Kutateladze-Malenkov model by a fraction that was a weak function of melt composition and temperature. In particular, the heat flux at the bottom of the melt pool is:

$$q_b'' = h_b (T_m - T_{dc}) \quad (2-243)$$

where:

$$h_b = C_{slag} h_{KM} \quad (2-244)$$

and C_{slag} is a constant and h_{KM} denotes the Kutateladze-Malenkov heat transfer coefficient that was previously defined in Eqs. 2-72 and 2-73. The explicit expression for h_b is thus of the form:

$$h_b = \begin{cases} 1.5 \cdot 10^{-3} C_{slag} \left(\frac{c_m P j}{k_m g} \right)^{2/3} \frac{k_m}{L_\lambda}; & j < j_{tr} \\ 1.5 \cdot 10^{-3} C_{slag} \left(\frac{c_m P j}{k_m g} \right)^{2/3} \left(\frac{j_{tr}}{j} \right)^{1/2} \frac{k_m}{L_\lambda}; & j \geq j_{tr} \end{cases} \quad (2-245)$$

where the nomenclature in the above expression was defined earlier following Eq. 2-72. Bradley found that $C_{slag} = 0.29 \pm 0.07$ regardless of whether the melt was composed of steel or core oxide. Factoring in all the other uncertainties associated with this type of analysis, Bradley's recommendation was that C_{slag} should be set to 0.29 regardless of melt composition or temperature. The model has been implemented in the code consistent with this recommendation.⁵

Although this correlation has been presented for the case of axial heat transfer, the user can also select this same model for calculating heat transfer to the concrete sidewalls for situations in which the 2-D cavity erosion model has been selected.

Note that aside from material properties, the Kutateladze-Malenkov^[40] correlation that forms the backbone of Bradley's model is a function of the melt superficial gas velocity, which in turn is a function of the heat transfer coefficient to the core-concrete interface. Thus, a coupling exists that makes straightforward application of the model difficult. In order to recast the correlation in a form that is amendable to forward integration while maintaining key modeling features, a quasi-steady concrete erosion sub-model is used to relate the gas sparging rate to the heat flux at the core-concrete interface. From Eq. 2-20, the desired relationship is deduced as:

$$j = \frac{\chi_g \rho_{con} \eta_b}{\rho_g} = \left(\frac{\chi_g}{\rho_g} \right) \frac{h_b (T_m - T_{dc})}{e_{con,d}} \quad (2-246)$$

where $\chi_g = \chi_{con,CO_2} + \chi_{con,H_2O}$ is the total gas content of the concrete, and the density of the decomposition gas mixture ρ_g is evaluated at T_{dc} through Eqs. 2-75 to 2-78. Substitution of Eq. 2-246 into 2-245 and solving yields the following alternative formulation for h_b :

$$h_b = \begin{cases} C_\beta^3 C_\xi^2 (T_m - T_{dc})^2; & j < j_{tr} \\ C_\beta^{6/5} C_\xi^{1/5} j_{tr}^{3/5} (T_m - T_{dc})^{1/5}; & j \geq j_{tr} \end{cases} \quad (2-247)$$

where:

⁵The constant C_{slag} is set to 0.29 for cases in which the user has selected either the quasi-steady concrete ablation model (Section 2.3.1) or the fully developed concrete dryout model (Section 2.3.2). For the transient dryout model (Section 2.3.3), the constant is set according to current state of the boundary condition at the interface. In particular, as the concrete surface heats up prior to ablation, C_{slag} is set to 1.0. Once ablation starts, C_{slag} is set to 0.29 if the slag is assumed to continuously drain through the crust. However, if the slag is assumed to accumulate as a continuous film beneath the crust, then C_{slag} is maintained at 1.0 as long as that boundary condition is applicable since the surface heat transfer model treats the slag film interfacial heat transfer resistance directly.

$$C_{\beta} = 1.5 \cdot 10^{-3} C_{slag} \left(\frac{c_m P}{k_m g} \right)^{2/3} \frac{k_m}{L_{\lambda}} \quad (2-248)$$

$$C_{\xi} = \frac{\chi_g}{\rho_g e_{con,d}} \quad (2-249)$$

and the expression $j = C_{\xi} h_b (T_m - T_{dc}) = [C_{\beta} C_{\xi} (T_m - T_{dc})]^3$ is used to determine if the superficial gas velocity lies above or below the transition velocity j_{tr} . Equation 2-247 is an alternative formulation of Bradley's correlation^[39] that has been recast with the melt temperature as the primary dependent variable, as opposed to the superficial gas velocity. This is the form of Bradley's model currently implemented in the code.

2.6.3.2 Gas Film Models

The second modeling options for evaluating the heat transfer to concrete surfaces are simplified versions of the gas film models that are implemented in CORCON Mod3.^[41] An illustration of the physical situation and nomenclature for this case is provided in Figure 2-13. The concrete decomposition gases are envisioned to produce a gas film that blankets the concrete surface. Heat transfer across the film is by convection and radiation. Whether or not a crust forms at the melt-film interface is determined by first solving the energy balance across the interface assuming that the crust is absent [e.g., see Figure 2-13(a)]. If this problem yields a solution for which $T_I \geq T_{frz}$, then that solution is valid and no further action is required. However, if $T_I < T_{frz}$, then the problem is recalculated with an interstitial crust at the interface [see Figure 2-13(b)], and the corresponding crust thickness is evaluated as part of the solution. The models differ depending upon whether or not the surface is horizontal or vertical, and so these two cases are addressed separately below.

For the axial situation in which a crust is absent, the energy balance across the film-melt interface is of the form:

$$q_b'' = h_m (T_m - T_I) = h_r (T_I - T_{dc}) + h_g (T_I - T_{dc}) \quad (2-250)$$

where h_r and h_g are the radiation and convection heat transfer coefficients across the gas film, respectively, and h_m is the melt side convection coefficient. For this work h_m is again evaluated with the Kutateladze-Malenkov^[40] correlation using the previously described modification that allows the correlation to be expressed in terms of melt temperature as opposed to gas velocity. For the gas film model, the effect of the slag film that arises during ablation is neglected.^[41] Thus, C_{slag} is set to 1.0 in Eq. 2-245. In addition, the relationship between the gas sparging rate and melt temperature is redefined from Eq. 2-246 in terms of the current boundary temperature as:

$$j = \left(\frac{\chi_g}{\rho_g} \right) \frac{h_m (T_m - T_I)}{e_{con,d}} \quad (2-251)$$

With these modifications, the correlation for h_m is deduced as:

$$h_m = \begin{cases} C_\beta^3 C_\xi^2 (T_m - T_l)^2; & j < j_{tr} \\ C_\beta^{6/5} C_\xi^{1/5} j_{tr}^{3/5} (T_m - T_l)^{1/5}; & j \geq j_{tr} \end{cases} \quad (2-252)$$

where:

$$C_\beta = 1.5 \cdot 10^{-3} \left(\frac{c_m P}{k_m g} \right)^{2/3} \frac{k_m}{L_\lambda} \quad (2-253)$$

and C_ξ is as defined in Eq. 2-249. Recall that for the purposes of evaluating h_m , the expression $j = [C_\beta C_\xi (T_m - T_l)]^3$ is used to determine if the gas velocity lies above or below the transition velocity $j_{tr} = 4.3 \cdot 10^{-4} \sigma_m / \mu_m$ at the interface.

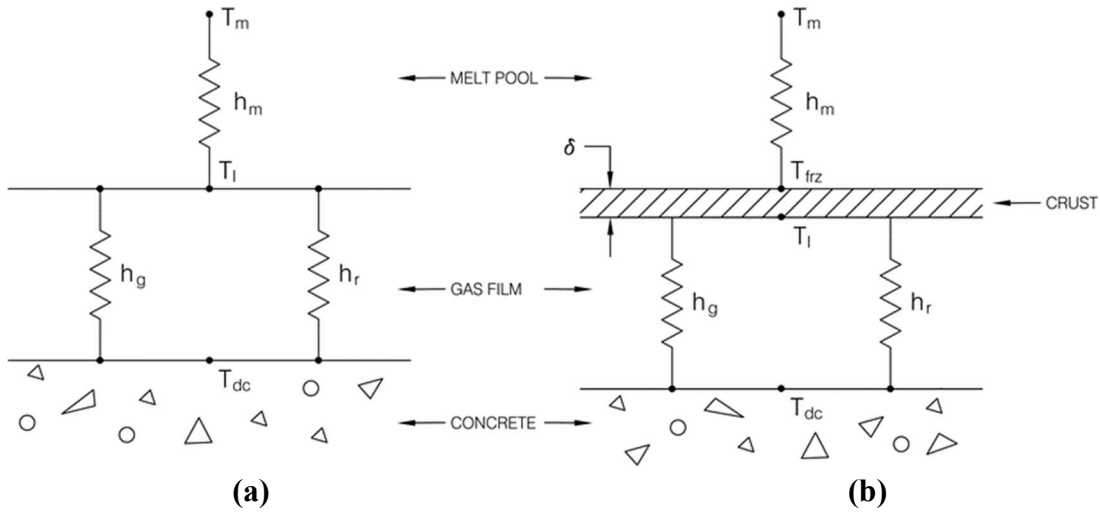


Figure 2-13. Illustration of the Basic Features of the Gas Film Model^[41] a) Without and b) With Crust Formation at the Melt-Film Interface.

On the gas film side, the radiation heat transfer coefficient across the gap is defined as:

$$h_r = \Omega_r (T_l^2 + T_{dc}^2) (T_l + T_{dc}) \quad (2-254)$$

where for this case:

$$\Omega_r = \frac{\sigma_{stef}}{1/\epsilon_m + 1/\epsilon_{con} - 1} \quad (2-255)$$

Finally, the convection coefficient on the gas side is evaluated using a model that is based on Taylor instability theory; i.e.,^[67,68]

$$h_g = C_o \frac{k_g}{L_\mu} \text{Re}^{-1/3} \quad (2-256)$$

where C_o is an empirical constant that is set equal to 0.326 according to the work of Alsmeyer and Barleon,^[70] and:

$$L_\mu = \left(\frac{\mu_g^2}{g \rho_g (\rho_m - \rho_g)} \right)^{1/3} \quad (2-257)$$

$$\text{Re} = \frac{\rho_g j L_\lambda}{\mu_g} \quad (2-258)$$

The Laplace constant L_λ in this expression was previously defined in Eq. 2-73. The model for h_g is also a function of gas velocity, and so Eq. 2-251 is used to redefine this expression in terms of melt temperature. The correlation thus takes on two different forms, depending upon where j lies with respect to j_{tr} ; i.e.,

$$h_g = \begin{cases} \frac{C_\gamma}{C_\beta C_\xi (T_m - T_l)}; & j < j_{tr} \\ \frac{C_\gamma}{[C_\beta C_\xi \sqrt{j_{tr}} (T_m - T_l)]^{2/5}}; & j \geq j_{tr} \end{cases} \quad (2-259)$$

where:

$$C_\gamma = C_o \frac{k_g}{L_\mu} \left(\frac{\mu_g}{\rho_g L_\lambda} \right) \quad (2-260)$$

With this collection of information, the transcendental equation for the interface temperature under the conditions in which $j < j_{tr}$ is found as:

$$T_l - T_{dc} = \frac{C_\beta^4 C_\xi^3}{C_\gamma} (T_m - T_l)^4 - \frac{\Omega_r C_\beta C_\xi}{C_\gamma} (T_l^4 - T_{dc}^4) (T_m - T_l) \quad (2-261)$$

This equation is solved using the Newton-Raphson technique by first forming:

$$f = T_l - T_{dc} - \frac{C_\beta^4 C_\xi^3}{C_\gamma} (T_m - T_l)^4 + \frac{\Omega_r C_\beta C_\xi}{C_\gamma} (T_l^4 - T_{dc}^4) (T_m - T_l) \quad (2-262)$$

with convergence obtained when $f \rightarrow 0$, and:

$$\frac{df}{dT_l} = 1 + \frac{4C_\beta^4 C_\xi^3}{C_\gamma} (T_m - T_l)^3 + \frac{\Omega_r C_\beta C_\xi}{C_\gamma} \{4T_l^3 (T_m - T_l) - (T_l^4 - T_{dc}^4)\} \quad (2-263)$$

Given these expressions, iteration is performed to find T_l using an approach identical to that outlined around Eq. 2-56. The solution for T_l is then used to calculate the gas velocity from $j = [C_\beta C_\xi (T_m - T_l)]^3$. If this result is $< j_{tr}$, then the solution for T_l is valid and a second decision is then made as to whether or not a crust exists at the interface based on this temperature. That scenario is addressed later in this section. However, if $j > j_{tr}$, the equations are solved a second time to obtain the solution with the correct form of h_m . For this case, the transcendental equation for T_l takes the form:

$$T_l - T_{dc} = \frac{C_\beta^{8/5} C_\xi^{3/5} j_{tr}^{4/5}}{C_\gamma} (T_m - T_l)^{8/5} - \frac{\Omega_r (C_\beta C_\xi)^{2/5} j_{tr}^{1/5}}{C_\gamma} (T_l^4 - T_{dc}^4) (T_m - T_l)^{2/5} \quad (2-264)$$

This equation is also solved with the Newton-Raphson technique by forming the expressions:

$$f = T_l - T_{dc} - \frac{C_\beta^{8/5} C_\xi^{3/5} j_{tr}^{4/5}}{C_\gamma} (T_m - T_l)^{8/5} + \frac{\Omega_r (C_\beta C_\xi)^{2/5} j_{tr}^{1/5}}{C_\gamma} (T_l^4 - T_{dc}^4) (T_m - T_l)^{2/5} \quad (2-265)$$

$$\frac{df}{dT_I} = 1 + \frac{\Omega_r (C_\beta C_\xi)^{2/5} j_{tr}^{1/5}}{C_\gamma} \left\{ 4T_I^3 (T_m - T_I)^{2/5} - \frac{2}{5} (T_I^4 - T_{dc}^4) (T_m - T_I)^{-3/5} \right\} + \frac{8C_\beta^{8/5} C_\xi^{3/5} j_{tr}^{4/5}}{5C_\gamma} (T_m - T_I)^{3/5} \quad (2-266)$$

With these expressions, iteration is performed to find T_I using the approach outlined around Eq. 2-56. The solution for T_I is then compared to the melt freezing temperature $T_{m,frz}$ to determine the next step in the solution methodology. For situations in which $T_I \geq T_{m,frz}$, the solution is valid and the downward heat transfer term $h_b(T_m - T_b)$ in the melt energy balance equation (Eq. 2-18) is evaluated by setting $T_b = T_{dc}$, with the effective heat transfer coefficient from the melt pool to the concrete set as:

$$h_b = \frac{h_m(T_m - T_I)}{T_m - T_{dc}} \quad (2-267)$$

For situations in which $T_I < T_{m,frz}$, the solution is recalculated with an interstitial crust placed at the interface of the melt pool and gas film. The crust thickness is then calculated as part of the solution. Consistent with the implementation of the gas film model in CORCON,^[41] when this particular model is employed the following assumptions are made regarding the crust growth process at the interface: i) the growth is quasi-steady so that at any time conduction heat transfer across the crust balances convection to the crust interface, ii) the crust is thin and so decay heat within the crust can be neglected, and iii) the composition of the crust is the same as that of the melt. Under these assumptions the heat balances across the melt-crust and crust-film interfaces are of the form:

$$h_m(T_m - T_{m,frz}) = k_m \frac{(T_{m,frz} - T_I)}{\delta_b} \quad (2-268)$$

$$k_m \frac{(T_{m,frz} - T_I)}{\delta_b} = h_r(T_I - T_{dc}) + h_g(T_I - T_{dc}) \quad (2-269)$$

Since the boundary temperature on the melt side of the interface is fixed at the freezing temperature, then the heat flux to that interface is also fixed for a given melt temperature. For this case the quasi-steady heat transfer assumption is also used to relate the gas sparging rate to the surface heat flux; i.e.,

$$j = \left(\frac{\chi_g}{\rho_g} \right) \frac{h_m(T_m - T_{m,frz})}{e_{con,d}} = C_\xi h_m(T_m - T_{m,frz}) \quad (2-270)$$

The Kutateladze-Malenkov correlation for the melt-side convective heat transfer coefficient then becomes:

$$h_m = \begin{cases} C_\beta^3 C_\xi^2 (T_m - T_{m,frz})^2; & j < j_{tr} \\ C_\beta^{6/5} C_\xi^{1/5} j_{tr}^{3/5} (T_m - T_{m,frz})^{1/5}; & j \geq j_{tr} \end{cases} \quad (2-271)$$

where the gas velocity check is performed with $j = [C_\beta C_\xi (T_m - T_{m,frz})]^3$. For cases in which $j \leq j_{tr}$, then this is the gas velocity used in the evaluation of the gas film convection heat transfer coefficient which, from Eq. 2-256, can be expressed as $h_g = C_\gamma / j^{1/3}$. With this background, then

for the case in which $j < j_{tr}$ the transcendental equation for the interface temperature on the bottom side of the crust is derived from Eq. 2-269 as:

$$T_I - T_{dc} = \frac{q_b''}{h_g} - \frac{\Omega_r}{h_g} (T_I^4 - T_{dc}^4) \quad (2-272)$$

where $q_b'' = h_m(T_m - T_{m,frz}) = C_\beta^3 C_\xi^2 (T_m - T_{m,frz})^3$. This equation is solved using the Newton-Raphson technique by forming the expressions:

$$f = T_I - T_{dc} + \frac{\Omega_r}{h_g} (T_I^4 - T_{dc}^4) - \frac{q_b''}{h_g} \quad (2-273)$$

$$\frac{df}{dT_I} = 1 + \frac{4\Omega_r}{h_g} T_I^3 \quad (2-274)$$

Given these results, iteration is then performed to find T_I using the approach outlined around Eq. 2-56. With T_I known, the crust thickness at the interface is then found from:

$$\delta_b = \frac{k_m(T_m,frz - T_I)}{h_m(T_m - T_{m,frz})} \quad (2-275)$$

Additionally, the downward heat transfer term $h_b(T_m - T_b)$ in the melt energy balance equation (Eq. 2-18) is evaluated by setting $T_b = T_{dc}$, with the effective heat transfer coefficient from the melt pool to the concrete set as:

$$h_b = \frac{h_m(T_m - T_{m,frz})}{T_m - T_{dc}} \quad (2-276)$$

For the case in which in the check velocity $j = [C_\beta C_\xi (T_m - T_{m,frz})]^3$ is $> j_{tr}$, then the actual gas velocity is recalculated through Eqs. 2-270 and 271 to be $j = j_{tr}^{3/5} [C_\beta C_\xi^6 (T_m - T_{m,frz})]^{6/5}$. With this result, the gas film heat transfer coefficient is reevaluated from $h_g = C_\gamma / j^{1/3}$. With this new information, the interface temperature, crust thickness, and input data for the solution of the melt energy balance Eq. 2-18 are recalculated using Eqs. 2-273 through 2-276.

For cases in which the 2-D cavity erosion option is selected, a simplified version of the CORCON gas film model^[41] can also be applied on vertical concrete surfaces. The flow in the film can be either laminar or turbulent, depending upon the Reynolds number in the film. The correlations for the Nusselt number for these two cases are of the form:^[41]

$$Nu = \frac{h_g \delta_g}{k_g} = \begin{cases} 1, & \text{laminar} \\ 0.0325 Pr_g^{1/3} Re^{3/4}, & \text{turbulent} \end{cases} \quad (2-277)$$

where δ_g is the gas film thickness and $Pr_g = \mu_g c_g / k_g$ is the Prandtl number for the gas film. The Reynolds number is based on the film thickness and is defined as:^[41]

$$Re = \frac{\rho_g \bar{u} \delta_g}{\mu_g} \quad (2-278)$$

where \bar{u} is the gas flow velocity parallel to the concrete wall.

Correlations for the film thickness under both laminar and turbulent flow conditions are also provided.^[41] These correlations are functions of the film inclination angle with respect to vertical. Consistent with the simple cavity geometries assumed in this work (see Section 2.2), the concrete wall is assumed to be vertically oriented. For this case the film thickness correlations are:

$$\delta_g^3 = \begin{cases} 5.61 \text{Re} L_\mu^3, & \text{laminar flow} \\ 0.0469 \text{Re}^{7/4} L_\mu^3, & \text{turbulent flow} \end{cases} \quad (2-279)$$

where the length scale L_μ is defined in Eq. 2-257.

In order to employ this model, the film flow velocity \bar{u} in the Reynolds number definition (Eq. 2-278) needs to be specified. Assuming: i) that the vertical wall can be modeled as a simple rectilinear structure of uniform width, and ii) 100 % of the concrete decomposition gases flow vertically upwards in the film as opposed to being released into bulk pool, then the fully developed 1-D momentum equation governing gas flow in the film takes the form:

$$\frac{d}{dx}(\bar{u} \delta_g) = j_s \quad (2-280)$$

where in this case j_s is the superficial gas velocity from the concrete sidewall due to ablation. Integration of this equation over the axial extent of the voided melt pool yields the following expression for gas flow velocity at the exit:

$$\bar{u} = \frac{j_s H_{m,v}}{\delta_g} \quad (2-281)$$

The film flow Reynolds number can then be redefined as:

$$\text{Re} = \frac{\rho_g j_s H_{m,v}}{\mu_g} \quad (2-282)$$

The modeling past this point resembles that for the horizontal surface gas film model described above. In particular, the Kutateladze-Malenkov correlation^[40] is used to evaluate the heat transfer coefficient from the bulk melt pool to the interface. However, as noted earlier, 100 % of the gas flow from sidewall decomposition is assumed to stay in the film, and so the melt superficial gas velocity in the correlation is based on that from the bottom of the melt pool; i.e.,

$$h_m = \begin{cases} 1.5 \cdot 10^{-3} \left(\frac{c_m P j_b}{k_m g} \right)^{2/3} \frac{k_m}{L_\lambda}; & j_b < j_{tr} \\ 1.5 \cdot 10^{-3} \left(\frac{c_m P j_b}{k_m g} \right)^{2/3} \left(\frac{j_{tr}}{j_b} \right)^{1/2} \frac{k_m}{L_\lambda}; & j_b \geq j_{tr} \end{cases} \quad (2-283)$$

where j_b is the gas sparging rate from decomposition of the concrete basemat.

The second similarity in the modeling is that a quasi-steady concrete ablation assumption is used to relate the sidewall superficial gas velocity to the heat transfer rate at the surface and therefore the boundary temperatures near the sidewall. Solving first for the case in which the melt-film interface is assumed to be crust free, then the heat flux to the wall is given by $q_s'' = h_m (T_m - T_l)$ and the sidewall gas velocity can thus be deduced from Eq. 2-251 as:

$$j_s = \frac{\chi_g \rho_{con} \dot{\eta}_s}{\rho_g} = \left(\frac{\chi_g}{\rho_g} \right) \frac{h_m (T_m - T_l)}{e_{con,d}} \quad (2-284)$$

With this expression and Eqs. 2-277, 2-279, and 2-282, the convective heat transfer coefficient in the gas film can then be written as:

$$h_g = \begin{cases} \frac{C_{lam}}{(T_m - T_l)^{1/3}}, & \text{la min ar flow} \\ C_{turb} (T_m - T_l)^{1/6}, & \text{turbulent flow} \end{cases} \quad (2-285)$$

where the laminar and turbulent correlation constants are given by:

$$C_{lam} = \frac{0.56 k_g}{L_\mu} \left(\frac{\mu_g e_{con,d}}{H_{m,v} \chi_g h_m} \right)^{1/3} \quad (2-286)$$

$$C_{turb} = 0.09 \frac{k_g Pr_g^{1/3}}{L_\mu} \left(\frac{\chi_g H_{m,v} h_m}{\mu_g e_{con,d}} \right)^{1/6} \quad (2-287)$$

The energy balance across the melt-film interface for the crust-free surface boundary condition is then of the form:

$$q_s'' = h_m (T_m - T_l) = \Omega_r (T_l^4 - T_{dc}^4) + h_g (T_l - T_{dc}) \quad (2-288)$$

As a reminder, the constant Ω_r is defined in Eq. 2-255. For the laminar flow case, combination of Eqs. 2-285 and 2-288 yields the following equation for the melt-film interface temperature:

$$T_l = T_m - \frac{\Omega_r}{h_m} (T_l^4 - T_{dc}^4) - \frac{C_{lam}}{h_m} \cdot \frac{(T_l - T_{dc})}{(T_m - T_l)^{1/3}} \quad (2-289)$$

This transcendental equation is solved using the Newton-Raphson technique by forming the equations:

$$f = T_l - T_m + \frac{\Omega_r}{h_m} (T_l^4 - T_{dc}^4) + \frac{C_{lam}}{h_m} \cdot \frac{(T_l - T_{dc})}{(T_m - T_l)^{1/3}} \quad (2-290)$$

$$\frac{df}{dT_l} = 1 + \frac{4\Omega_r T_l^3}{h_m} + \frac{C_{lam}}{3h_m} \cdot \frac{(3T_m - 2T_l - T_{dc})}{(T_m - T_l)^{4/3}} \quad (2-291)$$

Given these expressions, iteration is then performed to find T_l using the approach outlined around Eq. 2-56. With T_l known, the gas film convection heat transfer coefficient in the laminar regime, $h_{g,lam}$, is then calculated from Eq. 2-285.

For the turbulent flow case, the equation for the interface temperature is deduced from Eqs. 2-285 and 2-288 as:

$$T_l = T_m - \frac{\Omega_r}{h_m} (T_l^4 - T_{dc}^4) - \frac{C_{turb}}{h_m} (T_m - T_l)^{1/6} (T_l - T_{dc}) \quad (2-292)$$

This transcendental equation is also solved using the Newton-Raphson technique by forming the expressions:

$$f = T_I - T_m + \frac{\Omega_r}{h_m}(T_I^4 - T_{dc}^4) + \frac{C_{turb}}{h_m}(T_m - T_I)^{1/6}(T_I - T_{dc}) \quad (2-293)$$

$$\frac{df}{dT_I} = 1 + \frac{4\Omega_r T_I^3}{h_m} + \frac{C_{turb}}{6h_m} \cdot \frac{(6T_m - 5T_I - T_{dc})}{(T_m - T_I)^{5/6}} \quad (2-294)$$

With these expressions, iteration is then performed to find T_I using the approach outlined around Eq. 2-56 and with that result known, the gas film convection heat transfer coefficient in the turbulent flow regime, $h_{g,turb}$, is then evaluated from Eq. 2-285.

Consistent with the CORCON modeling approach,^[41] the decision upon whether or not the flow in the film is laminar or turbulent is then based on the relative values of the heat transfer coefficients calculated for these two regimes; i.e.,

$$h_g = \langle h_{g,lam}, h_{g,turb} \rangle \quad (2-295)$$

where again the operator $\langle \bullet, \bullet \rangle$ denotes the larger of the two arguments. Based upon this result, the melt-film interface temperature T_I is set accordingly. The interface temperature is then compared to the melt freezing temperature $T_{m,frz}$ to determine the next step in the solution process. For situations in which $T_I \geq T_{m,frz}$, the solution is valid and the sideward heat transfer term $h_s(T_m - T_s)$ in the melt energy balance equation (Eq. 2-18) is evaluated by setting $T_s = T_{dc}$, with the effective heat transfer coefficient from the melt pool to the concrete set as:

$$h_s = \frac{h_m(T_m - T_I)}{T_m - T_{dc}} \quad (2-296)$$

For situations in which $T_I < T_{m,frz}$, the solution is recalculated with an interstitial crust placed at the interface of the melt pool and gas film. The crust thickness is then evaluated as part of the solution. As noted earlier, the same simplifying assumptions⁶ made in CORCON^[41] regarding crust growth at the interface for the gas film model are made as part of this study. With this background the heat balances across the melt-crust and crust-film interfaces on the sidewall are of the form:

$$h_m(T_m - T_{m,frz}) = k_m \frac{(T_{m,frz} - T_I)}{\delta_s} \quad (2-297)$$

$$k_m \frac{(T_{m,frz} - T_I)}{\delta_s} = \Omega_r(T_I^4 - T_{dc}^4) + h_g(T_I - T_{dc}) \quad (2-298)$$

The definition of the melt-side convective heat transfer coefficient, h_m , is the same as that provided in Eq. 2-283, but the sidewall superficial gas velocity used to redefine the gas side convection heat transfer coefficient is rewritten in terms of the new boundary temperature as:

$$j_s = \left(\frac{\chi_g}{\rho_g} \right) \frac{h_m(T_m - T_{m,frz})}{e_{con,d}} \quad (2-299)$$

Given this expression and Eqs. 2-271, 2-279, and 2-282, the convective heat transfer coefficient in the gas film is then redefined as:

⁶As a reminder, these simplifying assumptions are as follows: i) the growth is quasi-steady so that at any time conduction heat transfer across the crust balances convection to the crust interface, ii) the crust is thin and so decay heat within the crust can be neglected, and iii) the composition of the crust is the same as that of the melt at anytime.

$$h_g = \begin{cases} \frac{C_{lam}}{(T_m - T_{m,frz})^{1/3}}, & \text{laminar flow} \\ C_{turb} (T_m - T_{m,frz})^{1/6}, & \text{turbulent flow} \end{cases} \quad (2-300)$$

Given this background, the solution methodology for this case is basically the same as that used for the crust-free boundary condition; i.e., solutions are obtained for both laminar and turbulent film flow conditions, and the decision regarding the applicable flow regime is then made on the basis of the relative values of the gas film convection heat transfer coefficients calculated for these two cases. For the laminar flow regime, the expression for the interface temperature at the bottom of the crust is then deduced from Eqs. 2-297 to 2-300 as:

$$T_I - T_{dc} = \frac{(T_m - T_I)^{1/3}}{C_{lam}} \left\{ h_m (T_m - T_{m,frz}) - \frac{\Omega_r}{h_m} (T_I^4 - T_{dc}^4) \right\} \quad (2-301)$$

This equation is also solved using the Newton-Raphson technique by forming the expressions:

$$f = T_I - T_{dc} - \frac{(T_m - T_{m,frz})^{1/3}}{C_{lam}} \left\{ h_m (T_m - T_{m,frz}) - \frac{\Omega_r}{h_m} (T_I^4 - T_{dc}^4) \right\} \quad (2-302)$$

$$\frac{df}{dT_I} = 1 + \frac{4\Omega_r T_I^3}{C_{lam}} (T_m - T_{m,frz})^{1/3} \quad (2-303)$$

With these expressions, iteration is then performed to find T_I using the approach outlined around Eq. 2-56 and with that result known, the gas film convection heat transfer coefficient in the laminar flow regime, $h_{g,lam}$, is evaluated from Eq. 2-300.

The next step is to solve for the turbulent convection heat transfer coefficient with a crust present. The expression for the interface temperature in this case is deduced as:

$$T_I - T_{dc} = \frac{1}{C_{turb} (T_m - T_I)^{1/6}} \left\{ h_m (T_m - T_{m,frz}) - \frac{\Omega_r}{h_m} (T_I^4 - T_{dc}^4) \right\} \quad (2-304)$$

This equation is also solved using the Newton-Raphson technique by forming:

$$f = T_I - T_{dc} - \frac{1}{C_{turb} (T_m - T_{m,frz})^{1/6}} \left\{ h_m (T_m - T_{m,frz}) - \frac{\Omega_r}{h_m} (T_I^4 - T_{dc}^4) \right\} \quad (2-305)$$

$$\frac{df}{dT_I} = 1 + \frac{4\Omega_r T_I^3}{C_{turb} (T_m - T_{m,frz})^{1/6}} \quad (2-306)$$

With these expressions, iteration is then performed to find T_I using the approach outlined around Eq. 2-56 and with that result known, the gas film convection heat transfer coefficient in the turbulent flow regime, $h_{g,turb}$, is then evaluated from Eq. 2-300. The decision upon whether or not the flow in the film is laminar or turbulent is then made on the basis of Eq. 2-295, and the melt-

film interface temperature T_I is set accordingly. The sideward heat transfer term $h_s(T_m - T_s)$ in the melt energy balance equation (Eq. 2-18) is then evaluated by setting $T_s = T_{dc}$, with the effective heat transfer coefficient from the melt pool to the concrete set as:

$$h_s = \frac{h_m(T_m - T_{m,frz})}{T_m - T_{dc}} \quad (2-307)$$

Finally, the crust thickness at the sidewall interface is found from:

$$\delta_s = \frac{k_m(T_{m,frz} - T_I)}{h_m(T_m - T_{m,frz})} \quad (2-308)$$

which completes the solution for the sidewall gas film model.

2.6.3.3 Gas Film - Slag Film Transition Model

One concept that was raised during the analysis of the CCI tests conducted as part of the OECD/MCCI program was whether or not a bifurcation in boundary conditions at the core-concrete interface could explain differences in ablation behavior observed for limestone/common sand and siliceous concrete types. This concept is not new; Kao, Lee, and Kazimi^[71] proposed a film collapse model in an effort to explain changes in axial ablation rate that occurred during the course of several BETA tests conducted at KfK.^[72] In this approach, two critical gas velocity criteria were considered:

- 1) Kutateladze flooding limit: when the gas velocity exceeds a critical value (several m/sec), transition to a gas film heat transfer model would occur.
- 2) Berenson minimum gas flux to stabilize a gas film (minimum film boiling point): when gas velocity falls below a minimum value (few cm/sec), melt-concrete contact is reestablished.

A simplified version of this overall modeling concept has been adopted in the code. In particular, for the axial ablation case, a transition model can be selected where initially the simplified version of the gas film model described in Section 2.6.3.2 is assumed to be the applicable boundary condition. When the gas velocity falls below the Berenson flooding limit, a transition to the slag film model described in Section 2.6.3.1 is then assumed to occur. The minimum gas velocity at the transition point is defined as:^[52,71]

$$j_{min} = 0.09M_B \left(\frac{g\sigma_m(\rho_m - \rho_g)}{(\rho_m + \rho_g)^2} \right)^{1/4} \quad (2-309)$$

where M_B is a (user-specified) multiplier constant, which Kao *et al.*^[71] set to 6.0 based on CORCON simulations of the BETA tests.

In contrast to axial ablation modeling, no radial gas-slag film transition model has been implemented in the code; either the Bradley, Sevón (see next section), or gas film models can be selected, and that boundary condition is applied to the vertical concrete surface throughout the duration of the simulation.

2.6.3.4 Sevón Correlations

Sevón^[42] analyzed CCI test data to develop empirical correlations for axial and lateral heat transfer coefficients for limestone/common sand and siliceous concrete types. As outlined below,

these correlations have been included as user options to increase the range of heat transfer models that are available within the code.

For both limestone/common and siliceous concrete types, Sevon found that the axial heat transfer coefficient data were correlated well through the following single empirical expression:

$$h_b = 49 + 2906j_b \quad (2-310)$$

where j_b is the local gas sparging rate (units of m/sec) from the concrete bottom surface that is evaluated at the concrete decomposition temperature, and h_b has units of W/m²-K. Decomposition temperature is a user-input (see Section 3). Sevon developed Eq. 2-310 (as well as Eq. 2-311 below) assuming that the decomposition temperature equals the concrete liquidus.

Unlike the axial data, Sevon found that two different correlations were required to correlate the lateral heat transfer data depending on concrete type; i.e.

$$h_s = \begin{cases} 57 + 3206j_s, & \text{limestone / common sand concrete} \\ 26 + 5736j_s, & \text{siliceous concrete} \end{cases} \quad (2-311)$$

where j_s is the local gas sparging rate from the concrete lateral surface (again evaluated at the concrete decomposition temperature). The units in this equation are the same as in Eq. 2-310.

Initial exercising of the code with these models revealed that the core-concrete heat transfer rate is strongly coupled to gas sparging rate which, in turn, is strongly coupled to heat transfer rate. As a result, extremely rapid transients developed if the initial melt temperature specified by the user was substantially different (i.e., higher) than the equilibrium temperature calculated by the code given the input power and corresponding heat transfer rates to concrete surfaces. To dampen these transients, the heat transfer coefficients predicted by these models are (somewhat arbitrarily) capped at 2500 W/m²-K within the code.⁷

2.7 Water Inventory Modeling

The previous sections have outlined the various models that have been implemented in CORQUENCH for calculating heat transfer to an overlying water pool. The code has also been structured to provide both simplified and detailed water inventory modeling capabilities; these models are summarized in this section.

With respect to simplified modeling capabilities, user options allow a water boundary condition to be applied at the water upper surface at a specified time, or at a specified axial ablation depth. For both of these cases, the code maintains the height fixed at a user-specified ‘downcomer’ height, H_{dc} . The water temperature is maintained at saturation corresponding to the cavity pressure at any given time during the calculation.

The overall approach used for the detailed water inventory model is to solve coupled mass, momentum, and energy equations for the water layer to calculate local depths, velocities, and boiloff rates while factoring in the potential for water injection as well as spillover into downcomers that may exist in the cavity. In particular, drawing on the methods developed for the MELTSPREAD code^[8] for the analysis of core melt spreading in containments, the water inventory model performs a spatially dependent fluid dynamics calculation of the gravity driven

⁷The axial heat transfer coefficient cap (HCAP) is set in subroutine HTRANB, while the lateral coefficient cap is set in subroutine HTRANS.

motions of a water spreading in a one-dimensional flow channel of varying cross-sectional area. The underlying substrate can consist of either core debris undergoing core-concrete interaction, or uncovered containment floor. The velocity of the flowing water is dependent upon the local gravity head of the water layer. In particular, the fluid velocity is assumed to satisfy the equation,

$$\frac{\partial U_w}{\partial t} + \frac{1}{2} \frac{\partial U_w^2}{\partial z} = g \frac{\partial}{\partial z} [H_w + E] - \frac{4\tau}{\rho_l D}, \quad (2-312)$$

where:

$$\begin{aligned} U_w &= \text{local water spreading velocity,} \\ H_w &= \text{local collapsed water depth,} \\ D &= \text{equivalent water hydraulic diameter} = 4H_w, \\ E &= \text{local substrate elevation,} \end{aligned}$$

and τ is the frictional shear stress at the water-debris interface that is evaluated as,

$$\tau = \frac{1}{2} \rho_l f U_w |U_w|, \quad (2-313)$$

where f is the flow friction factor. Note that the non-conservative form of the one-dimensional momentum equation is implied because it reduces to Bernoulli's law in the limit of negligible frictional resistance. Also note that the effect of voiding on local water height due to boiling heat transfer at the debris-water interface has been neglected in Eq. 2-312. Consistent with classical theories on gravity currents (e.g., see Benjamin^[73]), the pressure head driving the flow is assumed to equal the local hydrostatic head. In this manner, solution of Eq. 2-312 in the limit of frictionless flow yields the correct theoretical leading edge spreading velocity^[8,73] after transient affects have died away.

Spreading is restricted to occur such that the water depth at the leading edge does not fall below the minimum depth at which surface tension balances gravity,⁸

$$H_{w,min} = \sqrt{\frac{2\sigma_l}{\rho_l g}}. \quad (2-314)$$

The friction factor f in Eq. 2-312 is dependent upon the local water Reynolds number which is defined through the equation,

$$Re = \frac{\rho_l D |U_w|}{\mu_l}. \quad (2-315)$$

For Reynolds numbers below a transition value of ~ 2300 , the friction factor is evaluated as,

$$f = \frac{24}{Re}. \quad (2-316)$$

Note that the coefficient on the right hand side of Eq. 2-316 (i.e., 24) is based on the assumption of a fully developed parabolic velocity profile within the water. Thus, over short flow distances where the velocity profile has not become fully developed, the friction factor will be

⁸ The minimum depth is found by setting the gravity head at the leading edge ($\rho_l g H_w$) equal to the effective surface tension pressure ($2\sigma_l/H_w$).

underestimated through the use of this equation. However, the treatment of a developing velocity profile is beyond the scope of this work, and therefore Eq. 2-316 is used to estimate the friction factor under laminar flow conditions.

For Reynolds numbers above ~ 2300 , the friction factor is assumed to be given by the fully developed turbulent flow equation,^[74]

$$f = \frac{1}{4x^2}, \quad (2-317)$$

where x satisfies the transcendental equation,

$$x = 1.74 - \frac{2}{\ln(10)} \ln \left(\frac{2 R_{sand}}{D} + \frac{18.7x}{Re} \right). \quad (2-318)$$

and R_{sand} is the equivalent sand roughness. This parameter is internally set within the code to $R_{sand} = 1$ mm for inert surfaces (e.g., steel or concrete) not covered by core debris, and $R_{sand} = 1$ cm for core debris to reflect observed surface imperfections^[47] in this type of material that has been cooled by overlying water. One additional shortcoming in the current approach for calculating frictional flow resistance of water spreading over core debris is that the effect of particle beds has not been considered. These types of porous structures would clearly increase the flow resistance, but this effect is not addressed in the current analysis. Finally, note that although laminar-turbulent transition nominally occurs at a Reynolds number of ~ 2300 , the method used to evaluate the friction factor within the code is to take the larger of the two friction factors predicted by Eqs. 2-316 and 2-317 to maintain continuity in the friction factor at the transition point.

The general form of the conservation of mass equation for the water layer is as follows,

$$S \frac{\partial}{\partial t}(\rho_l H_w) + \frac{\partial}{\partial z}(S \rho_l H_w U_w) = S \dot{m}_w'', \quad (2-319)$$

where

$$\begin{aligned} S &= \text{local flow channel width normal to flow,} \\ \dot{m}_w'' &= \text{net local } \textit{influx} \text{ of water from extraneous sources.} \end{aligned}$$

The coolant mass conservation equation is thus of the form:

$$\dot{m}_w = \dot{m}_w'' A = \dot{m}_{inj} - \dot{m}_{st} - \dot{m}_{dc} \quad (2-320)$$

where A is local surface area and subscript *inj* denotes the external water supply, *st* denotes coolant steaming rate due to heat transfer from the core debris, and *dc* denotes the local gravity-driven mass flowrate into downcomers that may be present on the containment floor. The rate of local coolant loss due to boiling is expressed as:

$$\dot{m}_{st} = \begin{cases} \frac{q_{wat}'' A}{\Delta e_{lv}}; & T_w = T_{sat} \\ 0; & T_w < T_{sat} \end{cases} \quad (2-321)$$

where q_{wat}'' is the local heat flux from the debris to the overlying coolant. This function can take on different forms, depending upon the local boundary condition at the debris upper surface. For instance, if the heat transfer mode is either bulk cooling or conduction across a stable impervious crust, then $q_{wat}'' = h_{wat}(T_{t,l} - T_{sat})$; see Sections 2.5.1, 2.5.2 and 2.5.6.1 for definitions of h_{wat} and

$T_{t,l}$. If the crust is permeable to water ingression, then the applicable expression for the heat transfer to the pool from the crust is $q''_{wat} = q''_{c,dry} - \rho_v h_{lv} j \big|_{T_{sat}}$; see Sections 2.5.4 and 2.5.6.2. Finally, if eruptions are occurring then the additional heat transfer to the pool due to quenching and stabilization of the ejected material (i.e., Eq. 2-180) is included in the evaluation of q''_{wat} , with suitable checks to ensure that the crust and/or debris bed dryout limits are not exceeded.

As noted, water flow into downcomers (i.e., spillover points) can be calculated at specified locations as a user option. The available flow area for water to enter each downcomer is calculated as the water height above the downcomer inlet times a ‘cord length’, C_{dc} that is specified as part of the user input. For instance, if the downcomer is a circular pipe with a horizontally oriented opening, then the cord length would simply be the pipe diameter. The water flow velocity is calculated using a simple 1-D quasi-steady solution to Bernoulli’s equation that relates the flow velocity over the edge to the local water height above the edge; i.e., $u_{dc} = \sqrt{2g\Delta H}$, where $\Delta H = H_w - H_{dc}$ is the water height over the top of the downcomer. With this background, then by conservation of mass the water flowrate into each downcomer is given by:

$$\dot{m}_{dc} = \begin{cases} \rho_l \sqrt{2g} C_{dc} \Delta H^{3/2}; & H_w \geq H_{dc} \\ 0; & H_w < H_{dc} \end{cases} \quad (2-322)$$

As noted earlier, the effect of coolant voiding on pool swell and onset of spillover into the downcomers is not accounted for in this simplified model.

A water conservation of energy equation is solved to evaluate coolant heatup for situations in which the coolant is subcooled. The water specific enthalpy is found by solving the equation,

$$S \frac{\partial}{\partial t} (\rho_l H_w e_w) + \frac{\partial}{\partial z} (S \rho_l H_w e_w U_w) = S (q''_{wat} + \dot{m}''_{inj} e_{inj} - \dot{m}''_{dc} e_w) \quad (2-323)$$

where:

- e_w = water specific enthalpy,
- e_{inj} = injection water specific enthalpy,
- \dot{m}''_{inj} = local mass flux of water injection, and
- \dot{m}''_{dc} = local mass flux of water into spillover points.

The approach to solving Eqs. 2-312 through 2-319 is to utilize an implicit, Eulerian finite difference numerical scheme which removes numerical stability limitations corresponding to material convection, heat diffusion, and heat transfer between the water and underlying substrate or overlying medium. The nomenclature for the spreading mesh cells is illustrated in Figure 2-14. In formulating the finite difference equations for the spreading water, a staggered mesh is employed in which velocities are defined at the edges of the numerical grid cells, and other variables such as the layer depths and enthalpies (temperatures) are defined at cell centers. Thus, the fundamental velocity, $U_{j-1/2}$, in Figure 2-14 is that at the edge of the j^{th} and $j-1^{\text{st}}$ cells.

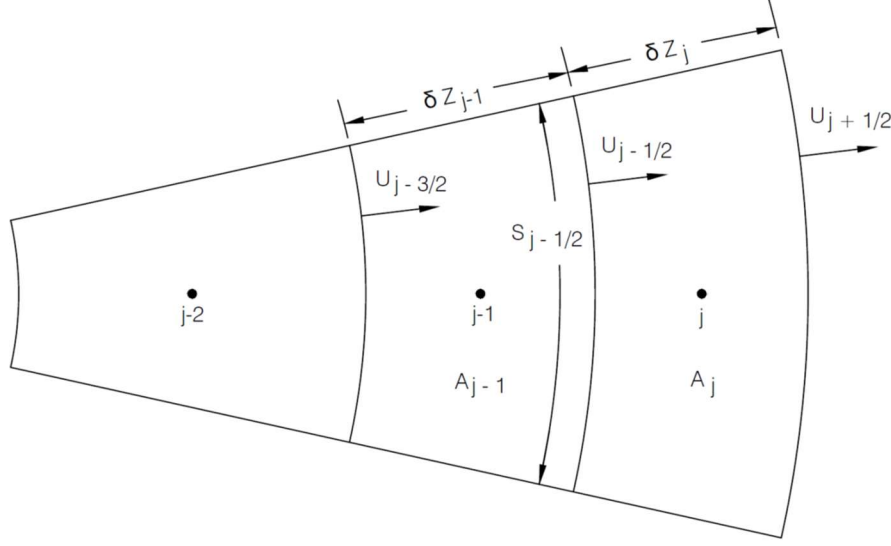


Figure 2-14. Illustration of Geometry and Nomenclature for Differencing of Water Spreading Equation.

The substrate surface is assumed to be discretized into $j = 1, 2, \dots, J$ numerical grid cells. At interior grid cell interfaces, for which $2 \leq j \leq J$, the finite difference approximation to the conservation of momentum equation (Eq. 2-312) is of the form,

$$\begin{aligned}
 & \frac{U_{w,j-1/2}^{n+1} - U_{w,j-1/2}^n}{\delta t} + \frac{1}{2} \frac{\delta z_j}{\delta z_j \delta z_{j-1}} (1 + \text{sgn}(u)) U_{w,j-1/2}^{n+1} (U_{w,j-1/2}^{n+1} - U_{w,j-3/2}^{n+1}) \\
 & + \frac{1}{2} \frac{\delta z_{j-1}}{\delta z_j \delta z_T} (1 - \text{sgn}(u)) U_{w,j-1/2}^{n+1} (U_{w,j+1/2}^{n+1} - U_{w,j-1/2}^{n+1}) \\
 & = \frac{-g}{(\delta z_j + \delta z_{j-1})} \left[\frac{H_{w,j}^{n+1}}{1 - \alpha_j^n} + E_j^n - \frac{H_{w,j-1}^{n+1}}{1 - \alpha_{j-1}^n} - E_{j-1}^n \right] - \frac{1}{2} f_{j-1/2} \frac{U_{w,j-1/2}^{n+1}}{H_{w,j}^n} |U_{w,j-1/2}^{n+1}| \quad (2-324)
 \end{aligned}$$

where:

- δt = timestep size,
- n = superscript denoting beginning of timestep value,
- $n+1$ = superscript denoting end of timestep value,
- $\text{sgn}(u) = \begin{cases} +1, & U_{w,j-1/2}^{n+1} > 0 \\ -1, & U_{w,j-1/2}^{n+1} < 0 \end{cases}$,
- $\delta z_T = \delta z_j + \delta z_{j-1} + \text{sgn}(u)(\delta z_j + \delta z_{j-1})$,
- δz_j = spreading grid cell size,
- j = subscript denoting center on j^{th} numerical grid cell,
- $j-1$ = denoting center of $j-1^{\text{st}}$ numerical grid cell, and
- $j-1/2$ = subscript denoting common edge of j^{th} and $j-1^{\text{st}}$ numerical grid cells.

Note that the advection term in Eq. 2-312 has been conservatively differenced using the donor cell method as developed by Hotchkiss.^[75] This method is adopted due to the inherent numerical

stability in comparison to other differencing techniques, such as the central difference approximation, and is also applicable to fixed as well as variable mesh sizes.

Equation 2-312 is solved assuming no flow across the system boundaries. Thus, the boundary conditions on the discretized momentum equation are, for $j=I$,

$$U_{w,j-1/2}^{n+1} = 0, \quad (2-325)$$

and for $j=J+I$,

$$U_{w,j+1/2}^{n+1} = 0. \quad (2-326)$$

The local velocities are calculated from Eqs. 2-312 through 2-326 in conjunction with the conservation of mass equation, the differenced form of which is developed below.

Employing the donor cell method for differencing of the convective mass flux term, the finite difference approximation to the simplified conservation of mass equation is of the form,

$$\begin{aligned} \frac{A_j}{\delta t} [H_{w,j}^{n+1} - H_{w,j}^n] + S_{j-1/2} \langle -U_{w,j-1/2}^{n+1}, 0 \rangle H_{w,j}^{n+1} + S_{j+1/2} \langle U_{w,j+1/2}^{n+1}, 0 \rangle H_{w,j}^{n+1} \\ - S_{j-1/2} H_{w,j-1}^{n+1} \langle U_{w,j-1/2}^{n+1}, 0 \rangle - S_{j+1/2} H_{w,j+1}^{n+1} \langle U_{w,j+1/2}^{n+1}, 0 \rangle = \dot{m}_{w,j}^{n+1} / \rho_l \end{aligned} \quad (2-327)$$

and here the operator, $\langle \cdot, \cdot \rangle$, denotes the largest of the two arguments; i.e.,

$$\langle U_{w,j+1/2}^{n+1}, 0 \rangle = \begin{cases} U_{w,j+1/2}^{n+1}, & U_{w,j+1/2}^{n+1} > 0 \\ 0, & U_{w,j+1/2}^{n+1} < 0 \end{cases} \quad (2-328)$$

The constraint that the water depth at the leading edge does not fall below the minimum depth at which surface tension balances gravity (Eq. 2-314) is applied to the differenced form of the equations by performing a local check on the water depth relative to the minimum spreading depth. If h_j^{n+1} and h_{j-1}^{n+1} are less than h_{min} , then $U_{j-1/2}$ is set equal to zero.

Care must be exercised in solving Eqs. 2-312 and 2-319 over substrate surfaces with physical discontinuities in elevation that exist as an initial condition. This situation is depicted in Figure 2-15. If the elevation discontinuity lies between the j -1st and the j th numerical grid cells and $E_j > E_{j-1}$, then for this case there will be flow across the cell boundary if the following condition is satisfied,

$$H_{w,j-1} + E_{j-1} > E_j. \quad (2-329)$$

If the condition defined by Eq. 2-329 is not satisfied, then the cell edge velocity across the substrate discontinuity is set equal to zero; i.e. $U_{w,j-1/2} = 0$. If Eq. 2-329 is satisfied, then flow across the cell boundary is calculated with the gravity head evaluated as in Eq. 2-312. It is important to note the following two points: a) if the conditional check defined by Eq. 2-329 is not applied and $H_{w,j-1} + E_{j-1} < E_j$, then an artificial adverse pressure drop across the discontinuity will be applied resulting in a physically unrealistic solution; and b) the conditional check defined in Eq. 2-329 is applied only to initial discontinuities in the substrate elevation (i.e., the condition

is not applied to discontinuities which arise as a result of variations in debris upper surface elevation).

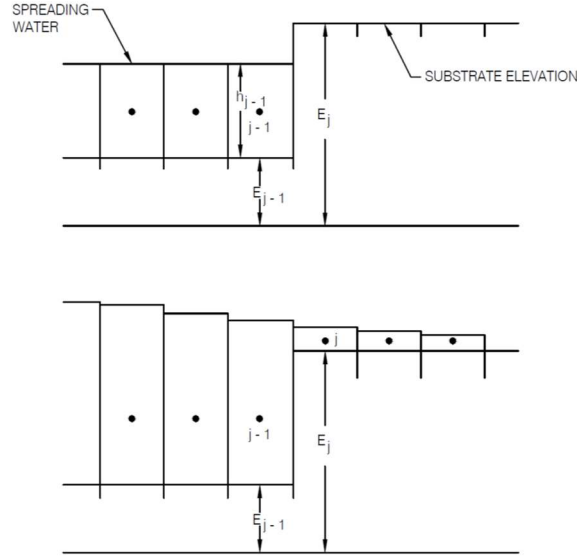


Figure 2-15. Illustration of Flow over Large Elevation Discontinuities in Substrate Surface.

Given the local water velocities as calculated through solution of Eqs. 2-312 to 2-319, the water conservation of energy equation is then then solved to obtain the end of timestep nodal water temperatures. The energy equation is solved using an Eulerian finite difference scheme in which convective terms are differenced using the donor cell differencing approach. This numerical scheme will give rise to so-called “Eulerian mixing” effects which will tend to artificially equilibrate water depths and temperatures more rapidly than purely physical processes, and will also somewhat reduce the peak calculated depths and temperatures. The degree of approximation introduced by Eulerian mixing depends upon the shape of the depth and temperature profiles, as well as the numerical grid cell size.

Employing the donor cell method for differencing of the convective energy flux term, the finite difference approximation to the conservation of energy equation (Eq. 2-323) is of the form,

$$\begin{aligned} & \frac{A_j}{\delta t} [(\rho_l H_w e_w)_j^{n+1} - (\rho_l H_w e_w)_j^n] - S_{j-1/2} \langle U_{w,j-1/2}^{n+1}, 0 \rangle (\rho_l H_w e_w)_{j-1}^{n+1} \\ & + S_{j-1/2} \langle -U_{w,j-1/2}^{n+1}, 0 \rangle (\rho_l H_w e_w)_j^{n+1} + S_{j+1/2} \langle U_{w,j+1/2}^{n+1}, 0 \rangle (\rho_l H_w e_w)_j^{n+1} \\ & - S_{j+1/2} \langle -U_{w,j+1/2}^{n+1}, 0 \rangle (\rho_l H_w e_w)_{j+1}^{n+1} = A_j (q_{wat})_j^{n+1} + (\dot{m}_{inj} e_{inj})_j^{n+1} \\ & - (\dot{m}_{dc} e_w)_j^{n+1} \end{aligned} \quad (2-330)$$

The local variables to be determined from the above difference equations are the water specific enthalpy, height, and velocity. At the start of the calculation for the current timestep, the cell edge velocities and water depths are first determined through the simultaneous solution of Eqs. 2-324 and 2-327 by performing an iterative calculation on the linearized form of these equations. To this end, the cell edge velocities are expanded as,

$$U_{w,j-1/2}^{r+1} = U_{w,j-1/2}^r + \delta U_{w,j-1/2} \quad (2-331)$$

where:

$$\begin{aligned} \delta U_{w,j-1/2} &= \text{incremental change in cell edge velocity, and} \\ r &= \text{iteration step.} \end{aligned}$$

Similar expressions apply at the $j+1/2$ and $j-3/2$ cell edges. The end of timestep water depths in Eq. 2-324 are forward eliminated in terms of the incremental changes in cell edge velocities. Substitution of Eq. 2-331 into Eq. 2-319 and linearizing the resultant expression yields,

$$H_{w,j}^{r+1} = H_{w,j}^r + F_j^r + G_j^r \delta U_{w,j-1/2} + I_j^r \delta U_{w,j+1/2} \quad (2-332)$$

where:

$$\begin{aligned} F_j = \frac{\delta t}{A_j} \left\{ \frac{(\dot{m}_w)_j^r}{\rho_l} + S_{j-1/2} < U_{w,j+1/2}^r, 0 > H_{w,j-1}^r + S_{j+1/2} < -U_{w,j+1/2}^r, 0 > H_{w,j+1}^r \right. \\ \left. - S_{j-1/2} < -U_{w,j-1/2}^r, 0 > H_{w,j}^r - S_{j+1/2} < U_{j+1/2}^r, 0 > H_{w,j}^r \right\}, \end{aligned} \quad (2-333)$$

$$G_j = \frac{\delta t S_{j-1/2}}{A_j} \{ H_{w,j-1}^r < \text{sgn}(U_{w,j-1/2}^r), 0 > -H_{w,j}^r < -\text{sgn}(U_{w,j-1/2}^r), 0 > \}, \quad (2-334)$$

$$I_j = \frac{\delta t S_{j+1/2}}{A_j} \{ H_{w,j+1}^r < \text{sgn}(U_{w,j+1/2}^r), 0 > -H_{w,j}^r < -\text{sgn}(U_{w,j+1/2}^r), 0 > \}. \quad (2-335)$$

The forward elimination for $H_{w,j-1}^{r+1}$ in Eq. 2-324 is obtained by setting $j=j-1$ in Eqs. 2-332 through 2-335. Substitution of Eqs. 2-331 through 2-335 into the momentum equation, Eq. 2-312 and linearizing the resulting expression yields, for $j=2, \dots, J$,

$$O_j^r \delta U_{w,j-1/2} + P_j^r \delta U_{w,j+1/2} + Q_j^r \delta U_{w,j-3/2} + R_j = 0, \quad (2-336)$$

where:

$$\begin{aligned} O_j^r = \frac{1}{\delta t} + \frac{\delta z_j \left(1 + \text{sgn}(U_{w,j-1/2}^r) \right)}{2\delta z_T \delta z_{j-1}} \cdot \left(2U_{w,j-1/2}^r - U_{w,j-3/2}^r \right) \\ + \frac{\delta z_{j-1} \left(1 - \text{sgn}(U_{w,j-1/2}^r) \right)}{2\delta z_j \delta z_T} \cdot \left(U_{w,j+1/2}^r - 2U_{w,j-1/2}^r \right) \\ + \frac{\text{sgn}(U_{w,j-1/2}^r)}{H_{w,j}^n} f_{j-1/2}^r U_{w,j-1/2}^r + \frac{g}{(\delta z_j + \delta z_{j-1})} (G_j^r - I_{j-1}^r) \end{aligned} \quad (2-337)$$

$$P_j^r = \delta z_{j-1} \frac{(1 - \text{sgn}(U_{w,j-1/2}^r))}{2\delta z_j \delta z_T} U_{w,j-1/2}^r + \frac{g I_j^r}{(\delta z_j + \delta z_{j-1})} \quad (2-338)$$

$$Q_j^r = -\delta z_j \frac{\left(1 + \text{sgn}(U_{w,j-1/2}^r) \right)}{2\delta z_{j-1} \delta z_T} U_{j-1/2}^r - \frac{g G_{j-1}^r}{(\delta z_j + \delta z_{j-1})}, \quad (2-339)$$

$$\begin{aligned}
R_j^r = & \frac{U_{w,j-1/2}^r - U_{w,j-1/2}^n}{\delta t} + \frac{\delta z_j (1 + \text{sgn}(U_{w,j-1/2}^r))}{2\delta z_T \delta z_{j-1}} U_{j-1/2}^r (U_{w,j-1/2}^r - U_{w,j-3/2}^r) \\
& + \frac{\delta z_{j-1} (1 - \text{sgn}(U_{w,j-1/2}^r))}{2\delta z_j \delta z_T} U_{w,j-1/2}^r (U_{w,j+1/2}^r - U_{w,j-3/2}^r) + \frac{1}{2} \frac{f_{j-1/2}^r}{H_{w,j}^n} U_{w,j-1/2}^r |U_{w,j-1/2}^r| \\
& + \frac{g}{(\delta z_j + \delta z_{j-1})} (H_{w,j}^r + F_j^r + E_j^n - H_{w,j-1}^r + F_{j-1}^r - E_{j-1}^n)
\end{aligned} \tag{2-340}$$

For $j=I$, the coefficients for the no flow boundary condition are

$$\begin{aligned}
O_1^r &= 1, \\
P_1^r &= 0, \\
Q_1^r &= 0, \\
R_1^r &= 0.
\end{aligned} \tag{2-341}$$

Similarly, for $j=J+I$, the coefficients are of the form

$$\begin{aligned}
O_{j+1}^r &= 1, \\
P_{j+1}^r &= 0, \\
Q_{j+1}^r &= 0, \\
R_{j+1}^r &= 0.
\end{aligned} \tag{2-342}$$

Equation 2-336 constitutes a linear set of equations, in the form of a tri-diagonal matrix, for the incremental changes in the cell edge velocities. Given the current estimate of the edge velocities and water heights, Eq. 2-336 is solved to obtain the incremental velocity changes. The end of timestep velocities are then updated through Eq. 2-331. Given the updated velocities, Eq. 2-327 is then solved to obtain the updated water heights. This procedure is then repeated until the incremental velocity changes decrease below user-specified convergence criteria (See Section 3).

Given the end of timestep velocities and heights, the water conservation of energy equation, Eq. 2-330, is then solved. Similar to the approach used to solve for the water flow velocities, the water specific enthalpy and temperature are expanded as,

$$e_{w,j}^{r+1} = e_{w,j}^r + \delta e_{w,j} \tag{2-343}$$

$$T_{w,j}^{r+1} = T_{w,j}^r + \frac{dT}{de_w} \delta e_{w,j} = T_{w,j}^r + \delta e_{w,j} / c_l \tag{2-344}$$

Linearization of the water conservation of energy equation, Eq. 2-330, then yields:

$$S_j^r \delta e_{w,j} + T_j^r \delta e_{w,j+1} + V_j^r \delta e_{w,j-1} + W_j^r = 0 \tag{2-345}$$

where:

$$S_j^r = \left[\frac{A_j}{\delta t} + S_{j-1/2} \langle -U_{w,j-1/2}^{n+1}, 0 \rangle + S_{j+1/2} \langle U_{w,j+1/2}^{n+1}, 0 \rangle \right] (\rho_l H_w)_j^r + \frac{A_j(h_{wat})_j^r}{c_l} + (\dot{m}_{dc})_j^{n+1} \quad (2-346)$$

$$T_j^r = -S_{j+1/2} \langle -U_{w,j+1/2}^{n+1}, 0 \rangle (\rho_l H_w)_{j+1}^r \quad (2-347)$$

$$V_j^r = S_{j-1/2} \langle U_{w,j-1/2}^{n+1}, 0 \rangle (\rho_l H_w)_{j-1}^r \quad (2-348)$$

$$\begin{aligned} W_j^r = & \frac{A_j}{\delta t} [(\rho_l H_w e_w)_j^r - (\rho_l H_w e_w)_j^n] - S_{j-1/2} \langle U_{w,j-1/2}^{n+1}, 0 \rangle (\rho_l H_w e_w)_{j-1}^r \\ & - S_{j+1/2} \langle -U_{w,j+1/2}^{n+1}, 0 \rangle (\rho_l H_w e_w)_{j+1}^r + [S_{j-1/2} \langle -U_{w,j-1/2}^{n+1}, 0 \rangle \\ & + S_{j+1/2} \langle U_{w,j+1/2}^{n+1}, 0 \rangle] (\rho_l H_w e_w)_j^r - A_j(q''_{wat})_j^r - (\dot{m}_{inj} e_{inj})_j^{n+1} \\ & + (\dot{m}_{dc})_j^{n+1} e_{w,j}^r \end{aligned} \quad (2-349)$$

Equation 2-345 constitutes a linear set of equations, in the form of a tri-diagonal matrix, for the incremental changes in water specific enthalpy. Given the current enthalpy estimates, Eq. 2-344 is solved to obtain the incremental enthalpy changes. The end of timestep enthalpies are then updated through Eq. 2-343. This procedure is repeated until the incremental enthalpy changes decrease below user-specified convergence criteria (See Section 3). Within the iteration, a specific check on the local coolant specific enthalpy is made to determine if it has reached the saturation point. If this case is encountered, then the tri-diagonal matrix coefficients are set to yield a null change in local coolant enthalpy; i.e.,

$$\begin{aligned} S_j^r &= 1, \\ T_j^r &= 0, \\ V_j^r &= 0, \\ W_j^r &= 0. \end{aligned} \quad (2-350)$$

2.8 Automated Multi-Nodal Analysis Capability

2.8.1 Overview of Multi-Nodal Modeling Approach

As noted at the onset of this report, CORQUENCH was originally developed to be a single node MCCI analysis code, which is similar to most other codes that are available for MCCI analysis. In this approach, the core melt is treated as a single pool at a uniform temperature, with heat transfer to radial and axial concrete boundaries driving concrete ablation and cooling to overlying structure or water, depending upon whether or not the cavity is flooded (see Figure 2-1). The primary focus of these types of models is the analysis of heat transfer to the various boundaries of the pool as well as chemical reactions between metallic water constituents and concrete decomposition gases that produce combustible gases (H₂ and CO) that are a safety concern during a severe accident.

Although these single node models provide detailed treatment of localized physical phenomena, they lack the ability to capture global behavior in actual containment geometries like the Mark I (see Figure 2-16) in which structures like sumps and compartments can lead to varying melt accumulations within containment that can impact the cavity flooding strategy as well as the ability to quench and thermally stabilize core debris.

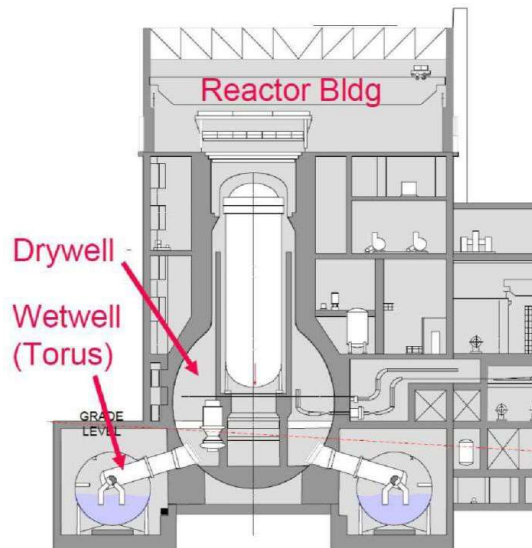


Figure 2-16. Illustration of BWR Mark I Containment.⁹

Based on this background, CORQUENCH has been upgraded to incorporate a multi-nodal analysis capability. However, the ability to do single node analysis has been retained, as this capability is important and relevant for isolated treatment of structures such as sumps, as well as the fact that validation experiments can be mocked up quite well using the single node approximation. The multi-nodal capability was achieved as follows. All common blocks in the main program were first analyzed to determine what variables were common to any given node, as well as those that were dependent upon local conditions (these include water depth, composition, specific enthalpy, boundary condition state, and cavity conditions such as area, 1-D versus 2-D erosion characteristics, etc.). With the dependent variables identified, additional common blocks were developed that allowed dependent variables for each node to be saved at each time step. The main program was then vectorized to analyze across an array of nodes, each of which is characterized by user-defined input data. A series of single node core-concrete analyses are thus carried out in parallel, with appropriate bridging software that allows integral quantities across the various nodes to be tallied for output to printing and plotting files. In terms of node geometric characteristics, a variety of options have been supplied to allow physical features of containments (e.g., sumps, walls, doorways, flow channels, etc.) to be mocked up in an integral fashion. The multi-nodal analysis capability was then integrated with the water inventory model described in Section 2.7 to yield a tool capable of analyzing spatially dependent MCCI behavior, coupled with a realistic water inventory model that can be used for core debris coolability analyses.

⁹ https://upload.wikimedia.org/wikipedia/commons/a/a0/BWR_Mark_I_Containment%2C_diagram.png

2.8.2 *Remaining Modeling Deficiencies*

In terms of insights related to modeling of long-term, water limited accident scenarios, early scoping calculations with the upgraded version of CORQUENCH for Fukushima-type accident scenarios¹⁰ indicate that it is critical to be able to calculate local core debris quench, dryout, reheating, and transition back into MCCI in order to reasonably mock up situations when cavity flooding can be interrupted for a significant length of time (e.g., hours). The model has been partially upgraded to accomplish this goal, with the methodology used to calculate reheating and melting of thick crust material formed by water ingress cooling described in Section 2.5.4.2. However, the current version does not analyze heat transfer from particle beds after they have completely dried out. In order to move meet the overall modeling goals, the beds are currently treated as adequately cooled as long as there is some degree of water left in the bottom of the bed. However, after the bed dries out the decay heat in the bed will offset, or possibly lead to heating, of the crust upper surface and thereby increase the crust melting rate. For sufficiently deep beds, the beds themselves may reheat and melt. This may not be a major factor for plants with siliceous concrete basemats, as the amount of material rendered into the form of a bed by melt eruptions is relatively small in comparison to other concrete types. However, this could become a significant distortion for high gas concretes like limestone/common sand or limestone/limestone in which the extent of eruptions can be substantial.^[47,66] Related to this area, early scoping calculations with the upgraded version of MELTSPREAD^[8] indicate that for low melt pour rate scenarios, significant debris fragmentation can occur if water is present on the cavity floor at the time of vessel failure. Thus, this can be another source of debris bed material even for low gas concretes like siliceous.

Another point not fully appreciated at the start of this work was the extent that lateral ablation can alter the original cavity configuration that we have attempted to model using a fixed mesh approach. For example, in early scoping calculations carried out for a MAAP melt pour sequence, the cavity floor area was predicted to increase by 60 % over 100 hours of interaction. Currently, the water spreading model treats node spacing and flow arc lengths as constant, with the node surface area increased to account for lateral ablation. Thus, the meshing treatment needs to be improved. However, there is a larger distortion that is due to the fact that the nodes are treated as isolated and so there is currently no interaction. This approach needs to be improved particularly in the pedestal region where the sump node can grow to overtake the radial ring between the sump and pedestal wall. Thus, the nodes need to communicate and the meshing adjusted to provide a more realistic treatment when 2-D ablation is modeled at the interface between adjacent nodes.

¹⁰ For example, see M. T. Farmer and K. R. Robb, “Status Report on Ex-Vessel Coolability and Water Management,” ANL/NE-16/18, September 2016.

3.0 DESCRIPTION OF CODE INPUT

3.1 Overview

CORQUENCH4.1 reads all information required to perform the calculation from an unformatted data file called 'quenchin.dat'. This file is opened as Unit 5 of the main program. Data input is performed through subroutine READER. The overall layout for the input file is shown in Table 3-1, while detailed descriptions of all input variables are provided in Table 3-2. This table also provides a description of the various modeling choices (see Section 2.0) that can be invoked through the setting of input parameters.

The variable names shown in Tables 3-1 and 3-2 are the same as those used in the code, with the exception of those listed for Line 49. In this case, the code uses a single vector YC(N,I) for all the dependent variables, with N denoting the node in the mesh if a multi-nodal model is employed. In this array, the *melt* mass constituents occupy I = 8-29 (30 is the total melt mass), the *top crust* constituents occupy I = 31-52 (53 is total crust mass), the *particle bed* constituents occupy I=54-75 (76 is total particle bed mass), the *bottom crust* constituents occupy I=77-98 (99 is the total bottom crust mass), and finally the *side crust* constituents occupy I=100-121 (122 is the total side crust mass). Indices are set in subroutine SETINDX. Within the code, the vector FC(N,I) denotes the rate equations for this same set of dependent variables that are integrated using a 4th order Runge Kutta (Gill) method to find the numerical solution as a function of time.

The constituents in the concrete and corium are assigned numerical (integer) values for identification within the input file and the code itself. The indexing scheme is shown in Table 3-3. These numerical assignments are treated symbolically in the code; numerical values are assigned in subroutine SETINDX. This approach allows additional constituents, and/or additional models for different processes, to be implemented in the code with minimal effort.

As part of the numerical solution, CORQUENCH4.1 updates the dependent variable array YC(N,I) at the end of every timestep, and does not use memory to maintain historical data as the calculation moves forward. Thus, there are essentially no vector or array size limitations that need to be considered in the selection of modeling assumptions, timestep, or total duration of the calculation, with two exceptions. First, the vectors and arrays in the code are currently set up to handle up to N=199 nodes as part of a containment multi-nodal analysis.

Second, the code is currently capable of treating a composite basemat that can be divided into NCOMP discrete layers, each of which has different chemical composition, melting points, and layer thickness (see Line 3 in input file that is described in Table 3-1, and input variable descriptions described in Table 3-2).¹¹ Currently, the vectors and arrays that are associated with this part of the calculation are dimensioned such that up to 100 discrete basemat layers can be modeled (i.e., NCOMP \leq 100).

¹¹This option is provided to model, among other things, reinforcing bar in the containment basemat.

Table 3-1. Summary Format for CORQUENCH4.1 Input File ‘quenchin.dat’.

Line No.	Variable Name(s)	Notes
1	TITLE	70-character string title for the calculation; written to output file ‘quenchout.dat.’
2	TCNOT	
3	ICTC, NCOMP, NABBL, NUMNOD, NMIX /N	If NUMNOD>1, then set NCOMP=1 (i.e. composite basemat model is not available if NUMNOD>1). Note that NUMNOD is currently capped at 199 nodes.
4	NABLB, NFAILB, NBCB, CFAILB, DCFAILB, TIMEFB	
5	NABLS, NFAILS, NBCS, CFAILS, DCFAILS, TIMEFS	
6	TCSL(I), TCLL(I), TDCL(I), XFLH2O(I), XFLCO2(I), DEPTH(I)	<i>If ICTC <4, Lines 7-11 are omitted. If ICTC = 4, Lines 6-11 are repeated NCOMP times. If ICTC < 4, then there is only one Line 6.</i>
7	XWTC(I,1) – XWTC(I,4)	Weight % CO ₂ , H ₂ O, K ₂ O, and Na ₂ O, respectively, in I-th concrete layer. Omitted if ICTC<4.
8	XWTC(I,5) – XWTC(I,8)	Weight % TiO ₂ , SiO ₂ , CaO, and MgO, respectively, in I-th concrete layer. Omitted if ICTC<4.
9	XWTC(I,9) – XWTC(I,12)	Weight % Al ₂ O ₃ , FeO, Fe ₂ O ₃ , and Fe ₃ O ₄ , respectively, in I-th concrete layer. Omitted if ICTC<4.
10	XWTC(I,13) – XWTC(I,16)	Weight % Fe, Cr, Ni, and Zr, respectively, in I-th concrete layer. Omitted if ICTC<4.
11	XWTC(I,17) – XWTC(I,18)	Weight % ZrO ₂ and B ₂ O ₃ , respectively, in I-th concrete layer. Omitted if ICTC<4.
12	TFWS, TFWL	
13	TBWS, TBWL	
14	TMCAS, TMCAL	
15	TCAS, TCAL	
16	IPHASE, IEUTEC, NSOLID	If IPHASE < 3, Lines 17-20 are omitted.
17	NSOLP	
18	XWTSOL(I), FSOLP(I)	Line 18 is repeated NSOLP times.
19	NLIQP	
20	XWTLIQ(I), FLIQP(I)	Line 20 is repeated NLIQP times.

Table 3-1 (Contd.). Summary Format for CORQUENCH4.1 Input File ‘quenchin.dat’.

Line No.	Variable Name(s)	Notes
21	NPOURS	<i>If NPOURS = 0, Lines 22-24 are omitted. If NPOURS>0, Lines 22-24 are repeated NPOURS times.</i>
22	TST(I), TSTOP(I), AINTP(I), BINTP(I)	Pour interval start and stop times, and melt temperature coefficients over pour interval. Melt temperature may vary linearly; i.e., $T_{melt}=AINTP(I)+BINTP(I) \bullet (t-TST(I))$
23	NISTP	Number of melt constituents draining from RPV over pour interval.
24	IT, APOUR(IT,I), BPOUR(IT,I)	Pour rate coefficients for IT-th melt constituent; the pour rate can vary linearly; i.e., $Rate=APOUR(IT,I)+BPOUR(IT,I) \bullet (t-TST(I))$
25	SIGYCR, FRZFR	
26	NINGRS, PERM, CINGRES, CHFMULT, CCRIT	
27	NENTR, ENSPEC, ENRICO, DBED, POROSBED	
28	NVISC, ALPMAX	
29	NKSPEC, FKS	
30	NUSGAP, NBUBSP, CCRGAP	
31	NBUBRS	
32	NCHEM	
33	NBOTBC, NSIDEBC, NVOID, XMULTBR, XBMULT, XSMULT	
34	NDEC, NPOINT	If NDEC = 1, Line 36 is omitted. Note: NDEC=2 modeling option is not available when NUMNOD>1.
35	CON1, CON2, PCORE, XMFUEL, FRACFP, TEFPD	
36	TDEC(I), DEC(I)	Line 36 is repeated NPOINT times.
37	NPRES, PDRYWL, EDRYWL, TSTRUC	
38	TPRES(I), PPRES(I)	If NPRES = 1, Line Group 38 is omitted. If NPRES > 1, then Line 38 is repeated NPRES times (minimum is NPRES=2).

Table 3-1 (Contd.). Summary Format for CORQUENCH4.1 Input File ‘quenchin.dat’.

Line No.	Variable Name(s)	Notes
39	NADD, TADD,DEPAB,HDOWNC, TWATI, ELWATI	<i>If $NADD \leq 2$, (i.e., cavity remains dry or a simple cavity flooding model is invoked), Lines 40-45 are omitted.</i>
40	NINJ	<i>Lines 41-42 are omitted if $NINJ=0$.</i>
41	NISTR(I), NISTP(I),NPTINJ(I)	
42	TIMINJ(I,L), XDTINJ(I,L), TDTINJ(I,L)	
43	NDOWNC	<i>Lines 43-44 are omitted if $NINJ=0$.</i>
44	NDC(I), ELDCO(I), NPTDC(I)	
45	ELDCX(I,L), CRDCX(I,L)	
46	NACTIV(I), N2DCALCC(I), NSMP(I), ABMATC(I), XWID2DC(I), XLEN2DC(I), RINOTC(I)	Lines 46-49 are repeated NUMNOD times.
47	IFLGA(I), DXNODE(I), RAD(I), ARC(I), ELO(I)	
48	TMELTIC(I)	Initial melt temperature at I-th node. If $NACTIV(I)=0$, this line and Line 49 are omitted.
49	YC(I,K), ZC(I,K), ZBC(I,K)	Initial mass of K-th debris constituent at I-th node in melt, crust, and particle bed regions, respectively. This Line is repeated 22 times for $8 \leq K \leq 29$; see Table 3-3 for constituent nomenclature.
50	NVELP, NITMAXW, DAVMXW, DVMXW	
51	NENMXW, DEAVMXW, DEMXW	
52	TIMEO, DTIME, TMAX	
53	TSTRTI	
54	NPRINT, NPLOT	
55	I, NPRT(I),NPLT(I), ABXLIMC(I), ABRLIMC(I)	This line is repeated NUMNOD times.
56	NTIMSPC	
57	TIMSPC(I)	This line is repeated NTIMSPC times.

Table 3-2. CORQUENCH4.1 Input Variable Descriptions for ‘quenchin.dat.’ [Note: unless noted, input is in SI units; m, kg, s, K].

Line No.	Variable Name(s)	Definition/Function
1	TITLE	70 Character string title for the calculation; written as a header to the output file ‘quenchout.dat.’
2	TCNOT	Initial concrete temperature; used in the evaluation of the concrete decomposition specific enthalpy.
3	ICTC	Set ICTC=1 for default limestone/common sand concrete, ICTC=2 for default siliceous concrete, ICTC=3 for default limestone/limestone concrete, or ICTC=4 for a user specified concrete composition. <i>Note: If ICTC =4, then the basemat can consist of a single layer, or multiple layers with variable composition from layer to layer (see NCOMP definition below).</i>
	NCOMP	If ICTC=4, then set NCOMP equal to the number of distinct layers into which the basemat is subdivided. If $ICTC \leq 3$, then the settings of NCOMP, TCSL(I), and TCLL(I) are arbitrary. <i>Note 1: Only set NCOMP > 1 if a 1-D axial ablation calculation is being performed, since the code reassigns all concrete data as new basemat layers are entered based on the axial ablation depth alone.</i> <i>Note 2: Multi-layer basemat modeling option (i.e. NCOMP>1) is only available if NUMNOD=1.</i>
	NABBL	Set NABBL=0 for quasi-steady concrete decomposition model, NABBL=1 for concrete dryout model that is initiated with a fully developed thermal boundary layer with no surface crust present and the surface temperature is initially at the concrete decomposition temperature, or NABBL=2 for the concrete dryout model that considers formation of a surface crust and the surface temperature is initially at TCNOT.
	NUMNOD	Set NUMNOD equal to the number of MCCI nodes to be analyzed simultaneously. <i>Note: NUMNOD is capped at 199.</i>
	NMIX	Parameter controlling internodal heat and mass transfer for cases in which NUMNOD>1. These models have not been fully validated in the current code version. Set NMIX=0 to bypass this option (if not, the code does this automatically).
4	NABLB	Parameter controlling axial core-concrete boundary condition modeling if detailed (NABBL=2) modeling option is chosen. Set NABLB=0 to recover the normal fully developed (NABBL=1) concrete dryout model while maintaining this Line in the input file, set NABLB=1 for transient surface growth in which the crust is assumed to be porous allowing slag to drain through to the overlying melt once ablation begins, or set NABLB=2 for crust growth with slag retained as a film beneath the crust.
	NFAILB	Parameter controlling bottom crust failure criterion. Set NFAILB=1 if the crust fails after thinning to a user-specified thickness (DCFAILB; see below); set NFAILB=2 if crust fails after thinning to the point that the crust is no longer stable under the applied load of the melt head; or set NFAILB=3 if crust fails at a user-specified time (TIMEFB; see below).
	NBCB	Parameter controlling bottom crust freezing temperature assumption. Set NBCB=1 to calculate the freezing temperature based on melt composition, or set NBCB=2 to calculate based on crust composition. <i>Note: Setting is irrelevant if NABLB=0.</i>
	CFAILB	When NFAILB=2, this is the empirical constant in the bottom crust failure pressure head correlation (see Line 30 for appropriate settings of this parameter based on various geometry and failure mode modeling assumptions).
	DCFAILB	When NFAILB=1, this is the user-specified minimum bottom crust thickness at failure.
	TIMEFB	When NFAILB=3, this is the user-specified time at bottom crust failure.

Table 3-2 (contd.). CORQUENCH4.1 Input Variable Descriptions for ‘quenchin.dat.’

Line No.	Variable Name(s)	Definition/Function
5	NABLS	Parameter that controls side (radial) core-concrete boundary condition modeling if detailed (NABBL=2) modeling option is chosen. If N2DCALC=2, then set NABLS=0 to recover the normal fully developed (NABBL=1) concrete dryout model (while maintaining this line in the input file), set NABLS=1 for transient surface crust growth in which the crust is assumed to be porous thus allowing slag to drain through to the adjacent melt once ablation begins, or set NABLB=2 for crust growth with the slag retained as a film beneath the crust. <i>Note: If N2DCALC=1 (i.e., 1-D calculation is being performed), then settings on this line are arbitrary.</i>
	NFAILS	Parameter controlling side crust failure (disappearance) criterion. Set NFAILS=1 if the crust fails after thinning to a user-specified thickness (DCFAILS; see below); set NFAILS=2 if crust fails after thinning to the point that the crust is no longer mechanically stable under the applied load of the melt head; or set NFAILS=3 if crust fails after a user-specified time (TIMEFS; see below).
	NBCS	Parameter controlling side crust freezing temperature assumption. Set NBCS=1 to calculate the freezing temperature based on melt composition, or set NBCS=2 to calculate based on crust composition. <i>Note: Setting is irrelevant if NABLS=0.</i>
	CFAILS	When NFAILS=2, this is the empirical constant in the side crust failure pressure head correlation (see Line 30 for appropriate settings of this parameter based on various geometry and failure mode modeling assumptions).
	DCFAILS	When NFAILS=1, this is the user-specified minimum side crust thickness at failure.
	TIMEFS	When NFAILS=3, this is the user-specified time at side crust failure.
6	TCSL(I), TCLL(I)	When ICTC=4, these are the concrete solidus and liquidus temperatures, respectively, for I-th basemat layer, starting from the top and moving down. If ICTC<4, supply values here, but they are ignored. Instead, the concrete solidus/liquidus temperatures are internally set within the code to 1393/1568 K for limestone/common sand concrete (ICTC=1), 1403/1523 K for siliceous concrete (ICTC=2), or 1495/2577 K for limestone/limestone concrete (ICTC=3). <i>Note 1: If ICTC < 4, Lines 7-11 are omitted.</i> <i>Note 2: If ICTC = 4, Lines 6-11 are repeated NCOMP times.</i> <i>Note 3: If ICTC < 4, then there is only one Line 6.</i>
	TDCL(I)	For any setting of ICTC, this is the user-specified concrete decomposition temperature for the I-th basemat layer, which must satisfy TCSL(I)<TDCL(I)<TCLL(I).
	XFLH2O(I), XFLCO2(I)	For any setting of ICTC, these are the respective decimal fractions of H ₂ O and CO ₂ concrete decomposition gases which migrate upwards through the melt pool from the I-th basemat layer; the balance of the decomposition gas is assumed to be lost from the system (this option was provided to examine experiment behavior).
	DEPTHL(I)	Thickness of the I-th basemat layer; setting is arbitrary if ICTC≤3 or NCOMP=1.

Table 3-2 (contd.). CORQUENCH4.1 Input Variable Descriptions for ‘quenchin.dat.’

Line No.	Variable Name(s)	Definition/Function
7	XWTC(I,1) – XWTC(I,4)	Weight % CO ₂ , H ₂ O, K ₂ O, and Na ₂ O, respectively, in I-th concrete layer. Note: Lines 7-11 omitted if ICTC<4.
8	XWTC(I,5) – XWTC(I,8)	Weight % TiO ₂ , SiO ₂ , CaO, and MgO, respectively, in I-th concrete layer. Note: Lines 7-11 omitted if ICTC<4.
9	XWTC(I,9) – XWTC(I,12)	Weight % Al ₂ O ₃ , FeO, Fe ₂ O ₃ , and Fe ₃ O ₄ , respectively, in I-th concrete layer. Note: Lines 7-11 omitted if ICTC<4.
10	XWTC(I,13) – XWTC(I,16)	Weight % Fe, Cr, Ni, and Zr, respectively, in I-th concrete layer. Note: Lines 7-11 omitted if ICTC<4.
11	XWTC(I,17) – XWTC(I,18)	Weight % ZrO ₂ and B ₂ O ₃ , respectively, in I-th concrete layer. Note: Lines 7-11 omitted if ICTC<4.
12	TFWS, TFWL	Concrete decomposition temperature range for dryout of free water; typical values are 417/437 K.
13	TBWS, TBWL	Concrete decomposition temperature range for dryout of bound water in Ca(OH) ₂ (typical values are 853/873 K.
14	TMCAS, TMCAL	Concrete decomposition temperature range for dryout of CO ₂ bound in MgCa(CO ₃) ₂ ; typical values are 1033/1053 K.
15	TCAS, TCAL	Concrete decomposition temperature range for dryout of CO ₂ bound in CaCO ₃ ; typical values are 1172/1192 K.
16	IPHASE	Parameter controlling the phase diagram calculation. Set IPHASE=1 to use the ANL (i.e., Roche et al.) data for fully oxidized core melt containing limestone/common sand concrete, set IPHASE=2 to use the Roche data for corium containing siliceous concrete, set IPHASE=3 to use the Roche data for corium containing limestone/limestone concrete, or set IPHASE=4 to utilize a user-specified oxide phase diagram. <i>Note: If IPHASE ≤ 3, Lines 17-20 are omitted.</i>
	IEUTEC	Set IEUTEC=0 if unoxidized Zr is assumed to exist in the metal phase from the oxide, or set IEUTEC=1 if Zr is assumed to be soluble in the oxide. This parameter only affects the evaluation of corium thermo-physical properties.
	NSOLID	Set NSOLID=1 to evaluate the oxide phase solid fraction from the phase diagram for the particular melt composition, or set NSOLID=2 to evaluate the solid fraction based on the assumption that the solid fraction varies linearly between the oxide phase solidus and liquidus.
17	NSOLP	If IPHASE=4 (i.e., user-specified oxide phase diagram), then NSOLP equals the total number of points in the interpolation table for the oxide-phase solidus versus wt % concrete in the melt.
18	XWTSOL(I), FSOLP(I)	I-th point in the interpolation table for the oxide solidus vs. wt % concrete in the melt, 1≤I≤NSOLP. <i>Note: Line 18 is repeated NSOLP times.</i>
19	NLIQP	NLIQP is the number of points in the oxide-phase liquidus interpolation table vs. wt % concrete in the melt.
20	XWTLIQ(I), FLIQP(I)	I-th point in the interpolation table for the oxide liquidus vs. wt % concrete in the melt, 1≤I≤NLIQP. <i>Note: Line 20 is repeated NSOLP times.</i>

Table 3-2 (contd.). CORQUENCH4.1 Input Variable Descriptions for ‘quenchin.dat.’

Line No.	Variable Name(s)	Definition/Function
21	NPOURS	Number of time intervals into which the RPV pour is subdivided. If NPOURS=0, then the mass flowrate of corium relocating from the vessel into the MCCI zone is assumed to equal zero over the computed time domain. <i>Note: If NPOURS=0, Lines 22-24 are omitted. If NPOURS>0, Lines 22-24 are repeated NPOURS times.</i>
22	TST(I), TSTOP(I)	I-th pour interval start and stop times, respectively.
	AINTP(I), BINTP(I)	Melt temperature coefficients for the relocating corium over the pour interval. Melt temperature may vary linearly; i.e., $T_{melt} = AINTP(I) + BINTP(I) \cdot (t - TST(I))$
23	NISTP	Total number of corium constituents (1-22) draining from the RPV in the I-th pour interval.
24	IT, APOUR(IT,I), BPOUR(IT,I)	Pour rate coefficients for IT-th melt constituent; the pour rate for each constituent can vary linearly; i.e., $Rate = APOUR(IT,I) + BPOUR(IT,I) \cdot (t - TST(I))$
	SIGYCR	Crust structural yield strength; this parameter is only important if the crust anchoring computational option is selected (i.e., NUSGAP=1; see Line 30 description below).
	FRZFR	Solid fraction at which “freezing” is assumed to occur in the crust; parameter is included to mock up “mushy zone behavior.” Set FRZFR=1 to use the oxide-phase solidus temperature as the crust freezing temperature, or set FRZFR=0 to use the oxide liquidus. Set $0 < FRZFR < 1$ to interpolate the freezing temperature from the temperature/solid fraction relationship assumed for the calculation (see NSOLID definition in Line 16).
26	NINGRS	If water is added during the calculation (i.e., NADD>0; see Line 39), then set NINGRS=0 if the crust is considered impervious with respect to water ingress; set NINGRS=1 if water ingress into a growing crust of user-specified permeability is to be calculated; or set NINGRS=2 if water ingress into a growing crust is calculated, with the time (composition) dependent crust dryout limit calculated with the Lister/Epstein model.
	PERM	Crust permeability (m^2) when water ingress into a growing crust is to be calculated (i.e., NADD>0 and NINGRS=1). If NINGRS = 0 or 2, then the setting of PERM is arbitrary.
	CINGRES	Empirical constant in the ANL dryout heat flux model; if NINGRS=0 or 1, then the setting of CINGRES is arbitrary.
	CHFMULT	With water present, CHFMULT is a CHF multiplier used as one criterion for determining if when film boiling breaks down with a stable crust present; i.e., if the debris-water heat flux falls below $CHFMULT \cdot q_{CHF}$, then transition to nucleate boiling occurs. This criterion is used in conjunction with the Henry minimum film boiling point model to determine when film boiling breaks down. Set CHFMULT=0 to use only the Henry correlation.
	CCRIT	With water present, CCRIT is a CHF multiplier used as one criterion for determining when bulk cooling breaks down; i.e., if the debris-water heat flux falls below $CCRIT \cdot q_{CHF}$, then a stable crust growth calculation is initiated. This criterion is used in conjunction with the critical superficial gas velocity criterion for determining when stable crust formation occurs. Set CCRIT=0 to use only the minimum gas velocity correlation.

Table 3-2 (contd.). CORQUENCH4.1 Input Variable Descriptions for ‘quenchin.dat.’

Line No.	Variable Name(s)	Definition/Function
27	NENTR	If water is added during the calculation (i.e., NADD>0; see Line 39), set NENTR=0 if the crust is considered impervious with respect to melt eruptions; set NENTR=1 if eruptions with subsequent particle bed formation is calculated using a constant, user-specified, melt entrainment coefficient; set NENTR=2 if eruptions/bed formation is calculated using the Ricou-Spalding entrainment rate correlation; or set NENTR=3 if eruptions/bed formation is calculated using the ANL mechanistic model for melt eruptions that is based on single-phase flow. <i>Note: If NENTR=0, the settings of the four parameters below are arbitrary.</i>
	ENSPEC	When NENTR=1, ENSPEC is the user-specified <i>fractional</i> melt entrainment coefficient.
	ENRICO	When NENTR=2, ENRICO is the empirical constant multiplier in the Ricou-Spalding correlation ($0.06 \leq \text{ENRICO} \leq 0.12$, with ENRICO=0.10 typically used).
	DBED	If NENTR>0, DBED is the (assumed uniform) particle diameter in the debris bed. This is used in the evaluation of the bed dryout heat flux with Lipinski’s model.
	POROSBED	If NENTR>0, POROSBED is the particle bed porosity used to evaluate the bed dryout heat flux with Lipinski’s model.
28	NVISC	Set NVISC=1 to use the Ishii-Zuber correlation for viscosity enhancement due to buildup of solids in the melt, or set NVISC=2 to use the Kunitz solid-phase viscosity enhancement factor.
	ALPMAX	ALPMAX is the maximum solid fraction in the melt (i.e., viscosity $\rightarrow \infty$ as solid fraction \rightarrow ALPMAX).
29	NKSPEC	Set NKSPEC=0 to evaluate the top crust thermal conductivity using the property subroutines currently implemented in the code, or set NKSPEC=1 if the crust thermal conductivity is user-specified.
	FKS	If NKSPEC=1, FKS is the user-specified crust thermal conductivity.
30	NUSGAP	When water is added (NADD>0), set NUSGAP=0 if the top crust always floats atop the melt, or set NUSGAP=1 if crust anchoring and gap formation between the melt and crust is to be calculated if the crust thickness exceeds the minimum required to be mechanically stable in the test section span under the applied loads of the crust and particle bed weights; or set NUSGAP=2 to calculate the previous case but with the overlying water head included in the applied load evaluation.
	NBUBSP	If crust anchoring & gap formation could occur, then set NBUBSP=0 if the crust is considered separated when the separation distance exceeds zero, or set NBUBSP=1 if the crust is considered separated when the distance exceeds the sparging gas bubble radius. This option accounts for melt surface roughness in the evaluation of the separation time.
	CCRGAP	Constant relating the test section area and crust yield strength (SIGYCR; see Line 30) to the minimum crust depth for structural stability in the given cavity span through the equation: Applied Load = CCRGAP•SIGYCR•(Crust Thickness) ² . For reference, values of CCRGAP for various modeling assumptions under a uniform load are as follows: Circular plate, simply supported edges: CCRGAP=4.71 for ductile failure, or CCRGAP=2.53 for brittle failure. Circular plate, fixed edges: CCRGAP=8.84 for ductile failure, or CCRGAP=4.18 for brittle failure. Square plate, supported edges: CCRGAP=5.48 for ductile failure.

Table 3-2 (contd.). CORQUENCH4.1 Input Variable Descriptions for ‘quenchin.dat.’

Line No.	Variable Name(s)	Definition/Function
31	NBUBRS	Set NBUBRS=0 to use the Taylor instability model for sparging gas bubble diameter and the inviscid flow solution for terminal rise velocity, or set NBUBRS=1 to include an ANL viscous flow model in the gas bubble diameter evaluation (i.e., $D_{bub} = \text{AMAX1}(D_{inviscid}, D_{viscous})$), along with the Peebles-Garber correlation for the bubble terminal rise velocity.
32	NCHEM	Set NCHEM=0 if condensed phase chemical reactions between metallic Zr and SiO ₂ are to be neglected, or set NCHEM=1 if these reactions are to be calculated.
33	NBOTBC	Set NBOTBC=1 if the axial melt/concrete interfacial heat transfer coefficient is to be calculated with Bradley’s modification to Malenkov-Kutateladze correlation; set NBOTBC=2 to use the CORCON gas film model; set NBOTBC=3 to use the CORCON gas film model with a transition to the Bradley model if the gas velocity falls below the Berenson modified gas sparging limit for film collapse (see XMULTBR below); or set NBOTBC=4 to use the Sevon axial heat transfer correlation. <i>Note: Gas film modeling options (i.e. NBOTBC=2 or 3) should not be used if NABBL=2 in Line 3 as this model its own unique quasi-steady crust model.</i>
	NSIDEBC	Set NSIDEBC=1 if the radial melt/concrete interfacial heat transfer coefficient is calculated with Bradley’s modification to Malenkov-Kutateladze correlation; set NSIDEBC=2 to use the CORCON gas film model based on an average film thickness; set NSIDEBC=3 to use the Sevon radial heat transfer correlation for limestone/common; or set NSIDEBC=4 to use the Sevon correlation for siliceous concrete. <i>Note: Gas film modeling option (i.e. NSIDEBC=2) should not be used if NABBL=2 in Line 3 as this model has its own unique quasi-steady crust model.</i>
	NVOID	Set NVOID=1 if the melt void fraction is evaluated with Brockmann’s correlation, set NVOID=2 if void fraction is evaluated with the Wallis correlation, or set NVOID=3 if void fraction is evaluated with the Kataoka-Ishii correlation.
	XMULTBR	Set XMULTBR to the Berenson minimum gas velocity multiplier for film collapse; see NBOTBC description above.
	XBMULT	Empirical multiplier for user manipulation of bottom heat transfer coefficient; set XBMULT=1.0 to maintain the user-specified correlation (viz. setting of NBOTBC) without modification.
	XSMULT	Empirical multiplier for user manipulation of sidewall heat transfer coefficient; set XSMULT=1.0 to maintain the user-specified correlation (viz. setting of NSIDEBC) without modification.

Table 3-2 (contd.). CORQUENCH4.1 Input Variable Descriptions for ‘quenchin.dat.’

Line No.	Variable Name(s)	Definition/Function
34	NDEC	<p>If NDEC=1 the melt decay heat <i>density</i> is evaluated as P_{melt} (W/kg UO₂) using the ANSI/ANS-5.1-1994 decay heat function for thermal fission of U-235. In this case the decay in the crust and particle bed regions are calculated from $P_{\text{crust}} = \text{CON1} \cdot P_{\text{melt}}$ and $P_{\text{bed}} = \text{CON2} \cdot P_{\text{melt}}$, respectively.</p> <p>If NDEC=2 the <i>gross</i> (melt+crust+bed) decay heat level (W) is evaluated from user-supplied data (see Line 36). In this case, the decay heat delivered to the melt, crust, and particle bed zones are evaluated as $P_{\text{melt}} = (1 - \text{CON1} - \text{CON2}) \cdot P$, $P_{\text{crust}} = \text{CON1} \cdot P$, and $P_{\text{bed}} = \text{CON2} \cdot P$, respectively, where P is power interpolated from user-supplied data.</p> <p>If NDEC=3 the melt specific power <i>density</i> (W/kg UO₂) is evaluated from user-supplied data (see Line 36). In this case, the power <i>densities</i> in crust and particle bed zones are evaluated in the same manner as for the case NDEC=2.</p> <p>Note 1: If NDEC=1, then ‘time zero’ defined in Line 52 should correspond to the time of reactor scram.</p> <p>Note 2: Gross input power modeling assumption (i.e. NDEC=2) is not available when NUMNOD>1.</p>
	NPOINT	<p>If NDEC ≥ 2, NPOINT equals the number of points in the user-supplied decay heat interpolation table.</p> <p>Note: If NDEC=1, the setting of NPOINT is arbitrary.</p>
35	CON1, CON2	Constants used in the evaluation of the decay heat in the crust and particle bed zones; see NDEC definition in Line 34.
	PCORE, XMFUEL	<p>For the case in which NDEC = 1, this is the core thermal power level (W) and the fuel mass (kg UO₂) in the core. These two parameters are used to calculate the fuel power density (i.e. PCORE/XMFUEL) prior to scram. If you would rather specify power density, then set PCORE to the desired power density and XMFUEL=1.0 kg.</p> <p>Note: settings are irrelevant if NDEC≠1</p>
	FRACFP	Fraction of decay heat left in the core debris involved in the MCCI; i.e., this parameter can be used to account for the effect of the loss of volatile fission products from the melt earlier in the accident sequence if desired. Set FRACFP=1 to bypass and assume all decay heat is deposited in the core debris involved in the MCCI.
	TEFPD	Total number of <i>days</i> for which the core is at full power before the accident is initiated
36	TDEC(I), DEC(I)	If NDEC > 2, this is the I-th point in the user-supplied decay heat power level (DEC) versus time (TDEC) table; 1 < I < NPOINT. Note: If NDEC = 1, this line is omitted.
37	NPRES	Logic control parameter for system pressure. Set NPRES=1 if pressure is constant at PDRYWL over the course of the calculation. Set NPRES>1 if pressure is calculated from a user-supplied time-pressure interpolation table (see Line 38); in this case, NPRES is set equal to the number of points in that table (2 minimum)
	PDRYWL	Cavity absolute pressure (MPa). Note: Setting of this parameter is irrelevant if NPRES>1.
	EDRYWL	Cavity radiation emissivity.
	TSTRUC	Temperature of upper cavity structure. This temperature is used as the overlying radiation temperature boundary condition when the cavity is dry.
38	TPRES(I), PPRES(I)	User-supplied interpolation table if NPRES>1; if NPRES=1, this line is omitted. If NPRES>1, then there are NPRES points provided.

Table 3-2 (contd.). CORQUENCH4.1 Input Variable Descriptions for ‘quenchin.dat.’

Line No.	Variable Name(s)	Definition/Function
39	NADD	Parameter which controls water addition during the calculation. Set NADD=0 if the cavity remains dry. Set NADD=1 if saturated water is maintained over the MCCI after time TADD. Set NADD=2 if saturated water is maintained over the MCCI after an ablation depth of DEPAB is reached. Set NADD=3 if a detailed water inventory model is used with heatup, boiloff, injection, spillover, and spreading between nodes. Injection and spillover are modeled with NINJ and NDOWNC parameters. <i>Note: If $NADD \leq 2$, (i.e., cavity remains dry or a simple cavity flooding model is invoked), Lines 40-45 are omitted from the input file.</i>
	TADD	If NADD=1, this is the time when the cavity is filled to a uniform water depth of HDOWNC at T_{sat} .
	DEPAB	If NADD=2, this is the axial ablation depth (at any node in the mesh if NUMNOD>1) at which the cavity is filled to a uniform water depth of HDOWNC at T_{sat} .
	HDOWNC	If NADD=1 or 2, this is the uniform water fill depth in the cavity.
	TWATI	If NADD=3, this is the initial temperature of the water inventory on the cavity floor.
	ELWATI	If NADD=3, this is the initial depth of the water inventory on the cavity floor.
40	NINJ	Number of water injection sources if detailed water inventory model is selected (NADD=3). <i>Note: Lines 41-42 are omitted if NINJ=0.</i>
41	NISTR(J), NISTP(J), NPTINJ(I)	For the I-th injection source, NISTR(I)-NISTP(I) node range over which injection is occurring, and NPTINJ(I) = number of points in the water injection flowrate and temperature interpolation tables at this location (see Line 42). <i>Note: The injection sources should not spatially overlap. If they do, then the regions where they do overlap should be combined and input as a distinct, new water injection source.</i>
42	TIMINJ(I,L), XDTINJ(I,L), TDTINJ(I,L)	For injection in node range NISTR(I)-NISTP(I), these are the L-th time, mass flowrate (kg/sec), and temperature points, respectively, for interpolation of injection flowrate and temperature given the current time, $1 \leq L \leq NPTINJ(I)$. The flow is assumed to be uniformly distributed (based on an area weighting) over this range of nodes.
43	NDOWNC	Number of nodes from which water can spillover and be lost from the calculation if the water depth reaches a user-defined height (see below). <i>Note: Lines 44-45 are omitted if NINJ=0.</i>
44	NDC(I), ELDCO(I), NPTDC(I)	For I-th spillover point, NDC(I) = node at which spillover can occur; ELDCO(I) is the lowest elevation at which spillover can begin, and NPTDC(I) is the number of interpolation points in the cord length function that is used to calculate spillover area as a function of water height above elevation ELDCO(I).

Table 3-2 (contd.). CORQUENCH4.1 Input Variable Descriptions for ‘quenchin.dat.’

Line No.	Variable Name(s)	Definition/Function
45	ELDCX(I,L), CRDCX(I,L)	For the spillover point at node NDC(I), these are the L-th elevation (m) and cord length (m) points, respectively, for interpolation of cord length available for spillover at this location; $1 \leq L \leq \text{NDC}(I)$. Note 1: the elevation points ELDCX(I,L) are input as absolute relative to the initial floor level elevation. Note 2: At least two points are required [i.e. $\text{NPTDC}(I) \geq 2$ on Line 44] Note 3: The ‘cord length’ CRDCX(I) is defined such that the water height above the spillover inlet multiplied by the interpolated cord length equals the water flow area into the downcomer. For example, if the downcomer is a circular pipe with a horizontal opening, then the cord length is simply the pipe circumference.
46	NACTIV(I)	For the I-th node, set NACTIV(I) = 0 if the node is inactive (i.e. inert, without melt present), or set NACTIV(I) = 1 if this is an active MCCI node. This parameter allows inert node volumes to exist in the mesh that can harbor water if the detailed (NADD = 3) water inventory model is selected. Note 1: if NUMNOD=1, then NACTIV(I) must be set to 1; Note 2: Lines 46-49 are repeated NUMNOD times.
	N2DCALCC(I)	For the I-th node, set N2DCALCC(I) = 1 to perform a 1-D (axial) basemat erosion calculation, N2DCALCC(I) = 2 to perform a 2-D (axial plus radial; right cylinder geometry assumed) erosion calculation, set N2DCALCC(I) = 3 to perform a 2-D notch-geometry calculation with two opposing, ablating walls, set N2DCALCC(I)=4 to perform a 2-D notch-geometry calculation with one wall ablating and the other inert, or set N2DCALCC(I)=5 to perform a 2-D cylindrical annulus calculation with the inner radius fixed and the outer wall ablating.
	NSMP(I)	For the I-th node, set NSMP(I) = 0 if the node is not considered to be a sump with a pre-existing elevation difference between adjacent node(s) that could limit sidewall ablation area relative to the pool height available for ablation. For instance, if the melt pool surface elevation at the node is greater than the sump depth, then sidewall ablation area is limited by the sump wall height as opposed to depth. If the node is considered to be a sump, then set NSMP(I) = 1 if the melt surface elevation is to be compared to the concrete elevation of the node to the right (i.e. I + 1) to determine the controlling sidewall height, or set NSMP(I) = 2 if the comparison is made to the node to the left (i.e. I - 1). Finally, if N2DCALCC(I) = 3, then set NSMP(I) = 3 if both left and right walls are compared.
	ABMATC(I)	Initial basemat axial surface area in contact with melt at I-th node.
	XWID2DC(I), XLEN2DC(I)	When N2DCALCC(I) = 3 or 4, these are the rectilinear dimensions of the basemat; XLEN2DC(I) is the initial distance between the ablating concrete walls, while XWID2DC(I) is the width between the adiabatic wall(s).
	RINOTC(I)	When N2DCALCC(I) = 5, this is the inner radius of the cylindrical annulus that is fixed over the calculation.

Table 3-2 (contd.). CORQUENCH4.1 Input Variable Descriptions for ‘quenchin.dat.’

Line No.	Variable Name(s)	Definition/Function
47	IFLGA(I)	Parameter specifying if the I-th node cell is a receptor of melt relocating from the RPV during the calculation. Set IFLAG(I) = 0 if it is not a receptor, or = 1 if it is a receptor. The setting is irrelevant if NPOURS=0 (see Line 21).
	DXNODE(I)	When NADD = 3 (detailed water inventory model selected), this is the overall length of the node parallel to the flow direction. Value is arbitrary if NADD < 3.
	RAD(I)	When NADD = 3, this is the radial location (i.e. distance along spreading path) within the cell at which the node is located; i.e., the node does not have to be cell-centered. Value is arbitrary if NADD < 3.
	ARC(I)	When NADD = 3, this is the arc length available for water spreading between the I-th and I+1 nodes. The arc length times water height determines the flow area for relocation between nodes. Value is arbitrary if NADD<3.
	ELO(I)	Regardless of the setting of NADD, this is the initial concrete surface elevation for the I-th node.
48	TMELTIC(I)	Initial melt temperature at I-th node.
49	YC(I,K), ZC(I,K), ZBC(I,K)	For I-th node, this is the initial mass of K-th corium constituent in melt, crust, and particle bed regions, respectively (8 ≤ K ≤ 29; see Table 3-3).
50	NVELP, NITMAXW, DAVMXW, DVMXW	<p>If NADD = 3, then these are the numerical control parameters for the water velocity spreading model. Set NVELP = the number of subintervals into which the main CORQUENCH timestep (DTIME; see Line 51) is subdivided. Depending upon DTIME, a smaller timestep for the fluid mechanics calculation may be needed. Set NVELP ≥ 1. NITMAXW is the maximum number of attempts allowed for the water spreading model numerical scheme to meet the convergence criteria DAVMXW and DVMXW. DAVMXW is the maximum allowable average change in water spreading velocity between iterations across all nodes (m/s), while DVMXW is the maximum change in spreading velocity at any node (m/s).</p> <p><i>Note: Settings for these parameters are irrelevant if NADD<3; see Line 39.</i></p> <p><i>User Guidance: Typical settings for these parameters are 2, 5, 0.001 m/s and 0.005 m/s.</i></p>
51	NENMXW, DEAVMXW, DEMXW	<p>If NADD = 3, then these are the numerical control parameters for the water conservation of energy spreading model. NENMXW is the maximum number of attempts allowed for the conservation of energy equation to meet the convergence criteria DEAVMXW and DEMXW. DEAVMXW is the maximum allowable average change in water specific enthalpy between iterations across all nodes (J/kg), while DEMXW is the maximum change in specific enthalpy at any node (J/kg).</p> <p><i>Note: Settings for these parameters are irrelevant if NADD<3; see Line 39.</i></p> <p><i>User Guidance: Typical values for these parameters are 20, 300 J/kg, and 600 J/kg</i></p>
52	TIMEO	Start time for the calculation (seconds).
	DTIME	Calculation timestep (seconds)
	TMAX	Maximum time to which the calculation is to be performed (seconds), unless an axial or radial ablation limit is reached; see below.

Table 3-2 (contd.). CORQUENCH4.1 Input Variable Descriptions for ‘quenchin.dat.’

Line No.	Variable Name(s)	Definition/Function
53	TSTRTI	Time at which the evaluation of numerically integrated quantities (e.g., gross decay heat input, cumulative energy transfer to boundaries, cumulative gas release) is to be initiated.
54	NPRINT	Print frequency to text output file ‘quenchout.dat’; the data are printed every NPRINT timesteps.
	NPLOT	Print frequency to Excel-compatible plotting files; the data are written out every NPLOT timesteps. File definitions are provided in Lines 55-57 below.
55	I, NPRT(I),NPLT(I)	For the multi-nodal option (NUMNOD > 1), this line allows the user to select nodes at which detailed data are to be written to text and excel plotting files, respectively. This line is repeated NUMNOD times. For the I-th node, set NPRT(I) = 0 if the data for that node is not to be written to the text output file ‘quenchout.dat’, or set NPRT(I) = 1 if the data are to be written every NPRINT timesteps. All nodes for which NPRT (I) = 1 are sequentially written to the same file, quenchout.dat. Similarly, set NPLT(I) = 1 if a comprehensive time-dependent output file is to be written for the I-th node for input into the excel plotting package, or set NPLT(I) = 0 if this node is bypassed. If NPLT(I) = 1, then the data are written to a file denoted fort.lxxx, where xxx corresponds to the node number. For instance, for the 17-th node, the output file would be fort.1017, while for node 152, the file would be fort.1152. If NPLT(I)=1, a smaller file is written to fort.10xxx that contains most of the key thermalhydraulic data of interest for analysis (e.g. ablation profiles, melt temperature, zone masses/decay heat levels, energy balance data).
	ABAXLIM	Maximum allowable axial ablation; calculation terminated if this limit is reached.
	ABRDLIM	Maximum allowable radial ablation; calculation terminated if this limit is reached.
56	NTIMSPC	Set NTIMSPC equal to the number of times at which spatially dependent data (i.e., NUMNOD > 1) are to be written out.
57	TIMSPC(I)	These are the user-specified times (seconds) at which spatially dependent data are to be written to an individual output files denoted ‘fort,x’, where x=I is the sequential data file identifier for that particular time. For instance, for the 3 rd specified time at which data are to be written, the output file is denoted fort.3. This line is repeated NTIMSPC times, and there are NTIMSPC files created at the end of the run.

Table 3-3. Summary of Indicial Scheme for Melt/Concrete Interactions.

Index	Constituent	Notes
1	Ca(OH)_2	Decomposable Concrete Constituents
2	CaCO_3	
3	$\text{MgCa(CO}_3)_2$	
4	$\text{H}_2\text{O (liquid)}$	
5	$\text{H}_2\text{O (vapor)}$	
6	$\text{K}_2\text{O (solid)}$	
7	$\text{K}_2\text{O (vapor)}$	
8	Na_2O	Concrete & Corium Constituents
9	TiO_2	
10	SiO_2	
11	CaO	
12	MgO	
13	Al_2O_3	
14	FeO	
15	Fe_2O_3	
16	Fe_3O_4	
17	Fe	
18	Cr	
19	Ni	
20	Zr	
21	ZrO_2	
22	B_2O_3	
23	U	Corium Constituents
24	B_4C	
25	Si	
26	SiC	
27	Cr_2O_3	
28	NiO	
29	UO_2	

The code currently does not make timestep adjustments to meet a user-specified integration tolerance. Thus, for a particular case, a few different timesteps (see Line 52 in Tables 3-1 and 3-2) should be tried to verify that the solution has adequately converged. A one second timestep has been found to provide good convergence in most cases in which the quasi-steady concrete ablation model is used (i.e., NABBL=0). However, for situations in which concrete dryout models are selected (i.e., NABBL=1 or 2), then a smaller timestep is required to resolve the thermal boundary layer evolution early in the transient. A typical timestep for this case would be 0.1 seconds. If this timestep is too large, an error message will be written to the diagnostics file 'diag.dat' informing the user to this effect, and the run will terminate.

3.2 Input File Description

As described in Section 2, the overall approach for implementing a multi-nodal MCCI modeling capability in CORQUENCH4.1 is to make a common set of assumptions regarding concrete composition, modeling approaches for melt-concrete and melt-atmosphere heat transfer, and core debris thermo-physical modeling methods that are uniformly applied across all active nodes involved in the analysis. Local conditions that can be initialized include debris mass, composition, physical state (i.e., melt, crust, and particle bed), and temperature; initial node dimensions and ablation characteristics (i.e., 1-D or 2-D); and spatial orientation of nodes with respect to each other. This latter information is required when the detailed water inventory model is invoked so that water relocation between nodes can be calculated. The input file (Table 3-2) is structured to reflect these variations in the types of information that are required to carry out an integrated simulation, and are described in greater detail below.

The first line in the input file is a 70-character string 'TITLE' that is written as a header to the ASCII output file 'quenchout.dat'; this provides the user the opportunity for labeling output files if needed. The second line defines the variable 'TCNOT' which is the initial concrete temperature used in the evaluation of the concrete decomposition specific enthalpy. Lines 3 through 15 define the overall concrete decomposition modeling assumptions and concrete content(s) to be used at each node in the calculation. The number of nodes, NUMNOD, is set in line 3 (NUMNOD \geq 1). Note that additional data regarding the node geometries is specified later in the input file (i.e., Lines 46-47). Also in Line 3, set ICTC=1, 2, or 3 to select the default limestone/common sand concrete, siliceous concrete, or limestone/limestone concrete types (see Table 3-4), respectively, or set ICTC=4 to input a user-specified composition. If ICTC=4, then the basemat can consist of a single layer, or multiple layers with variable composition from layer to layer. However, note that the multi-layer basemat option can only be exercised when a single node (NUMNOD=1) analysis is being performed. If ICTC=4, then set NCOMP equal to the number of distinct layers into which the basemat is subdivided (NCOMP \leq 100; see Section 3.2). If ICTC \leq 3, then the settings of NCOMP and the user-specified concrete solidus and liquidus temperatures (TCSL(I), and TCLL(I); see Line 6) are arbitrary, since the default data are used (see Table 3-5). Further note that the composite basemat model (NCOMP $>$ 1) should only be used if a 1-D axial ablation calculation is being performed, since the code reassigns all concrete data as new basemat layers are entered based on the axial ablation depth alone. The parameter NABBL controls the type of concrete ablation model that is employed. Set NABBL=0 to use the quasi-steady concrete decomposition model (Section 2.3.1); set NABBL=1 to use the concrete dryout model that is initiated with a fully developed thermal boundary layer with no surface crust present and the surface temperature is initially at the concrete decomposition temperature (see Section

2.3.2); or set NABBL=2 to use the concrete dryout model that considers formation of a surface crust and the surface temperature is initially at TCNOT (see Section 2.3.3).

Table 3-4. Default Concrete Breakdowns in Terms of Simple Oxides.^[76-77]

Constituent	Limestone-Common Sand		Siliceous		Limestone-Limestone	
	Weight %	Mole %	Weight %	Mole %	Weight %	Mole %
SiO ₂	28.8	22.8	69.7	60.7	7.0	5.2
CaO	26.4	22.4	13.7	12.8	42.4	34.0
Al ₂ O ₃	3.6	1.7	4.0	2.1	1.9	0.8
K ₂ O	0.6	0.3	1.4	0.8	0.4	0.2
Fe ₂ O ₃	1.6	0.5	1.0	0.3	0.8	0.2
TiO ₂	0.1	0.1	0.8	0.5	0.1	0.1
MgO	9.8	11.6	0.7	0.9	7.3	8.2
Na ₂ O	1.1	0.8	0.7	0.6	0.0	0.0
H ₂ O	6.2	16.4	6.91	20.0	6.9	17.3
CO ₂	21.8	23.4	1.00	1.2	33.2	34.0

Table 3-5. Solidus and Liquidus Temperatures for Several Concrete Types.^[78]

Temperature	Concrete Type		
	Limestone/common sand	Siliceous	Limestone-limestone
Solidus (K)	1393	1403	1495
Liquidus (K)	1568	1523	2577

Lines 4 and 5 control the general axial and radial modeling assumptions at the core-concrete interface when the transient concrete dryout model is used (NABBL=2). The modeling options are identical on both surfaces, and so only the input for the axial case (Line 4) is described. If the user wants to use the fully-developed concrete dryout model (NABBL=1) while maintaining Line 4 in the input file, then set NABLB=0. Conversely, set NABLB=1 to invoke the transient surface crust growth model for the case in which the crust is assumed to be porous so that slag continuously drains through the crust to the overlying melt pool once ablation begins. Finally, set NABLB=2 to invoke the crust growth model in which the slag is retained as a film beneath the crust. For cases in which NABLB>0, the parameter NFAILB controls the bottom surface crust failure (disappearance) criterion. Set NFAILB=1 if the crust fails after thinning to a user-specified thickness DCFAILB; set NFAILB=2 if the crust fails after thinning to the point that the crust is no longer mechanically stable under the applied load of the melt (Eq. 2-68); or set NFAILB=3 if the crust fails after a user-specified time TIMEFB. If NFAILB=2, then CFAILB is used as the empirical constant in the bottom crust failure pressure head correlation that is defined in Eq. 2-68. See the discussion below regarding Line 30 of the input file (i.e. CCRGAP definition) for appropriate settings of this constant based on various geometry and failure mode modeling assumptions. Finally, the parameter NBCB in Line 4 controls the bottom crust freezing temperature assumption used in the calculation; i.e., set NBCB=1 to calculate the freezing temperature based on the melt composition, or set NBCB=2 to calculate this temperature based on the crust composition.

Line 6 of the input file defines six additional parameters that are required to further characterize the decomposition properties of the Ith layer of the concrete basemat, starting from the top and moving downward. The concrete solidus, liquidus, and decomposition temperatures

(TCSL(I), TCLL(I), and TDCL(I)) are first defined. Regardless of the setting of ICTC, the user must input values for all three of these parameters, but if $ICTC < 4$, only the decomposition temperature TDCL(I) is used as the solidus and liquidus points are overwritten using the experimentally measured values for the selected default concrete type (see Table 3-5). Note that the decomposition temperature should satisfy $TCSL(I) \leq TDCL(I) \leq TCLL(I)$. In addition, for any setting of ICTC, XFLH₂O(I) and XFLCO₂(I) are the decimal fractions of H₂O and CO₂ concrete decomposition gases, respectively, that are assumed to migrate upwards through the melt pool from the Ith basemat layer; the balance of the decomposition gases is assumed to be lost from the system. (This option was provided to mock up experiments in which some of the decomposition gas escaped from the bottom of the test crucible). The parameter DEPTH_L(I) defines the thickness (or depth) of the Ith basemat layer; if $ICTC \leq 3$ or NCOMP=1 the setting of this parameter is arbitrary.

If $ICTC=4$, then lines 7-11 define the user-specified concrete composition (wt %) for CO₂, H₂O, K₂O, Na₂O (on Line 7); TiO₂, SiO₂, CaO, MgO (on Line 8); Al₂O₃, FeO, Fe₂O₃, Fe₃O₄ (on Line 9); Fe, Cr, Ni, Zr (on Line 10); and ZrO₂, and B₂O₃ (on Line 11). If $ICTC < 4$, this array is omitted from the input file. Conversely, if $ICTC=4$, then this array (along with line 6) is repeated NCOMP times.

Lines 12 through 15 respectively define the decomposition temperature ranges for the dryout of free water (H₂O; TFWS, TFWL), bound water in calcium hydroxide (Ca(OH)₂; TBWS, TBWL), CO₂ bound in dolomite (MgCa(CO₃)₂; TMCAS, TMCAL), and finally CO₂ bound in calcium carbonate (CaCO₃; TCAS, TCAL). Typical data are: i) free water: saturation temperature; ii) calcium hydroxide: 785 K, iii) calcium carbonate: 1098 K; and iv) dolomite: 1172 K. Onset and completion of these decomposition processes are typically assumed to occur over a 20 K temperature range.

Lines 16 through 20 control the phase diagram assumptions for the calculation (see Section A.1.2). In particular, set IPHASE=1 to use curve fits to the Roche et al.^[78] phase diagram data for a fully oxidized core melt composition containing limestone/common sand concrete, set IPHASE=2 to use the phase diagram data for corium containing siliceous concrete, or set IPHASE=3 to use the data for corium containing limestone/limestone concrete. Conversely, set IPHASE=4 to input a user-specified oxide phase diagram. If IPHASE=4, then NSOLP equals the total number of points in the interpolation table for the user-specified oxide-phase solidus versus wt % concrete in the melt. The vectors XWTSOL(I) and FSOLP(I) form the x-y dataset for this interpolation table, with $1 \leq I \leq NSOLP$. The vectors XWTLIQ(I) and FLIQP(I) with $1 \leq I \leq NLIQP$ form the analogous dataset for the user-specified liquidus table.

The parameter IEUTEC controls the assumption of where unoxidized Zr resides in the melt. Set IEUTEC=0 if the Zr is assumed to exist in a discrete metal phase (along with any other metals present in the melt) from the oxide, or set IEUTEC=1 if the Zr is assumed to be soluble in the oxide. This parameter is only important in the evaluation of the corium thermophysical properties; i.e., whether or not the oxide phase freezing range is modified by the presence of Zr (see Section A.1.2). The parameter NSOLID controls the evaluation of the oxide phase solid fraction as a function of temperature. Set NSOLID=1 to evaluate the solid fraction from the phase diagram for the particular melt composition (again see Section A.1.2), or set NSOLID=2 to

evaluate the solid fraction based on the assumption that the solid fraction varies linearly between the oxide phase solidus and liquidus.

The parameter NPOURS in Line 21 defines the number of intervals in time into which the pour conditions from the RPV is subdivided. If NPOURS=0, then the mass flowrate of corium relocating from the vessel into the MCCI zone is assumed to equal zero over the time interval. However, if NPOURS>0, then TST(I) and TSTOP(I) denote the start and stop times of the I-th pour interval, while AINTP(I) and BINTP(I) are the melt temperature coefficients for the relocating corium over the interval. The melt temperature is assumed to vary linearly; i.e., $T_{\text{melt}} = \text{AINTP}(I) + \text{BINTP}(I) \cdot (t - \text{TST}(I))$. For the I-th melt pour interval, NISTP denotes the total number of corium constituents (NISTP can range from 1 to 22) included in the melt pour stream. The code then reads in NISTP lines of input in the form of IT, APOUR(IT,I), and BPOUR(IT,I) wherein IT denotes the index for the pour constituent (e.g., IT=29 denotes UO_2 ; see Table 3-3), and APOUR(IT,I) and BPOUR(IT,I) are the pour rate coefficients for that constituent over the interval. The rate can vary linearly; i.e., $\text{rate (kg/sec)} = \text{APOUR}(IT,I) + \text{BPOUR}(IT,I) \cdot (t - \text{TST}(I))$.

Lines 25 through 27 define parameters that are used to evaluate heat transfer behavior associated predominately with the crust that forms at the melt-water interface. The parameter SIGYCR is the crust structural yield strength used in the crust anchoring calculation (modeling options are selected in Line 30 of the input that is described below). This parameter is only important if the user makes the choice to perform the crust anchoring analysis. Corium crust strength data obtained by Lomperski *et al.*^[22] suggest that this strength lies in the range of 1-3 MPa. The parameter FRZFR is used to define the effective “freezing” or “solidus” temperature for the core oxide-metal mixture, as well as for the various crusts (top, side, bottom) that can form during the calculation. This parameter is included to mock up “mushy zone behavior.” Set FRZFR=1 to calculate the freezing temperature of the oxide-metal mixture based on the solidus temperatures for the two phases, or set FRZFR=0 to use liquidus temperatures. Set $0 < \text{FRZFR} < 1$ to interpolate the freezing temperature from the temperature/solid fraction relationship assumed for the calculation (see NSOLID definition in Line 16).

If water is added during the calculation (i.e., NADD>0; see Line 39), then NINGRS controls the water ingress modeling assumptions (see Section 2.5.4). Set NINGRS=0 if the crust is considered impervious with respect to water ingress, or set NINGRS=1 if water ingress into a growing crust of user-specified permeability is to be calculated, or set NINGRS=2 if water ingress into a growing crust is calculated with the time (i.e., composition) dependent crust dryout limit calculated with the Lister/Epstein model as modified by Lomperski and Farmer.^[20] Set PERM equal to the crust permeability for the case in which that parameter is utilized (NADD>0 and NINGRS=1). If NINGRS=0 or 2, then the setting of PERM is arbitrary. Conversely, set CINGRES equal to the empirical constant in the Lister/Epstein dryout heat flux model if that case is selected (Eq. 2-186). If NINGRS=0 or 1, then the setting of CINGRES is arbitrary.

When water is present, CHFMULT is the critical heat flux multiplier that is used as one criterion for determining when film boiling breaks down with a stable crust present; i.e., if the debris-water heat flux falls below $q_{\text{crit},fb}'' = C_{\text{CHF}} q_{\text{CHF}}''$ in film boiling, then transition to nucleate boiling occurs (see Section 2.5.2). This criterion is used in conjunction with the Henry^[58] minimum

film boiling point model for determining when film boiling breaks down. Set CHFMULT=0 to rely on the Henry correlation alone. In addition, CCRIT is a second critical heat flux multiplier that is used as a criterion for determining when bulk cooling breaks down; i.e., if the debris-water heat flux falls below $q''_{crit,bc} = C_{crit} q''_{CHF}$ during bulk cooling, then a stable crust growth calculation is initiated. This criterion is used in conjunction with the critical superficial gas velocity criterion for determining when stable crust formation occurs (see Section 2.5.1). Set CCRIT=0 to rely on the minimum gas velocity correlation alone.

The parameter NENTR in Line 27 controls the melt entrainment (eruption) modeling assumptions if water is added during the calculation (see Section 2.5.3). Set NENTR=0 if the crust is considered impervious with respect to melt eruptions, or set NENTR=1 if eruptions with subsequent particle bed formation are to be calculated based on a user-specified, constant melt entrainment coefficient 'ENSPEC' (fractional, not %). Conversely, set NENTR=2 if eruptions/bed formation are to be calculated using the Ricou-Spalding entrainment rate correlation^[44] (see Eq. 2-163), with 'ENRICO' ($0.06 \leq \text{ENRICO} \leq 0.12$) defined as the empirical constant in this expression. Finally, set NENTR=3 if eruptions with particle bed formation are to be calculated using the model developed by Farmer.^[30] If NENTR>0, then set DBED and POROSBED equal to the particle diameter and porosity that is formed by eruptions; these data are used to evaluate the bed dryout heat flux with Lipinski's model.^[43] Note that if NENTR=0, the settings of the above melt entrainment parameters are arbitrary.

Lines 28 and 29 of the input file control modeling assumptions regarding the local corium material properties evaluation. Set NVISC=1 to use the Ishii-Zuber correlation^[33] for viscosity enhancement due to buildup of solids in the melt, or set NVISC=2 to use the Kunitz^[34] solid-phase viscosity enhancement factor. The parameter ALPMAX is the maximum solid fraction in the melt (i.e., viscosity $\rightarrow \infty$ as solid fraction $\rightarrow \text{ALPMAX}$). This parameter is only used in the melt viscosity evaluation and is separate from the solid fraction used to evaluate the effective melt solidus (FRZFR; see Line 25). The parameter NKSPEC controls the corium top crust thermal conductivity evaluation. Set NKSPEC=0 to evaluate the top crust conductivity using the property subroutines currently implemented in the code, or set NKSPEC=1 if the thermal conductivity is user-specified as FKS. Note that FKS is only used in the heat transfer analysis for the top crust; the sidewall and bottom crust thermal properties are calculated using the code subroutines.

Line 30 of the input file controls the top crust anchoring calculation (see Sections 2.5.5 and 2.5.6) that can be performed if water is added to the test section (NADD>0). Set NUSGAP=0 if the crust is assumed to always floats atop the melt at each node, or set NUSGAP=1 if crust anchoring and gap formation between the melt and crust is to be calculated if the local crust thickness exceeds the minimum required to be mechanically stable in the cavity span under the applied loads of the *local crust and particle bed weights*. Conversely, set NUSGAP=2 to calculate the previous case but with the local overlying water head included in the applied load evaluation. If crust anchoring occurs, then set NBUBSP=0 if the crust is treated as separated when the separation distance exceeds zero, or set NBUBSP=1 if the crust is considered separated when the separation distance exceeds the sparging gas bubble radius. This option is included to account for melt surface roughness caused by sparging concrete decomposition gases in the evaluation of the separation time. The parameter CCRGAP is the constant relating the test section area and crust yield strength (SIGYCR; see Line 30) to the minimum crust depth for structural stability in the

given cavity span through the equation: $\text{Applied Load} = \text{CCRGAP} \bullet \text{SIGYCR} \bullet (\text{Crust Thickness})^2$; see Eq. 2-193. Suggestions for the appropriate setting of CCRGAP for various modeling assumptions under a uniformly applied load are as follows:^[45]

- Circular plate crust with simply supported edges: CCRGAP=4.71 for ductile failure, or CCRGAP=2.53 for brittle failure.
- Circular plate crust with fixed edges: CCRGAP=8.84 for ductile failure, or CCRGAP=4.18 for brittle failure.
- Square plate crust with simply supported edges: CCRGAP=5.48 for ductile failure.

Note that one modeling limitation in the current code version is that the unique user-specified value for CCRGAP is used for all nodes in the analysis, regardless of node geometry. However, this is not thought to be a large modeling limitation as an anchored crust boundary condition is not deemed to be prototypic^[1] but rather an experiment artifact due to size limitations in experiments. Moreover, a single node analysis is usually adequate for experiment applications for which this modeling capability was principally developed.

Lines 31 through 33 of the input file control general heat transfer, thermalhydraulic, and chemistry modeling assumptions that can be selected by the user. In line 31, set NBUBRS=0 to use the Taylor instability model for sparging gas bubble diameter and the inviscid flow solution for terminal rise velocity, or set NBUBRS=1 to include the viscous flow model documented in this report (see Section 2.6.2). In the latter case, the gas bubble diameter is evaluated as the larger of that calculated with the inviscid and viscous flow models, and the Peebles-Garber correlation^[51] is used to calculate the bubble terminal rise velocity. In Line 32, set NCHEM=0 if condensed phase chemical reactions between metallic Zr and SiO₂ are to be neglected, or set NCHEM=1 if these reactions are to be calculated along the lines of that described in Section 2.2.

In Line 33, set NBOTBC as described below in order to calculate the heat transfer coefficient at the axial melt/concrete interface:

- NBOTBC=1: Bradley's modification to Malenkov-Kutateladze correlation (see Section 2.6.3.1);
- NBOTBC=2: gas film axial heat transfer model (see Section 2.6.3.2);
- NBOTBC=3: gas film axial heat transfer model with transition to the Bradley model if the gas velocity falls below the modified Berenson limit for film collapse (see Section 2.6.3.3)
- NBOTBC=4: Sevón's axial heat transfer correlation (see Section 2.6.3.4).

If NBOTBC=3, then set XMULTB equal to the Berenson minimum gas velocity multiplier for film collapse (see Eq. 2-309 in Section 2.6.3.3). Note that if the transient surface crust formation option is selected (NABBL=2), then the user should not set NBOTBC=2 or 3 since the gas film models have their own quasi-steady crust growth models embedded within.

If a 2-D calculation is being performed (N2DCALC>1), then set NSIDEBC as described below in order to calculate the heat transfer coefficient at the vertical melt/concrete interface:

- NSIDEBC=1: Bradley's modification to Malenkov-Kutateladze correlation (see Section 2.6.3.1);
- NSIDEBC=2: gas film radial heat transfer model (see Section 2.6.3.2);

- NSIDEBC=3: Sevon's lateral heat transfer correlation for limestone/common sand concrete (see Section 2.6.3.4)
- NSIDEBC=4: Sevon's lateral heat transfer correlation for siliceous concrete (see Section 2.6.3.4)

As noted for the axial case, if NABBL=2, then the user should not set NSIDEBC=2 since the gas film model has its own embedded quasi-steady crust growth model.

The parameter NVOID on Line 33 controls the melt void fraction correlation used in the calculation. Set NVOID=1, 2, or 3 to calculate the melt void fraction using the Brockmann *et al.*,^[35] Wallis,^[36] or Kataoka and Ishii^[37] correlations, respectively; see Section 2.6.1. Finally, the empirical multipliers XBMULT and XSMULT on Line 33 allow the user to manipulate the bottom and side heat transfer coefficients for parametric analysis; set XBMULT=1.0 and XSMULT=1.0 to maintain the user-specified correlation (viz. settings of NBOTBC and NSIDEBC) without modification.

Lines 34 through 36 define the decay heat (or input power) for the calculation, as well as how that power is distributed through the various debris zones that can form during the interaction. There are three options that can be employed for calculating the input distribution, as outlined below:

- If NDEC=1, the decay heat *density* in the melt, ' P_{melt} ,' (in units of W/kg UO₂), is calculated from the ANSI/ANS-5.1-1994 decay heat function for thermal fission of U-235.^[79] In this case the decay densities in the crust and particle bed regions are calculated from $P_{\text{crust}} = \text{CON1} \cdot P_{\text{melt}}$ and $P_{\text{bed}} = \text{CON2} \cdot P_{\text{melt}}$, respectively.
- If NDEC=2, the *gross* (melt+crust+bed) decay heat level (W) is evaluated from user-supplied data that are defined in Line 36. In this case, the decay heat delivered to the melt, crust, and particle bed zones are evaluated as $P_{\text{melt}} = (1 - \text{CON1} - \text{CON2}) \cdot P$, $P_{\text{crust}} = \text{CON1} \cdot P$, and $P_{\text{bed}} = \text{CON2} \cdot P$, respectively, where P is power interpolated from user-supplied data. Note that this option (NDEC=2) is not available when NUMNOD>1.
- If NDEC=3, the melt specific power *density* (W/kg UO₂) is evaluated from user-supplied data defined in Line 36. In this case, the power *densities* in crust and particle bed zones are evaluated in the same manner as that described above for the case NDEC=2.

The constants CON1 and CON2 are defined in Line 35 and allow the user to partition power input as needed to mock up plant cases or experiments. For instance, in plant cases where the power density is specified as a function of time, then NDEC should be set as 1 or 3 depending upon how the decay heat curve is specified, and the constants CON1 and CON2 should both be set to 1.0. Conversely, to model experiments like those carried out in the OECD/MCCI program^[1] in which the input power is only delivered to the melt zone, then the appropriate model is NDEC=2 with CON1 and CON2 both be set to 0.0.

For the case in which NDEC = 1, other data are input on Line 35 to complete the evaluation of the decay heat curve using the ANS standard.^[79] The fuel power density is calculated as PCORE/XMFUEL, where PCORE corresponds to the core power level at time of scram, and XMFUEL is the fuel mass (kg UO₂). If the user would rather just specify power density, then set PCORE to the desired power density and XMFUEL=1.0 kg. Time t=0 for this case (defined later

at Line 52) should correspond to the time of reactor scram. The parameter FRACFP is also included to allow the fraction of the overall decay heat left in the core debris involved in the MCCI to be specified; i.e., this parameter can be used to account for the effect of the loss of volatile fission products from the melt earlier in the accident sequence if desired. Set FRACFP=1.0 to bypass this option and assume that all fission products remain in the melt over the course of the MCCI and decay according to the ANS standard. Finally, TEFDP is defined as the total number of days for which the core was at full power before the reactor was scrammed.

If $NDEC \geq 2$, then NPOINT on Line 34 corresponds to the number of points in the user-supplied decay heat interpolation table. The x-y data for the power curve are then read in as defined in Line 36 in the form of the vectors TDEC(I) and DEC(I) with $1 \leq I \leq NDEC$.

Lines 37 and 38 define the cavity pressure and radiation boundary condition modeling assumptions. NPRES is the logic control parameter for system pressure. Set NPRES=1 if pressure is constant at PDRYWL over the course of the calculation, or set NPRES>1 if pressure is calculated from a user-supplied time-pressure interpolation table. PDRYWL is the cavity absolute pressure *in units of MPa*. Note that the setting for this parameter is irrelevant if NPRES>1 as the pressure is then interpolated from the input table. EDRYWL is the cavity radiation emissivity, and TSTRUC is the temperature of upper cavity structure and is used as the overlying radiation temperature boundary condition when the cavity is dry. For the case in which NPRES>1, TPRES(I) and PPRES(I) on Line 38 is the user-supplied pressure interpolation table; if NPRES=1, this line is omitted. If NPRES>1, then there are NPRES points provided.

Lines 39 to 45 define the cavity atmospheric boundary conditions used over the course of the calculation. The parameter NADD controls whether or not water is added, and if so, how the water pool is modeled. The various cases that can be addressed are outlined below. On Line 39, set the water cavity flooding parameter NADD as follows:

- Set NADD=0 if the cavity remains dry.
- Set NADD=1 if saturated water is maintained over the MCCI after time TADD.
- Set NADD=2 if saturated water is maintained over the MCCI after an ablation depth of DEPAB is reached.
- Set NADD=3 if a detailed water inventory model is used with water heatup, boiloff, injection, spillover, and spreading between nodes calculated.

For the simple cavity flooding model cases (i.e., NADD=1 or 2), the water height in the cavity is set with the parameter HDOWNC that is also defined on Line 39. The overall height of the core debris in the cavity (including overlying particle bed) is tracked during the calculation, and if the upper surface of the debris exceeds the water height HDOWNC, then upwards heat transfer is switched to a dry cavity boundary condition. For the case NADD=3, other data defined on Line 39 includes the initial water depth and temperature on the cavity floor, TWATI and ELWATI, respectively. The setting of these two parameters is arbitrary if $NADD \leq 2$.

For the case NADD=3, water injection and spillover can be modeled with the input parameters defined on lines 40-45. Note that if $NADD < 2$, (i.e., the cavity remains dry or a simple cavity flooding model is invoked), then these lines are omitted from the input file.

Lines 40-42 provide the information needed to model water injection into the cavity over the course of the calculation if the detailed water inventory model is selected (NADD=3). Set NINJ equal to the number of water injection sources (e.g. discrete pumps) that inject water over the calculation; note that Lines 41-42 are omitted if NINJ=0. If NINJ>0, then for the I-th injection source, set NISTR(I) and NISTP(I) equal to the node range over which that water is injected; the water source is assumed to be uniformly distributed (based on an area weighting) over these nodes. The node range must be continuous; if there are intervening nodes that do not receive the water from the source, then a new source needs to be defined (i.e., increase NINJ by one). For a given source, NPTINJ(I) is the number of points in the interpolation table for water injection source (XDTINJ(I)) and temperature (TDTINJ(I)) over the calculation. The requirements for the injection input tables are provided in Table 3-2. Note that Lines 41-42 are repeated NINJ times.

Similarly, the parameter NDOWNC in Line 43 provides the capability to model water spillover at user-defined locations in the mesh if the local water height reaches the spillover inlet elevation(s). An example are the downcomers into the Torus of the Mk I containment. If there are spillover points, set NDOWNC equal to the number of nodes in the spreading mesh where spillover can occur. Note that if NDOWNC = 0, Lines 44-45 are omitted from the input file. If NDOWNC > 0, then Lines 44-45 are used to define water spillover points as follows. For the I-th spillover point, NDC(I) is the node in the spreading mesh where spillover can occur. ELDCO(I) is the elevation above substrate at which spillover can begin, and NPTDC(I) is the number of points in the interpolation table that provides the spillover ‘cord length’ as a function of elevation above the spillover inlet. The input table with NPTDC(I) line entries defines the elevation above the spillover inlet height (i.e., local water depth minus the inlet elevation), and the equivalent cord length at that elevation available for spillover. The cord length is defined such that the water height above the spillover inlet multiplied by the interpolated cord length equals the water flow area into the downcomer. For instance, if the downcomer is a circular pipe with a horizontal opening, then the cord length is simply a constant that is equal to the pipe circumference.

Lines 46 through 49 define the overall cavity geometry, spatial orientation, and core debris initial conditions for each node in the MCCI analysis; these lines are repeated NUMNOD times. For the I-th node, set NACTIV(I)=0 if the node is considered to be inactive (i.e. inert, not containing core debris), or set NACTIV(I)=1 if the node contains core debris. This parameter allows inert node volumes to exist in the mesh that can harbor water if the detailed (NADD=3) water inventory model is selected. Note that if NUMNOD=1, then NACTIV(1) must be set to 1.

The second parameter on Line 46 controls the cavity ablation modeling assumptions. In particular, for the I-th node, set:

- N2DCALCC(I)=1 to perform a 1-D (axial) basemat erosion calculation;
- N2DCALCC(I)=2 to perform a 2-D cylindrical cavity (axial plus radial; right cylinder geometry assumed) erosion calculation;
- N2DCALCC(I)=3 to perform a 2-D notch-geometry calculation with two opposing, ablating walls, or
- N2DCALCC(I)=4 to perform a 2-D notch-geometry calculation with one wall ablating and the others inert.
- N2DCALCC(I)=5 to perform a 2-D cylindrical annulus (axial plus radial; right cylinder geometry assumed with inner radius fixed) erosion calculation;

For the I-th node, also set NSMP(I)=0 if the node is not considered to be a sump with a pre-existing elevation difference between adjacent node(s) that could limit sidewall ablation area relative to the pool height available for ablation. For instance, if the melt pool surface elevation at the node is greater than the sump depth, then sidewall ablation area is limited by the sump wall height as opposed to depth. If the node is considered to be a sump, then set NSMP(I)=1 if the melt surface elevation is to be compared to the concrete elevation of the node to the right (i.e., I + 1) to determine the controlling sidewall height, or set NSMP(I)=2 if the comparison is made to the node to the left (i.e., I - 1). Finally, if N2DCALCC(I)=3, then set NSMP(I)=3 if both left and right walls are compared.

Other input information is specified on line 46 are as follows (see Figure 3-1). Set ABMATC(I) equal to the initial basemat axial surface area in contact with melt at the I-th node. When N2DCALCC(I)=2, the initial cavity radius is then calculated as $R_o(I) = \sqrt{ABMATC(I)/\pi}$. When N2DCALCC(I)=3 or 4, then XWID2DC(I) and XLEN2DC(I) are the rectilinear dimensions of the basemat, with XLEN2DC(I) equal to the initial distance between the *ablating* concrete sidewalls, and XWID2DC(I) is the width between the two *adiabatic* sidewalls. In these two cases the initial basemat surface area is calculated as $ABMATC(I) = XLEN2DC(I) \cdot XWID2DC(I)$. Finally, if N2DCALCC(I)=5, the initial cavity inner radius RINOTC(I) is specified, and the initial outer radius is calculated as $R_o(I) = \sqrt{ABMATC(I) / \pi + RINOTC(I)^2}$.

For cases in which the detailed water inventory model is invoked (i.e., NADD=3), and/or melt relocates from the RPV over the course of the calculation, Line 47 defines nodes that are receptors of the melt pour, as well as the physical characteristics of the nodalization scheme that are important in the water spreading calculation. The integer IFLGA(I) specifies the node as a receptor of corium draining from the RPV. Set IFLGA(I)=1 if the node is a receptor, or set IFLGA(I)=0 if the node is not a receptor. The setting of this parameter is arbitrary if NPOURS=0; see Line 21.

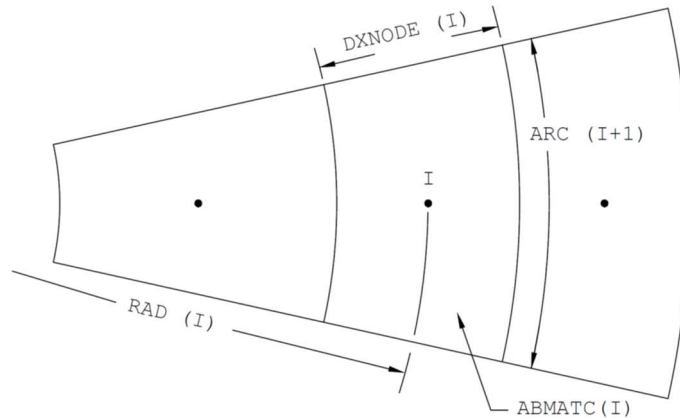


Figure 3-1. Illustration of Nomenclature for Water Spreading Model Nodalization Scheme.

Additionally, when NADD=3, set DXNODE(I) equal to the overall length of the node parallel to the flow direction; set RAD(I) equal to the node radial location (i.e. distance along spreading path) within the cell at which the node is located (note that the node does not have to be cell-centered); and set ARC(I) equal to the arc length available for water spreading between the I-

th and I+1 nodes. Note that the values of DXNODE(I), RAD(I), and ARC(I) are arbitrary if NADD<3. However, regardless of the setting of NADD, set ELO(I) equal to the initial concrete surface elevation for the I-th node.

Lines 48 and 49 define the initial core debris conditions at the I-th node location. In Line 48 set TMELTIC(I) equal to the initial melt temperature. The initial compositions of the melt, top crust, and particle bed zones at each node location (i.e., YC(I,K), ZC(I,K), ZBC(I,K), respectively) are then input through Line 49 for the 22 core debris constituent considered as part of the analysis (see Table 3-3 for $8 \leq K \leq 29$).

For cases in which the detailed water inventory model is invoked (NADD=3), Line 51 defines the integration control parameters for the gravity-driven water spreading fluid mechanics calculation. Due to the non-linearity in the advection term in the momentum equation, the fluid mechanics calculation may not be numerically stable at time steps suitable for the solution of the coupled water conservation of energy equation, along with the other equations considered as part of the analysis. Thus, the time step for the fluid mechanics calculation is taken as an integer multiple of the time step for the main integration (defined in Line 52); i.e.

$$\delta t_{fluid} = DTIME / NVELP \quad (3-1)$$

The-end-of-time step cell-edge velocities needed for the solution of the water conservation of energy equation are then calculated by taking NVELP smaller time steps. DAVMXW and DVMXW are the iteration convergence tolerances on the average and maximum incremental changes in melt cell edge velocities that are defined as:

$$DAVMXW \leq \frac{1}{N_s} \sum_i |\delta u_{w,i}| \quad (3-2)$$

$$DVMXW \leq \max(|\delta u_{w,i}|), \quad (3-3)$$

where N_s = the number of nodes containing water ($h > 0$), and $\max(\cdot)$ denotes the largest element of the vector. NITMAX is the maximum number of iterations allowed to meet the convergence criteria defined in Eqs. 3-2 and 3-3. Recommended values are NVELP=2, NITMAXW=20, DAVMXW=0.005 m/s, and DVMXW=0.01 m/s. If convergence is not achieved, an error message is written to the diagnostics file 'diag.dat' but the calculation *is not* terminated.

Line 52 similarly defines the integration convergence criteria for the solution of the water conservation of energy equation. DEAVMXW and DEMXW are the iteration convergence tolerances on the average and maximum incremental changes in water specific enthalpy which are defines as,

$$DEAVMXW \leq \frac{1}{N_s} \sum_i |\delta e_{w,i}| \quad (3-4)$$

$$DEMXW \leq \max(|\delta e_{w,i}|) \quad (3-5)$$

In Line 52, NENMXW is the maximum number of iterations allowed to meet the convergence criteria defined in Eqs. 3-4 and 3-5. Recommended values are NENMXW=20, DEAVMXW=300 J/kg and DEMXW= 600 J/kg. If convergence is not achieved, an error message is written to the diagnostics file 'diag.dat' but the calculation *is not* terminated.

Lines 52 through 57 define parameters that control the duration of the calculation as well as the density of the information written to output text and plotting files. TIMEO in Line 52 is the start time for the calculation, DTIME is the integration timestep, and TMAX is the maximum time to which the calculation is to be performed, unless an axial or radial ablation limit is reached at one of the nodes; see; see Line 55 in Table 3-2. In Line 53, TSTRTI is the time at which the evaluation of numerically integrated quantities (e.g., gross decay heat input, cumulative energy transfer to boundaries, cumulative gas release, ...) is to be initiated. In Line 54, NPRINT is the printing frequency to the output text file 'quenchout.dat'; i.e., the data are printed every NPRINT timesteps. Similarly, NPLOT in Line 54 is the print frequency to the Excel plotting files; the data are written out every NPLOT timesteps. File definitions are provided in Lines 55-57 and are summarized in further detail below.

For the multi-node modeling option (NUMNOD > 1), Line 55 allows the user to select nodes at which detailed data are to be written to text and excel plotting files, respectively. This line is repeated NUMNOD times. For the I-th node, set NPRT(I)=0 if the data for that node are *not* to be written to the text output file 'quenchout.dat', or set NPRT(I)=1 if the data are to be written every NPRINT timesteps. All nodes for which NPRT (I)=1 are sequentially written to the same file, quenchout.dat. Similarly, set NPLT(I)=1 if a comprehensive time-dependent plotting file is to be written for the I-th node for input into an excel plotting package, or set NPLT(I)=0 if this node is bypassed. If NPLT(I)=1, then the data for that node are written to a file denoted 'fort.1xxx,' where xxx corresponds to the node number. For instance, for the 17-th node, the output file would be fort.1017, while for node 152, the file would be fort.1152. Details regarding the text and plot files are provided in the next section.

If NPLT(I)=1, a smaller plotting file denoted 'fort.10xxx' is also created for the I-th node. This file is more manageable than the fort.1xxx file described above, yet it contains most of the key thermalhydraulic data of interest for MCCI and debris coolability analysis (e.g. ablation profiles, melt temperature, zone masses/decay heat levels, heat fluxes, and energy balance data). The file labeling scheme is the same as that described for the fort.1xxx files above.

Finally, additional run termination control parameters are input on Line 55. Set ABAXLIM equal to the maximum allowable axial ablation for a given node; the calculation is terminated if this limit is reached. Similarly, set ABRDLIM equal to the maximum allowable radial ablation before the calculation is terminated if a 2-D calculation is being performed. If the user wishes to bypass this option; set these limits to artificially large numbers that will not be reached over the calculation. In this case, the run will terminate based on the maximum run time set in Line 52 (TMAX).

Additional spatially dependent (i.e. NUMNOD>1) plotting files can be generated via Lines 56 and 57. Set NTIMSPC equal to the number of times at which these profiles are to be written out. The output includes debris elevation, temperature, water level, and heat flux distributions; see the next section for a full description. Set NTIMSPC=0 to bypass this option. If NTIMSPC>0, then the specific times (TIMSPC(I)) the data are to be written are input through Line 57. At each of these times, a file denoted 'fort.x' is created, where x is the sequential data file identifier for that particular time. As an example, for the 3rd specific time TIMSPC(I) for which the data are to be written, the output file denoted fort.3 is created. This line is repeated NTIMSPC times, and there are NTIMSPC files created at the end of the run. If NTIMSPC=0, then Line 57 is omitted.

4.0 DESCRIPTION OF CODE OUTPUT

The results of each CORQUENCH4.1 calculation are written to two text files and up to four plotting files; see Table 4-1 for a summary of the file names and the information that each provides. Additional details regarding these files and their use are provided below.

4.1 Text Output and Diagnostics File

The code produces an output text file entitled 'quenchout.dat' that is opened as Unit 6 in the main program. This file summarizes key input data and modeling assumptions, and also tabulates the current results of the calculation at a user-specified printing frequency. The first entry into 'quenchout.dat' is an echo-write of the input file 'quenchin.dat' that is provided to document the input data. Based on this information, a fairly extensive text descriptions of the processed input data and user-specified modeling assumptions is then provided. This portion of the output is self-explanatory.

Following the input data, the code produces a tabulation of results at a user-specified printing interval of NPRINT timesteps, defined in Line 54 of the input file (see Table 3-2). A typical copy of the output information at a given timestep and at two nodes [the first active (NACTIV=1), while the second is inactive (NACTIV=2)] is provided in Figure 4-1. Descriptions have been added near the margins in the figure that explains the meanings of the various file entries. The code automatically produces a copy of the initial conditions at the start of the calculation (i.e., user defined $t = t_0$) at each node. In addition, the code writes out the conditions at the time the calculation is terminated by reaching a user-defined time or ablation limit. The code auto-adjusts the output file to minimize the presentation of extraneous material; e.g., if a 1-D calculation is performed, then only the axial ablation data are presented, and not the radial (null-set) data. As additional examples, particle bed data are not presented during periods in which the cavity is dry, or if melt eruptions are not modeled as part of the run.

Finally, a diagnostics file called 'diag.dat' is produced. Any warnings generated during the run are written to this file. In addition, the time at which key events occur are written out in chronological order; for instance, crust anchoring, initiation of water ingress into the crust, debris quenching at a node site, or debris dryout and restart of MCCI. Search for the string 'TIME=' in this dataset for the identification of these events.

4.2 Plotting Package Output Files

The code produces up to four plotting files to aid in evaluating the results. As noted earlier, these files are summarized in Table 4-1. The names of Excel spreadsheets developed to provide standardized plots of key information are also given in the table. Time-dependent data are written to these files every NPLOTT timesteps (see Line 54 in Table 3-2), whereas spatially-dependent data are written out at discrete, user-specified times (see Line 56 in Table 3-2). Definitions of information written to each of the four plotting files are provided in Tables 4-2 to 4-5, respectively.

Table 4-1. Summary of CORQUENCH4.1 Data Output Files.

No.	File Name	Summary Description
1	quenchout.dat	Text file summarizing: i) input data and modeling assumptions, and ii) computed information at user-specified time intervals. See Figure 4-1 for explanations.
2	diag.dat	Text diagnostics file in which the time of key events such as debris quenching, dryout and restart of MCCI, etc., at different nodes is written out for reference. In addition, if problems with convergence or other issues arise during the run, an error message is written providing a few details. If convergence issues in the water inventory model arise, those can be addressed by reducing the integration time step and/or by increasing the number of iterations in Lines 50-51 of the input file (see Table 3-2 in Section 3).
3	fort.x	Plotting file providing spatially dependent MCCI data at user-specified times; see Table 4-2 for contents description. Spatial data can be written out at up to 999 different times with 'x' in fort.x sequentially corresponding to the user-specified times defined in Lines 56-57 of the input file (see Table 3-2). The data at any given time can be copied into the excel spreadsheet 'spaceplot.x' that provides graphs of key information.
4	fort.1xxx	Large plotting file providing a comprehensive set of 102 different time-dependent variables at user-specified node locations; see Table 4-3 for contents description. Up to NUMNOD files can be generated by this option, with 'xxx' in fort.1xxx corresponding to the nodes specified in Line 55 of the input file (see Table 3-2). The data for any given node can be copied into the excel spreadsheet 'bigplots.1xxx' that provides a comprehensive set of graphs for user evaluation.
5	fort.10xxx	Smaller plotting file providing key sets of calculated time-dependent data at user-specified node locations; see Table 4-4 for contents description. Up to NUMNOD files can be generated by this option, with 'xxx' in fort.10xxx corresponding to the nodes specified in Line 55 of the input file (see Table 3-2). The data for any given node can be copied into the excel spreadsheet 'quickplot.10xxx' that provides graphs for user evaluation.
5	integraldata.dat	Plotting file providing time-dependent data integrated over all nodes involved in the MCCI; see Table 4-5 for contents description. Note that this file is not generated if NUMNOD=1 as this case is covered by File Nos. 4 and 5 above. The information in this file can be copied into the excel spreadsheet 'integralplot' that provides graphs of key information for user evaluation.

Figure 4-1. Typical Code Output at Print Timestep.

TIME= 0.29434E+06 SECONDS, NODE= 1

Current time (seconds) and Node Number

CURRENT MELT, TOP CRUST, & PARTICLE BED BREAKDOWNS

CONSTITUENT	MELT		TOP CRUST		PART. BED	
	MASS (KG)	WT FR	MASS (KG)	WT FR	MASS (KG)	WT FR
UO2	28555.	0.18655	6616.9	0.18991	428.68	0.20395
ZRO2	21200.	0.13850	4912.6	0.14100	318.26	0.15142
CR2O3	3575.4	0.23357E-01	822.16	0.23597E-01	39.232	0.18665E-01
NIO	11.486	0.75037E-04	2.6616	0.76392E-04	0.0000	0.0000
B2O3	0.0000	0.0000	0.0000	0.0000	0.0000	0.0000
FE	10266.	0.67068E-01	2385.7	0.68472E-01	181.88	0.86534E-01
CR	0.0000	0.0000	4.3375	0.12449E-03	9.8818	0.47015E-02
NI	1042.7	0.68121E-02	241.63	0.69351E-02	15.654	0.74478E-02
ZR	0.0000	0.0000	0.0000	0.0000	0.0000	0.0000
U	0.0000	0.0000	0.0000	0.0000	0.0000	0.0000
B4C	0.0000	0.0000	0.0000	0.0000	0.0000	0.0000
SI	0.0000	0.0000	0.0000	0.0000	0.0000	0.0000
SIC	0.0000	0.0000	0.0000	0.0000	0.0000	0.0000
NA2O	0.0000	0.0000	0.0000	0.0000	0.0000	0.0000
TIO2	0.0000	0.0000	0.0000	0.0000	0.0000	0.0000
SIO2	53855.	0.35183	12108.	0.34752	699.56	0.33283
CAO	11001.	0.71865E-01	2473.3	0.70986E-01	142.89	0.67985E-01
MGO	0.0000	0.0000	0.0000	0.0000	0.0000	0.0000
AL2O3	13201.	0.86238E-01	2967.9	0.85184E-01	171.47	0.81582E-01
FEO	5104.3	0.33345E-01	1123.3	0.32239E-01	25.981	0.12361E-01
FE2O3	5261.1	0.34370E-01	1182.9	0.33950E-01	68.341	0.32515E-01
FE3O4	0.0000	0.0000	0.0000	0.0000	0.0000	0.0000
TOTAL	0.15307E+06		34842.		2101.8	

Mass and weight fractions in melt, top crust, and particle bed regions.

CURRENT THERMOPHYSICAL PROPERTIES

MATERIAL	K (W/M*K)	P (KG/M**3)	CP (J/KG*K)	U (KG/M*S)	SIGMA (N/M)	EMIS (-)	LATENT HEAT (KJ/KG)
MELT	3.7052	3486.3	992.53	8.1624	0.56406	0.81070	
CRUST	3.4655	3727.0				0.81124	862.27
PART. BED		3830.1					1311.6
DECOMP GAS	0.52948	0.52903E-01	6558.7	0.12055E-02			
COOLANT	0.68588	947.38	4196.0	0.23881E-03	0.55899E-01		2217.3
COOLANT VAP	0.26189E-01	0.94906	2098.3	0.12630E-04			

As applicable, the thermal conductivity, density, specific heat, viscosity, surface tension, emissivity, and latent heat of melt, crust, particle bed, sparging gas, coolant, and coolant vapor

MECHANICAL/PERMEABILITY PROPERTIES

MATERIAL	TENSILE STRENGTH (MPA)	YOUNGS MODULUS (GPA)	LINEAR EXP. COEF. (1/K) *10**6	PERM. (1/M**2) *10**9
CRUST	86.704	151.86	4.5026	0.22408
MELT	87.740	153.14	4.6445	0.19100

Crust and melt mechanical strength and permeability data (melt data is based on the material composition if it were quenched)

KEY MELT THERMALHYDRAULIC CONDITIONS

TMELT=	1632.5	K	EMELT=	1.1154	MJ/KG
TOX, SOL=	1403.0	K	TOX, LIQ=	2461.1	K
TM, SOL=	1734.2	K	TM, LIQ=	1755.6	K
VOXSOL=	0.72919		VTOTSOL=	0.74950	
VCRIT=	7.1813	CM/S	JGAS=	0.12505	CM/S
VSTRT=	4.2120	CM/S	NSTRT=	1 (0/1/2=MX/MB/OB)	
VOIDF=	0.57722E-02		QCHEM=	42.909	KW
RBUBBLE=	2.3115	CM	UBRISE=	23.308	CM/S
QDECM=	733.86	KW	QDECCR=	1177.0	KW

Melt temperature, specific enthalpy, oxide phase solidus/liquidus, metal phase solidus/liquidus, oxide phase and combined (metal+oxide) phase solid fractions, critical superficial gas velocity to preclude top crust formation, actual superficial velocity, minimum gas velocity to preclude metal/oxide phase segregation*, melt mixing state (MX=mixed, MB=metal on bottom, OB=oxide on bottom)*, melt void fraction, chemical reaction heat, sparging bubble radius and terminal rise velocity, and decay heat in melt and top crust zones, respectively.

MELT UPPER SURFACE HEAT TRANSFER DATA

TINT=	387.75	K	HWAT=	0.0000	W/M**2*K	QWAT=	5501.9	KW
TTOP=	1415.2	K	HTOP=	70.547	W/M**2*K	QTOP=	691.22	KW
TFRT=	1415.2	K	DCRT=	297.60	MM	FCRS=	1.0000	
NCRT=	2		NUCB=	1		NING=	1	

Coolant/crust interface temperature, heat transfer coefficient (only calculated if water ingress is not occurring) and cooling power. Also, crust/melt interface temperature, heat transfer coefficient, heat load, interface freezing temperature, and crust thickness. Finally, NCRT=0 if crust is absent, NCRT=1 if thin crust segments exist, or NCRT=2 if stable crust exists; NUCB=0 if film boiling or NUCB=1 if nucleate boiling; and NING=0 if crust water ingress is not active, or NING=1 if active.

PARTICLE BED THERMALHYDRAULIC DATA

BED HEIGHT=	2.9116	CM	QDECBED=	25.331	KW
TOP DRYOUT=	3185.2	KW/M**2	BOT. DRYOUT=	3184.4	KW/M**2

Particle bed height, decay heat level, and dryout limit evaluated at the top and bottom surfaces of the bed, respectively. If ANL melt eruption model is selected, other data on hole diameter, threshold gas velocity for eruptions, etc. is also displayed.

MELT LOWER SURFACE HEAT TRANSFER DATA

ADEP=	211.45	CM	BLDEP=	49.836	CM	ARATE=	0.20287	MM/MIN
HBOT=	18.652	W/M**2*K	QBOT=	162.38	KW			

Axial ablation and boundary layer depths, ablation rate, heat transfer rate, interface temperature, slag film, and crust depth. When gas film model is used, then NTRN=0 if gas film exists, or NTRN=1 if film has broken down and slag model is invoked. Also when gas film model is used, then the interface crust depth and critical gas velocity for film breakdown are shown.

MELT RADIAL SURFACE HEAT TRANSFER DATA

ADEP=	200.17	CM	BLDEP=	22.154	CM	ARATE=	0.29879	MM/MIN
HSID=	37.305	W/M**2*K	QSID=	250.11	KW			

Radial ablation and boundary layer depths, ablation rate, interface heat transfer coefficient, and heat transfer rate. When gas film model is used, then the interfacial crust depth is also shown. Also, NLMTRB=0 if flow in the film is laminar, or NLMTRB=1 if flow is turbulent.

*CORQUENCH4.1 has been structured to evaluate metal/oxide phase segregation as well as inter-nodal heat and mass transfer for multi-nodal cases. However, these models have not been fully checked out and validated in Version 4.1. These two outputs describe the phase segregation criteria and state and are included in Version 4.1. The code is currently set up internally assuming that the metal/oxide are

TERM-BY-TERM COMPONENTS OF ENERGY EQUATION

QNTBN= 4532.7	KW	QDCML= 733.86	KW	QBOTE= -58.680	KW
QSIDE= 0.0000	KW	QTOPE= -282.01	KW	QBMBN= 0.0000	KW
QCRBN= -4509.3	KW	QOXTO= 42.909	KW	QERUP= -32.463	KW
QMASB= -9.0846	KW	QDRPV= 0.0000	KW	QNODE= 0.0000	KW
DENDT= 426.99	KW				

From left-to-right, melt source/sink terms due to: i) melt mass times rate change of melt specific enthalpy, ii) decay heat, iii) axial heat transfer to concrete, iv) radial heat transfer to concrete, v) heat transfer to upper surface, vi) mass transfer of slag into melt, vii) mass transfer into top crust, viii) chemical reactions, ix) net power due to all heat source/sinks, x) total of source/sinks due to mass transfer (i.e., QNTBN+QBMBN+ QCRBN), and xi) mass transfer from RPV, and xii) resultant rate of change of melt specific enthalpy.

INTEGRATED ENERGY SOURCE/SINK DATA

E->ATMOSPHERE=-0.65539E+06 MJ	E->CHEM. RXS.= 85194.	MJ
E->DOWN ABL.= -53196.	E->SIDE ABL.= -57926.	MJ
E->DECAY HEAT= 0.56171E+06 MJ	E->SLAG INGR.= 98860.	MJ
E->CRUST DEP.= 0.12806E+06 MJ	E->MELT ERUP.= -2728.9	MJ
E->MELT POUR= 0.0000 MJ	E->ADJ. NODES= 0.0000	MJ

From left-to-right, integrated energy transfer due to: i) heat loss to overlying structure, ii) chemical reactions, iii) downward ablation, iv) sidewall ablation, v) decay heat, vi) slag ingress into melt, vii) crust formation, viii) melt eruptions, ix) melt pour, and x) energy transfer to adjacent node(s)*.

WATER COOLANT INVENTORY DATA

TEMP= 387.75	K	COLLAPSED DEPTH= 0.72118	M	PRESSURE= 0.17000	MPA
--------------	---	--------------------------	---	-------------------	-----

Water inventory temperature, mass, and makeup mass flowrate.

METAL GAS AND CONDENSED PHASE REACTION FRACS.

ZR/GAS= 0.0000	SI/GAS= 0.0000	ZR/SIO2= 0.0000
CR/GAS= 0.0000	FE/GAS= 1.0000	ZR/SI= 1.0000

Fractions of gases (H₂O and CO₂) and SiO₂ from ablation that react with metallic melt constituents. Important for cases in which reaction rates are limited by rate of metal incorporation into melt from ablation, as opposed to mass flux from concrete ablation.

CUMULATIVE NONCONDENSABLE GAS RELEASE (MOLES)

MOLES H2= 0.42317E+06	MOLES H2O= 0.0000	MOLES CO= 38962.
MOLES CO2= 0.0000	MOLES SIO= 0.0000	TOT MOLES= 0.46213E+06

Cumulative moles of gas released from concrete, including oxidation reactions with metallic melt constituents.

.
.

.

TIME= 0.29434E+06 SECONDS, NODE= 5

WATER COOLANT INVENTORY DATA

TEMP= 387.75	K	COLLAPSED DEPTH= 0.13084	M	PRESSURE= 0.17000	MPA
--------------	---	--------------------------	---	-------------------	-----

Additional lines for inactive nodes that display the water temperature, depth, and system pressure for each node only, as inactive nodes do not contain core debris.

.
.

.

Table 4-2. Variable Definitions in Plotting File ‘spaceplot.x’.

Column No.	Variable Name	Description	Units
1 (A)	X	Distance along spreading length	m
2 (B)	TMPRNT	Bulk Melt Temperature	K
3 (C)	TSOXC	Oxide Phase Solidus	K
4 (D)	TLOXC	Oxide Phase Liquidus	K
5 (E)	ELEV DNC	Concrete Surface Elevation	cm
6 (F)	HTPCRFXC	Top Surface Fractured Crust	cm
7 (G)	HGAPPC	Top of Melt Pool	cm
8 (H)	HBTCRFXC	Bottom Surface Upper Crust	cm
9 (I)	HTPBFXC	Top Surface of Particle Bed	cm
10 (J)	ABSPLTC	Sidewall Ablation Location	cm
11 (K)	QFLXBC	Debris-Concrete Axial Heat Flux	kW/m ²
12 (L)	QFLXWC	Debris-Atmosphere Heat Flux	kW/m ²
13 (M)	QFLXSC	Debris-Concrete Radial Heat Flux	kW/m ²
14 (N)	QFLXPC	Decay Heat Flux in Debris	kW/m ²
15 (O)	QOXP	Heat Flux Due to Chemical Reactions	kW/m ²
16 (P)	DWATCP	Water Depth	cm
17 (Q)	DWATEV	Top Surface of Water Pool	cm
18 (R)	TWATCC	Water Temperature	K
19 (S)	VLWAV	Water Spreading Velocity at Cell Center	m/s
20 (T)	FCRUST	Fraction of heat that can be removed from crust surface upper surface by water present at the node	-
21 (U)	FBED	Fraction of heat that can be removed from overlying particle bed by water present at the node	-
22 (V)	FCOV	Fraction of particle bed that is submerged by available water at the node	-
23 (W)	FDC	Correction factor related to particle bed porosity that relates the actual depth of the water pool to the collapsed depth; i.e., actual collapsed depth = actual depth times the actual depth.	-

Table 4-3. Variable Definitions in Plotting File ‘bigplots.1xxx’.

Col. No.	Var. Name	Description	Units
1 (A)	TIMSV	Calculation time	minutes
2 (B)	ELEVDN	Current basemat elevation	cm
3 (C)	HGAPP	Elevation of the top surface of the melt pool	cm
4 (D)	HBTCRFX	Elevation of the bottom surface of the top crust	cm
5 (E)	HTPCRFX	Elevation of the top surface of the top crust	cm
6 (F)	HTPCRBX	Elevation of the top surface of the bottom crust	cm
7 (G)	HTPBFX	Elevation of the top surface of the particle bed	cm
8 (H)	QWAT	Total heat loss up to water (wet) or structure (dry)	kW
9 (I)	QBOT	Total heat loss into underlying concrete	kW
10 (J)	QSID	Total heat loss to concrete lateral surfaces	kW
11 (K)	QOX	Heat production in melt due to metals oxidation in melt	kW
12 (L)	PCTOT	Total decay heat in melt, crust, and particle beds	kW
13 (M)	ABBPLT	Axial ablation depth	cm
14 (N)	BLBPLT	Axial thermal boundary layer depth	cm
15 (O)	ABRTBP	Axial ablation rate	mm/min
16 (P)	ABSPLT	Radial ablation depth	cm
17 (Q)	BLSPLT	Radial thermal boundary layer depth	cm
18 (R)	ABRTSP	Radial ablation rate	mm/min
19 (S)	TMPLT	Bulk melt temperature	K
20 (T)	TSOX	Oxide phase solidus temperature	K
21 (U)	TLOX	Oxide phase liquidus temperature	K
22 (V)	TFZXP	Effective melt freezing temperature	K
23 (W)	VDPLT	Melt void fraction	-
24 (X)	VGPLT	Melt superficial gas velocity	cm/sec
25 (Y)	VGPLTB	Melt superficial velocity from basemat (axial) erosion	cm/sec
26 (Z)	VGPLTS	Melt superficial velocity from sidewall (radial) erosion	cm/sec
27 (AA)	DCRPLT	Top crust depth	mm
28 (AB)	WTMPLT	Water mass over melt	kg
29 (AC)	TWTPLT	Water temperature over melt	K
30 (AD)	BUBDP	Sparging gas bubble diameter	cm
31 (AE)	URISEP	Sparging gas bubble rise velocity	cm/sec
32 (AF)	PCMLT	Decay heat in melt zone	kW
33 (AG)	PCCR	Decay heat in top crust	kW
34 (AH)	PCBED	Decay heat in particle bed over crust	kW
35 (AI)	XMMELT	Melt zone mass	kg
36 (AJ)	XMCRIT	Top crust mass	kg
37 (AK)	XMBED	Particle bed mass	kg
38 (AL)	XMTOT	Total debris (melt+crust+particle bed) mass	kg
39 (AM)	XMZR	Zirconium metal mass in melt	kg
40 (AN)	XMSI	Silicon metal mass in melt	kg
41 (AO)	XMCON	Concrete slag mass in melt	kg
42 (AP)	XWTCM	Concrete fraction in melt	-
43 (AQ)	XWTCCR	Concrete fraction in top crust	-
44 (AR)	XWTCB	Concrete fraction in particle bed	-
45 (AS)	QFLXW	Surface heat flux to water (wet) or structure (dry)	kW/m ²
46 (AT)	QFLXB	Surface heat flux to concrete basemat	kW/m ²
47 (AU)	QFLXS	Surface heat flux to concrete sidewalls	kW/m ²
48 (AV)	QFLXP	Decay heat in melt expressed as average flux	kW/m ²

Table 4-3 (Contd.). Variable Definitions in Plotting File ‘bigplots.1xxx’.

Column No.	Variable Name	Description	Units
49 (AW)	VISCM	Melt viscosity	kg/m-sec
50 (AX)	ECHEM	Integrated metals oxidation energy	MJ
51 (AY)	EWAT	Integrated heat removal to water(wet) or structure (dry)	MJ
52 (AZ)	EDECAY	Integrated decay heat energy	MJ
53 (BA)	EBOT	Integrated heat input into basemat concrete decomposition	MJ
54 (BB)	ESID	Integrated heat input into sidewall concrete decomposition	MJ
55 (BC)	DGAPP	Gap thickness between melt and bridge crust if anchoring occurs	cm
56 (BD)	CRSTLP	When crust anchors, 2 nd crust thickness that forms on melt surface	cm
57 (BE)	VIEWP	Radiation view factor between melt surface and underside of crust when a bridge crust forms	-
58 (BF)	HBEDPL	Particle bed height above crust, including porosity	cm
59 (BG)	FZRG	Reaction fraction between H ₂ O/CO ₂ gases and Zr in melt	-
60 (BH)	FZRC	Reaction fraction between SiO ₂ and Zr in the melt	-
61 (BI)	FCRG	Reaction fraction between H ₂ O/CO ₂ gases and Cr in melt	-
62 (BJ)	FFEG	Reaction fraction between H ₂ O/CO ₂ gases and Fe in melt	-
63 (BK)	FZRSI	Fraction of Zr/SiO ₂ reactions producing Si(l) vs. SiO(g)	-
64 (BL)	FSIG	Reaction fraction between H ₂ O/CO ₂ gases and Si in melt	-
65 (BM)	VSMP	Solid fraction in melt metal phase	-
66 (BN)	VSOP	Solid fraction in melt oxide phase	-
67 (BO)	VSTP	Total solid fraction in combined metal and oxide phases	-
68 (BP)	FNMH2	Number of moles of H ₂ produced during interaction	moles
69 (BQ)	FNMH2O	Number of moles of H ₂ O produced during interaction	moles
70 (BR)	FNMCO	Number of moles of CO produced during interaction	moles
71 (BS)	FNMCO2	Number of moles of CO ₂ produced during interaction	moles
72 (BT)	FNMSIO	Number of moles of SiO(g) produced during interaction	moles
73 (BU)	FNMTOT	Total number of moles of gas produced	moles
74 (BV)	TRPV	Temperature of melt draining from RPV	K
75 (BW)	XMRPV	Total mass flowrate of melt draining from RPV	kg/sec
76 (BX)	TTOPP	Upper surface temperature of melt pool or crust	K
77 (BY)	VCRITP	Critical gas velocity to preclude crust formation at melt upper surface	(cm/s)
78 (BC)	VBERP	Berenson critical gas velocity (corrected) for breakdown of gas film model over the concrete surface	(cm/s)
79 (CA)	HBOTP	Heat transfer coefficient from melt to concrete bottom surface	(W/m ² -K)
80 (CB)	HSIDEP	Heat transfer coefficient from melt to concrete sidewall surface	(W/m ² -K)
81(CC)	QDRYC	Crust dryout heat flux	kW/m ²
82 (CD)	QDRYCI	Crust dryout heat flux corrected for counter-current flow of noncondensable gases	kW/m ²
83 (CE)	DCRBOT	Thickness of crust at basemat core/concrete interface	(mm)
84 (CF)	DCRSIDE	Thickness of crust at sidewall core/concrete interface	(mm)
85 (CG)	DHOLP	Crust melt eruption hole diameter	(mm)
86 (CH)	XNDEN	Crust melt eruption hole site density	(1/m ²)
87 (CI)	COEFPC	Average melt entrainment coefficient due to eruptions	(%)
88 (CJ)	VTHRSP	Threshold melt superficial gas velocity for onset of eruptions	(cm/s)
89 (CK)	FRCHLP	Percentage of concrete decomposition gases that pass through crust vent holes	(%)

Table 4-3 (Contd.). Variable Definitions in Plotting File ‘bigplots.1xxx’.

Column No.	Variable Name	Description	Units
90 (CL)	DSLGBP	Thickness of slag layer beneath bottom crust	(mm)
91 (CM)	TSURFB	Temperature of concrete surface at bottom of pool	(K)
92 (CN)	DSLGBP	Thickness of slag layer beneath side crust	(mm)
93 (CO)	TSURFS	Temperature of concrete surface at side of pool	(K)
94 (CP)	DCMINB	Minimum thickness of stable crust at bottom of pool	(mm)
95 (CQ)	DCMINS	Minimum thickness of stable crust at side of pool	(mm)
96 (CR)	TFRZCRB	Freezing temperature of crust at bottom of pool (based on crust composition)	(K)
97 (CS)	TFRZCRS	Freezing temperature of crust at side of pool (based on crust composition)	(K)
98 (CT)	TFRZCR	Crust freezing temperature (based on pool composition)	(K)
99 (CU)	XMCRB	Mass of bottom crust	(kg)
100 (CV)	XMCRS	Mass of side crust	(kg)
101(CW)	XWTCRB	Weight fraction concrete in bottom crust	(-)
102 (CX)	XWTCRS	Weight fraction concrete in side crust	(-)

Table 4-4. Variable Definitions in Plotting File ‘quickplots.10xxx’.

Column No.	Variable Name	Description	Units
1 (A)	TIMSV	Calculation time	minutes
2 (B)	ABBPLT	Axial ablation depth	cm
3 (C)	ABSPLT	Radial ablation depth	cm
4 (D)	TMPLT	Bulk melt temperature	K
5 (E)	TSOX	Oxide phase solidus temperature	K
6 (F)	TLOX	Oxide phase liquidus temperature	K
7 (G)	FNMH2	Number of moles of H ₂ produced during interaction	moles
8 (H)	FNMCO	Number of moles of CO produced during interaction	moles
9 (I)	FNMCO2	Number of moles of CO ₂ produced during interaction	moles
10 (J)	QFLXW	Surface heat flux to water (wet) or structure (dry)	kW/m ²
11 (K)	XWTM	Concrete fraction in melt	-
12 (L)	XWTCCR	Concrete fraction in top crust	-
13 (M)	XWTCB	Concrete fraction in particle bed	-
14 (N)	ELEVDN	Current basemat elevation	cm
15 (O)	HBTCRFX	Elevation of the bottom surface of the top crust	cm
16 (P)	HTPCRFX	Elevation of the top surface of the top crust	cm
17 (Q)	HTPBFX	Elevation of the top surface of the particle bed	cm
18 (R)	HGAPP	Elevation of the top surface of the melt pool	cm
19 (S)	XMTOT	Total debris (melt+crust+particle bed) mass	kg
20 (T)	XMMELT	Melt zone mass	kg
21 (U)	XMCR	Top crust mass	kg
22 (V)	XMBED	Particle bed mass	kg
23 (W)	COEFPC	Melt eruption entrainment coefficient	(%)
24 (X)	PCTOT	Total decay heat (melt, crusts, and particle beds)	kW
25 (Y)	PCMLT	Decay heat in melt zone	kW
26 (Z)	PCCR	Decay heat in top crust	kW
27 (AA)	PCBED	Decay heat in particle bed over crust	kW

Table 4-5. Variable Definitions in Plotting File ‘integralplot’.

Column No.	Variable Name	Description	Units
1 (A)	TIME	Time	sec
2 (B)	FINJ	Water Injection Flowrate	kg/sec
3 (C)	FDC	Flowrate into Downcomers	kg/sec
4 (D)	FSTM	Total Steam Production	kg/sec
5 (E)	TINJ	Total Water Injection	kg
6 (F)	TDC	Total Water Flow into Downcomers	kg
7 (G)	TSTM	Total Steam Production	kg
8 (H)	TWATFLR	Remaining Water on Floor	kg
9 (I)	WBAL	Water Mass Balance	kg
10 (J)	EWMS	Heat removal by water	MJ
11 (K)	EWCO	Total Upwards Heat Removal	MJ
12 (L)	ENTB	Axial Ablation Heat Transfer	MJ
13 (M)	ENTS	Radial Ablation Heat Transfer	MJ
14 (N)	ENOX	Metals Oxidation Energy	MJ
15 (O)	EDEC	Decay Heat	MJ
16 (P)	ESLG	Slag Heat Source	MJ
17 (Q)	ECRD	Crusting Heat Sink	MJ
18 (R)	ERUP	Eruption Heat Sink	MJ
19 (S)	EINJ	Melt Pour Heat Source	MJ
20 (T)	NMH2	H2 Production	moles
21 (U)	NMCO	CO Production	moles
22 (V)	NCO2	CO2 Production	moles
23 (W)	NTOT	Total Non-condensables	moles
24 (X)	QNTW	Heat Transfer to Water	kW
25 (Y)	QTWA	Total Upwards Heat Transfer	kW
26 (Z)	QNTB	Axial Ablation Heat Transfer	kW
27 (AA)	QNTS	Radial Ablation Heat Transfer	kW
28 (AB)	QNOX	Metals Oxidation Energy	kW
29 (AC)	QDEC	Decay Heat	kW
30 (AD)	MLTM	Melt Mass	kg
31 (AE)	CRTP	Top Crust Mass	kg
32 (AF)	CRSD	Side Crust Mass	kg
33 (AG)	CRBT	Bottom Crust Mass	kg
34 (AH)	MBED	Particle Bed Mass	kg
35 (AI)	MTOT	Total Debris Mass	kg
36 (AJ)	AREA	MCCI Surface Area	m ²
37 (AK)	PRES	System Pressure	MPa

5.0 REFERENCES

1. M. T. Farmer, D. J. Kilsdonk, and R. W. Aeschlimann, "Corium Coolability under Ex-Vessel Accident Conditions for LWRs," *Nucl. Eng. Technol.*, **41**, 575 (2009).
2. M. T. Farmer, J. J. Sienicki, and B. W. Spencer, "CORQUENCH: A Model for Gas Sparging-Enhanced, Melt-Water, Film Boiling Heat Transfer," *ANS Winter Meeting on the Thermal Hydraulics of Severe Accidents*, Washington, D.C. USA, November 11-15, 1990.
3. M. T. Farmer *et al.*, "Modeling and Database for Melt-Water Interfacial Heat Transfer," *2nd CSNI Specialist Meeting on Core Debris-Concrete Interactions*, Karlsruhe, Germany, April 1-3, 1992.
4. M. T. Farmer, "Modeling of Ex-Vessel Corium Coolability with the CORQUENCH Code," *Proceedings 9th Int. Conf. on Nucl. Eng.*, Nice, France, April 8-12, 2001.
5. M. T. Farmer, "The CORQUENCH Code for Modeling of Ex-Vessel Corium Coolability under Top Flooding Conditions, Code Manual – Version 3.03," OECD/MCCI-2010-TR03, March 2010.
6. Nuclear Energy Institute, "Industry Guidance for Compliance with Order EA-13-109," NEI 13-02, Rev. 2, December 2014 (ADAMS Accession No. ML13316A853).
7. E.J. Leeds, EA-13-109, "Issuance of Order to Modify Licenses with Regard to Reliable Hardened Containment Vents Capable of Operation under Severe Accident Conditions," USNRC, June 6, 2013.
8. M. T. Farmer, "The MELTSPREAD Code for Modelling of Ex-Vessel Core Melt Spreading in Containments, Code Manual-Version 3-beta," ANL-18/30, September, 2018.
9. M. T. Farmer (editor), R. Bunt, M. Corradini, P. Ellison, M. Francis, J. Gabor, R. Gauntt, C. Henry, R. Linthicum, W. Luangdilok, R. Lutz, C. Paik, M. Plys, C. Rabiti, J. Rempe, K. Robb, and R. Wachowiak, "Reactor Safety Gap Evaluation of Accident Tolerant Components and Severe Accident Analysis," ANL/NE-15/4, March 2015.
10. T. G. Theofanous, C. Liu, and W. W. Yuen, "Coolability and Quench of Corium-Concrete Interactions by Top-Flooding," MACE-TR-D14, Electric Power Research Institute (1998).
11. R. E. Blose, J. E. Gronager, A. J. Suo-Anttila, and J. E. Brockman, "SWISS: Sustained Heated Metallic Melt/Concrete Interactions With Overlying Water Pools," NUREG/CR-4727 (1987).
12. R. E. Blose, D. A. Powers, E. R. Copus, J. E. Brockmann, R. B. Simpson, and D. A. Lucero, "Core-Concrete Interactions with Overlying Water Pools - The WETCOR-1 Test," NUREG/CR-5907 (1993).
13. H. Nagasaka, M. Kato, I. Sakaki, Y. Cherepnin, Y. Vasilyev, A. Kolodeshnikov, V. Zhdanov, and V. Zuev, "COTELS Project (1): Overview of Project to Study FCI and MCCI During a Severe Accident," *OECD Workshop on Ex-Vessel Debris Coolability*, Karlsruhe, Germany, November 15-18, 1999.

14. H. Nagasaka, I. Sakaki, M. Kato, Y. Vasilyev, A. Kolodeshnikov, and V. Zhdanov, "COTELS Project (3): Ex-vessel Debris Cooling Tests," *OECD Workshop on Ex-Vessel Debris Coolability*, Karlsruhe, Germany, November 15-18, 1999.
15. M. T. Farmer, B. W. Spencer, D. J. Kilsdonk, and R. W. Aeschlimann, "Results of MACE Corium Coolability Experiments M0 and M1b," *Proceedings 8th Int. Conf. on Nucl. Eng.*, Baltimore, MD USA, April 2-6, 2000.
16. M. T. Farmer, B. W. Spencer, J. L. Binder, and D. J. Hill, "Status and Future Direction of the Melt Attack and Coolability Experiments (MACE) Program at Argonne National Laboratory," *Proceedings 9th Int. Conf. on Nucl. Eng.*, Nice, France, April 8-12, 2001.
17. M. T. Farmer, S. Lomperski, and S. Basu, "Results of Reactor Material Experiments Investigating 2-D Core-Concrete Interaction and Debris Coolability," *Proceedings ICAPP '04*, Pittsburgh, PA USA, June 13-17, 2004.
18. M. T. Farmer, S. Lomperski, and S. Basu, "The Results of the CCI-2 Reactor Material Experiment Investigating 2-D Core-Concrete Interaction and Debris Coolability," *11th Int. Topical Meeting on Nucl. Reactor Thermal-Hydraulics (NURETH-11)*, Avignon, France, October 2-6, 2005.
19. M. T. Farmer, S. Lomperski, D. Kilsdonk, R. W. Aeschlimann, and S. Basu, "A Summary of Findings from the Melt Coolability and Concrete Interaction (MCCI) Program," *Proceedings ICAPP '07*, Nice, France, May 13-18, 2007.
20. S. Lomperski and M. T. Farmer, "Experimental Evaluation of the Water Ingression Mechanism for Corium Cooling," *Nucl. Eng. Design*, **237**, 905 (2006).
21. S. Lomperski, M. T. Farmer, and S. Basu, "Experimental Investigation of Corium Quenching at Elevated Pressure," *Nucl. Eng. Design*, **236**, 2271 (2006).
22. S. Lomperski and M. T. Farmer, "Corium Crust Strength Measurements," *Nucl. Eng. Design*, **238**, 2551 (2009).
23. M. T. Farmer and B. W. Spencer, "Status of the CORQUENCH Model for Calculation of Ex-Vessel Corium Coolability by an Overlying Water Layer," *OECD Workshop on Ex-Vessel Debris Coolability*, Karlsruhe, Germany, November 15-18, 1999.
24. C. R. B. Lister, "Qualitative Theory on the Deep End of Geothermal Systems," *Proceedings 2nd UN Symposium on Development and Use of Geothermal Resources*, San Francisco, CA USA, May 20-29, 1975.
25. M. Epstein, "Dryout Heat Flux During Penetration of Water Into Solidifying Rock," *J. Heat Transfer*, **128**, 847 (2006).
26. H. Bjornsson, S. Bjornsson, and Th. Sigurgeirsson, "Penetration of Water into Hot Rock Boundaries of Magma at Grimsvotn," *Nature*, **295**, 580 (1982).
27. J. M. Bonnet and J. M. Seiler, "Coolability of Corium Spread Onto Concrete Under Water, the PERCOLA Model," *2nd CSNI Specialist Meeting on Core Debris-Concrete Interactions*, Karlsruhe, Germany, April 1-3, 1992.

28. B. Tourniaire, J. M. Seiler, J. M. Bonnet, and M. Amblard, "Liquid Ejection Through Orifices by Sparging Gas – The PERCOLA Program," *Proceedings 10th Int. Conf. on Nucl. Eng.*, Arlington, VA USA, April 2-6, 2000.
29. B. Tourniaire and J. M. Seiler, "Modeling of Viscous and Inviscid Fluid Ejection through Orifices by Sparging Gas," *Proceedings ICAPP '04*, Pittsburgh, PA USA, June 13-17, 2004.
30. M. T. Farmer, "Phenomenological Modeling of the Melt Eruption Cooling Mechanism During Molten Corium Concrete Interaction (MCCI)," Paper 6165, *Proceedings ICAPP '06*, Reno, Nevada USA, June 6-8, 2006.
31. G. Nazare, G. Ondracek, G., and B. Shulz, "Properties of Light Water Reactor Core Melts," *Nucl. Tech.*, **32**, 239 (1977).
32. H. R. Shaw, "Viscosities of Magmatic Silicate Liquids: An Empirical Method of Prediction," *American J. of Science*, **272**, 870 (1972).
33. M. Ishii and N. Zuber, "Drag Coefficient and Relative Velocity in Bubbly, Droplet, or Particle Flows," *AIChE Journal*, **25**, 843 (1979).
34. M. Kunitz, "An Empirical Formula for the Relationship between Viscosity of Solution and Volume of Solute," *J. General Physiology*, **9**, 715 (1926).
35. J. E. Brockmann, F. E. Arellano, and D. A. Lucero, "Validation of Models of Gas Holdup in the CORCON Code," NUREG/CR-5433 (1989).
36. G.B. Wallis, *One-Dimensional Two-Phase Flow*, 2nd Edition, McGraw Hill, New York, 1979.
37. Kataoka and M. Ishii, "Drift Flux Model for Large Diameter Pipe and New Correlation for Pool Void Fraction," *Int. J. Heat Mass Transfer*, **30**, 1927 (1987).
38. M. L. Corradini, "A Transient Model for the Ablation and Decomposition of Concrete," *Nucl. Tech.*, **62**, 263 (1983).
39. D. R. Bradley, "Modeling of Heat Transfer Between Core Debris and Concrete," *ANS Proc. 1988 National Heat Transfer Conf.*, Houston, Texas USA, July 24-28, 1988.
40. S. S. Kutateladze and I. G. Malenkov, "Boiling and Bubbling heat Transfer under the Conditions of free and Forced convection," *6th Int. Heat Transfer Conf.*, Toronto, Canada, August 7-11, 1978.
41. D. R. Bradley and D. R. Gardner, "CORCON-MOD3: An Integrated Computer Model for the Analysis of Molten Core-Concrete Interactions," NUREG/CR-5843 (1992).
42. T. Sevón, "A Heat Transfer Analysis of the CCI Experiments 1-3," *Nucl. Eng. Design*, **238**, 2377 (2008).
43. R. J. Lipinski, "A Particle-Bed Dryout Model with Upward and Downward Boiling," *Trans. Amer. Nucl. Soc.*, **35**, 358 (1980).
44. F. B. Ricou and D. B. Spalding, "Measurements of Entrainment of Axisymmetrical Turbulent Jets," *J. Fluid Mechanics*, **11**, 21 (1961).

45. R. J. Roark and W. C. Young, *Formulas for Stress and Strain*, 6th Ed., McGraw Hill, New York, 1975. (see pp. 480-482).
46. M. W. Chase *et al.*, *JANAF Thermochemical Tables*, 3rd Ed., American Chemical Society, Washington, D.C., 1985.
47. M. T. Farmer, S. Lomperski, D. J. Kilsdonk, and R. W. Aeschlimann, "OECD MCCI Project Final Report," OECD/MCCI-2005-TR06 (2006).
48. M. T. Farmer, R. W. Aeschlimann, D. J. Kilsdonk, and, S. Lomperski, "2-D Core Concrete Interaction (CCI) Tests: CCI-4 Final Report," OECD/MCCI-2007-TR06 (2007).
49. M. T. Farmer, D. J. Kilsdonk, S. Lomperski, and R. W. Aeschlimann, "CCI-5 Data Report," OECD/MCCI-2009-TR06 (2009).
50. F. G. Blottner, "Hydrodynamics and Heat Transfer Characteristics of Liquid Pool with Bubble Agitation," SAND79-1132, NUREG/CR-0844 (1979).
51. F. N. Peebles and H. J. Garber, "Study of Motion of Gas Bubbles in Liquids," *Chem. Eng. Prog.*, **44**, 88 (1953).
52. P.J. Berenson, "Film-Boiling Heat Transfer from a Horizontal Surface," *J. Heat Transfer*, **83**, 351 (1961).
53. G. I. Taylor, "The Instability of Liquid Surfaces when Accelerated in a Direction Perpendicular to Their Planes," *Proceedings of the Royal Society of London. Series A: Mathematical and Physical Sciences*, **201**, 192 (1950).
54. J. Szekely, "Mathematical Model for Heat and Mass Transfer at the Bubble-Stirred Interface of Two Immiscible Liquids," *Int. J. Heat Mass Transfer*, **6**, 307 (1963).
55. Sakurai, M. Shiotsu, and K. Hata, "Effect of System Pressure on Film-Boiling Heat Transfer, Minimum Heat Flux, and Minimum Temperature," *Nucl. Science and Eng.*, **88**, 321 (1984).
56. H. J. Ivey and D. J. Morris, "Critical Heat Flux of Saturation and Subcooled Pool Boiling in Water at Atmospheric Pressure," *Proceedings 3rd Int. Heat Trans. Conf.*, **3**, 129 (1966).
57. N. Zuber, "On the Stability of Boiling Heat Transfer," *Transaction of ASME*, **80**, 711 (1958).
58. R. E. Henry, "A Correlation for the Minimum Wall Superheat in Film Boiling," *Trans. Amer. Nucl. Soc.*, **15**, 420 (1972).
59. W. M. Rohsenow, "A Method of Correlating Heat Transfer Data for Surface Boiling Liquids," *Transactions of ASME*, **74**, 969 (1952).
60. F. Moreaux, J. C. Chevrier, and G. Beck, "Destabilization of Film Boiling by Means of a Thermal Resistance," *Int. J. Multiphase Flow*, **2**, 183 (1975).
61. M. T. Farmer, B. G. Jones and B. W. Spencer, "Analysis of Transient Contacting in the Low Temperature Film Boiling Regime, Part II: Comparison with Experiment," Proceedings 24th National Heat Transfer Conference, Pittsburgh, PA, August 9-12, 1987.
62. M. T. Farmer, R. W. Aeschlimann, D. J. Kilsdonk, and B. W. Spencer, "Results of MACE Test M3b Posttest Debris Characterization," EPRI/ACEX-TR-C32 (2000).

63. S. W. Jones, M. Epstein, S. G. Bankoff, and D. R. Pedersen, "Dryout Heat Fluxes in Particulate Beds Heated Through the Base," *Journal Heat Trans.* **106**, 176 (1984).
64. R. Seigel and J. R. Howell, *Thermal Radiation Heat Transfer*, 2nd Ed., McGraw Hill, New York, 1981. (see pp. 824).
65. B. Tourniaire, E. Dufour, and B. Spindler, "Foam Formation in Oxidic Pool with Application to MCCI Real Material Experiments," *Nucl. Eng. Design*, 239, 1971 (2009).
66. M. T. Farmer, S. Lomperski, D. J. Kilsdonk, and R. W. Aeschlimann, "OECD MCCI-2 Project Final Report," OECD/MCCI-2010-TR07 (2010).
67. L. Rayleigh, "On the Pressure Developed in a Liquid During the Collapse of a Spherical Cavity," *Phil. Mag.*, **34**, 94 (1917).
68. B. B. Chakraborty and G. S. Tuteja, "Motion of Expanding Spherical Bubble in a Viscous Liquid under Gravity," *Phys. Fluids A*, **5**, 1879 (1993).
69. V. K. Dhir, J. N. Castle, and I. Catton, "Role of Taylor Instability Sublimation of Horizontal Slab of Dry Ice," *J. Heat Transfer*, **99**, 411 (1977).
70. H. Alsmeyer and L. Barleon, "A Model Describing the Interaction of a Core Melt with Concrete," NURE/TR-0039 (1978).
71. L. S. Kao, M. Lee, and M. S. Kazimi, "Assessment of Heat Transfer Models for Corium-Concrete Interaction," *Proc. 3rd Int. Topical Mtg. on Reactor Thermal Hydraulics*, Newport, RI, October 15-18, 1985.
72. H. Alsmeyer, "BETA Experiments in Verification of the Wechsl Code: Experimental Results on the Melt-Concrete Interaction," *Nucl. Eng. Design*, **103**, 115 (1987).
73. T. Brooke Benjamin, "Gravity Currents and Related Phenomena," *J. Fluid Mech.*, Vol. 31, Part 2, pp. 209-248.
74. C. F. Colebrook, "Turbulent Flow in Pipes with Particular Reference to the Transition Region Between the Smooth and Rough Pipe Laws," *J. Institution Civil Engineering* (1939).
75. R. S. Hotchkiss, "Simulation of Tank Draining Phenomena with the NASA SOLA-VOF Code," LA-8163-MS, December 1979.
76. D. H. Thompson, J. K. Fink, D. R. Armstrong, B. W. Spencer, and B. R. Sehgal, "Thermal-Hydraulic Aspects of the Large-Scale MCCI Tests in the ACE Program," 2nd CSNI Specialist Meeting on Core Debris-Concrete Interactions, NEA/CSNI/R(92)10, Karlsruhe, Germany, April 1-3, 1992.
77. D. H. Thompson, M. T. Farmer, J. K. Fink, D. R. Armstrong, and B. W. Spencer, "ACE Phase C Final Report: Volume I-MCCI Thermalhydraulic Results," EPRI/ACE-TR-C42 (1997).
78. M. F. Roche, L. Leibowitz, J. K. Fink, and L. Baker, Jr., "Solidus and Liquidus Temperatures of Core-Concrete Mixtures," NUREG/CR-6032 (1993).
79. American National Standard for Decay Heat Power in Light Water Reactors, ANSI/ANS5.1-1994, American Nuclear Society, August 1994.

80. Barin and O. Knacke, *Thermophysical Properties of Inorganic Substances*, Springer-Verlag, New York, 1973.
81. J. H. Keenan and F. G. Keyes, *Thermodynamic Properties of Steam Including Data for the Liquid and Solid Phases*, J. Wiley and Sons, London, 1936.
82. M. W. Chase et al., *JANAF Thermochemical Tables*, 3rd Edition, American Institute of Physics, New York, 1986.
83. R. R. Hultgren, *Selected Values of the Thermodynamic Properties of the Elements*, American Society for Metals, Metals Park, Ohio, 1973.
84. G. V. Samsonov, Editor, *The Oxide Handbook*, 2nd Edition, translated from Russian by R. K. Johnston, IFI Plenum Press, New York, 1982.
85. G. V. Samsonov, Editor, *The Oxide Handbook*, translated from Russian by C. N. Turton and T. I. Turton, IFI Plenum Press, New York, 1973.
86. J. K. Fink, M. G. Chasanov, and L. Leibowitz, "Thermophysical Properties of Uranium Oxide," *J. Nucl. Materials*, **102**, 17 (1981).
87. R. C. Weast, Editor, *CRC Handbook of Chemistry and Physics*, 61st Edition, CRC Press, Boca Raton, Florida, 1981.
88. W. A. Lambertson and M. H. Mueller, "Uranium Oxide Phase Equilibrium Systems: III, $\text{UO}_2\text{-ZrO}_2$," *J. Am. Ceram. Soc.*, **36**, 365 (1953).
89. P. Y. Chevalier, E. Fischer, and B. Cheynet, "Progress in the Thermodynamic Modeling of the O-U-Zr Ternary System," *Computer Coupling of Phase Diagrams and Thermochemistry*, **28**, 15 (2004).
90. M. T. Farmer, B. W. Spencer, and R. W. Aeschlimann, "Liquidus/Solidus and Zr Solubility Measurements for PWR and BWR Core Melt Compositions," *OECD Workshop on Ex-Vessel Debris Coolability*, Karlsruhe, Germany, November 15-18, 1999.
91. ASM Handbook, *Alloy Phase Diagrams*, **3**, ASM International, Materials Park, OH, 1992.
92. P. Y. Chevalier, "Presentation of the OXY5-GEMINI2 Code," *Advanced Containment Experiments (ACE) Technical Advisory Committee Meeting*, EPRI Headquarters, Palo Alto, CA, November 4-8, 1991.
93. Y. S. Touloukian and C. Y. Ho, Editors, *Properties of Selected Ferrous Alloying Elements*, **III-1**, McGraw-Hill/CINDAS Data Series on Material Properties Evaluation, McGraw-Hill Book Company, New York, 1981.
94. Y. S. Touloukian, R. W. Powell, C. Y. Ho, and P. G. Klemens, Editors, *Thermophysical Properties of Matter. Thermal Conductivity of Metallic Elements and Alloys*, **1**, IFI Plenum Press, New York, 1970.
95. Y. S. Touloukian, R. W. Powell, C. Y. Ho, and P. G. Klemens, Editors, *Thermophysical Properties of Matter. Thermal Conductivity of Nonmetallic Solids*, **2**, IFI Plenum Press, New York, 1970.
96. R. Brandt and G. Neuer, "Thermal Conductivity and Thermal Radiation Properties of UO_2 ," *J. Non-Equilibrium Thermodynamics*, **1**, 3 (1976).

97. O. Wiener, "The Theory of Mixtures for Fields with Constant Currents," *Akademie der Wissenschaften, Leipzig, Math-Phys.Kl, Abhandlungen*, **32**, 507 (1912).
98. K. Lichteneker, "The Electrical Conductivity of Periodic and Random Aggregates," *Physikallsche Zeitschrift*, **27**, 115 (1926).
99. R. K. Cole, D. P. Kelley, and M. A. Ellis, "CORCON-MOD2: A Computer Program for Analysis of Molten Core-Concrete Interactions," NUREG/CR-3920 (1984).
100. L. S. Kao and M. S. Kazimi, "Thermal Hydraulics of Core/Concrete Interaction in Severe LWR Accidents," MITNE-276 (1987).
101. E. A. Brandes, Editor, *Smithells Metals Reference Book*, 6th Edition, Butterworths, Inc., London, 1983.
102. S. Z. Beer, Editor, *Liquid Metals Chemistry and Physics*, Marcel Dekker, Inc., New York, 1972.
103. Y. S. Touloukian, R. K. Kirby, R. E. Taylor, and J. Y. R. Lee, Editors, *Thermophysical Properties of Matter Thermal Expansion Nonmetallic Solids*, **13**, IFI Plenum Press, New York, 1977.
104. Y. S. Touloukian, R. K. Kirby, R. E. Taylor, and J. Y. R. Lee, Editors, *Thermophysical Properties of Matter Thermal Expansion Metallic Elements and Alloys*, **12**, IFI Plenum Press, New York, 1977.
105. Metals and Ceramics Information Center, *Engineering Property Data on Selected Ceramics, Single Oxides*, **3**, MCIC-HB-07, Battelle Columbus, 1981.
106. S. Glasstone and S. Sesonske, *Nuclear Reactor Engineering*, Van Nostrand Reinhold Co., New York, 1981.
107. T. Z. Harmathy, "Thermal Properties of Concrete at Elevated Temperatures," *J. Materials*, **5**, 47 (1970).
108. L. Baker, Jr., F. B. Cheung, and J. D. Bingle, "Transient Heat Transfer in Concrete," *European Appl. Res. Reports*, **1**, 281 (1979).
109. http://www.engineeringtoolbox.com/water-thermal-properties-d_162.html
110. http://www.engineeringtoolbox.com/saturated-steam-properties-d_101.html
111. http://www.engineeringtoolbox.com/water-surface-tension-d_597.html
112. https://en.wikipedia.org/wiki/Vapour_pressure_of_water
113. J. H. Lienhard, *A Heat Transfer Textbook*, Prentice Hall, New Jersey, 1981.
114. http://www.engineeringtoolbox.com/saturated-steam-properties-d_457.html
115. http://www.engineeringtoolbox.com/steam-viscosity-d_770.html
116. <https://srdata.nist.gov/CeramicDataPortal/Pds/Scdscs>
117. L. L. Snead et al., "Handbook of SiC properties for Fuel Performance Modeling," *Journal of Nuclear Materials* **371** 329 (2007).

118. C. Y. Ho, R. W. Powell, and P. El. Liley, "Thermal Conductivity of the Elements: A Comprehensive Review," *American Chemical Society Journal of Physical and Chemical Reference Data*, **3**, Supplement No. 1, 1974.
119. E. R. Copus, "Sustained Uranium Dioxide/Concrete Interaction Tests: The SURC Test Series," *2nd CSNI Specialist Meeting on Core Debris-Concrete Interactions*, NEA/CSNI/R(92)10, Karlsruhe, Germany, April 1-3, 1992.
120. C. Journeau et al., "Severe Accident Research at the PLINIUS Prototypic Corium Platform," *Proceedings ICAPP '04*, Seoul, Korea, May 15-19, 2005.
121. C. Journeau, P. Piluso, J.-F. Haquet, S. Saretta, E. Boccaccio, and J.-M. Bonnet, "Oxide-Metal Corium –Concrete Interaction Test in the VULCANO Facility," *Proceedings ICAPP '07*, Nice, France, May 13-18, 2007.
122. B. W. Spencer, M. Fischer, M. T. Farmer and D. R. Armstrong, "MACE Scoping Test Data Report," EPRI/MACE-TR-D03 (1991).
123. M. T. Farmer, J. K. Fink, and B. W. Spencer, "Results of MACE Scoping Test Chemical, Thermal, and Structural Property Measurements," EPRI/MACE-TR-D08 (1993).
124. M. T. Farmer, R. W. Aeschlimann, W. Gunther, D. Kilsdonk, and B. W. Spencer, "Results of MACE Scoping Test Sidewall Ablation Profile Measurements," EPRI/ACEX-TR-C-18 (1998).
125. M. T. Farmer, B. W. Spencer and D. R. Armstrong, "MACE Test M1b Data Report," EPRI/MACE-TR-D06 (1992).
126. M. T. Farmer et al., "MACE Test M3b Data Report - Vols. I-II," EPRI/ MACE-TR-D13 (1997).
127. M. T. Farmer, B. W. Spencer, D. R. Armstrong, D. J. Kilsdonk, and R. W. Aeschlimann, "MACE Test M4 Data Report," EPRI/MACE-TR-D15 (1999).
128. M. T. Farmer, S. Lomperski, D. J. Kilsdonk, R. W. Aeschlimann, and S. Basu, "2-D Core Concrete Interaction (CCI) Tests: CCI-2 Test Data Report-Thermalhydraulic Results," OECD/MCCI-2004-TR05 (2004).
129. M. T. Farmer, "The CORQUENCH Code for Modeling of Ex-Vessel Corium Coolability under Top Flooding Conditions, Additional Validation Against MACE Tests – Version 4.1-beta," ANL-NE/23, August 2018.

APPENDIX A: MATERIAL PROPERTIES EVALUATION

The objective of this appendix is to document the thermo-physical property subroutines incorporated into CORQUENCH4.1. The methods for evaluating the corium properties are described first, followed by a description of the methods used for evaluating the properties of the concrete. Finally, the methods for calculating the properties of the water coolant/vapor and concrete decomposition gases are described. Except where otherwise noted, SI units (kilograms, meters, seconds, degrees Kelvin) are used in all of the subroutines.

A.1 Corium Property Evaluation

A.1.1 Corium Enthalpy-Temperature Relationship

Given the mole fraction breakdown of the various metal and oxide constituents in the corium and the bulk corium temperature, subroutine ETF evaluates the corium specific enthalpy and the derivative of the specific enthalpy with respect to temperature. Conversely, given the corium specific enthalpy and the mole fraction breakdown, subroutine TEF evaluates the corium temperature and the derivative of the specific enthalpy with respect to temperature. In these subroutines, the corium is assumed to consist of distinct oxide and metal phases each of which is characterized by a solidus and liquids temperature. The solidus and liquids temperatures are required to be distinct (i.e., non-equal), and the enthalpy of each phase is assumed to vary linearly between the solidus and liquidus values. The metal and oxide corium constituents currently modeled in the code are shown in Table A-1.

For a given corium constituent below the solidus, a parabolic relationship between specific enthalpy and temperature is assumed; i.e.,

$$e_i(T) = a_{so,i} T^2 + b_{sol,i} T + c_{sol,i}, \quad (A-1)$$

where $a_{sol,i}$, $b_{sol,i}$, and $c_{sol,i}$ are the solid phase specific enthalpy coefficients. Conversely, above the liquidus, a linear relationship between corium specific enthalpy and temperature is assumed,

$$e_i(T) = b_{liq,i} T + c_{liq,i}, \quad (A-2)$$

where $b_{liq,i}$ and $c_{liq,i}$ are the liquid phase enthalpy coefficients. The solid and liquid phase coefficients are summarized in Table A-2 for the various corium/concrete constituents currently modeled in the code. These coefficients are initialized in subroutine CPROPI. The constituents with indices 1-22 in Table A-1 are treated as components of concrete, while constituents with indices 8-28 are treated as components of corium and solidified debris. The overlap of constituents with indices 8-22 accounts for the fact that concrete decomposition products are incorporated into the corium during concrete ablation. Thus, these constituents are common to both zones. The coefficients in Table A-2 have been defined such that specific enthalpy of the solid phase is equal to zero at a reference temperature of 298 K, with the exception of the decomposable concrete constituents $Ca(OH)_2$, $CaCO_3$, $CaMg(CO_3)_2$, Fe_2O_3 , and K_2O . The solid phase coefficients for these constituents have been defined such that the molar specific enthalpy evaluated from Eq. A-1 equals the heat of formation from the oxides at the reference temperature of 298 K. The assumed heats of formation for the decomposable concrete constituents are shown in Table A-3. Condensed water in the concrete also undergoes evaporation at the saturation temperature corresponding to the system pressure. However, the condensed ("solid") phase coefficients for this constituent have been defined such that the molar specific enthalpy at 298 K equals zero, while the vapor ("liquid")

phase coefficients have been defined such that the molar enthalpy at the saturation temperature ($T_{liq,H2O}$) equals the liquid phase enthalpy plus the latent heat of vaporization.

With the exception of the decomposable and evaporable concrete constituents, the liquid phase coefficients in Table A-2 have been defined such that the latent heat of fusion for a given corium constituent is given through the relationship,

$$\Delta e_{freeze,i} = e_i(T_{liq,i}) - e_i(T_{sol,i}) \quad (A-3)$$

where $T_{sol,i}$ and $T_{liq,i}$ are the constituent solidus/liquidus temperatures, which are taken equal to the solidus/liquidus for the particular (metal or oxide) phase of which the i^{th} corium constituent is a member.

Table A-1. Summary of Indicial Scheme for Corium/Concrete Interactions.

Index	Constituent	Notes
1	Ca(OH) ₂	Decomposable Concrete Constituents
2	CaCO ₃	
3	MgCa(CO ₃) ₂	
4	H ₂ O(l)	
5	H ₂ O(v)	
6	K ₂ O(s)	
7	K ₂ O(v)	
8	Na ₂ O	Concrete/Corium Constituents
9	TiO ₂	
10	SiO ₂	
11	CaO	
12	MgO	
13	Al ₂ O ₃	
14	FeO	
15	Fe ₂ O ₃	
16	Fe ₃ O ₄	
17	Fe	
18	Cr	
19	Ni	
20	Zr	
21	ZrO ₂	
22	B ₂ O ₃	Corium Constituents
23	U	
24	B ₄ C	
25	Si	
26	SiC	
27	Cr ₂ O ₃	
28	NiO	
29	UO ₂	

Table A-2. Summary of Solidus/Liquidus Specific Enthalpy Coefficients for the Materials Treated in CORQUENCH4.1.

Index	Constituent	$a_{sol} \cdot 10^3$ (J/mol·K ²)	b_{sol} (J/mol·K)	$c_{sol} \cdot 10^{-4}$ (J/mol)	b_{liq} (J/mol·K)	$c_{liq} \cdot 10^{-4}$ (J/mol)	Ref. No.
1	Ca(OH) ₂	12.37	90.61	-13.75	0.00	0.00	80
2	CaCO ₃	16.79	88.73	-20.57	0.00	0.00	80
3	MgCa(CO ₃) ₂	45.31	142.5	-74.38	0.00	0.00	80
4	H ₂ O(l)	18.56	62.80	-2.051	0.00	0.00	81
5	H ₂ O(v)	0.00	0.00	note a	0.00	note a	81
6	K ₂ O(s)	20.94	72.14	-38.65	0.00	0.00	80
7	K ₂ O(v)	0.00	0.00	0.00	0.00	note b	80
8	Na ₂ O	-2.452	106.5	-3.152	104.6	1.402	80
9	TiO ₂	2.717	67.5	-2.041	100.4	-1.093	82
10	SiO ₂	5.312	57.92	-1.773	85.77	-4.225	80
11	CaO	2.843	47.11	-1.429	62.76	4.331	80
12	MgO	2.533	44.85	-1.359	60.67	3.807	80
13	Al ₂ O ₃	6.587	108.3	-3.287	192.5	-8.202	82
14	FeO	4.719	49.32	-1.512	68.20	0.939	80
15	Fe ₂ O ₃	1.444	140.4	-12.19	142.3	3.915	80
16	Fe ₃ O ₄	0.0	203.4	-6.060	213.4	5.872	80
17	Fe	2.481	33.58	-1.023	46.02	-1.082	83
18	Cr	7.696	17.84	-0.600	39.33	0.075	83
19	Ni	2.036	29.16	-0.888	43.10	-0.938	83
20	Zr	0.00	33.07	-0.989	33.47	0.618	83
21	ZrO ₂	0.00	85.48	-2.549	100.4	1.713	84
22	B ₂ O ₃	42.89	44.68	-1.713	129.7	-3.212	82
23	U	0.00	44.34	-1.322	47.91	-0.971	83
24	B ₄ C	13.28	84.74	-2.645	136.0	3.749	82
25	Si	3.409	17.08	-0.539	31.38	2.995	83
26	SiC	0.00	49.57	-1.478	27.20	4.036	116-117
27	Cr ₂ O ₃	5.467	115.1	-3.480	156.9	2.312	82
28	NiO	3.922	48.15	-1.469	59.87	2.948	80, 84, 85
29	UO ₂	18.17	40.90	-0.808	130.9	-3.091	86

$$^a c = a_{sol,H_2O,liq} (T_{liq,H_2O})^2 + b_{sol,H_2O,liq} T_{liq,H_2O} + c_{sol,H_2O,liq} + 8.534 \cdot 10^{-2} (T_{liq,H_2O})^2 + 13.645 T_{liq,H_2O} + 4.752 \cdot 10^4$$

$$^b c = a_{sol,K_2O,liq} (T_{CaCO_3,liq})^2 + b_{sol,K_2O,liq} T_{CaCO_3,liq} + c_{sol,K_2O,liq}$$

Table A-3. Heat of Formation from the Oxides for the Various Concrete Decomposition Reactions Treated in CORQUENCH4.1.

Decomposition Reaction	Heat of Formation from the Oxides (kJ/mole)	Reference
$CaMg(CO_3)_2 \rightarrow CaO + MgO + 2 CO_2$	-697.26	82
$CoCO_3 \rightarrow CaO + CO_2$	-177.82	87
$Ca(OH)_2 \rightarrow CaO + H_2O$	-109.45	82
$K_2O, sol \rightarrow K_2 + 1/2 O_2$	-363.17	82
$Fe_2O_3 \rightarrow 2/3 Fe_3O_4 + 1/6 O_2$	-79.7	82

Within the freezing temperature range, a linear relationship between the corium specific enthalpy and temperature is assumed,

$$e_i(T)c_{freeze,i} + b_{freeze,i}T, \quad (A-4)$$

where:

$$c_{freeze,i} = e_i(T_{sol,i}) - T_{sol,i} \frac{\Delta e_{freeze,i}}{T_{liq,i} - T_{sol,i}}, \quad (A-5)$$

$$b_{freeze,i} = \frac{\Delta e_{freeze,i}}{T_{liq,i} - T_{sol,i}}. \quad (A-6)$$

Given the corium temperature, the corium specific enthalpy is then evaluated in subroutine ETF through the following expression:

$$e(T) = AT^2 + BT + C, \quad (A-7)$$

where:

$$A = \frac{1}{\bar{M}} \sum_i x_i a_i, \quad (A-8)$$

$$B = \frac{1}{\bar{M}} \sum_i x_i b_i, \quad (A-9)$$

$$C = \frac{1}{\bar{M}} \sum_i x_i c_i, \quad (A-10)$$

and $\bar{M} = \sum X_i M_i$. In these expressions, x_i is the mole fraction of the i^{th} corium constituent and is given by:

$$x_i = \frac{\frac{h_i \rho_i}{M_i}}{\sum_i \frac{h_i \rho_i}{M_i}}, \quad (A-11)$$

where m_i and M_i are the mass and molecular weights of the i^{th} corium constituent in the debris region under consideration, and a_i , b_i , and c_i are the corium specific enthalpy coefficients that are defined relative to the corium freezing temperature ranges as:

$$a_i = \begin{cases} a_{sol,i}; & T \leq T_{sol,i} \\ 0; & T_{sol,i} < T < T_{liq,i} \\ a_{liq,i}; & T \geq T_{liq,i} \end{cases} \quad (A-12)$$

$$b_i = \begin{cases} b_{sol,i}; & T \leq T_{sol,i} \\ b_{freeze,i}; & T_{sol,i} < T < T_{liq,i} \\ b_{liq,i}; & T \geq T_{liq,i} \end{cases} \quad (A-13)$$

$$c_i = \begin{cases} c_{sol,i}; & T \leq T_{sol,i} \\ c_{freeze,i}; & T_{sol,i} < T < T_{liq,i} \\ c_{liq,i}; & T \geq T_{liq,i} \end{cases} \quad (A-14)$$

The derivative of corium specific enthalpy with respect to temperature is used to evaluate the specific heat, and this is calculated from the derivative of Eq. A-7, viz.,

$$\frac{dT}{de} = \frac{1}{2AT+B}. \quad (A-15)$$

Given the specific enthalpy, subroutine TEF evaluates the corium temperature. This is accomplished by first calculating the specific enthalpy at the solidus and liquidus for both the metal and oxide phases of the corium with Eqs. A-7 through A-14 (i.e., four enthalpy- temperature points are determined). Given the enthalpies at the solidus and liquidus, the coefficients in Eq. A-7 are evaluated with Eqs. A-8 through A-11, in conjunction with the following expressions which are slightly revised forms of Eqs. A-12 through A-14,

$$a_i = \begin{cases} a_{sol,i}; & e \leq e_{sol,i} \\ 0; & e_{sol,i} < e < e_{liq,i} \\ a_{liq,i}; & e \geq e_{liq,i} \end{cases} \quad (A-16)$$

$$b_i = \begin{cases} b_{sol,i}; & e \leq e_{sol,i} \\ b_{freeze,i}; & e_{sol,i} < e < e_{liq,i} \\ b_{liq,i}; & e \geq e_{liq,i} \end{cases} \quad (A-17)$$

$$c_i = \begin{cases} c_{sol,i}; & e \leq e_{sol,i} \\ c_{freeze,i}; & e_{sol,i} < e < e_{liq,i} \\ c_{liq,i}; & e \geq e_{liq,i} \end{cases} \quad (A-18)$$

With the coefficients of Eq. A-7 determined, the corium temperature as a function of enthalpy is found by inverting this expression to obtain, for the case in which $A = 0$,

$$T = \frac{e-C}{B}, \quad (A-19)$$

and for the case in which $A \neq 0$,

$$T = \frac{1}{2} \frac{B}{A} + \sqrt{\frac{B^2}{4A^2} - \frac{(C-E)}{A}}. \quad (A-20)$$

Given the corium temperature from Eq. A-19 or A-20, the derivative of corium specific enthalpy with respect to temperature is then determined from Eq. A-15.

A.1.2 Corium Phase Diagram Evaluation

CORQUENCH4.1 evaluates the freezing temperature range (i.e., solidus and liquidus) for both the metal and oxide phases of the corium melt, and this data is used in the enthalpy-temperature evaluation described in the previous subsection. These temperatures are evaluated in subroutine PHASED.

The first step in this calculation is to determine the core-cladding mixture solidus-liquidus temperatures assuming fully oxidized conditions (UO_2 - ZrO_2). For the oxide phase, two sets of experimental data are used to evaluate these temperatures given the core-to-cladding ratio, as well as the type and amount of concrete oxides that are in solution with the core and cladding oxides. Given the U/Zr molar ratio, this is accomplished by first linearly interpolating the solidus and liquidus temperatures for the UO_2 - ZrO_2 mixture from a discretized version of the Lamberston-Mueller phase diagram;^[76] the data are shown graphically in Figure A-1. With these temperatures determined, the solidus-liquidus temperatures for the core-cladding-concrete mixture are then calculated using the data obtained by Roche et al.^[78] These solidus-liquidus data, obtained with PWR-type (i.e., $U/Zr = 1.64$) core melt compositions containing various amounts and types of concrete, are shown graphically in Figures A-2 and A-3. To facilitate extrapolation of this information to melt compositions for which the U/Zr ratio does not equal 1.64, Roche's data were converted to dimensionless form by defining the following parameters:

$$F_{sol} = \frac{T_{sol,L-M} - T_{sol,o}}{T_{sol,L-M} - T_{sol,con}} \quad (A-21)$$

$$F_{liq} = \frac{T_{liq,L-M} - T_{liq,o}}{T_{liq,L-M} - T_{liq,con}} \quad (A-22)$$

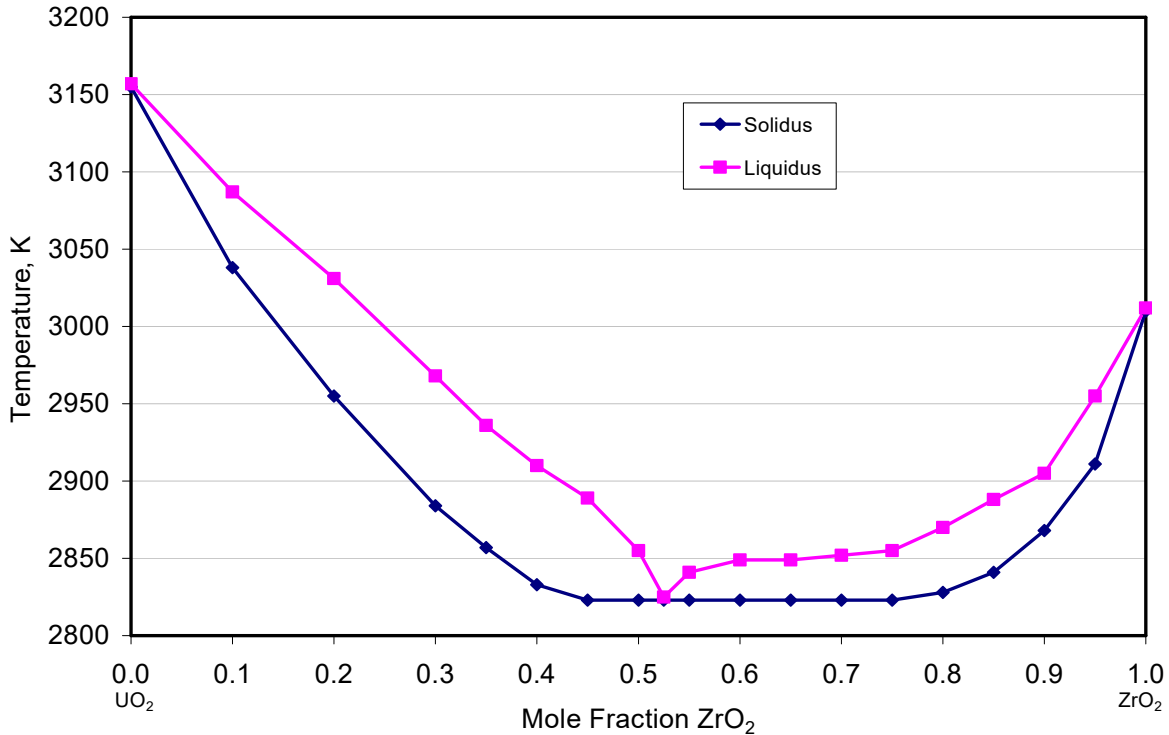


Figure A-1. Curve Fits to Lamberston and Mueller^[88] Phase Diagram Data.

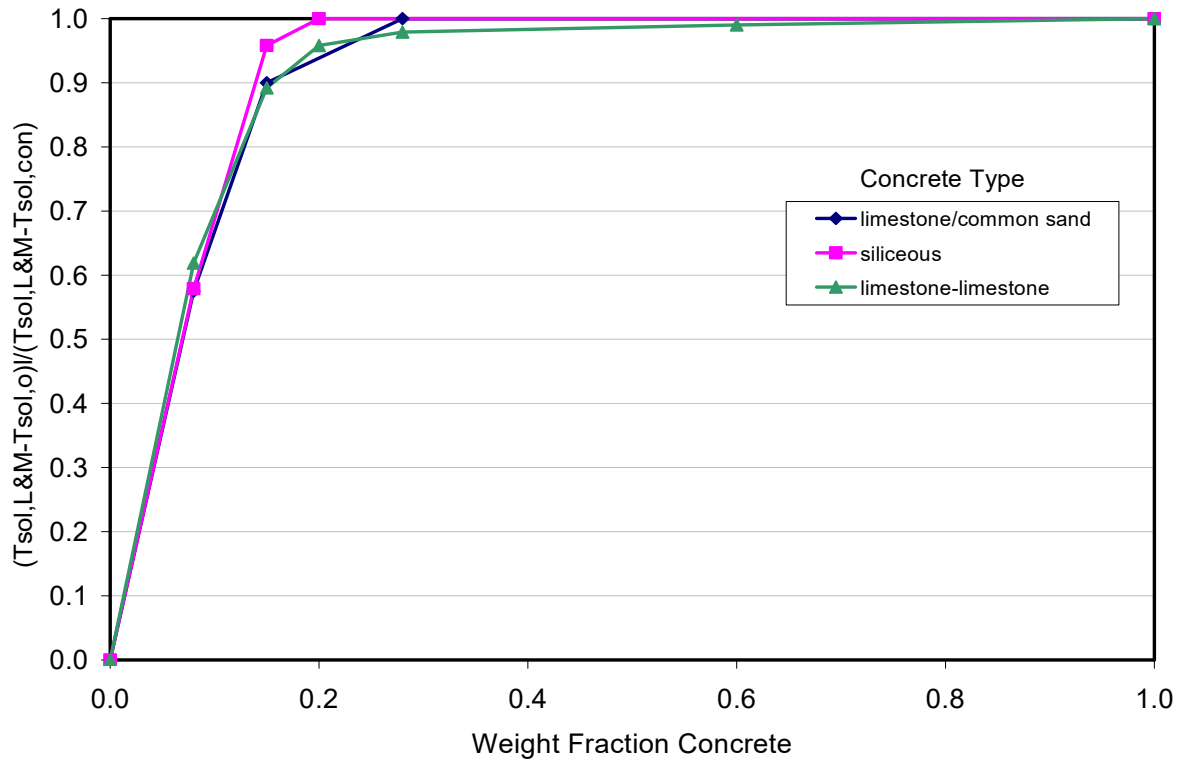


Figure A-2. Dimensionless Curve Fits to Roche et al.^[78] Solidus Temperature Data for PWR Corium Containing Various Levels and Types of Concrete.

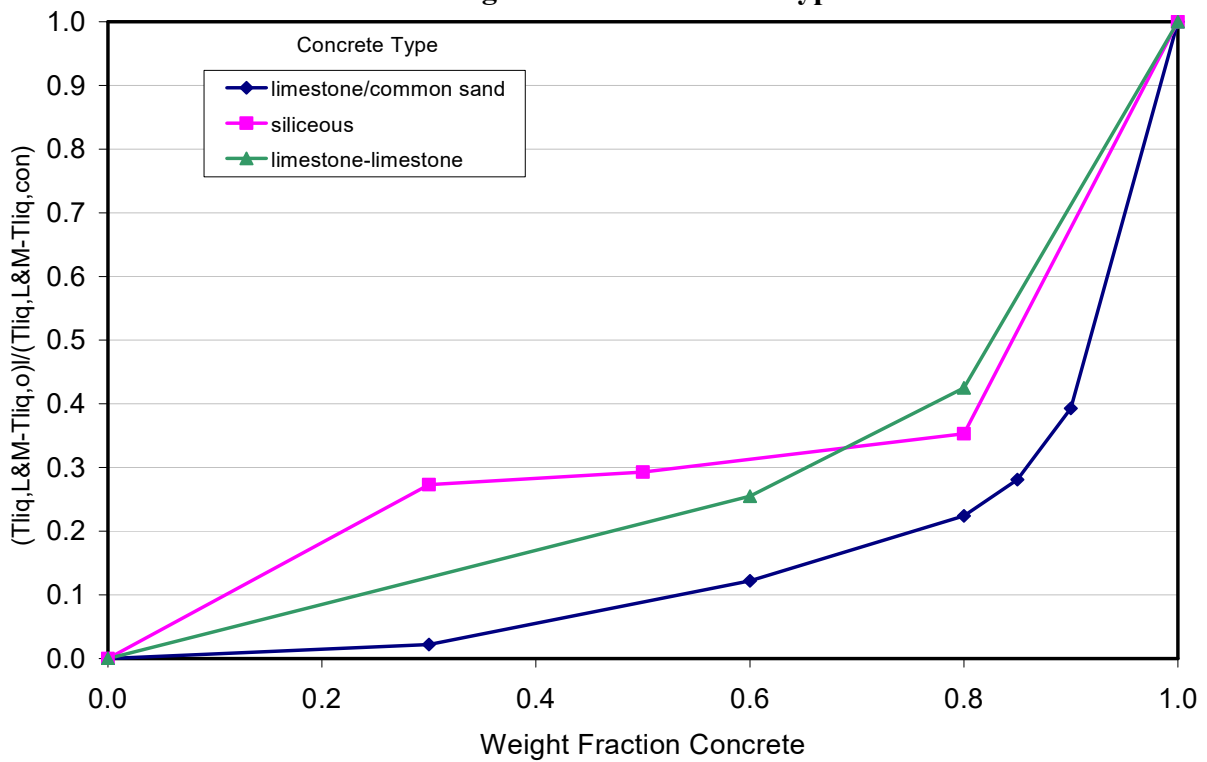


Figure A-3. Curve Fits to Roche et al.^[78] Liquidus Temperature Data for PWR Corium Containing Various Levels and Types of Concrete.

In Eq. A-21, $T_{sol,L-M}$ is the solidus temperature of the UO_2-ZrO_2 phase, $T_{sol,con}$ is the concrete solidus temperature, and $T_{sol,o}$ is the oxide phase solidus temperature. The variable definitions within the dimensionless liquidus function (Eq. A-22) are analogous to those for the solidus function. The solidus-liquidus temperatures for the various concrete types are provided in Table A-4; these data are also taken from Roche et al.^[78] Given the solidus-liquidus temperatures for the core-cladding mixture from the Lamberston-Muller data (Figure A-1), as well as the concrete solidus-liquidus data from Roche et al. (Table A-4), then the solidus-liquidus temperatures are determined by interpolation from the data shown in Figures A-2 and A-3, respectively, given the functions defined in Eqs. A-21 and A-22.

Table A-4. Solidus and Liquidus Temperatures for Several Concrete Types.^[78]

Temperature	Concrete Type		
	Limestone/common sand	Siliceous	Limestone-limestone
Solidus (K)	1393	1403	1495
Liquidus (K)	1568	1523	2577

Once the core-concrete oxide phase solidus and liquidus temperatures are evaluated under fully oxidized conditions, then the second step in the analysis is to calculate the solidus and liquidus temperatures for the fuel and cladding mixture if the cladding is only partially oxidized. This is accomplished by interpolating from the pseudo-binary $(U,Zr)O_{2-x}$ phase diagram that is shown in Figure A-4. This diagram has been constructed from various data sources. In particular, data shown on the left hand side of the graph for the UO_2-Zr vertical section are taken from the work of Chevalier et al.^[89] On the right hand side of the graph, the UO_2-ZrO_2 vertical section data are taken from the Lambertson-Mueller phase diagram^[88] shown in Figure A-1. Solidus-liquidus data in the range of 30-70 % cladding oxidation are taken from Farmer and Spencer.^[90] The balance of the data points have been estimated to provide a smooth transition between regions of the graph where data do not exist.

The overall methodology for calculating the oxide phase solidus-liquidus temperatures can then be summarized as follows. The solidus and liquidus are first calculated through Eqs. A-21 and A-22 assuming a fully oxidized melt with concrete present. Second, when Zr metal is present, the solidus and liquidus for the partially oxidized $(U,Zr)O_{2-x}$ phase are interpolated from the data shown in Figure A-4. The actual oxide phase solidus and liquidus temperatures used in the core-concrete interaction calculation are then set equal to the minimum values assessed using these two approaches. Although this approach is empirical, it nonetheless allows cases involving partially oxidized core melts to be treated with a systematic transition to fully oxidized melt conditions.

For the metal phase, the code first checks to see if stainless steel is present. If stainless is present, then the solidus and liquidus temperatures are calculated using an interpolation table that was developed on the basis of the $Fe-Cr-Ni$ ternary phase diagrams.^[91] If additional metals are present in the melt [e.g., Si , U , B_4C or Zr , if the Zr is assumed to be in solution with the metal phase (IEUTEC=0) as opposed to the core oxide phase (IEUTEC=1)], then the final metal phase solidus and liquidus temperatures are calculated based on a molar weighting of the melting points for the various metals present in the melt. This latter approach is admittedly first-order. However, evaluating the metal phase melting points on the basis of a detailed multi-component phase diagram analysis is beyond the scope of this work.

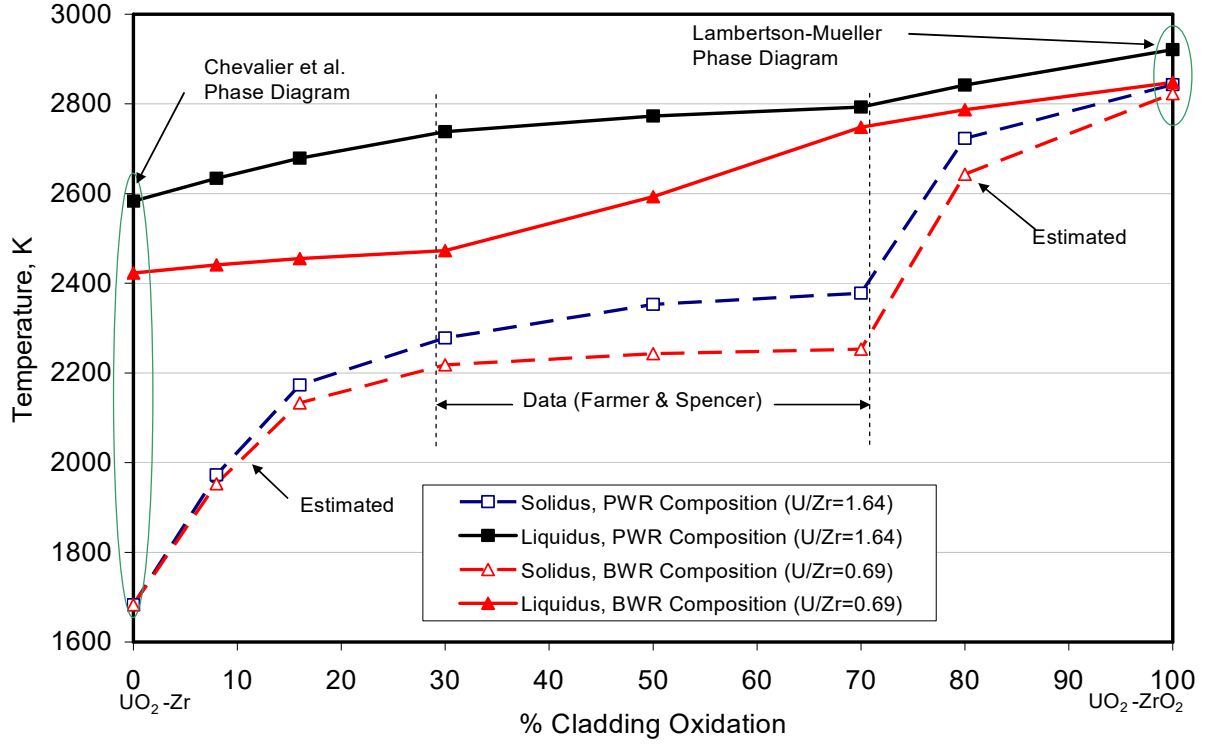


Figure A-4. (U,Zr)O_{2-x} Phase Diagram Constructed from Various Data Sources.

In terms of evaluating the melt solid fraction, which is important in the viscosity evaluation described later in this appendix, the code first evaluates the solid fractions of both the metal and oxide phases, and with these two results, the total melt solids fraction is evaluated from:

$$V_{sol} = (1 - \phi_o) V_o + (1 - \phi_m) V_m \quad (\text{A-23})$$

where ϕ_m and ϕ_o denote the solid fractions in the metal and oxide phases, respectively, and V_m and V_o are the volume fractions of these two phases in the melt. The volume fractions are evaluated through the equations:

$$V_m = \frac{\sum_{\text{metals}} m_i / \rho_i}{\sum_i m_i / \rho_i} \quad (\text{A-24})$$

$$V_o = 1 - V_m = \frac{\sum_{\text{oxides}} m_i / \rho_i}{\sum_i m_i / \rho_i} \quad (\text{A-25})$$

For the metal phase, the solid fraction in Eq. A-23 is assumed to vary linearly between the solidus and liquidus; i.e.,

$$\phi_m = \frac{T - T_{sol,m}}{T_{liq,m} - T_{sol,m}}; T_{sol,m} \leq T \leq T_{liq,m} \quad (\text{A-26})$$

where $T_{sol,m}$ and $T_{liq,m}$ denote the metal phase solidus/liquidus temperatures, respectively. For the oxide phase, the user has two options for evaluating the solid fraction. The first is that the fraction is assumed to vary linearly as for the metal phase (NSOLID = 2); i.e.,

$$\phi_o = \frac{T - T_{sol,o}}{T_{liq,o} - T_{sol,o}}; T_{sol,o} \leq T \leq T_{liq,o} \quad (A-27)$$

In the second case (NSOLID=1), the solid fraction is evaluated on the basis of early phase diagram calculations that were performed by Chevalier^[92] using the OXY5-GEMINI2 code for the case of PWR core melt containing siliceous concrete. As part of the current work, these computed results were normalized by defining the following dimensionless temperature:

$$F = \frac{T_{liq,o} - T}{T_{liq,o} - T_{sol,o}}; T_{sol,o} \leq T \leq T_{liq,o} \quad (A-28)$$

The result is shown in Figure A-5. Although this calculation is based on melt containing siliceous concrete, it is nonetheless used to evaluate the oxide phase solid fraction for other concrete types (e.g., limestone/common sand and limestone-limestone) by using the composition-specific solidus/liquidus temperatures in Eq. A-28. Ideally, different versions of Figure A-5 would be developed for different concretes, but the required data is not readily available in the open literature. In lieu of such information, the approach described above is used for evaluating the oxide phase solid fraction for all concrete types.

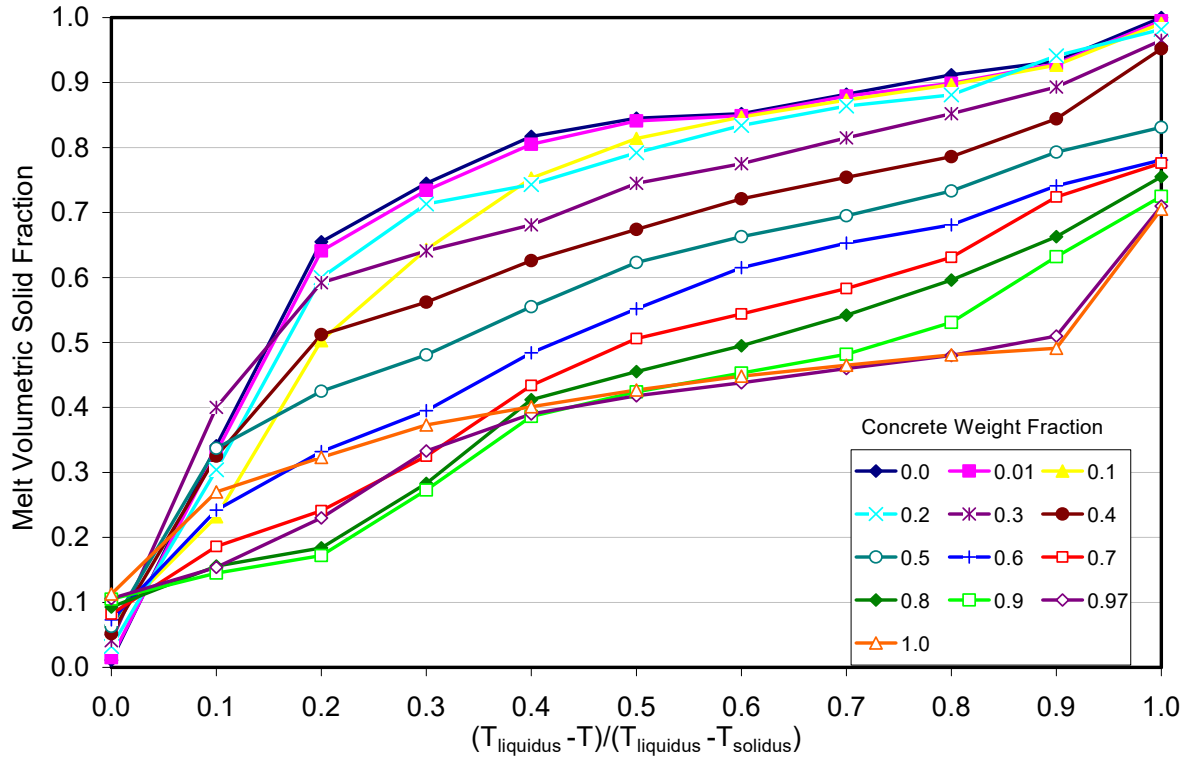


Figure A-5. Oxide Phase Solid Fraction vs. Normalized Temperature. (constructed on the basis of early OXY5-GEMINI2 calculations by Chevalier^[92]).

A.1.3 Corium Thermal Conductivity Evaluation

Given the corium constituent masses and the temperature, the thermal conductivity is evaluated through subroutine CONDF. In this subroutine, the corium is assumed to consist of distinct oxide and metal phases, each of which is characterized by a solidus and liquidus temperature. The metal and oxide phase conductivities are evaluated through the support routines CONDM and CONDO that are called by subroutine CONDF. For a given corium constituent, the thermal conductivity is evaluated through an expression of the form,

$$k_i = \sum_{j=0}^6 C_j^i (T_R^i)^j \quad (\text{A-29})$$

where C_j^i ($j=0, 1, \dots, 6$) are the thermal conductivity coefficients for the i^{th} corium constituent and T_R^i is the normalized corium temperature. The normalized temperature and conductivity coefficients are defined in Tables A-5 and A-6 for the corium metal and oxide phase constituents, respectively. For the metal phase below the solidus temperature, the effective thermal conductivity is evaluated using a volume weighting method based on the conductivities of the individual corium constituents; i.e.,

$$k_m = \sum_{\text{metals}} V_i k_i \quad (\text{A-30})$$

where:

$$V_i = \frac{m_i / \rho_i}{\sum_{\text{metals}} m_i / \rho_i} \quad (\text{A-31})$$

In this equation, ρ_i is the density of the i^{th} corium constituent and k_i is given through Eq. A-29. Note that the sum on i in Eqs. A-30 and A-31 is over the metal phase constituents of the corium. Above the metal phase liquidus, the effective thermal conductivity is approximated as a constant, and is calculated as,

$$k_{\text{liq}, m} = \frac{k_{\text{sol}, m}}{\beta_m} \quad (\text{A-32})$$

where $k_{\text{sol}, m} = k_m(T_{\text{sol}, m})$ denotes the metal phase conductivity evaluated at the metal solidus temperature through Eq. A-30, and β_m is a constant which is currently taken equal to 1.6. As discussed by Nazare *et al.*,^[31] this ratio is appropriate for metals such as iron that immediately below the solidus forms a crystalline structure in which each atom has eight nearest neighbors. When the corium temperature lies between the metal phase solidus and liquidus, the thermal conductivity is evaluated using the parallel conductance model proposed by Wiener^[97] assuming a linear relationship between corium temperature and liquid fraction within the freezing transition,

$$k_m = \frac{1}{\frac{1 - \phi_m}{k_{\text{sol}, m}} + \frac{\phi_m}{k_{\text{sol}, m}}} \quad (\text{A-33})$$

where the metal phase solid fraction is given by Eq. A-26.

Table A-5. Metal Phase Constituent Coefficients for Thermal Conductivity below the Solidus.

Metal Phase Constituent	Definition of T_R	C_0	C_1	C_2	C_3	C_4	C_5	C_6	Ref.
Stainless (Fe, Cr, Ni)	$\frac{1700 \cdot T}{T_{sol,m}}$	8.116	$1.618 \cdot 10^{-2}$	-----	-----	-----	-----	-----	93
Zr	$\frac{2098 \cdot T}{T_{sol,m}}$	7.510	$2.090 \cdot 10^{-2}$	$-1.450 \cdot 10^{-5}$	$7.670 \cdot 10^{-9}$	-----	-----	-----	94
U	$\frac{1405 \cdot T}{T_{sol,m}}$	21.64	$1.859 \cdot 10^{-2}$	$3.539 \cdot 10^{-6}$	-----	-----	-----	-----	94
B ₄ C	$\frac{2743 \cdot T}{T_{sol,m}}$	65.51	$-1.625 \cdot 10^{-1}$	$2.289 \cdot 10^{-4}$	$-1.786 \cdot 10^{-7}$	$7.892 \cdot 10^{-11}$	$1.833 \cdot 10^{-14}$	$1.736 \cdot 10^{-18}$	94
Si ¹	$\frac{1685 \cdot T}{T_{sol,m}}$	269.25	$-5.432 \cdot 10^{-1}$	$4.084 \cdot 10^{-4}$	$-1.009 \cdot 10^{-7}$	-----	-----	-----	118

¹Polynomial curve fit to the data in Reference [118].

Table A-6. Oxide Phase Constituent Coefficients for Thermal Conductivity Below the Solidus.

Oxide Phase Const.	Definition of T_R	C_0	C_1	C_2	C_3	C_4	C_5	C_6	Ref.
UO ₂	$\frac{3120 \cdot T}{T_{sol,o}}$	14.04	$-2.315 \cdot 10^{-2}$	$2.076 \cdot 10^{-5}$	$-9.661 \cdot 10^{-9}$	$1.797 \cdot 10^{-12}$	$1.101 \cdot 10^{-16}$	$-5.381 \cdot 10^{-20}$	96 ¹
ZrO ₂	$\frac{2973 \cdot T}{T_{sol,o}}$	0.835	$1.810 \cdot 10^{-4}$	-----	-----	-----	-----	-----	95
CaO	$\frac{2289 \cdot T}{T_{sol,o}}$	$2.619 \cdot 10^{-2}$	$2.209 \cdot 10^{-1}$	$-1.108 \cdot 10^{-3}$	$2.433 \cdot 10^{-6}$	$-2.731 \cdot 10^{-9}$	$1.534 \cdot 10^{-12}$	$-3.442 \cdot 10^{-16}$	95
MgO	$\frac{3098 \cdot T}{T_{sol,o}}$	$1.236 \cdot 10^{-2}$	$-3.792 \cdot 10^{-1}$	$5.394 \cdot 10^{-4}$	$-4.150 \cdot 10^{-7}$	$1.758 \cdot 10^{-10}$	$3.806 \cdot 10^{-14}$	$3.291 \cdot 10^{-18}$	95
SiO ₂	$\frac{1996 \cdot T}{T_{sol,o}}$	22.56	$-1.042 \cdot 10^{-1}$	$2.278 \cdot 10^{-4}$	$-2.354 \cdot 10^{-7}$	$9.425 \cdot 10^{-11}$	-----	-----	95
Fe ₃ O ₄	$\frac{1870 \cdot T}{T_{sol,o}}$	4.14	-----	-----	-----	-----	-----	-----	95
SiC ¹	$\frac{3003 \cdot T}{T_{sol,o}}$	26.3	-----	-----	-----	-----	-----	-----	116

¹Polynomial curve fit to the exponential expression recommended by Brandt and Neuer.^[96]

²SiC is clearly not an oxide but rather a carbide. CORQUENCH4.1 currently does not have the capability to treat a separate carbide phase; thus, SiC is lumped in with the oxides in order to evaluate the thermophysical properties. The thermal conductivity is at 1773 K^[116]

For the corium oxide phase below the oxide solidus, the effective thermal conductivity is also evaluated through a volume weighting of the individual constituent conductivities,

$$k_o = \sum_{oxides} V_i k_i \quad (\text{A-34})$$

where, in this case:

$$V_i = \frac{\frac{m_i}{\rho_i}}{\sum_{oxides} \frac{m_i}{\rho_i}} \quad (\text{A-35})$$

and k_i is given through Eq. A-29. Above the oxide liquidus, the effective thermal conductivity is currently assumed to equal the thermal conductivity at the oxide solidus, i.e.,

$$k_{liq,o} = k_o(T_{sol,o}) \quad (\text{A-36})$$

where $k_o(T_{sol,o})$ is evaluated through Eq. A-34.

Given the thermal conductivities of the metal and oxide phases, the effective mixture conductivity is evaluated as the weighted geometric mean of the metal/oxide phase conductivities using the correlation of Lichtenecker;^[98] i.e.,

$$k_{eff} = k_c^{V_c} k_d^{1-V_c} \quad (\text{A-37})$$

where V_c is the volume fraction of the continuous phase and is defined as:

$$V_c = \begin{cases} V_m, & V_m \geq 0.5, \\ V_o, & V_m < 0.5 \end{cases} \quad (\text{A-38})$$

with the metal and oxide phase volume fractions V_m and V_o in the corium mixture defined in Eqs. A-24 and A-25.

The continuous and dispersed phase thermal conductivities in Eq. A-37 are similarly defined as:

$$k_c = \begin{cases} k_m, & V_m \geq 0.5, \\ k_o, & V_m < 0.5 \end{cases} \quad (\text{A-39})$$

$$k_d = \begin{cases} k_o, & V_m \geq 0.5, \\ k_m, & V_m < 0.5 \end{cases} \quad (\text{A-40})$$

A.1.4 Corium Viscosity Evaluation

Given the corium temperature and melt constituent masses, subroutine VISCF evaluates the bulk corium dynamic viscosity. In this subroutine, the corium is assumed to consist of distinct oxide and metal phases, each of which is characterized by a solidus and liquidus temperature. The solidus and liquidus temperatures are required to be distinct, and the solid fraction in each phase is assumed to vary linearly between the solidus and liquidus values. The oxide and metal liquid phase viscosities are evaluated using the Da Andrade formula^[31] at a melting temperature corresponding to the solidus for each phase. For the metal liquid phase, the viscosity is evaluated through the equation,

$$\mu_m(T) = 6.12 \cdot 10^{-5} \frac{(T_{sol,m} A_m)^{1/2}}{V_m^{2/3}} \exp\left(\frac{Q_m}{RT} - \frac{Q_m}{RT_{sol,m}}\right), \quad (A-41)$$

where R is the ideal gas constant [8.3143 J/(mol·K)], A_m is the gram-atomic weight of metal phase, i.e.,

$$A_m = \frac{10^3 \cdot \sum_{metals} X_i M_i}{\sum_{metals} X_i}, \quad (A-42)$$

and V_m is the molar volume of metal phase in cm³; viz.,

$$V_m = \frac{10^6 \cdot \sum_{metals} X_i M_i / \rho_i}{\sum_{metals} X_i}, \quad (A-43)$$

Finally:

$$Q_m = 1.8033 T_{sol,m}^{1.348}. \quad (A-44)$$

Similarly, the oxide liquid phase viscosity is evaluated through the expression,

$$\mu_o(T) = 6.12 \cdot 10^{-5} \frac{(T_{sol,o} A_o)^{1/2}}{V_o^{2/3}} \exp\left(\frac{Q_o}{RT_{ev}} - \frac{Q_o}{RT_{sol,o}}\right), \quad (A-45)$$

where:

$$A_o = \frac{10^3 \cdot \sum_{oxides} X_i M_i}{\sum_{oxides} X_i}, \quad (A-46)$$

$$V_o = \frac{10^6 \cdot \sum_{oxides} X_i M_i / \rho_i}{\sum_{oxides} X_i}, \quad (A-47)$$

$$Q_o = 1.8033 T_{sol,o}^{1.348}. \quad (A-48)$$

$$T_{ev} = \begin{cases} T; & T \geq T_{sol,o} \\ T_{sol,o}; & T < T_{sol,o} \end{cases}. \quad (A-49)$$

When the oxide phase contains an appreciable amount of silica (SiO_2), the viscosity is increased substantially by the formation of bonded chains of SiO_4 tetrahedra.^[32] In this case the viscosity of the liquid oxide phase is evaluated using the Shaw¹² model,^[32]

$$\mu_o(T) = \exp[s(10^4/T_{ev} - 1.5) - 6.40], \quad (A-50)$$

where:

$$s = \frac{(\sum_i X_i Y_i S_i) X_{SiO_2}}{\sum_i X_i Y_i (\sum_i X_i + X_{SiO_2})}, \quad (A-51)$$

and the factors Y_i and S_i are provided in Table A-7. In subroutine VISCF, the actual oxide liquid phase viscosity $\mu_o(T)$ is set equal to the larger of the two viscosities predicted by the Da Andrade^[31] and Shaw^[32] viscosity models (i.e., Eqs. A-45 and A-50, respectively).

Given the above expressions for the temperature-dependent metal and oxide phase viscosities, then the effective liquid-solid mixture viscosity is evaluated using either the expressions proposed by Ishii and Zuber^[33] or Kunitz.^[34] Implementation of these models requires the specification of the liquid (continuous) and solid (dispersed) phase viscosities, as well as the

¹²The Shaw viscosity model was implemented in CORCON MOD2.^[99]

total volume fraction of the liquid and solid phases in the corium. The methods for calculating the metal and oxide phase solid fractions ϕ_m and ϕ_o were described previously in Section A.1.2. The metal and oxide fractions in the solid phase are then given through the following expressions:

$$V_{sol,m} = \frac{(1-\phi_m)V_m}{V_{sol}} \quad (A-52)$$

$$V_{sol,o} = \frac{(1-\phi_o)V_o}{V_{sol}} \quad (A-53)$$

where, as a reminder, V_m and V_o are the metal and oxide volume fractions in the corium mixture (see Eqs. A-24 and A-25), and the total solids fraction V_{sol} is given by Eq. A-23. Similarly, the metal and oxide fractions in the liquid phase are given through the expressions:

$$V_{liq,m} = \frac{\phi_m V_m}{1-V_{sol}}, \quad (A-54)$$

$$V_{liq,o} = \frac{\phi_o V_o}{1-V_{sol}}, \quad (A-55)$$

Table A-7. Factors Employed in the Shaw Viscosity Methodology^[32] for the Oxide Mixtures Containing Silica.

Constituent ¹	Y _i	S _i
TiO ₂	1.0	4.5
CaO	1.0	4.5
MgO	1.0	3.4
Al ₂ O ₃	2.0	6.7
FeO	1.0	3.4
Fe ₂ O ₃	2.0	3.4
Cr ₂ O ₃	2.0	3.4
UO ₂	1.0	4.5
ZrO ₂	1.0	4.5

¹Y_i and S_i are set equal to zero for any constituents not shown in the table

Given the above expressions, the continuous and dispersed phase viscosities are then calculated as,

$$\mu_c = V_{liq,m} \mu_m(T) + V_{liq,o} \mu_o(T), \quad (A-56)$$

$$\mu_d = V_{sol,m} \mu_m(T_{sol,m}) + V_{sol,o} \mu_o(T_{sol,o}), \quad (A-57)$$

where $\mu_m(T)$ and $\mu_m(T_{sol,m})$ are evaluated from Eq. A-41, $\mu_o(T_{sol,o})$ is evaluated from Eq. A-45, and $\mu_o(T)$ is evaluated from the larger of Eqs. A-45 and A-50. Given the viscosities of the continuous and dispersed phases, the effective liquid/solid mixture viscosity based on the Ishii-Zuber^[33] correlation is given as:

$$\mu = \mu_c \left(1 - \frac{V_{sol}}{V_{sol,max}} \right)^{-2.5 V_{sol,max} \left(\frac{\mu_d + 0.4 \mu_c}{\mu_d + \mu_c} \right)}, \quad (A-58)$$

where $V_{sol,max}$ is the maximum solid phase packing fraction which is a user-defined constant (See Section 3.0). Conversely, when the Kunitz correlation has been selected, the effective viscosity is calculated from:^[34]

$$\mu = \mu_c \left[\frac{1 + \frac{1}{2} \frac{V_{sol}}{V_{sol, \max}}}{\left(1 - \frac{V_{sol}}{V_{sol, \max}}\right)^4} \right] \quad (A-59)$$

A.1.5 Corium Emissivity Evaluation

Given the corium composition, subroutine EMISF evaluates the effective radiative emissivity based on a volumetric weighting of the emissivities for the metal and oxide phases. Currently, the emissivities of the metal and oxide phases are treated as constants using the following representative values for iron^[93] and UO₂^[86] respectively:

$$\epsilon_m = 0.30, \quad (A-60)$$

$$\epsilon_o = 0.83. \quad (A-61)$$

The effective metal/oxide mixture emissivity is thus evaluated through the equation,

$$\epsilon = V_m \epsilon_m + V_o \epsilon_o, \quad (A-62)$$

where V_m and V_o are defined in Eqs. A-24 and A-25, respectively.

A.1.6 Corium Surface Tension Evaluation

Given the corium composition, subroutine TEN evaluates the effective corium surface tension based on a volumetric weighting of the surface tensions for the metal and oxide phases. Currently, the surface tensions of the metal and oxide phases are treated as constants using the representative values suggested by Kao and Kazimi:^[100]

$$\sigma_m = 1.73, \quad (A-63)$$

$$\sigma_o = 0.52. \quad (A-64)$$

The effective metal/oxide mixture surface tension is thus evaluated through the equation,

$$\sigma = \sigma_m V_m + \sigma_o V_o, \quad (A-65)$$

where V_m and V_o are defined in Eqs. A-24 and A-25, respectively.

A.1.7 Corium Density Evaluation

Given the corium constituency, subroutine DENR evaluates the material density based on a volumetric weighting of the densities for the individual corium constituents. The assumed liquid and solid phase densities for the various corium constituents currently modeled in the code are shown in Table A-8. In particular, the average density of the metal/oxide mixture is calculated through the expression:

$$\rho = \frac{1}{\sum_i X_i / \rho_i} \quad (A-66)$$

where X_i is the mass fraction of the i-th constituent and ρ_i is the constituent density.

A.1.8 Corium Mechanical Properties Evaluation

Given the corium crust composition, the mechanical properties (i.e., linear expansion coefficient, tensile strength, and elastic modulus) are calculated using a volumetric weighting method. In particular, if P_i is defined as a mechanical property for the i^{th} corium constituent, then the mechanical property \bar{P} for the mixture is calculated as:

$$\bar{P} = \sum_{i=1} V_i P_i \quad (\text{A-67})$$

where V_i is the volume fraction of the i^{th} corium constituent. The linear expansion coefficient, tensile strength, and elastic modulus database^[101-106,116] for the various constituents used to calculate the crust mechanical properties from the above equation are summarized in Table A-9.

Table A-8. Assumed Liquid and Solid Phase Densities for the Various Corium Constituents Modeled by CORQUENCH4.1.

Index	Constituent	Solid Density (kg/m ³)	Reference	Liquid Density (kg/m ³)	Reference
1	Ca(OH) ₂	2240	87	----	
2	CaCO ₃	2710	87	----	
3	MgCa (CO ₃)	2872	87	----	
4	H ₂ O(l)	----		997	87
5	H ₂ O(v)	----		----	
6	K ₂ O(s)	2320	87	2320	footnote 1
7	K ₂ O(v)	----		----	
8	Na ₂ O	2270	87	2270	footnote 1
9	TiO ₂	4260	87	4021	103
10	SiO ₂	2200	87	2130	103
11	CaO	3250	87	2879	103
12	MgO	3580	87	3144	103
13	Al ₂ O ₃	3965	87	3741	103
14	FeO	5700	87	5329	103
15	Fe ₃ O ₃	5240	87	4950	103
16	Fe ₃ O ₄	5180	87	4725	103
17	Fe	7867	101	7010	102
18	Cr	7190	101	6280	101
19	Ni	8908	101	7770	102
20	Zr	6500	101	6060	102
21	ZrO ₂	5991	84	5800	103
22	B ₂ O ₃	1812	87	1812	footnote 1
23	U	19000	87	17905	103
24	B ₄ C	2520	87	2396	104
25	Si	2330	87	2570	104
26	SiC	3080	116	3080	116
27	Cr ₂ O ₃	5210	87	4942	103
28	NiO	6670	87	6043	103
29	UO ₂	10970	86	8739	86

¹Data not available; liquid phase density assumed equal to solid phase density.

Table A-9. Database^[101-106,116] for Evaluating Crust Mechanical Properties in CORQUENCH4.1.

Corium Constituent	Elastic Modulus (GPa)	Tensile Strength (MPa)	Linear Expansion Coefficient (10^{-6} m/m-K)
UO ₂	190	117	9.5
ZrO ₂	250	80	7.5
Cr ₂ O ₃	200 ^b	70 ^a	5.4
Fe ₂ O ₃	306	100 ^b	12.5
SiO ₂	72	50	0.9 ^d
CaO	175 ^c	77	12.6
MgO	308	129	11.6
Al ₂ O ₃	470	270	7.0
SiC	380	113	2.5
Zircaloy-2	95	300	6.5
Stainless Steel	193	340	17.2

^aTensile strength data not found, value shown is average of bend strength data. ^bNo data found, value is assumed. ^cOnly bulk modulus data found, elastic modulus evaluated as 1.5 times bulk modulus (same ratio as for UO₂). ^dFor quartz, which is consistent with the assumption of slow freezing. For fused SiO₂, the coefficients are $30.4 \cdot 10^{-6} \text{ K}^{-1}$ and $16.9 \cdot 10^{-6} \text{ K}^{-1}$ along two crystalline plains.

The author acknowledges that the volume-weighting approach for evaluating the crust mechanical properties is at best first order. However, at this point it is not intuitively obvious what scheme should be utilized for evaluating these properties, particularly since the phase structure of the crust material is not known. Thus, the volume-weighting method has been adopted until a better methodology can be identified.

A.2 Concrete Property Evaluation

The property subroutines in CORQUENCH4.1 that evaluate the enthalpy-temperature relationship for concrete implicitly account for the decomposition enthalpies associated with the generation of noncondensable gases. The concrete decomposition reactions that are currently modeled were summarized in Table A-3. The chemical composition of concrete is normally given in terms of stable binary metal oxides which reflect the actual elemental composition of the concrete. However, as shown in Table A-3, the actual mineral composition is required to mechanistically calculate the release of H_2O and CO_2 gases. The user-specified concrete composition in terms of the stable binary oxides is converted to the corresponding mineral composition in the initialization subroutine CPROPI. This method is described below.

Water is assumed to be present in concrete in two forms: i) free water, and ii) bound water, principally in the form of calcium hydroxide, $Ca(OH)_2$. Bound water is assumed to be present at a level of 2 wt%, which is based on an equation developed by Harmathy.^[107] The balance of the H_2O is assumed to be in the form of condensed phase free water. Carbon dioxide is assumed to be present as dolomite, $MgCa(CO_3)_2$, and calcium carbonate, $CaCO_3$. Dolomite is taken to be the principal carbonate form; the mole % of this constituent in the concrete is set equal to the minimum of the MgO and CaO mole percents after accounting for the CaO that has been allotted to $Ca(OH)_2$. If any CO_2 remains after the formation of dolomite, it is assumed to be present in the form of calcium carbonate. The mineral compositions of the three default concrete types that users can

currently select from as part of the code input are shown in Tables A-10 and A-11, while the corresponding breakdowns in terms of simple oxides are provided in Table A-12. Solidus and liquidus temperatures for these three concretes are shown in Table A-4.

Table A-10. Mineral Composition of Default Concretes.

Constituent	Mole % Constituent in Concrete		
	Limestone/Common Sand	Siliceous	Limestone/Limestone
Ca(OH) ₂	8.85	6.29	9.46
CaCO ₃	0.72	0.00	33.41
MgCa(CO ₃) ₂	19.38	0.64	15.42
H ₂ O(l)	9.29	7.72	11.59
H ₂ O(v)	9.29	7.72	11.59
K ₂ O(s)	0.51	0.84	0.36
Na ₂ O	1.41	0.64	0.00
TiO ₂	0.14	0.57	0.10
SiO ₂	38.21	65.74	9.93
CaO	8.57	6.91	6.11
MgO	0.00	0.34	0.00
Al ₂ O ₃	2.81	2.22	1.59
Fe ₂ O ₃	0.80	0.35	0.43

Table A-11. The Breakdown of CaO, MgO, H₂O, and CO₂ into Dolomite, Calcium Carbonate, Calcium Hydroxide, and Free Water for Default Concretes.

Constituent	Weight % Constituent in Concrete:		
	Limestone/Common Sand	Siliceous	Limestone/Limestone
H ₂ O	4.29	5.04	5.03
Ca(OH) ₂	8.40	8.44	8.43
CaCO ₃	0.93	0.00	19.78
MgCa(CO ₃) ₂	45.79	2.15	34.24

Table A-12. Default Concrete Breakdowns in Terms of Simple Oxides.

Constituent	Limestone-Common Sand		Siliceous		Limestone-Limestone	
	Weight %	Mole %	Weight %	Mole %	Weight %	Mole %
SiO ₂	28.8	22.8	69.7	60.7	7.0	5.2
CaO	26.4	22.4	13.7	12.8	42.4	34.0
Al ₂ O ₃	3.6	1.7	4.0	2.1	1.9	0.8
K ₂ O	0.6	0.3	1.4	0.8	0.4	0.2
Fe ₂ O ₃	1.6	0.5	1.0	0.3	0.8	0.2
TiO ₂	0.1	0.1	0.8	0.5	0.1	0.1
MgO	9.8	11.6	0.7	0.9	7.3	8.2
Na ₂ O	1.1	0.8	0.7	0.6	0.0	0.0
H ₂ O	6.2	16.4	6.91	20.0	6.9	17.3
CO ₂	21.8	23.4	1.00	1.2	33.2	34.0

A.2.1 Concrete Enthalpy-Temperature Evaluation

Given the initial concrete temperature and user-specified liquidus, solidus, and ablation temperatures, subroutine CPROPI evaluates the enthalpy-temperature relationship for the concrete, and thereby the ablation enthalpy. This is accomplished by constructing the enthalpy-temperature relationship by accounting for the decomposition reactions that are shown in Table A-3. Each decomposition reaction is assumed to be characterized by distinct, user specified, "solidus" and "liquidus" temperatures (i.e., the temperatures at the inception and completion of the decomposition reaction, respectively). In addition to these principal decomposition processes, the decomposition temperatures for K_2O and Fe_2O_3 (see Table A-2) are assumed to correspond to the $CaCO_3$ decomposition and concrete ablation solidus/liquidus temperatures, respectively. The effective molar enthalpy for a given decomposition process is assumed to vary linearly between the reactant and product enthalpies evaluated at the decomposition inception and completion temperatures, respectively. For example, the effective reactant/product molar enthalpy within the $CaCO_3$ decomposition temperature range is expressed as:

$$e_{CaCO_3} = Y_{CaCO_3} e_{sol,CaCO_3}(T) + Z_{CaCO_3} e_{sol,CaO}(T), \quad (A-68)$$

where:

$$Y_{CaCO_3} = \begin{cases} 1; & e_{max} \leq e(T_{in,CaCO_3}), \\ \frac{e(T_{CP,CaCO_3}) - e_{max}}{e(T_{CP,CaCO_3}) - e(T_{in,CaCO_3})}; & e(T_{in,CaCO_3}) < e_{max} < e(T_{CP,CaCO_3}), \\ 0; & e_{max} \geq e(T_{CP,CaCO_3}), \end{cases} \quad (A-69)$$

$$Z_{CaCO_3} = 1 - Y_{CaCO_3} \quad (A-70)$$

$T_{in,CaCO_3}$ = temperature at the inception of $CaCO_3$ decomposition,
 $T_{CP,CaCO_3}$ = temperature at completion of $CaCO_3$ decomposition,
 $e(T_{in,CaCO_3})$ = concrete specific enthalpy at the inception of $CaCO_3$ decomposition,
 $e(T_{CP,CaCO_3})$ = concrete specific enthalpy at completion of $CaCO_3$ decomposition,
 e_{max} = maximum specific enthalpy obtained by the concrete,

and the $CaCO_3$ and CaO solid phase molar specific enthalpies, $e_{sol,CaCO_3}$ and $e_{sol,CaO}$, are evaluated from Eq. A-1. The evaluation of the concrete specific enthalpy at inception and completion of the calcium carbonate decomposition process [i.e., $e(T_{in,CaCO_3})$ and $e(T_{CP,CaCO_3})$, respectively] is described below. Note that similar expressions apply to the decomposition of $Ca(OH)_2$, H_2O , and K_2O . For dolomite, the reactant/product molar enthalpy within the decomposition temperature range is written as:

$$e_{CaMg(CO_3)_2} = Y_{CaMg(CO_3)_2} e_{sol,CaMg(CO_3)_2} + Z_{CaMg(CO_3)_2} (e_{sol,CaO} + e_{sol,MgO}) \quad (A-71)$$

where $Y_{CaMg(CO_3)_2}$ and $Z_{CaMg(CO_3)_2}$ are defined in the same manner as Y_{CaCO_3} and Z_{CaCO_3} (see Eqs. A-69 and A-70). With the above expressions, the coefficients of the general concrete enthalpy-temperature relationship, Eq. A-7, can be written as:

$$A = \frac{1}{M} \sum_i \bar{X}_i a_i, \quad (A-72)$$

$$B = \frac{1}{\bar{M}} \sum_i \bar{X}_i b_i, \quad (\text{A-73})$$

$$C = \frac{1}{\bar{M}} \sum_i \bar{X}_i c_i, \quad (\text{A-74})$$

$$\bar{M} = \sum_i \bar{X}_i M_i, \quad (\text{A-75})$$

$$\bar{X}_i = \begin{cases} X_i Y_i; i = \text{CaCO}_3, \text{Ca(OH)}_2, \text{CaMg(CO}_3)_2, \text{K}_2\text{O, sol, H}_2\text{O, liq,} \\ X_i + X_{\text{CaCO}_3} Z_{\text{CaCO}_3} + X_{\text{CaMg(CO}_3)_2} Z_{\text{CaMg(CO}_3)_2} + X_{\text{Ca(OH)}_2} Z_{\text{Ca(OH)}_2}, i = \text{CaO,} \\ X_i + X_{\text{CaMg(CO}_3)_2} Z_{\text{CaMg(CO}_3)_2}, i = \text{MgO,} \\ X_i + X_{\text{K}_2\text{O, sol}} Z_{\text{CaCO}_3}, i = \text{K}_2\text{O, vap,} \\ X_i + X_{\text{H}_2\text{O, liq}} Z_{\text{H}_2\text{O, liq}}, i = \text{H}_2\text{O, vap,} \end{cases} \quad (\text{A-76})$$

and χ_i is the initial mineral composition (mole fraction) of the concrete.

Given the above set of equations, the concrete specific enthalpy-temperature relationship is completely determined once the specific enthalpies at inception and completion of the various concrete decomposition processes are specified in Eq. A-69. The concrete decomposition enthalpies are initialized in subroutine CPROPI. For example, the concrete specific enthalpy at inception of free water release, $e(T_{in, H_2O})$, is found by setting $T = T_{in, H_2O}$ in Eq. A-7; the coefficients A , B , and C are evaluated from Eqs. A-72 through A-76 by setting $Y_i = 1$ for all decomposition reactions. Similarly, the specific enthalpy at completion of free water release is found by setting $T = T_{CP, H_2O}$ in Eq. A-7; the enthalpy coefficients are evaluated from Eqs. A-72 through A-76 by setting $Y_{H_2O} = 0$ with $Y_{\text{CaCO}_3} = Y_{\text{Ca(OH)}_2} = Y_{\text{CaMg(CO}_3)_2} = Y_{\text{K}_2\text{O}} = 1$. Similar reasoning is used to evaluate the specific enthalpies at dryout of Ca(OH)_2 , $\text{CaMg(CO}_3)_2$, and CaCO_3 , in addition to the concrete solidus/liquidus specific enthalpies.

With this background, the concrete decomposition (or ablation) enthalpy can then be determined given the user-specified ablation temperature by interpolating from the enthalpy-temperature relationship established with this method. The actual value of the ablation enthalpy depends upon the particular concrete ablation model that is used in the analysis. For instance, in cases in which the quasi-steady concrete ablation model is employed ($\text{NABBL} = 0$; see Section 2.3.1), the decomposition enthalpy is set equal to the concrete specific enthalpy evaluated at the ablation temperature; i.e.

$$e_{dc} = e(T_{sol}) + \left(\frac{e(T_{liq}) - e(T_{sol})}{T_{liq} - T_{sol}} \right) (T_{dc} - T_{sol}) \quad (\text{A-77})$$

where T_{sol} , T_{liq} , and T_{dc} denote the concrete solidus, liquidus, and decomposition temperatures, and the assumption has clearly been made that $T_{sol} \leq T_{dc} \leq T_{liq}$.

Conversely, when one of the concrete dryout models is used ($\text{NABBL} > 0$; see Sections 2.3.2 and 2.3.3), the ablation enthalpy is set equal to the concrete latent heat of fusion, which is calculated as the difference between the concrete specific enthalpy at the ablation temperature minus the enthalpy at the concrete solidus temperature; i.e.,

$$\Delta e_{dc} = e(T_{dc}) - e(T_{sol}) \quad (\text{A-78})$$

In this case, the concrete specific heat that is also required for evaluation of the dryout models is set equal to the average value during the heatup from the initial concrete temperature to the concrete solidus, viz.,

$$c_{con} = \frac{e(T_{sol}) - e(T_o)}{T_{sol} - T_o} \quad (\text{A-79})$$

where T_o is the initial concrete temperature.

A.2.2 Concrete Density Evaluation

Given the initial mineral composition of the concrete, subroutine DENSEC evaluates the initial concrete density based on a molar average, i.e.,

$$\rho_o = \frac{\sum_i \chi_i M_i}{\sum_i \frac{\chi_i M_i}{\rho_i}} \quad (\text{A-80})$$

In addition, the concrete slag density is calculated using the above equation in subroutine CPROPI but with the liquid-phase constituent densities used, along with $Y_i = 0$ in Eq. A-76; i.e.,

$$\rho_{slag} = \frac{\sum_i \bar{\chi}_i M_i}{\sum_i \frac{\bar{\chi}_i M_i}{\rho_{i,l}}} \quad (\text{A-81})$$

A.2.3 Concrete Thermal Conductivity Evaluation

Given the concrete temperature and composition, subroutine CONDC evaluates the concrete thermal conductivity. For the default limestone/common sand and siliceous concretes (see Tables A-10 and A-12), as well as user-specified concrete compositions, the thermal conductivity is evaluated through the following polynomial curve fit to the basalt concrete data of Baker *et al.*^[108] over the temperature range of $373 \leq T \leq 1073 \text{ K}$,¹³

$$k = -21.79 + 2.102 \cdot 10^{-1} T - 7.243 \cdot 10^{-4} T^2 + 1.245 \cdot 10^{-6} T^3 \\ - 1.139 \cdot 10^{-9} T^4 + 5.299 \cdot 10^{-13} T^5 - 9.871 \cdot 10^{-17} T^6 \quad (\text{A-82})$$

For default limestone/limestone concrete (see A-10 and A-12), the thermal conductivity is evaluated through the following polynomial curve fit to the limestone concrete data of Baker *et al.*^[108] over the temperature range of $373 \leq T \leq 1073 \text{ K}$,

$$k = -76.32 + 7.925 \cdot 10^{-1} T - 3.115 \cdot 10^{-3} T^2 + 6.199 \cdot 10^{-6} T^3 + 6.668 \cdot 10^{-9} T^4 \\ + 3.701 \cdot 10^{-12} T^5 - 8.325 \cdot 10^{-16} T^6. \quad (\text{A-83})$$

¹³For brevity, only four significant figures are shown in Eqs. A-82 and A-83. The equations are actually coded with 10 significant figures. Use of these equations as written can result in up to the 58 % error; see subroutine CONDC for the full forms of these correlations.

A.2.4 Concrete Emissivity Evaluation

Given the concrete temperature and composition, subroutine EMISC is set up to evaluate the concrete radiative emissivity. However, the emissivity is currently assumed constant at 0.83.

A.3 Water Property Evaluation

Subroutine CONWAT evaluates the water coolant properties along the coolant saturation line. The properties are evaluated using polynomial curve fits to tabulated data found in several on-line sources.^[109-112] Given the system absolute pressure, the saturation temperature is evaluated from^[112]

$$T_{sat}[K] = \frac{5132.0}{13.766 - \ln(P[\text{bar}])} \quad (\text{A-84})$$

Given the saturation temperature (defined below as T for brevity), the thermal conductivity, density, specific heat, dynamic viscosity, specific enthalpy, and surface tension are respectively evaluated from the the following quadratic curve fits to data provided in References [109-111]:

$$k = -0.5841 + 6.9066 \cdot 10^{-3} T - 1.0916 \cdot 10^{-5} T^2 + 4.000 \cdot 10^{-9} T^3 \quad (\text{A-85})$$

$$\rho = 689.7904 + 2.6667 T - 6.5756 \cdot 10^{-3} T^2 + 3.6400 \cdot 10^{-6} T^3 \quad (\text{A-86})$$

$$C_p = 4481.727 - 1.4345 T + 6.6160 \cdot 10^{-4} T^2 + 2.9333 \cdot 10^{-6} T^3 \quad (\text{A-87})$$

$$\mu = 10^{-6} (30032.04 - 216.82 T + 0.52811 T^2 - 4.3093 \cdot 10^{-4} T^3) \quad (\text{A-88})$$

$$e = 10^3 (-1274.5669 + 5.4424 T - 3.9744 \cdot 10^{-3} T^2 + 4.1733 \cdot 10^{-6} T^3) \quad (\text{A-89})$$

$$\sigma = 10^{-3} (82.0450 + 0.1261 T - 6.5932 \cdot 10^{-4} T^2 + 4.1333 \cdot 10^{-7} T^3) \quad (\text{A-90})$$

where, as a reminder, all units are SI. The water latent heat of vaporization is then calculated by taking the difference between the vapor (see Eq. A-104) and liquid (Eq. A-89) phase specific enthalpies.

A.4 Gas Properties Evaluation

Given the gas temperature and system pressure, the water vapor and CO₂ gas properties are evaluated in subroutines CONH2O and CONCO2, respectively, while the properties of the oxidation byproduct gases H₂ and CO are evaluated in subroutines CONH2 and CONCO, respectively. For all gases except steam, the density is evaluated using the ideal gas law,

$$\rho = \frac{PM}{RT} \quad (\text{A-91})$$

where, as a reminder, M is the molecular weight of the gas, P is system pressure, and R is the ideal gas constant.

Simple curve fits to the data in Reference [113] are currently employed to estimate the properties of all gases except steam that are needed for the analysis. For CO₂ gas, the expressions for the thermal conductivity, specific heat, and viscosity in the range $300 \leq T \leq 2000 \text{ K}$ are of the form,

$$k = 1.657 \cdot 10^{-2} + 8.832 \cdot 10^{-5}(T - 300), \quad (\text{A-92})$$

$$C_p = 1326.5, \quad (\text{A-93})$$

$$\mu = 1.496 \cdot 10^{-5} + 3.957 \cdot 10^{-8}(T - 300), \quad (\text{A-94})$$

For carbon monoxide in the range $300 \leq T \leq 600$ K,

$$k = 2.525 \cdot 10^{-2} + 6.4033 \cdot 10^{-5}(T - 300), \quad (\text{A-95})$$

$$C_p = 1048.4, \quad (\text{A-96})$$

$$\mu = 1.7483 \cdot 10^{-5} + 3.919 \cdot 10^{-8}(T - 300), \quad (\text{A-97})$$

For hydrogen in the range $300 \leq T \leq 1333$ K,

$$k = 0.182 + 3.853 \cdot 10^{-4}(T - 300), \quad (\text{A-98})$$

$$C_p = 14,537.0 \quad (\text{A-99})$$

$$\mu = 1.095 \cdot 10^{-4} + 1.1796 \cdot 10^{-6}(T - 300), \quad (\text{A-100})$$

Finally the water vapor thermal conductivity, density, specific heat, specific enthalpy, and viscosity are evaluated along the saturation line for $300 \leq T \leq 443$ K from quadratic curve fits to data provided in References [114-115]:

$$k = 10^{-3}(-35.6212 + 0.403494T - 1.094794 \cdot 10^{-3}T^2 + 1.199994 \cdot 10^{-6}T^3) \quad (\text{A-101})$$

$$\rho = -56.33799 + 0.53218 T - 1.68066 \cdot 10^{-3} T^2 + 1.77744 \cdot 10^{-6} T^3 \quad (\text{A-102})$$

$$C_p = -817.0310 + 27.598 T - 9.6764 \cdot 10^{-2} T^2 + 1.1600 \cdot 10^{-4} T^3 \quad (\text{A-103})$$

$$e = 10^3(2313.321 - 1.3080 T + 1.0590 \cdot 10^{-2} T^2 - 1.200 \cdot 10^{-5} T^3) \quad (\text{A-104})$$

$$\mu = 10^{-6}(-0.36792 + 1.62815 \cdot 10^{-2} T + 7.70341 \cdot 10^{-5} T^2 - 8.39984 \cdot 10^{-8} T^3) \quad (\text{A-105})$$

where in the above T denotes the saturation temperature that is evaluated from Eq. A-84.

APPENDIX B: BACKGROUND MODELING MATERIAL

This appendix documents various equation sets and solution methodologies that are too cumbersome for presentation in the main body of the report.

B.1 Solution Method for Case 1) Anchored Impervious Crust Boundary Condition

This section summarizes the method used to solve the system of equations for the Case 1) anchored impervious crust boundary condition described in Section 2.5.6.1. The equation for the lower surface temperature of the bridge crust was derived as:

$$T_c = \frac{1}{C_\alpha + C_\beta} \left\{ C_\alpha T_m + C_\beta T_{sat} + \frac{\dot{Q}_{t,c} \delta_t}{2} \left(1 + \frac{C_\beta}{h_{wat}} \right) \right\} \quad (B-1)$$

where:

$$C_\alpha = \frac{h_r h_t}{h_r + h_t} \quad (B-2)$$

$$C_\beta = \frac{k_{t,c} h_{wat}}{\delta_t h_{wat} + k_{t,c}} \quad (B-3)$$

Equation B-1 is non-linear and requires an iterative solution. This is accomplished using the Newton-Raphson technique. In particular, Eq. B-1 is re-written in the following form:

$$f = T_c - \frac{1}{C_\alpha + C_\beta} \left\{ C_\alpha T_m + C_\beta T_{sat} + \frac{\dot{Q}_{t,c} \delta_t}{2} \left(1 + \frac{C_\beta}{h_{wat}} \right) \right\}, \quad (B-4)$$

with convergence obtained when $f \rightarrow 0$, and:

$$\begin{aligned} \frac{df}{dT_c} = 1 + \frac{1}{(C_\alpha + C_\beta)^2} & \left\{ (T_m - T_{sat}) \left(C_\alpha \frac{dC_\beta}{dT_c} + C_\beta \frac{dC_\alpha}{dT_c} \right) + \right. \\ & \left. \frac{\dot{Q}_{t,c} \delta_t}{2} \left[\left(1 + \frac{C_\beta}{h_{wat}} \right) \left(\frac{dC_\alpha}{dT_c} + \frac{dC_\beta}{dT_c} \right) - (C_\alpha + C_\beta) \left(\frac{1}{h_{wat}} \frac{dC_\beta}{dT_c} - \frac{C_\beta}{h_{wat}^2} \frac{dh_{wat}}{dT_c} \right) \right] \right\} \end{aligned} \quad (B-5)$$

with:

$$\frac{dC_\alpha}{dT_c} = \frac{C_\alpha^2}{h_r^2} \frac{dh_r}{dT_c} \quad (B-6)$$

$$\frac{dC_\beta}{dT_c} = \frac{C_\beta^2}{h_{wat}^2} \frac{dh_{wat}}{dT_c} \quad (B-7)$$

Given these expressions, iteration is performed in which the value of T_c is updated through the following expression until a convergence criterion is met:

$$T_c^{n+1} = T_c^n - \frac{f}{\frac{df}{dT_c}} \quad (\text{B-8})$$

With the solution for T_c determined then the other boundary temperatures can be calculated from Eqs. 2-198 through 2-200 in a straightforward manner. The derivative functions in Eqs. B-5 through B-7 can be further broken down into primitive variables; e.g.,

$$\frac{dh_{wat}}{dT_c} = \frac{dh_{wat}}{dT_I} \frac{dT_I}{dT_c} \quad (\text{B-9})$$

where dh_{wat}/dT_I is calculated from Eq. 2-130, 2-156, or 2-160 depending upon the particular mode of boiling heat transfer at the crust upper surface at the given time, and:

$$\frac{dT_I}{dT_c} = \frac{k_{t,c} / \delta_t}{k_{t,c} / \delta_t + h_{wat} + \frac{dh_{wat}}{dT_I} (T_I - T_{sat})} \quad (\text{B-10})$$

The derivative involving the radiation heat transfer coefficient in Eq. B-6 is broken down as:

$$\frac{dh_r}{dT_c} = \frac{\partial h_r}{\partial T_c} + \frac{\partial h_r}{\partial T_L} \frac{\partial T_L}{\partial T_c} \quad (\text{B-11})$$

with:

$$\frac{\partial h_r}{\partial T_c} = \Omega_r \{ 2T_c(T_L + T_c) + T_L^2 + T_c^2 \} \quad (\text{B-12})$$

$$\frac{\partial h_r}{\partial T_L} = \Omega_r \{ 2T_L(T_L + T_c) + T_L^2 + T_c^2 \} \quad (\text{B-13})$$

and:

$$\Omega_r = \frac{\sigma_{stef} F_{view}}{1/\varepsilon_m + 1/\varepsilon_{t,c} - 1} \quad (\text{B-14})$$

This is a complicated set of equations, and so it is worthwhile to outline the solution methodology in more detail. For the given iterated value of T_c^n from Eq. B-8, the melt surface temperature T_L is first solved from the energy balance given as Eq. 2-198. This equation can be rewritten as:

$$h_i(T_m - T_L) = \Omega_r(T_L^4 - T_c^4) \quad (\text{B-15})$$

This expression can be further rearranged and written in dimensionless form as:

$$\hat{T}_L^4 + \xi \hat{T}_L = 1 \quad (\text{B-16})$$

where:

$$\hat{T}_L \equiv T_L / T_o \quad (\text{B-17})$$

$$T_o = \left(\frac{h_t T_m}{\Omega_r} + T_C^4 \right)^{1/4} \quad (\text{B-18})$$

$$\xi = \frac{h_t}{\Omega_r T_o^3} \quad (\text{B-19})$$

The quartic equation given by Eq. B-16 has the following closed form solution:

$$\hat{T}_L = \frac{1}{2} \left\{ \sqrt{2\sqrt{\varphi^2 + 4} - \varphi} - \sqrt{\varphi} \right\} \quad (\text{B-20})$$

where:

$$\varphi = \left(\sqrt{\frac{\xi^4}{4} + \left(\frac{4}{3}\right)^3} + \frac{\xi^2}{2} \right)^{1/3} - \left(\sqrt{\frac{\xi^4}{4} + \left(\frac{4}{3}\right)^3} - \frac{\xi^2}{2} \right)^{1/3} \quad (\text{B-21})$$

With this solution for \hat{T}_L , the dimensional melt surface temperature is found from Eq. B-17, and that establishes the heat flux across the gap through Eq. B-15. The crust upper surface temperature is then found by rearranging Eq. 2-199; i.e.,

$$T_I = T_C - \left(\frac{\delta_t h_r (T_L - T_C)}{k_{t,c}} + \frac{\dot{Q}_{t,c} \delta_t^2}{2k_{t,c}} \right) \quad (\text{B-22})$$

With the crust upper surface temperature established, the heat transfer coefficient to the overlying coolant pool and the corresponding derivative can then be calculated. This provides all the information necessary to evaluate the next iterated value for T_c from Eq. B-8.

B.2 Solution Method for Case 2) Anchored Impervious Crust Boundary Condition

This section summarizes the solution methodology for the Case 2) anchored impervious crust boundary condition described in Section 2.5.6.1. The equation for the upper surface temperature of the bridge crust was derived as:

$$T_c = \frac{1}{h_r + C_\beta} \left\{ h_r T_L + C_\beta \left(T_{sat} + \frac{\dot{Q}_{t,c} \delta_t}{2h_{wat}} \right) + \frac{\dot{Q}_{t,c} \delta_t}{2} \right\} \quad (\text{B-23})$$

where C_β is given by Eq. B-3. This equation is non-linear and is solved using the Newton-Raphson technique by first forming:

$$f = T_c - \frac{1}{h_r + C_\beta} \left\{ h_r T_L + C_\beta \left(T_{sat} + \frac{\dot{Q}_{t,c} \delta_t}{2h_{wat}} \right) + \frac{\dot{Q}_{t,c} \delta_t}{2} \right\} \quad (B-24)$$

with convergence obtained when $f \rightarrow 0$, and:

$$\begin{aligned} \frac{df}{dT_c} = 1 + \frac{1}{(h_r + C_\beta)^2} & \left\{ (h_r + C_\beta) \left(\frac{C_\beta \dot{Q}_{t,c} \delta_t}{2h_{wat}^2} \frac{dh_{wat}}{dT_c} - h_r \frac{\partial T_L}{\partial T_c} \right) + \right. \\ & \left. \frac{dh_r}{dT_c} \left[\frac{\dot{Q}_{t,c} \delta_t}{2} \left(1 + \frac{C_\beta}{h_{wat}} \right) - C_\beta (T_L - T_{sat}) \right] + \frac{dC_\beta}{dT_c} \left[\frac{\dot{Q}_{t,c} \delta_t}{2} \left(1 - \frac{h_r}{h_{wat}} \right) + h_r (T_L - T_{sat}) \right] \right\} \end{aligned} \quad (B-25)$$

In the above, dC_β/dT_c is evaluated from Eq. B-7, dh_r/dT_c from Eqs. B-11 through B-14, and dh_{wat}/dT_c from Eqs. B-9 and B-10. The remaining derivative that requires specification is:

$$\frac{\partial T_L}{\partial T_c} = \left(\frac{T_c}{T_L} \right)^3 \quad (B-26)$$

The methodology for solving this set of equations is as follows. Given that a crust exists on the melt upper surface, then the heat flux across the boundaries is equal to $h_t(T_m - T_{m,fz})$. Thus, for the current estimate of T_c evaluated from Eq. B-8, the upper surface temperature of the lower crust is first determined by balancing the radiation heat flux across the gap to that transferred by convection to the bottom of the crust; i.e.,

$$h_t(T_m - T_{m,fz}) = \Omega_r(T_L^4 - T_c^4) \quad (B-27)$$

Thus,

$$T_L = \left(\frac{h_t(T_m - T_{m,fz})}{\Omega_r} + T_c^4 \right)^{1/4} \quad (B-28)$$

With the heat flux across the boundaries known, the crust upper surface temperature is also known through Eq. B-22, and so the heat transfer coefficient to the overlying coolant pool and the corresponding derivative can then be calculated. This provides all the information necessary to evaluate the next iterated value for T_c through Eq. B-8.

B.3 Solution Method for Case 3) Anchored Impervious Crust Boundary Condition

This section summarizes the solution methodology for the Case 3) anchored impervious crust boundary condition described in Section 2.5.6.1. The equation for the upper surface temperature of the bridge crust was derived as:

$$T_I = \left(\frac{k_{t,c}}{\delta_t} + h_{wat} \right)^{-1} \left[h_{wat} T_{sat} + \frac{k_{t,c}}{\delta_t} T_{t,frz} + \frac{\dot{Q}_{t,c} \delta_t}{2} \right] \quad (B-29)$$

This non-linear equation is first solved using the Newton-Raphson technique by forming:

$$f = T_I - T_{sat} - \frac{1}{k_{t,c} + h_{wat} \delta_t} \left[k_{t,c} (T_{t,frz} - T_{sat}) + \frac{\dot{Q}_{t,c} \delta_t^2}{2} \right] \quad (B-30)$$

with convergence obtained when $f \rightarrow 0$, and:

$$\frac{df}{dT_I} = 1 + \frac{\delta_t}{(k_{t,c} + h_{wat} \delta_t)^2} \left[k_{t,c} (T_{t,frz} - T_{sat}) + \frac{\dot{Q}_{t,c} \delta_t^2}{2} \right] \frac{dh_{wat}}{dT_I} \quad (B-31)$$

where dh_{wat}/dT_I is calculated from Eq. 2-130, 2-156, or 2-160 depending upon the mode of boiling heat transfer at the crust upper surface at a given time. Given these expressions, an iterative solution is obtained for T_I using an equation analogous to Eq. B-8. Once the solution for T_I is obtained, the heat removal to the overlying water pool from the upper surface of the crust can be determined.

Since for this case the crust bottom surface temperature is fixed at the melting point, the energy balance from the melt pool to the lower surface of the crust is solved as a separate problem. The heat balance across the gap takes the form:

$$h_t (T_m - T_L) = \Omega_r (T_L^4 - T_{t,frz}^4) \quad (B-32)$$

This equation can be rearranged and written in the same form as Eqs. B-16, B-17, and B-19, but with:

$$T_o = \left(\frac{h_t T_m}{\Omega_r} + T_{t,frz}^4 \right)^{1/4} \quad (B-33)$$

The closed form solution to Eq. B-16 for T_L is then provided by Eqs. B-20 and B-21. Given this result, the heat flux across the gap to the underside of the crust is known, which is required to determine the bridge crust melting rate, as discussed in Section 2.5.6.1.

B.4 Solution Method for Case 1) Anchored Permeable Crust Boundary Condition

This section summarizes the method used to solve the system of equations for the Case 1) anchored permeable crust boundary condition described in Section 2.5.6.2. The equation for the lower surface temperature of the bridge crust was derived as:

$$T_C = \frac{C_\alpha T_m + h_{eff} T_{sat}}{C_\alpha + h_{eff}} \quad (B-34)$$

where C_α is defined in Eq. B-2 and h_{eff} is defined in Eq. 2-217. This non-linear equation is solved using the Newton-Raphson technique by first forming

$$f = T_C - \frac{C_\alpha T_m + h_{eff} T_{sat}}{C_\alpha + h_{eff}} \quad (B-35)$$

with convergence obtained when $f \rightarrow 0$, and:

$$\frac{df}{dT_C} = 1 - \frac{(T_m - T_{sat})}{(C_\alpha + h_{eff})^2} \left(h_{eff} \frac{dC_\alpha}{dT_C} - C_\alpha \frac{dh_{eff}}{dT_C} \right) \quad (B-36)$$

with dC_α/dT_C is evaluated through Eqs. B-6 and B-11 to B-13. In addition,

$$\frac{dh_{eff}}{dT_C} = -\frac{h_{eff}}{(T_m - T_{sat})} \quad (B-37)$$

With these expressions, iteration is performed using Eq. B-8 until a convergence criterion for T_C is met. In particular, for the given iterated value of T_C^n , the melt surface temperature T_L is first solved using Eqs. B-14 and B-16 to B-21. This solution completes the required data that is needed to evaluate the radiation heat transfer coefficient across the gap (Eq. 2-201), as well as the associated derivate functions. With this information, the next iterated value of T_C can be calculated through Eq. B-8.

APPENDIX C: VALIDATION CALCULATIONS

C.1 Overview

The purpose of this appendix is to document the results of various validation calculations that were carried out as part of CORQUENCH4.1¹⁴ developmental activities. Although there have been both low- and high-temperature simulant material core-concrete interaction and debris coolability experiments reported in the literature, the validation effort focused primarily on oxidic reactor material experiments. This is due to the fact that CORQUENCH4.1 does not currently possess the capability to import or evaluate the complete set of thermophysical property data that would be needed to adequately calculate simulant material experiments. Second, the code does not possess the capability to calculate density-driven phase segregation as is required to model experiments in which segregation occurred (e.g. tests with iron-alumina thermite). On these bases, the tests shown in Table C-1 were selected for the current set of validation calculations.

Table C-1. Summary of Code Validation Experiment Characteristics.

Program	Test	Conc. Type	Cavity Configuration (size)	Melt Gen. Tech.	Corium Type	Clad Oxid. (%)	Initial Melt Depth	Cavity Cond.
ACE Phase C	L2	Siliceous	1-D rectilinear (50 cm square)	DEH	PWR	70	15 cm	Dry
	L4	Soviet	"	"	BWR	50	"	"
	L5	LCS	"	"	PWR	100	"	"
	L6	Siliceous	"	"	PWR	30	"	"
	L8	L-L	"	"	PWR	70	"	"
NRC-SNL	SURC1	L-L	1-D cylindrical (40 cm dia.)	Emb. Heaters	PWR	70	20 cm	"
	SURC2	Siliceous	"	"	PWR	70	"	"
MACE	M0	LCS	2-D rectilinear (30 cm square)	DEH	PWR		15 cm	Wet
	M1b	LCS	1-D rectilinear (50 cm square)	"	PWR		25 cm	"
	M3b	LCS	1-D rectilinear (120 cm square)	Thermite	BWR	100	20 cm	"
	M4	Siliceous	1-D rectilinear (50 cm square)	"	BWR	100	30 cm	"
OECD-MCCI	CCI-2	LCS	2-D rectilinear (50 cm square)	"	BWR	100	25 cm	Dry, late flooding
	CCI-3	Siliceous	"	"	BWR	100	"	"
	CCI-4	LCS	2-D rectilinear (50 cm x 40 cm)	"	BWR	78	"	Dry ^a
	CCI-5	Siliceous	2-D rectilinear (50 cm x 79 cm; one ablating wall)	"	BWR	100	"	Dry ^b
	CCI-6	Siliceous	2-D rectilinear (70 cm square)	"	BWR	100	28 cm	Wet

^aExperiment flooded late, but the presence of an impervious crust that formed in the upper region of the test section prior to flooding prevented the water from contacting the melt. Thus, this test was effectively a dry experiment.

^bExperiment not flooded due to the fact that the offgas system plugged early in the experiment sequence.

The matrix includes both 1-D and 2-D experiments; tests conducted with siliceous, limestone-common sand (LCS), and limestone-limestone (LL) concrete; and tests carried out under both wet and dry cavity conditions. Only experiments for which sufficient open-literature data was available to set up an adequate model were included in the matrix. Finally, only tests that ran for a fairly significant length of time (or ablation depth) were calculated so that the ability of the code to predict longer-term behavior could be assessed. In terms of dry cavity experiments, the matrix includes five tests conducted as part of the ACE/MCCI test series,^[76-77] two tests conducted as part of the SURC test series carried at Sandia National Laboratory,^[119] and finally

¹⁴The beta version used for these validation calculations corresponds to version 184 (i.e., cqwork184.f) in the CORQUENCH developmental version archive library.

two tests conducted as part of the OECD/MCCI program.^[66] One significant omission in this matrix is the dry cavity VULCANO tests conducted at CEA in France.^[120,121] However, details regarding the experiment conditions and results for the VULCANO program are proprietary, and so additional validation of the code against these test results was not possible.

In terms of wet cavity tests, the matrix includes four tests conducted as part of the MACE program,^[15,16,122-127] and three tests conducted as part of the OECD/MCCI program.^[17-19,66,128] The validation results for the MACE tests are provided in an addendum report;^[129] the validation results for the OECD/MCCI tests are provided later in this section.

The approach for this validation activity was to make a common set of user-specified modeling assumptions, and to apply those assumptions for all the tests that were calculated as part of this validation activity. In this manner, the reader is able to assess the ability (or lack thereof) of the code to match test results without tuning of the code input. The common set of modeling assumptions that were made as part of this validation exercise are outlined immediately below, with a description of the input that was modified to mock up the actual test conditions provided at the end of this introductory section. The results of the dry cavity test cases are then described, followed by the wet cavity cases at the end of this appendix. Note that parametric calculations were not carried to assess modeling sensitivities, since this lies beyond the current scope of work.

C.2 Summary of Modeling Assumptions

For all test cases, a single node (i.e. NUMNOD=1) analysis was performed. In addition, concrete heatup and decomposition for all cases was calculated using the concrete dryout models described in Section 2.3. However, the corium melts used in the experiments shown in Table C-1 were generated *in-situ* using one of two techniques: i) gradual powder melting using the direct electrical heating (DEH) or induction heating of tungsten susceptors embedded within the powders, or ii) rapid melt production through an exothermic thermite-type reaction. In the former case, melt production occurred over several hours, resulting in heatup of surrounding test section structures, including to some extent the underlying concrete basemat (and sidewalls, where applicable). For the latter case, the melt was suddenly brought into contact with cold concrete. The variation in the melt generation technique most likely resulted in variations in the initial boundary condition at the core-concrete interface, and code input was selected to best match the perceived initial condition. In particular, for tests in which the melt was produced by thermal heating (see Table C-1), the assumption was made that there was no initial transient crust growth and remelting phase since the concrete was already warm upon melt-concrete contact. Thus, these cases were run using the fully developed concrete dryout model described in Section 2.3.2 (i.e., NABBL = 1). However, for cases in which the melt was produced using a thermite reaction, the tests were run using the dryout model with initial crust growth assuming that the crust was permeable to the produced by ablation (i.e., NABBL = 2 with NABLB/NABLS = 1); see Section 2.3.3 for details. For this case, the crust freezing temperature was based on the melt composition (NBCB/NBCS=1). In addition, the crust was assumed to fail when the thickness fell below the mechanical stability limit under the applied hydrostatic load of the melt (NFAILB/NFAILS = 2) with the model constant set assuming that the high temperature crust undergoes a ductile failure and is rectangular in shape (CFAILB/CFAILS = 5.48). Dryout temperature ranges for free water, bound water [Ca(OH)₂], dolomite [MgCa(CO₃)₂], and calcium carbonate [CaCO₃] were set at 417/437 K, 853/873 K, 1030/1050 K, and 1172/1192 K, respectively. Heat transfer coefficients

to horizontal and vertical (where applicable) concrete surfaces were calculated with the Bradley model (NBOTBC/NSIDEBC=1).^[39] Based on experiment observations,^[47,66] the radial/axial heat transfer coefficient multipliers for 2-D tests with siliceous concrete were set to XSMULT=3.0 and XBMULT=1.0, respectively. For all other cases, both multipliers were set to unity.

For the wet cavity tests, the Rico-Spalding correlation (see Section 2.5.3) was used to calculate the melt entrainment rate due to eruptions (NENTR=2) for LCS tests, with the proportionality constant in the correlation set at the mid-range value of E=0.08. For tests with siliceous concrete, melt eruptions were not observed except for the integral effect experiment CCI-6 in which the cavity was flooded almost immediately after melt contact with the concrete basemat. Thus, melt eruptions were not calculated for any siliceous test (i.e., NENTR=0), except for CCI-6. For this test, eruptions were also calculated using the Rico-Spalding correlation with the proportionality constant set at E=0.08. All cases were run with the critical heat flux multipliers for determination of bulk cooling and film boiling breakdown (i.e., CCRIT and CHFMULT) set at 0.5. For tests in which particle beds formed, the bed porosity and average particle diameter were set to 40 % and 2.8 mm, respectively, which is based on posttest examination results reported as part of the MACE program.^[62] Water ingress was calculated using the modified Lister-Epstein model developed as part of the OECD/MCCI modeling activities (NINGRS=2), with the empirical constant *C* in the crust dryout heat flux model set at 9.0. This is the value recommended on the basis of previous code validation work,^[47] and no attempt has been made to further optimize this constant based on the upgraded version of the code that was used to carry out the validation calculations reported herein. For the MACE 1-D corium coolability experiments, the crust anchoring modeling option was selected since crust anchoring and separation clearly occurred in these tests. The assumption was made that the crust was subjected to the combined deadweight loads of the crust itself, the overlying particle bed, and the water pool head over the interaction (NUSGAP=2); see Section 2.5.5. The simple cavity flooding model was used (i.e. NADD=1) in which water is added at the time specified as part of the experiment operating procedure (TADD); the constant water depth (HDOWNC) was set to 50 cm as this was the normal operating condition following cavity flooding. The crust mechanical strength used in the anchoring analysis was set at 3.0 MPa based on the measurements and data assessment made as part of the OECD/MCCI program.^[22] The constant in the crust mechanical strength model was set according to the value that is consistent with brittle failure of the quenched material (i.e., CCRGAP=2.53). Once anchoring occurred in the calculation, the melt was declared to be separated from the crust when the separation distance exceeded the radius of the gas bubbles sparging through the pool and penetrating the pool upper surface (NBUBSP=1).

Other miscellaneous modeling assumptions are summarized as follows. For all cases in which unoxidized Zr cladding was present in the melt, the Zr was assumed to be in solution with the core oxide phase (IEUTEC=1), and condensed phase chemical reactions between Zr and SiO₂ were calculated (NCHEM=1). The top crust thermal conductivity was calculated using the code property subroutines (NKSPEC=0). The effect of solids buildup in the melt was modeled with the Ishii-Zuber correlation^[33] with the maximum solids fraction set at 1.0 (ALPMAX=1.0). The effective melt freezing temperature was based on the oxide phase solid temperature (FRZFR=1.0). For all cases the input power was modeled as being deposited directly in the melt zone with no heat input to crust or particle bed regions (NDEC = 2 with CON1 = CON2 = 0). This modeling assumption is consistent with the DEH heating technique used in the MACE and CCI test series.

Melt void fraction was modeled using the Brockmann *et al.*^[35] correlation (NVOID=1), and the sparging gas bubble radius was calculated using the model described herein (NBUBRS=1; see Section 2.6.2). Finally, all cases were run with a 0.1 second timestep, which was found to be adequate in terms of achieving a converged solution for all cases.

C.3 Dry Cavity Experiment Results

C.3.1 ACE/MCCI Experiments

The ACE/Phase C tests^[76,77] shown in Table C-1 were dry 1-D core concrete interaction experiments that were intended to provide thermal-hydraulic data for core-concrete interaction to support code validation efforts. A second and equally important objective was to provide information on the nature and extent of fission product release during the interaction using non-radioactive isotopes of key fission forms. As shown in Table C-1, five tests from this program were selected for analysis. However, two tests were omitted (i.e., L1 and L7) since only a few centimeters of concrete were eroded before the experiments were terminated due to anomalies.

A unique aspect of these tests was that metals and fission product mockups were introduced into the melt by ablation of concrete-metal inserts that were placed over the base concrete. This prevented early oxidation of the Zr cladding and release of the fission product mockups before basemat ablation began. As a result, the tests could effectively be divided into two (and for one test three) phases; i.e., early insert ablation and then the follow on basemat ablation phase. Thus, for tests where inserts were used, the composite basemat model was employed so that a continuous simulation of the tests from onset of insert ablation through test termination could be carried out.

The concrete-metal insert and concrete basemat compositions for the five tests are shown in Tables C-2 and C-3, respectively. Test L4 was conducted using a Soviet basemat layout that consisted of a 5.1 cm thick layer of Serpentine concrete between the insert and the underlying base concrete that was similar to siliceous concrete; the composition of the Serpentine layer is shown in Table C-4.

Table C-2. Composition of Metal-Concrete Inserts for ACE/MCCI Tests.

Constituent	Wt % for ACE/MCCI Test:			
	L2	L4	L6	L8
CO ₂	0.6	0.4	1.8	18.5
H ₂ O	2.2	6.3	1.5	3.4
K ₂ O	0.5	0.04	0.6	0.3
Na ₂ O	0.25	0.03	0.3	0.2
TiO ₂	0.28	0	0.3	0.1
SiO ₂	24.8	15.2	28.7	3.5
CaO	4.8	4.4	5.6	25.9
MgO	0.25	13.6	0.3	2
Al ₂ O ₃	1.5	0.8	1.7	1
Fe ₂ O ₃	0.35	2.8	0.4	0.5
Fe	0	0	11.8	0
Cr	0	0	3.1	0
Ni	0	0	1.8	0
Zr	64.4	56.4	42.1	44.6

Table C-3. Composition of Base Concretes for ACE/MCCI Tests.

Constituent	Wt % for ACE/MCCI Test:				
	L2	L4	L5	L6	L8
CO ₂	1.7	1.2	21.4	4.3	33.3
H ₂ O	6.2	1.9	6.1	3.7	6.1
K ₂ O	1.4	1.6	0.6	1.4	0.6
Na ₂ O	0.7	2.7	1.1	0.7	0.4
TiO ₂	0.8	0.15	0.15	0.8	0.09
SiO ₂	69.7	70.1	29	69.7	6.3
CaO	13.6	11	26.6	13.6	46.8
MgO	0.7	0.7	9.8	0.7	3.7
Al ₂ O ₃	4.1	8.9	3.6	4.1	1.78
Fe ₂ O ₃	1	1.7	1.65	1	0.9

Table C-4. Composition of L4 Serpentine Concrete Layer.

Constituent	Wt %
CO ₂	0.9
H ₂ O	14.4
K ₂ O	0.1
Na ₂ O	0.06
TiO ₂	0
SiO ₂	34.9
CaO	10
MgO	31.3
Al ₂ O ₃	1.8
Fe ₂ O ₃	6.5

Although the inserts effectively provided two tests in one, estimating the ablation temperature of these metal-heavy components was not (at least for the author) straightforward. On this basis, the solidus and liquidus temperatures for the inserts were estimated using a volume weighting of the melting points for the various metal and concrete constituents from which the insert was made; the results are shown in Table C-5, while the analogous data for the L4 serpentine layer is shown in Table C-6. These tables also provide the thicknesses of the inserts for the various tests. Finally, the ACE/MCCI off-gas system was heavily instrumented to measure offgas composition and flowrate. Thus, the data could be integrated to determine the fraction of concrete decomposition gases that were liberated upwards through the melt. (The bottom of the apparatus was not leak tight and as a result some of the gases escaped through the bottom and therefore bypassed the melt). The results of these calculations for the insert and basemat ablation phases of the tests are provided in Tables C-5 and C-6. These fractions were used as part of the code input (i.e., XFLH2O and XFLCO2) so that the correct integrated gas release from the various regions of the basemat would be calculated by the code.

The balance of the information required to carry out the analysis consists of the cavity geometry, initial corium composition at start of the interaction, the initial melt temperature, the overlying structure temperature and emissivity, and finally the input power as a function of time. The tests were all mocked up using the 1-D cavity model with the basemat surface area fixed at

the value of 0.247 m² as specified by the experimentalists. (Test section nominal cross section was 50 cm x 50 cm). The melt compositions for the various tests are shown Table C-7, while initial melt temperatures are shown in Table C-8, which also provides the overlying structure temperatures that were used in the upward radiation heat transfer calculation. The structure temperatures are based on readings taken just behind the tungsten heat shield that protected the lid of the apparatus during the tests. The assumed emissivity was 0.23 for the tungsten heat shield, which is typical of unoxidized tungsten at a temperature of 1700 K.

Table C-5. Assumed Properties of Concrete-Metal Inserts and Base Concretes for ACE/MCCI Tests.

Concrete-Metal Insert	ACE/MCCI Test:				
	L2	L4	L5	L6	L8
T _{solidus} (K)	1909	1797	N/A	1802	1945
T _{liquidus} (K)	1910	1798		1803	1946
T _{ablation} (K)	1910	1798		1803	1946
Fraction H ₂ O detected	0.102	0.686		0.426	0.305
Fraction CO ₂ detected	0.681	1.000		0.302	0.981
Thickness (cm)	1.27	6.27		5.84	3.45
Base Concrete					
T _{solidus} (K)	1403	1403	1393	1403	1495
T _{liquidus} (K)	1523	1523	1568	1523	2577
T _{ablation} (K)	1450	1450	1500	1450	1800
Fraction H ₂ O detected	0.102	0.686	0.181	0.426	0.305
Fraction CO ₂ detected	0.681	1	0.681	0.302	0.981

Table C-6. Assumed Properties for ACE/MCCI Test L4 Serpentine Concrete Layer.

Property	Value
T _{solidus} (K)	1909
T _{liquidus} (K)	1910
T _{ablation} (K)	1910
Fraction H ₂ O detected	0.102
Fraction CO ₂ detected	0.681
Thickness (cm)	5.1

Table C-7. Initial Melt Compositions for the ACE/MCCI Tests.

Constituent	Mass (kg) for Test:				
	L2	L4	L5	L6	L8
SiO ₂	20.9	16.8	0	16.9	3.4
CaO	3	0	0	7.3	20.6
MgO	0	7.2	0	0	0
Fe ₂ O ₃	0	0	54.1	0	0
Zr	5.46	0	0	0	0
ZrO ₂	42.5	43.2	34	18.5	41.6
Cr ₂ O ₃	0	0	13.4	0	0
UO ₂	216	192	184	219	211
Total	287.86	259.2	285.5	261.7	276.6

Table C-8. Assumed Initial Melt and Boundary Temperatures for the ACE/MCCI Tests.

Test	Initial Melt Temperature (K)	Upper Structure Temperature (K)
L2	2500	1700
L4	2100	1300
L5	1810	1320
L6	2500	1700
L8	2650	1700

Finally, the input power curves for the various tests are shown graphically in Figure C-1. Time $t=0$ in this figure and in the results that follow for the ACE/MCCI test series corresponds to onset of ablation in the base concrete layer, and data that is shown prior to $t=0$ corresponds to the insert ablation phase of the experiments. As shown in Figure C-1, there are brief periods during the tests in which the input power fell below zero. The sidewalls of the apparatus were water cooled, and so during periods when tap changes on the power supply were made, the net ‘input power’ actually fell below zero for a brief period of time.

Principal thermal-hydraulic results that were generated as part of the ACE/MCCI test series included melt temperature, ablation front location, and melt superficial gas velocity. Due to the fact that the apparatus was water-cooled, heat balances were also performed that allowed the melt-concrete and melt-atmosphere heat transfer rates to be evaluated. The code predictions for the five tests are compared with test results using a summary format below.

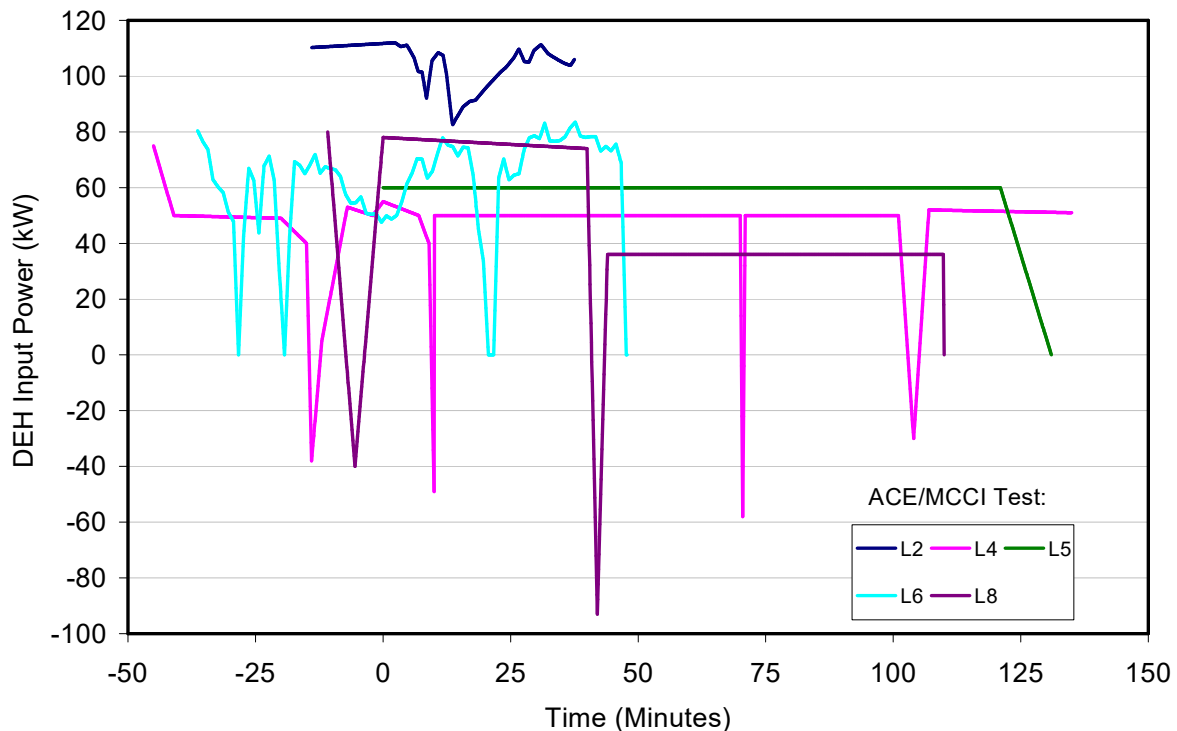


Figure C-1. DEH Input Power Relative to Onset of Basemat Ablation for ACE/MCCI Test Series.

C.3.1.1 ACE/MCCI Test L2

Code predictions of melt temperature, ablation front location, melt superficial gas velocity, and boundary heat fluxes are compared with data obtained from the ACE L2 experiment in Figures C-2 through C-5, respectively. The model does a reasonable job of predicting melt temperature. However, the rate of insert ablation is slightly over-predicted during the early part of the test, resulting in an offset that translates to the end of the calculation. Thus, the overall ablation depth is slightly over-predicted. The melt superficial gas velocity is reasonably predicted up until the point at which the offgas system was plugged due to excessive melt foaming. Past this point, comparison is no longer possible. Finally, the code slightly over-predicts the melt-atmosphere heat flux, and significantly under-predicts the heat flux to concrete.

C.3.1.2 ACE/MCCI Test L4

Predictions of melt temperature, ablation front location, melt superficial gas velocity, and boundary heat fluxes are compared with data from the ACE L2 experiment in Figures C-6 through C-9, respectively. Melt temperature is reasonably predicted during the first 50 minutes, but thereafter the prediction begins to drift and by the end of the test the temperature is under-predicted by ~ 250 K. Overall ablation is over-predicted by ~ 2.5 cm at test termination. The overall trend in the superficial gas velocity is reasonably replicated, despite offsets in timing that are related to the over-prediction in the length of time required to ablate through the concrete-metal insert for this test. The fidelity of the heat flux predictions varies as the test progresses, but by the end of the test, the upwards heat flux is well predicted, whereas the heat flux to underlying concrete is under-predicted.

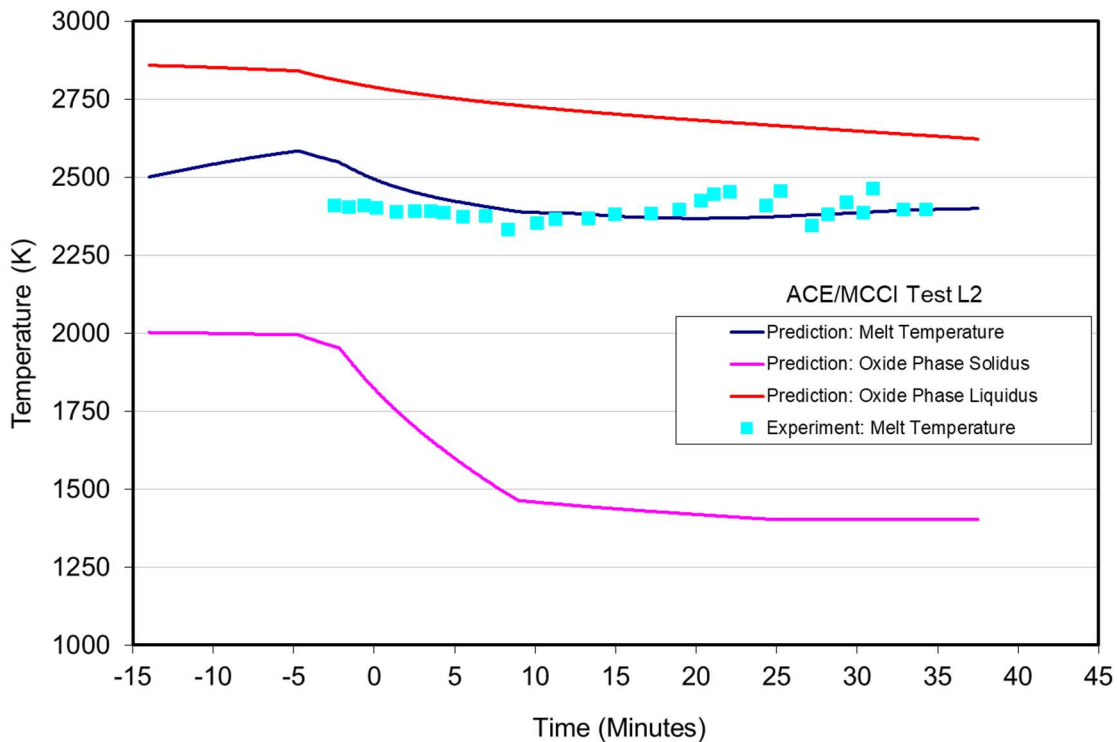


Figure C-2. Melt Temperature Prediction for ACE Test L2.

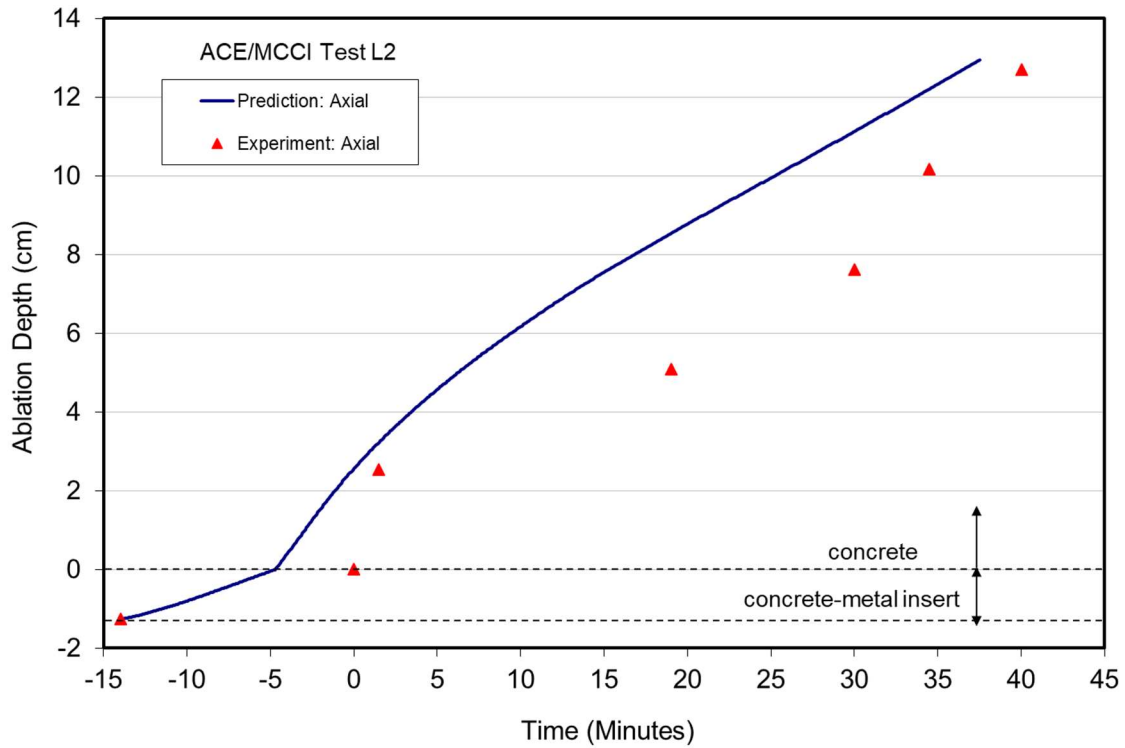


Figure C-3. Ablation Front Location Prediction for ACE Test L2.

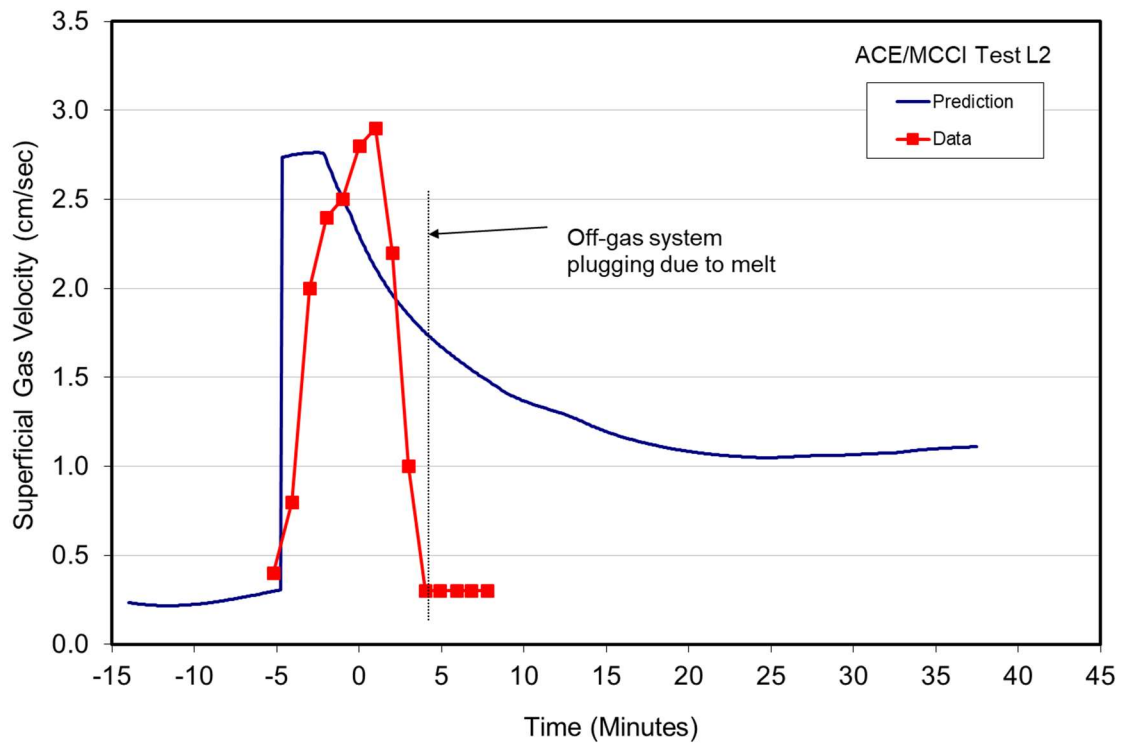


Figure C-4. Superficial Gas Velocity Prediction for ACE Test L2.

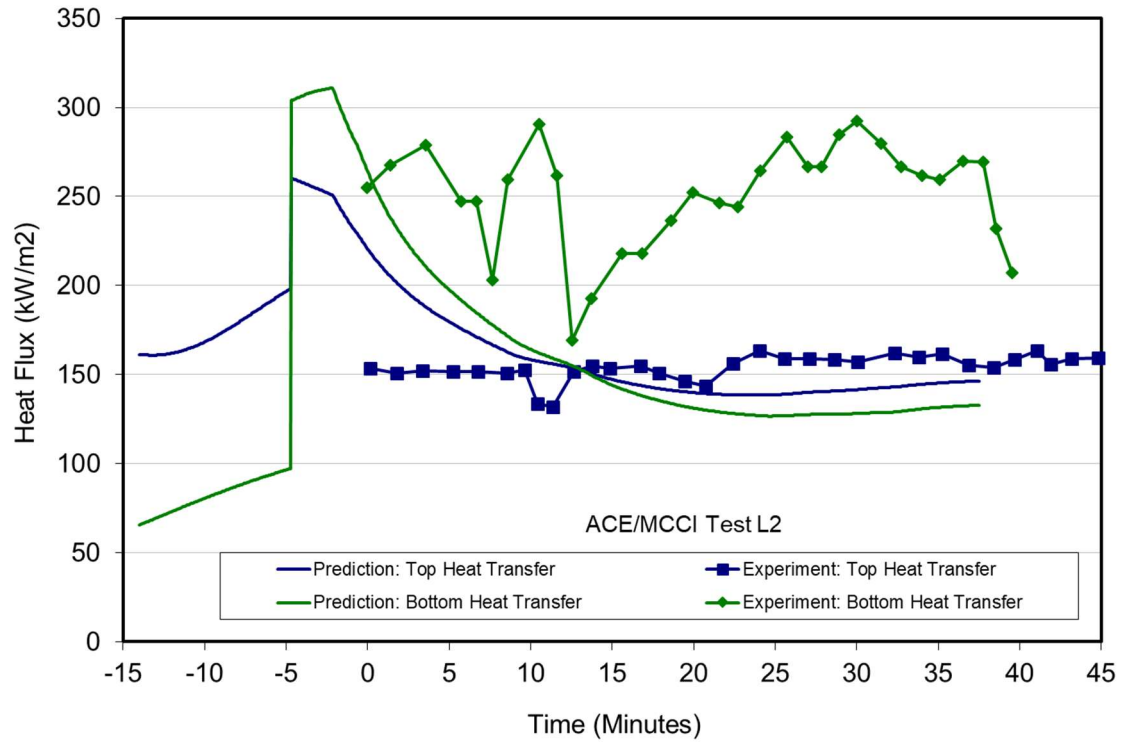


Figure C-5. Melt-Concrete and Melt-Atmosphere Heat Flux Prediction for ACE Test L2.

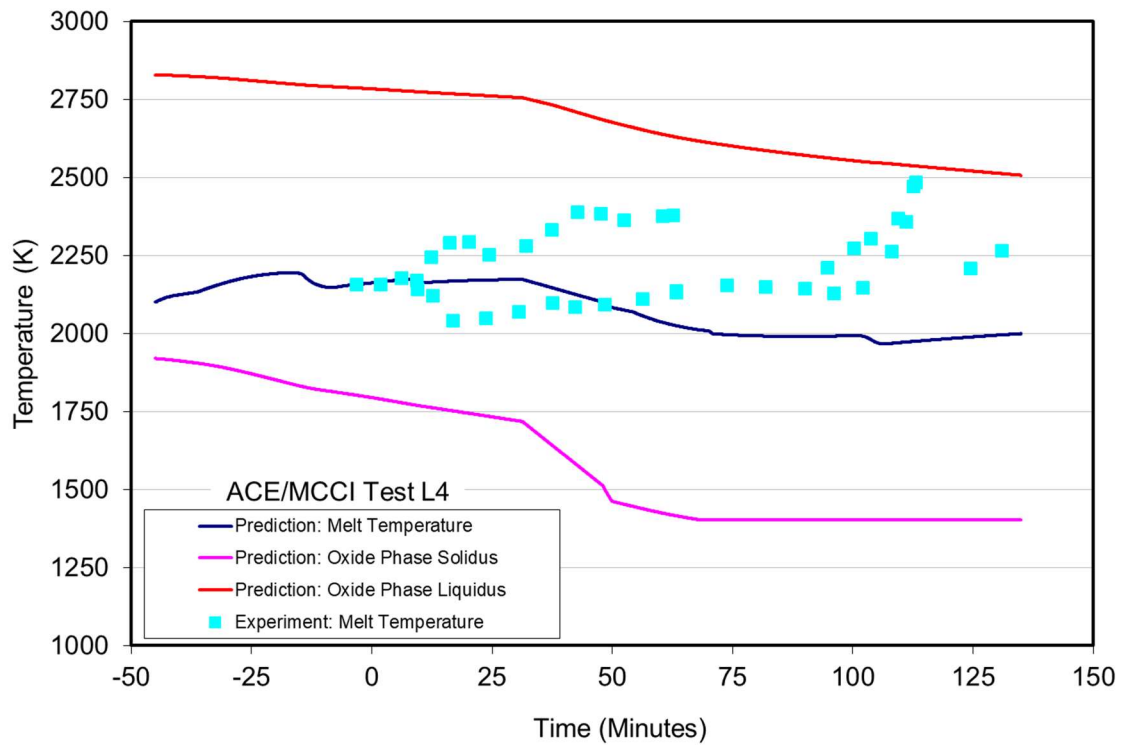


Figure C-6. Melt Temperature Prediction for ACE Test L4.

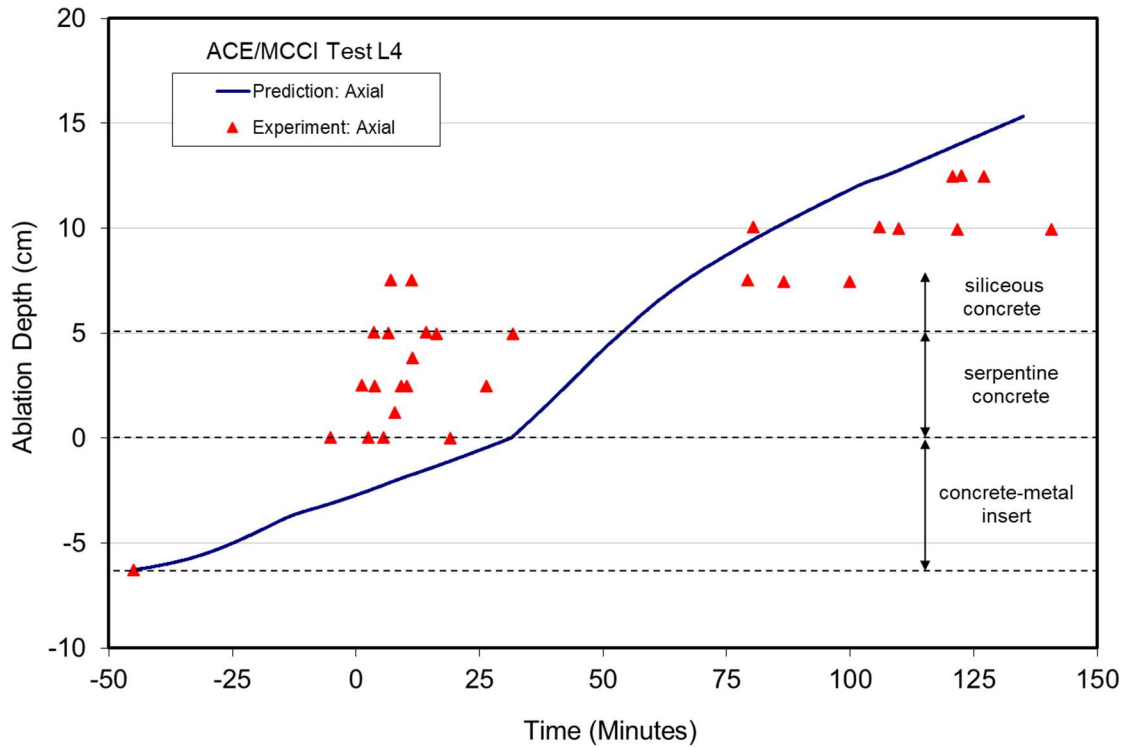


Figure C-7. Ablation Front Location Prediction for ACE Test L4.

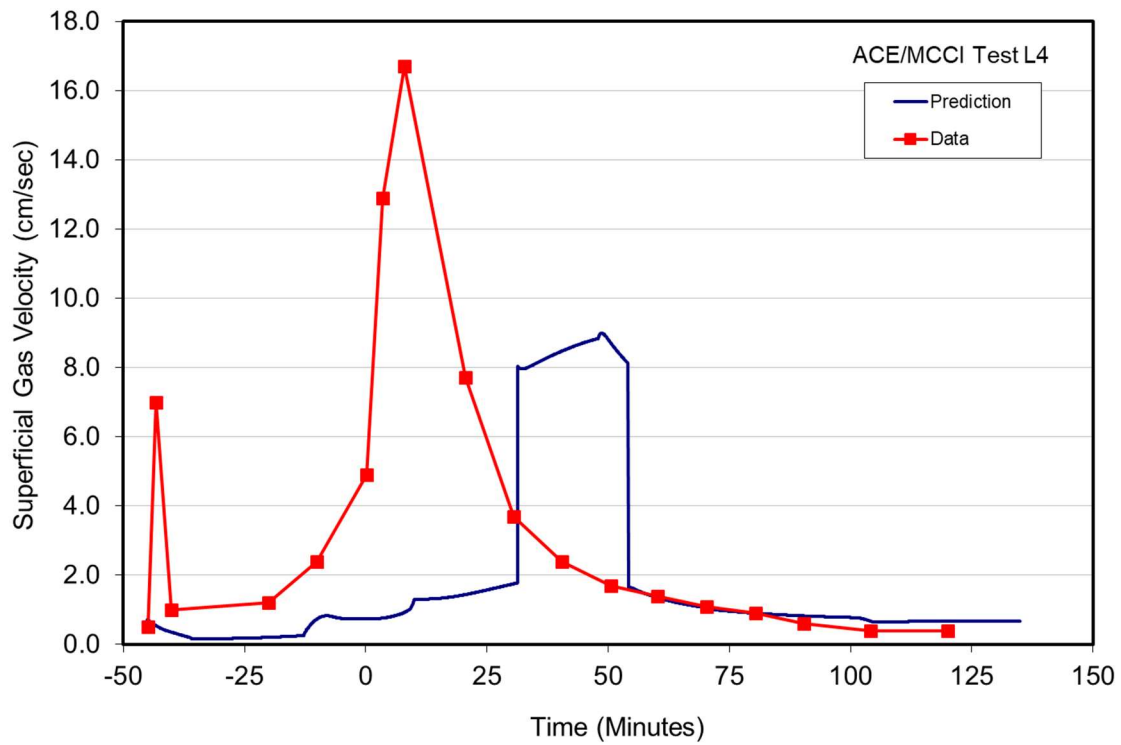


Figure C-8. Superficial Gas Velocity Prediction for ACE Test L4.

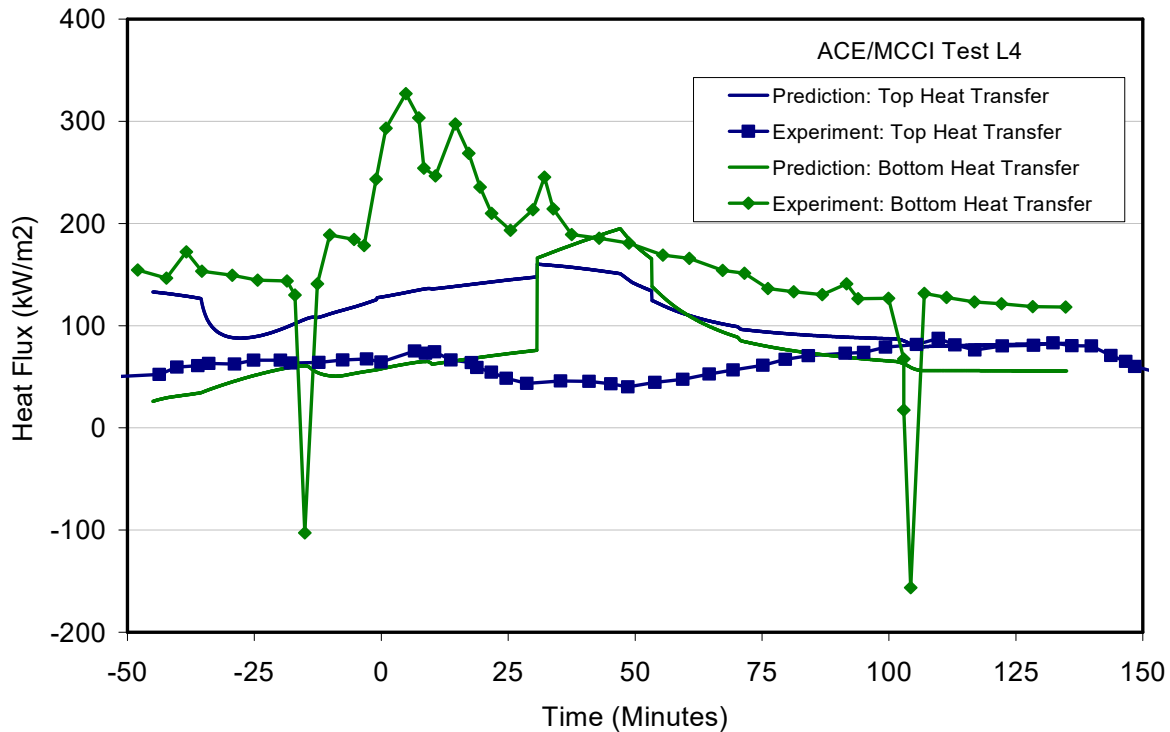


Figure C-9. Melt-Concrete and Melt-Atmosphere Heat Flux Prediction for ACE Test L4.

C.3.1.3 ACE/MCCI Test L5

Melt temperature, ablation front location, melt superficial gas velocity, and boundary heat flux predictions are compared with data from the ACE L5 experiment in Figures C-10 through C-13, respectively. Melt temperature and ablation depth are slightly over-predicted at the end of the test. The superficial gas velocity data are somewhat sporadic, but the trend is reasonable near test termination, as well as the magnitude of the prediction. Finally, the trend and magnitude of the melt-concrete and melt-atmosphere heat fluxes is reasonably predicted during the latter phase of the experiment.

C.3.1.4 ACE/MCCI Test L6

Melt temperature, ablation front location, melt superficial gas velocity, and boundary heat flux predictions are compared with data from the ACE L6 experiment in Figures C-14 through C-17, respectively. During the initial phase of concrete erosion, melt temperature is under-predicted, but the agreement improves late in the experiment. Conversely, ablation is slightly over-predicted early in the test, and then under-predicted during the late phase. Although the fluctuations in superficial gas velocity are not captured by the code, the magnitude of the gas flux is reasonably reproduced. Finally, the upwards heat flux is over-predicted early in the transient, but the agreement is reasonable during the late phase. The downward heat flux is under-predicted for early and late times, while the agreement is reasonable for intermediate times.

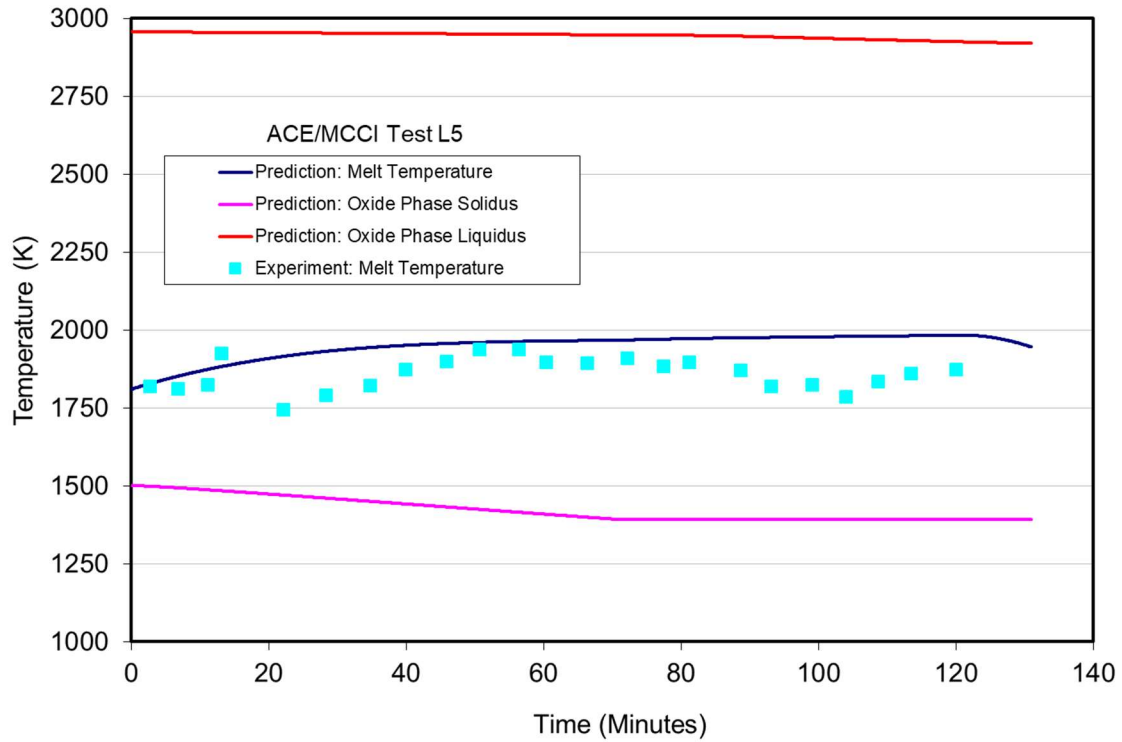


Figure C-10. Melt Temperature Prediction for ACE Test L5.

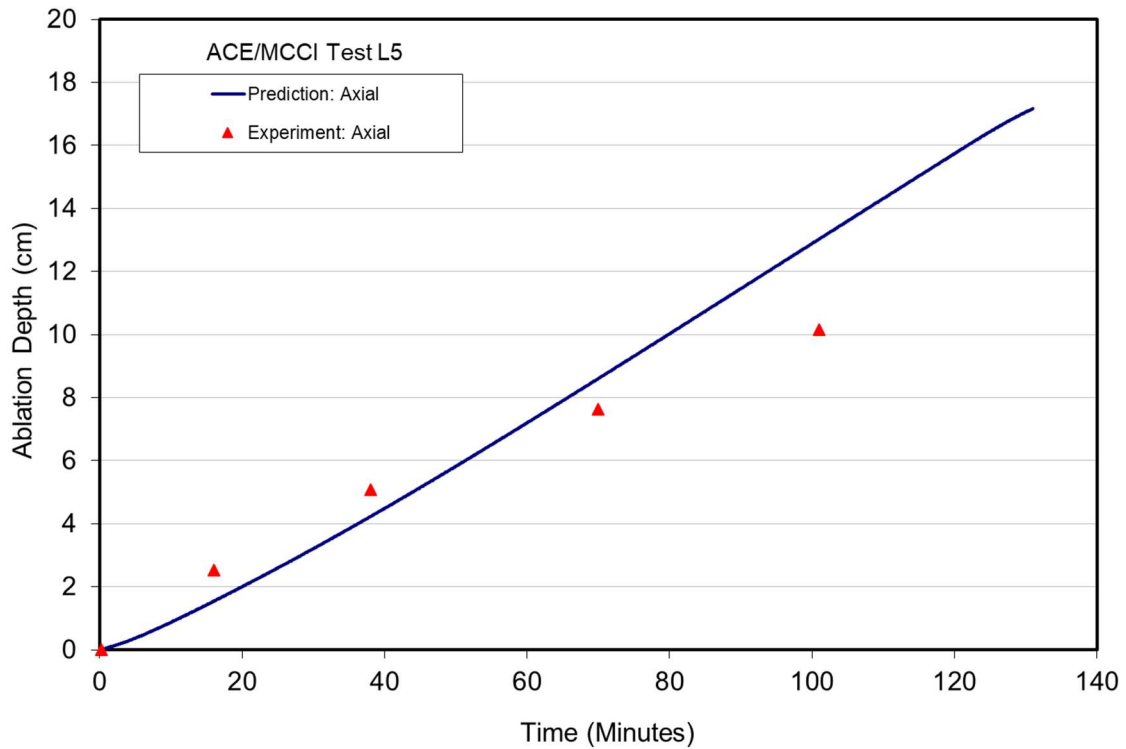


Figure C-11. Ablation Front Location Prediction for ACE Test L5.

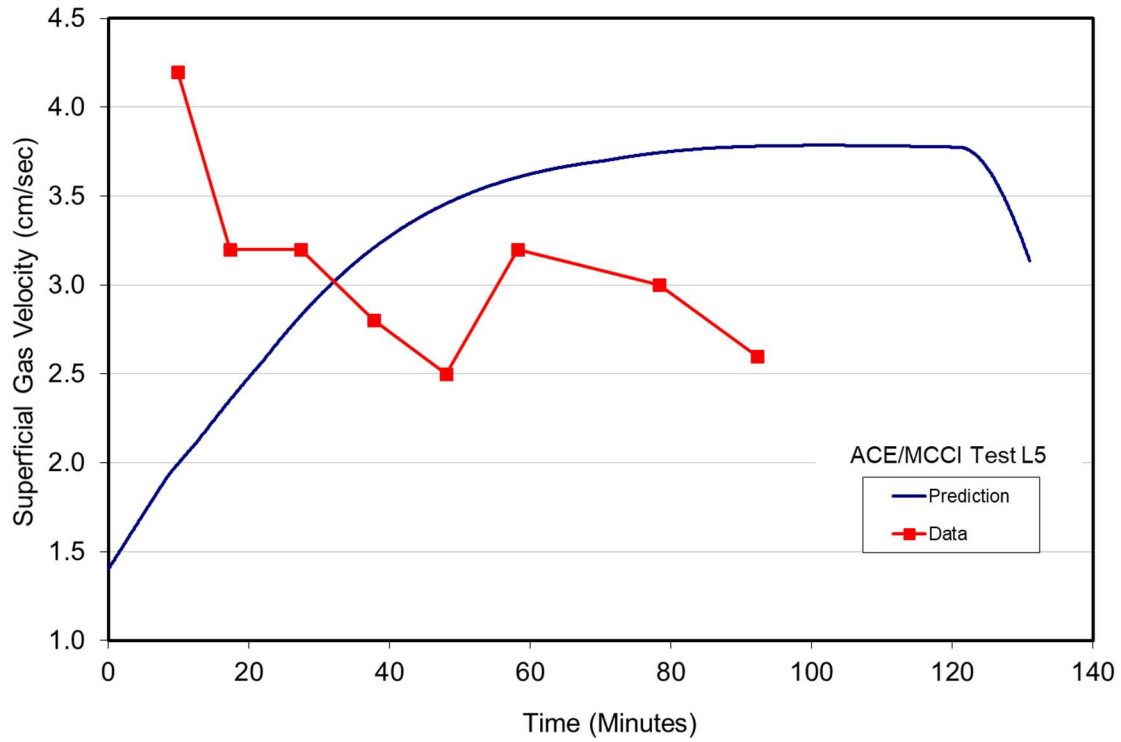


Figure C-12. Superficial Gas Velocity Prediction for ACE Test L5.

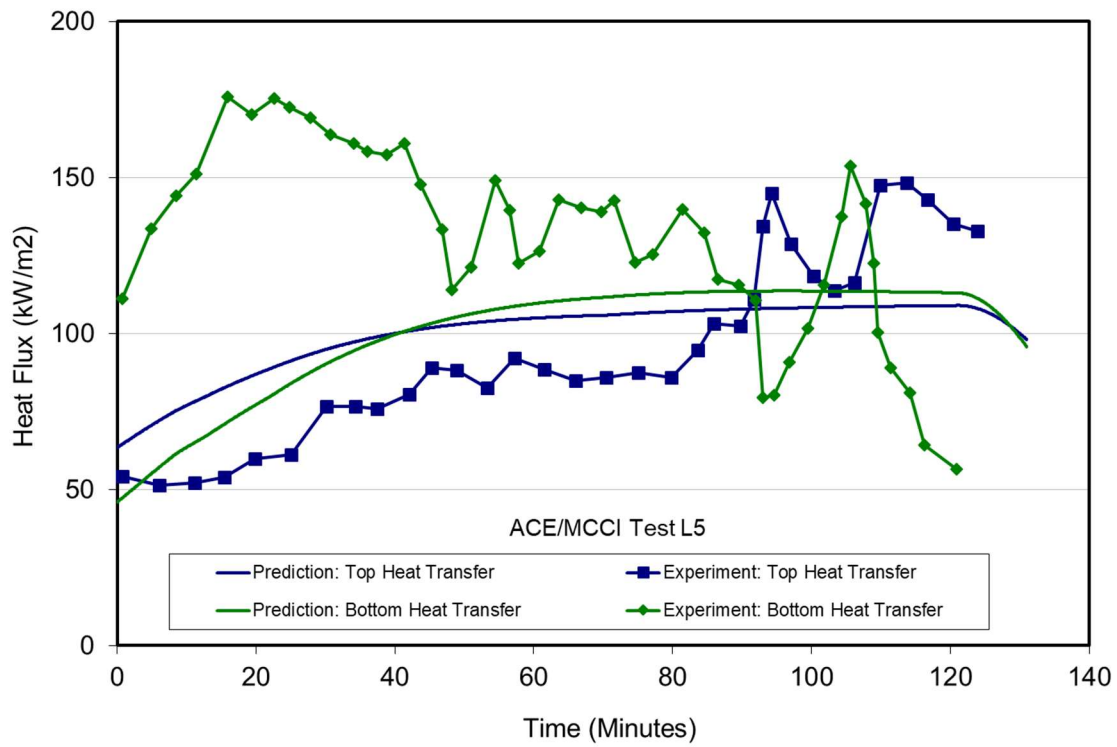


Figure C-13. Melt-Concrete and Melt-Atmosphere Heat Flux Prediction for ACE Test L5.

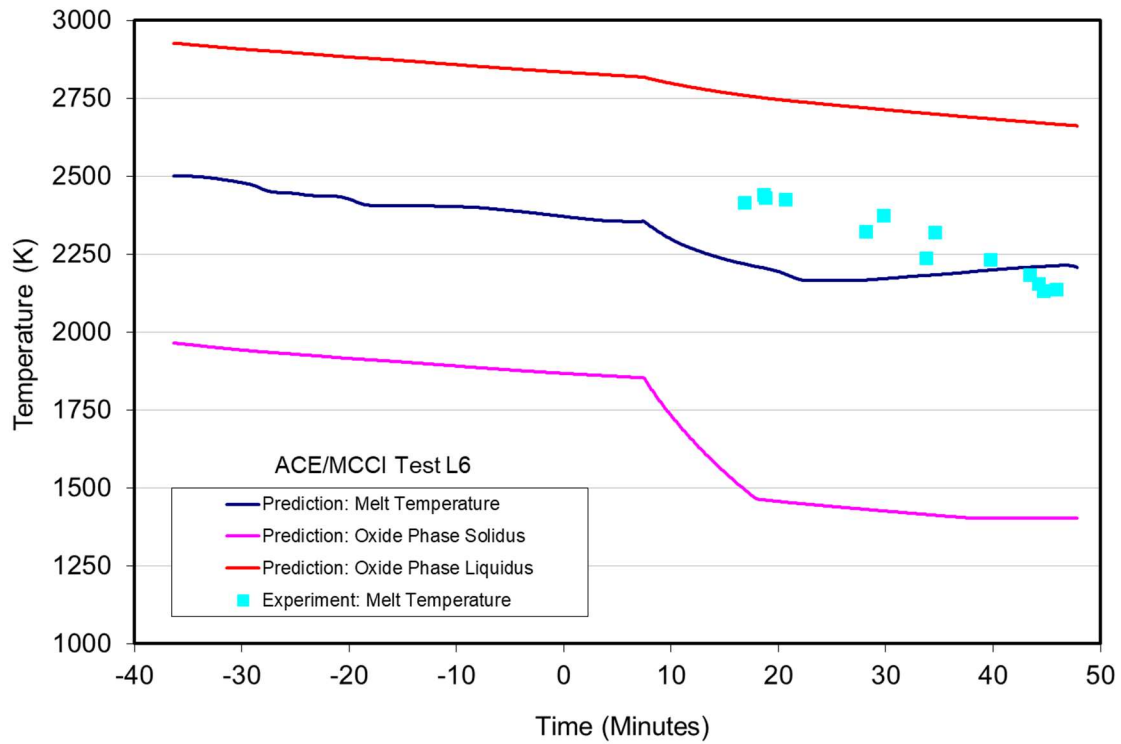


Figure C-14. Melt Temperature Prediction for ACE Test L6.

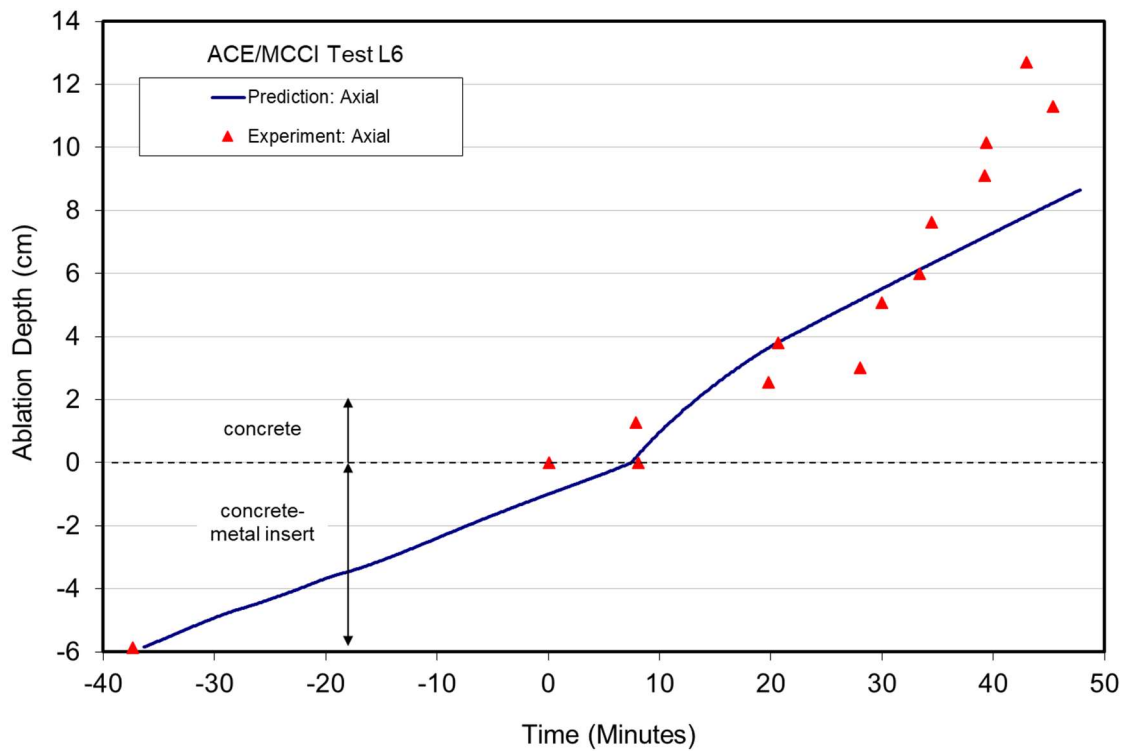


Figure C-15. Ablation Front Location Prediction for ACE Test L6.

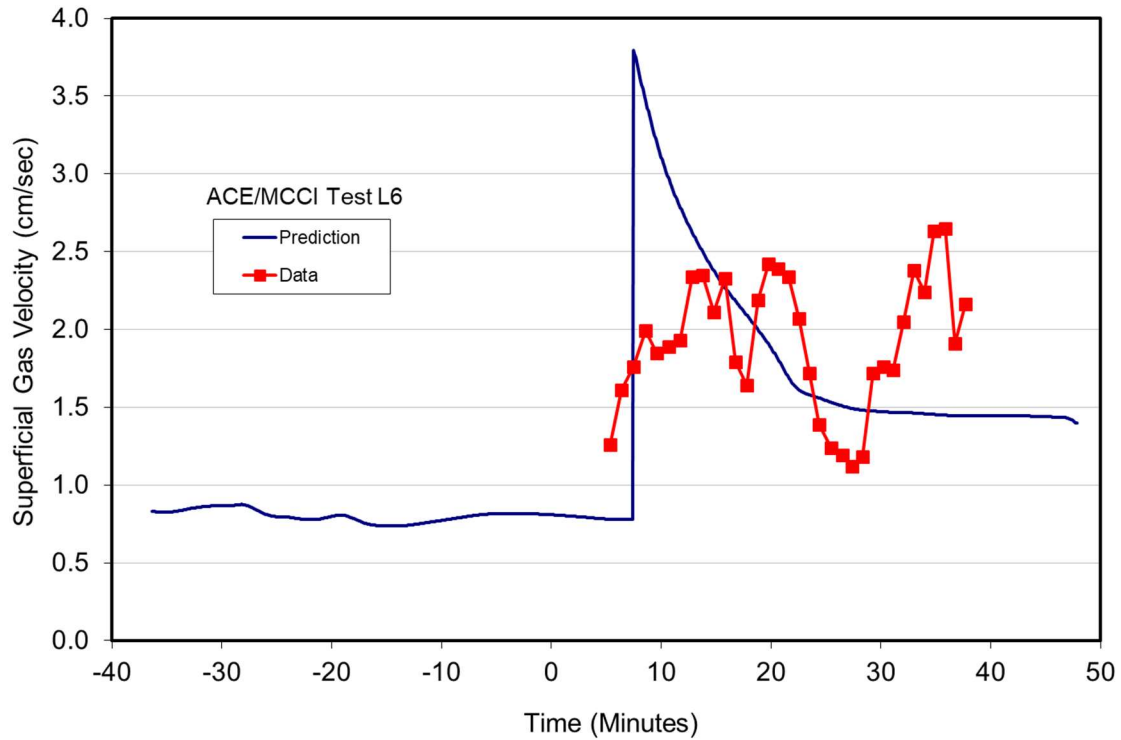


Figure C-16. Superficial Gas Velocity Prediction for ACE Test L6.

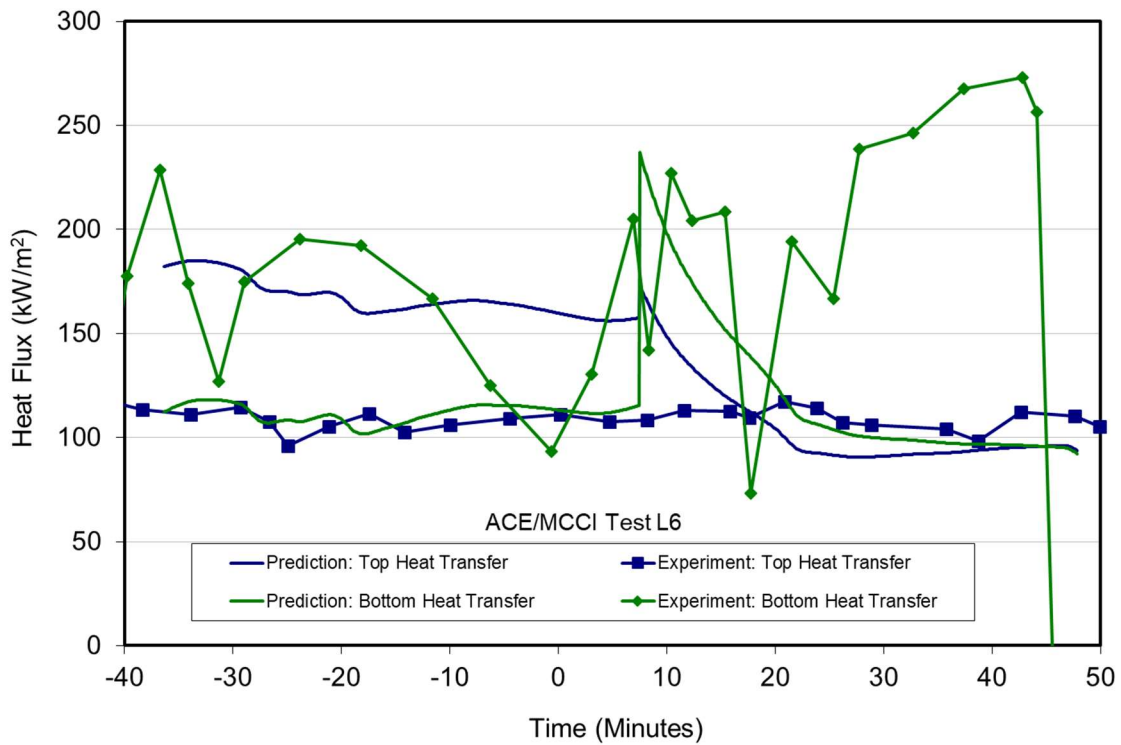


Figure C-17. Melt-Concrete and Melt-Atmosphere Heat Flux Prediction for ACE Test L6.

C.3.1.5 ACE/MCCI Test L8

Melt temperature, ablation front location, superficial gas velocity, and heat flux predictions are compared with data from the ACE L8 experiment in Figures C-18 through C-21, respectively. Melt temperature and ablation depth predictions are in reasonable agreement with the data, although ablation depth is slightly over-predicted. The overall trend and magnitude of the superficial gas velocity data are also reasonably reproduced. Finally, the top and bottom heat fluxes are generally reproduced, with the exception of the bottom heat flux that deviates substantially from the data after 30 minutes.

C.3.2 SNL SURC Tests

The SURC Tests^[119] shown in Table C-1 were also 1-D core concrete interaction experiments that were intended to provide thermal-hydraulic and fission product release data related to core-concrete interaction under dry cavity conditions to support code validation efforts. Both metal (stainless steel) and oxide tests were conducted as part of this test series; SURC-1 and SURC-2 were core oxide reactor material experiments, and so they were selected for analysis as part of this study. The test configuration differed from that used in the ACE/MCCI test series. In particular, the test section was cylindrical with inert MgO sidewalls. Heat input to the melt was provided by induction heating of tungsten susceptor rings that were placed at several different axial elevations inside the test crucible itself.

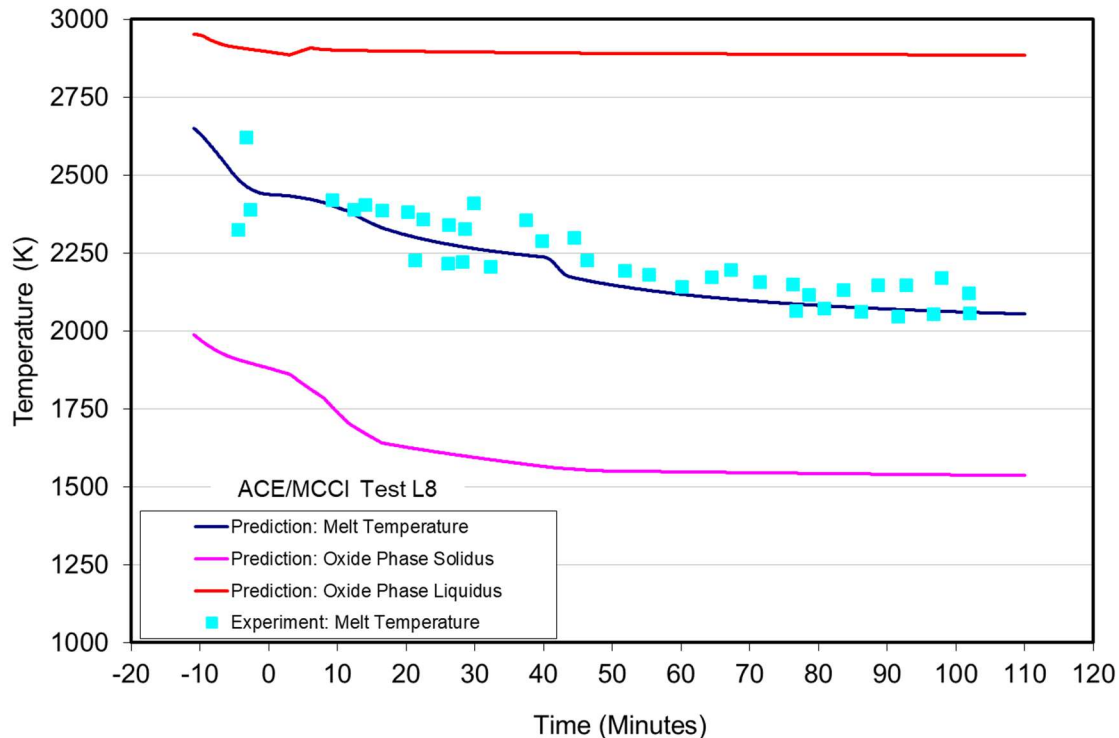


Figure C-18. Melt Temperature Prediction for ACE Test L8.

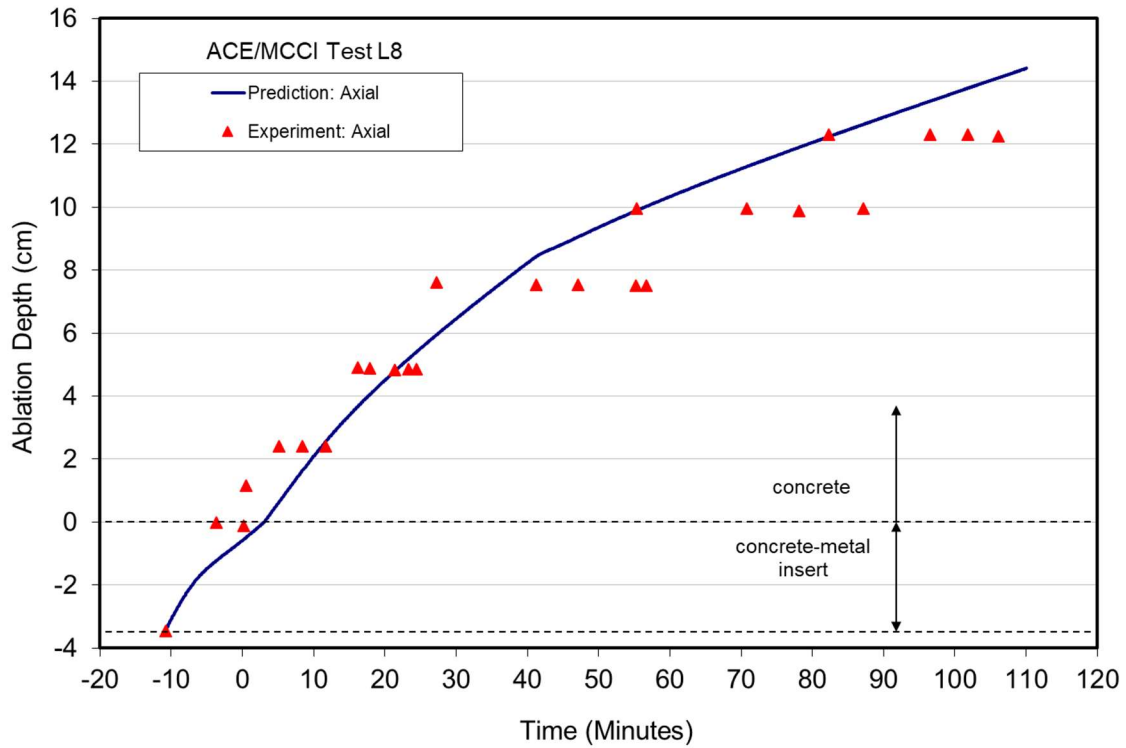


Figure C-19. Ablation Front Location Prediction for ACE Test L8.

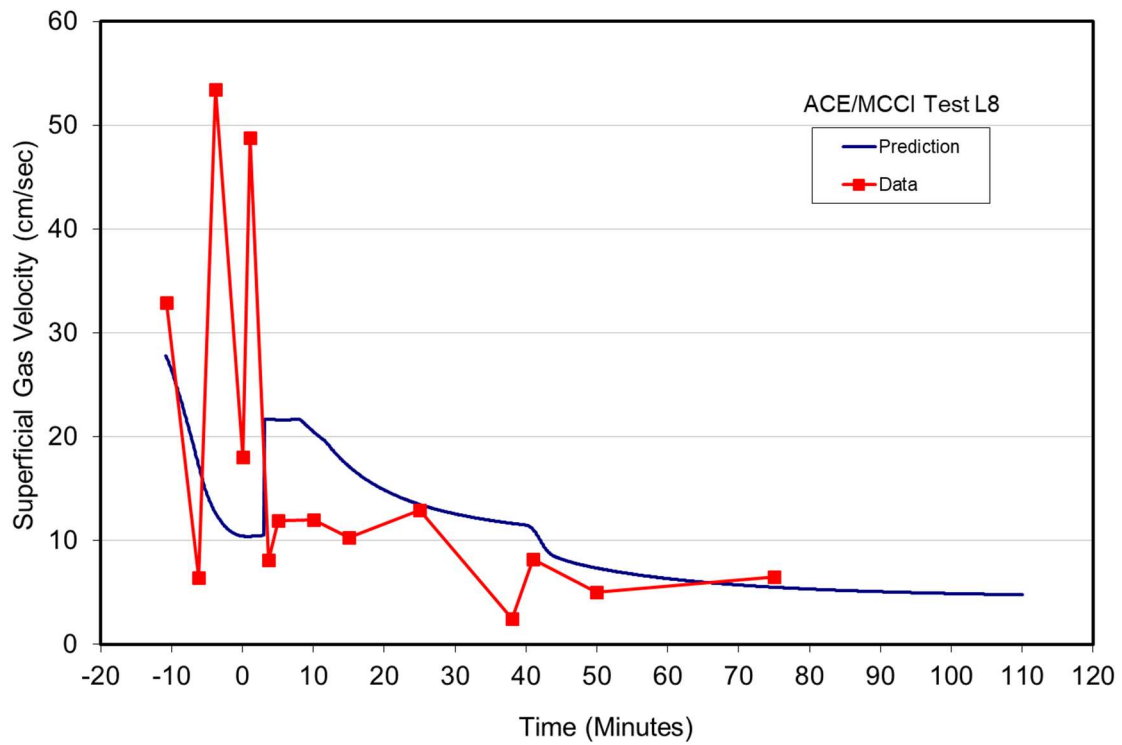


Figure C-20. Superficial Gas Velocity Prediction for ACE Test L8.

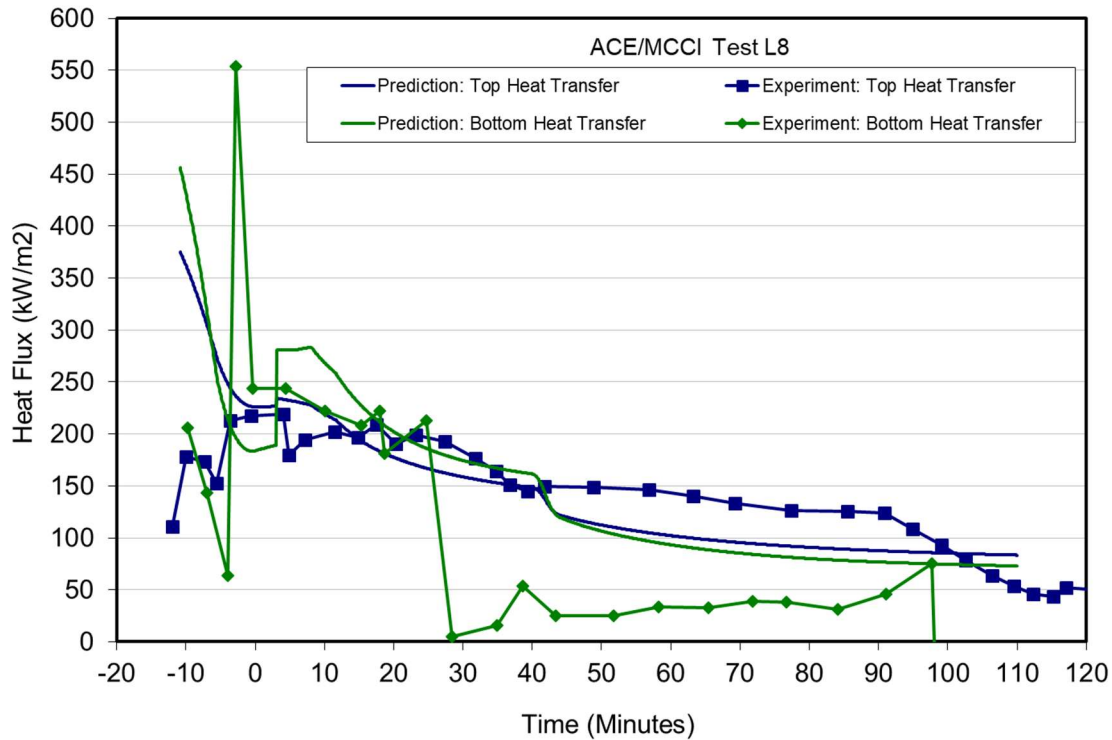


Figure C-21. Melt-Concrete and Melt-Atmosphere Heat Flux Prediction for ACE Test L8.

The concrete basemat compositions for the two experiments are shown in Table C-9. SURC-1 was conducted with limestone-limestone concrete, while SURC-2 was conducted with a basaltic concrete that is similar to siliceous. The concrete solidus and liquidus temperatures^[119] for these two materials are shown in Table C-10, along with the ablation temperatures that were assumed as part of this study. The facility was also instrumented with a gas detection system so that the composition and flowrate of the concrete decomposition gases could be measured during the test. This data was integrated, and as for the ACE/MCCI test series, the results revealed that not all decomposition gases migrated upwards. The release fractions deduced from this analysis are also shown in Table C-10; this information was used as part of the code input (i.e., XFLH2O and XFLCO2) for each test so that the correct integrated gas release would be calculated.

Table C-9. SURC-1 and -2 Concrete Compositions.

Constituent	Wt% for Test:	
	SURC-1	SURC-2
CO ₂	35.70	1.50
H ₂ O	4.10	5.00
K ₂ O	0.68	3.80
Na ₂ O	0.08	1.40
TiO ₂	0.12	0.80
SiO ₂	3.60	57.90
CaO	45.40	13.80
MgO	5.67	4.00
Al ₂ O ₃	1.60	7.20
Fe ₂ O ₃	1.20	4.40

Table C-10. Assumed Properties of Concretes for SURC Tests.

Property	SURC-1	SURC-2
T _{solidus} (K)	1635	1350
T _{liquidus} (K)	1873	1650
T _{ablation} (K)	1750	1500
Fraction H ₂ O detected	1.00	0.68
Fraction CO ₂ detected	0.38	1.00

The initial corium compositions and temperatures for the tests are shown in Tables C-11 and C-12, respectively. The latter table also provides the overlying structure temperatures that were used in the upward radiation heat transfer calculations. The structure temperatures are based on readings taken in the MgO lid that was used to seal the apparatus. The assumed emissivity was 0.80 for the MgO lid, which is typical of that for corium. This value was assumed due to the fact that posttest renderings of the debris indicated that the lid was covered with splattered melt. Finally, the input power curves for the two tests are provided graphically in Figure C-22. Time $t=0$ in this figure and in the results that follow corresponds to onset of the concrete basemat.

C.3.2.1 SNL SURC-1 Test

Melt temperature, ablation front location, superficial gas velocity, and upwards heat flux predictions are compared with data from the SURC-1 experiment in Figures C-23 through C-26, respectively. The trend in the melt temperature prediction in the early phase of the test does not match the test data. Based on the phase diagrams that are currently implemented, the model predicts that the melt temperature would have been close to the liquidus at the start of the test and hence very fluid. As a result, the temperature is predicted to drop rapidly as the melt convects heat to underlying concrete and overlying structure. Eventually, the temperature falls to the point where heat transfer to the boundaries balances the input power, and the temperature stabilizes. Thereafter, the temperature is predicted to increase as free Zr is oxidized and the melt solidus increases. Eventually, the solidus predicted from the (U,Zr)O_{2-x} phase diagram reaches the solidus predicted by the fully oxidized phase diagram that includes the effects of concrete decomposition products (See Section A.1.2). After this point, the solidus decreases monotonically as more slag is brought into the melt. The melt temperature follows the same trend. This overall affect would be reduced if the amount of free Zr present in the melt at the start of ablation was reduced. For instance, some of the free Zr present in the corium powders could have been oxidized during the 150 minute corium preheat phase of the test.^[119]

Table C-11. Initial Corium Compositions for SURC Tests.

Constituent	Mass (kg) for Test:	
	SURC-1	SURC-2
Zr	16.4	16.9
ZrO ₂	46.0	46.1
UO ₂	138.4	140.9
Total	200.8	203.9

Table C-12. Assumed Initial Melt and Boundary Temperatures for the SURC Tests.

Test	Initial Melt Temp. (K)	Upper Structure Temp. (K)
SURC-1	2611	800
SURC-2	2600	900

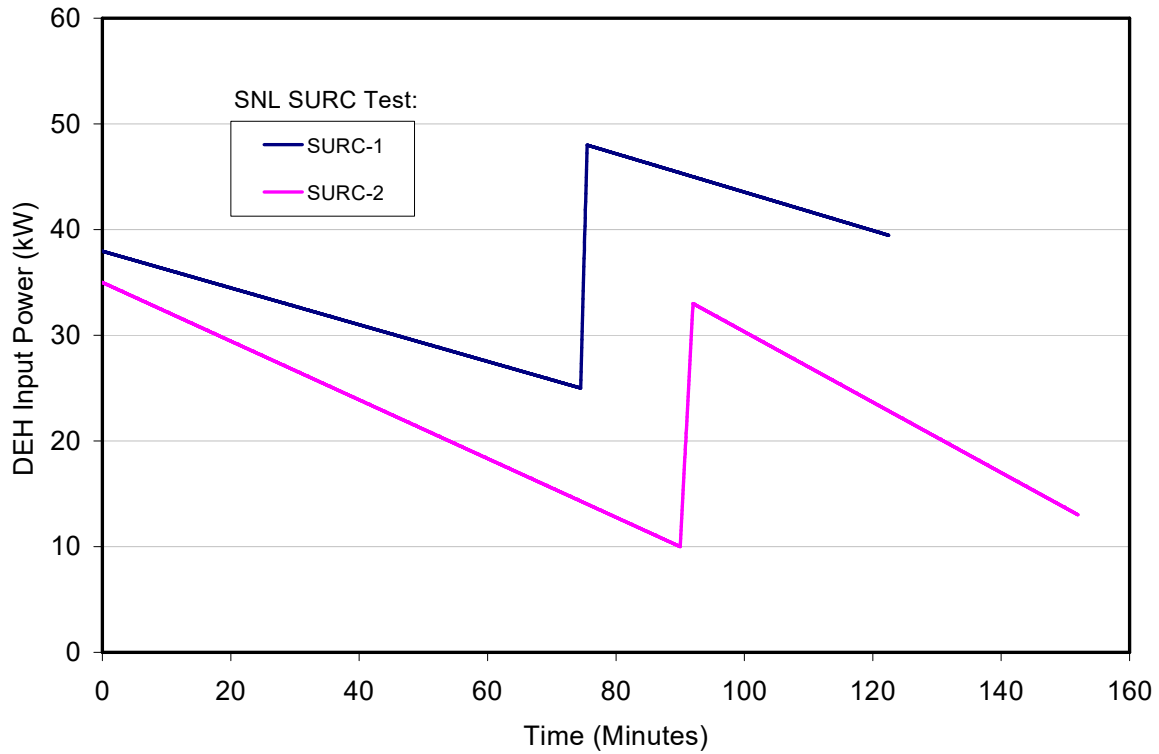


Figure C-22. Input Power Relative to Onset of Basemat Ablation for SURC-1 and -2.

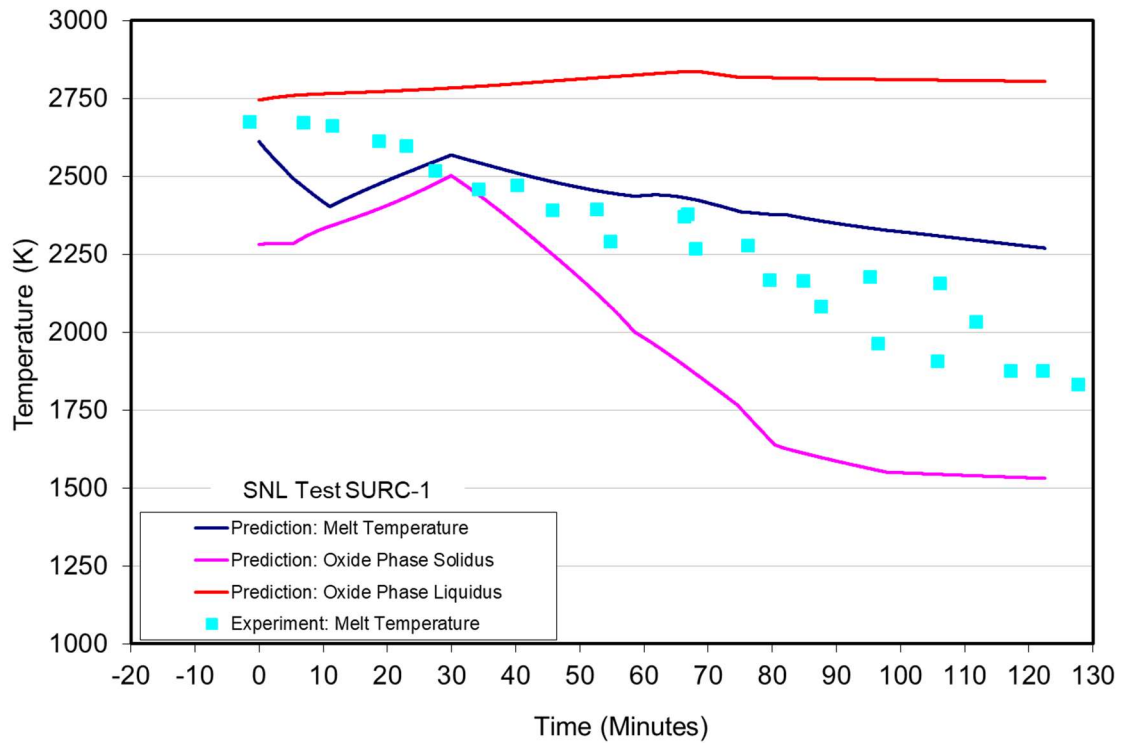


Figure C-23. Melt Temperature Prediction for SNL SURC-1 Test.

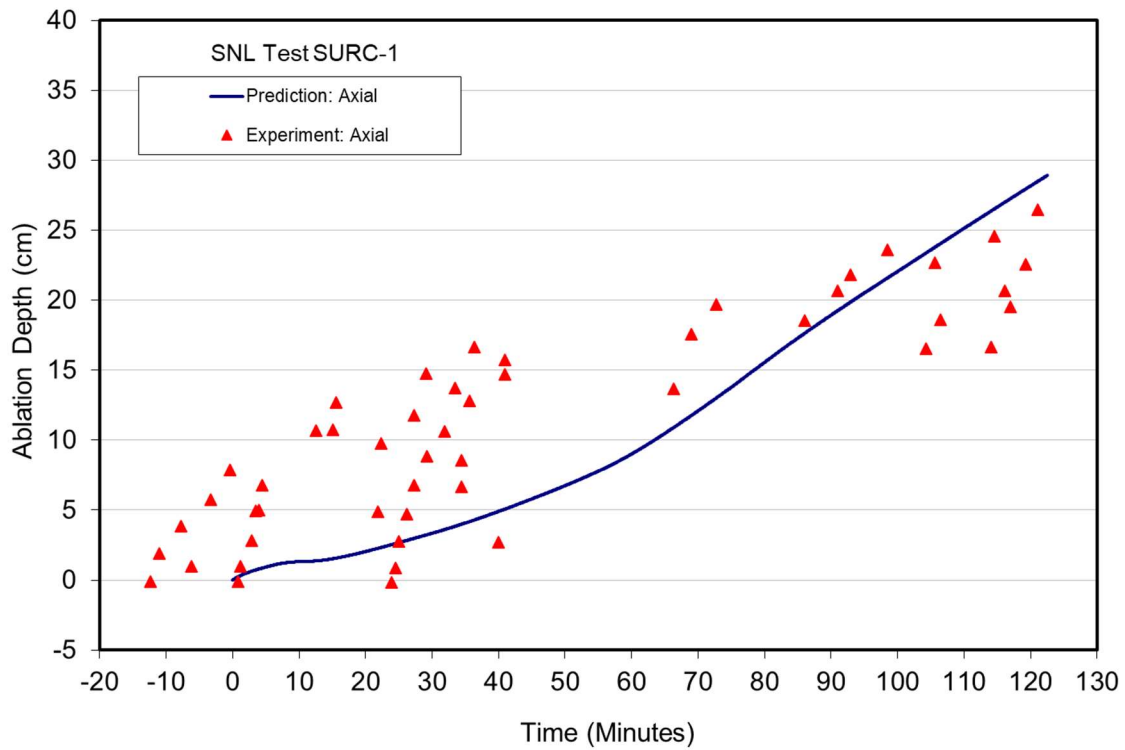


Figure C-24. Ablation Front Location Prediction for SNL SURC-1 Test.

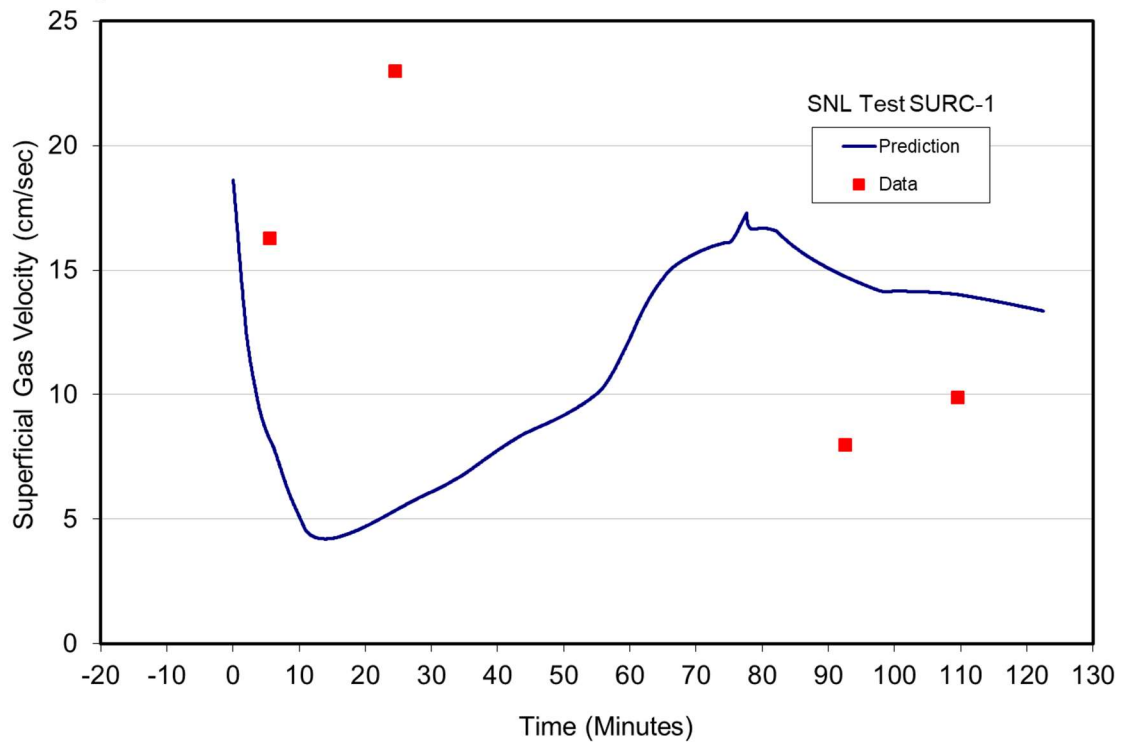


Figure C-25. Superficial Gas Velocity Prediction for SNL SURC-1 Test.

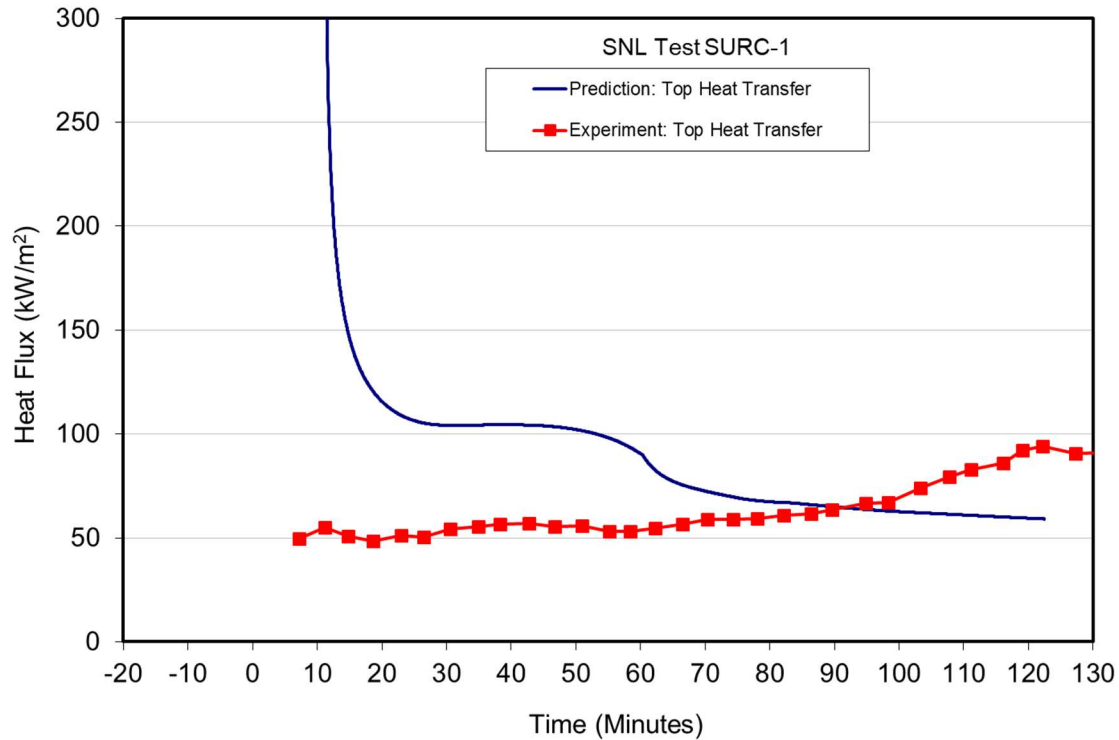


Figure C-26. Melt- Atmosphere Heat Flux Prediction for SNL SURC-1 Test.

Despite the discrepancies in melt temperature prediction early in the test, the overall trend and magnitude of the basemat ablation are captured reasonably well. The magnitude of the superficial gas velocity is also reasonably predicted, although there are insufficient data to make a detailed comparison. Finally, the upwards heat flux early in the test is over-predicted; the basis for the over-prediction was described above. However, after the initial transient has passed, the model reasonably replicates the magnitude and trend in the upwards heat flux.

C.3.2.2 SNL SURC-2 Test

Melt temperature, ablation front location, superficial gas velocity, and upwards heat flux predictions are compared with data from the SURC-2 experiment in Figures C-27 through C-30, respectively. The discussion provided in the previous section regarding melt temperature behavior early in the test is also applicable here, although in this case the data seem to agree better with the predicted trend. The ablation depth and upwards heat flux predictions agree reasonably well with the data. The trend in the superficial gas velocity data is also reasonably replicated, but the magnitude is slightly under-predicted.

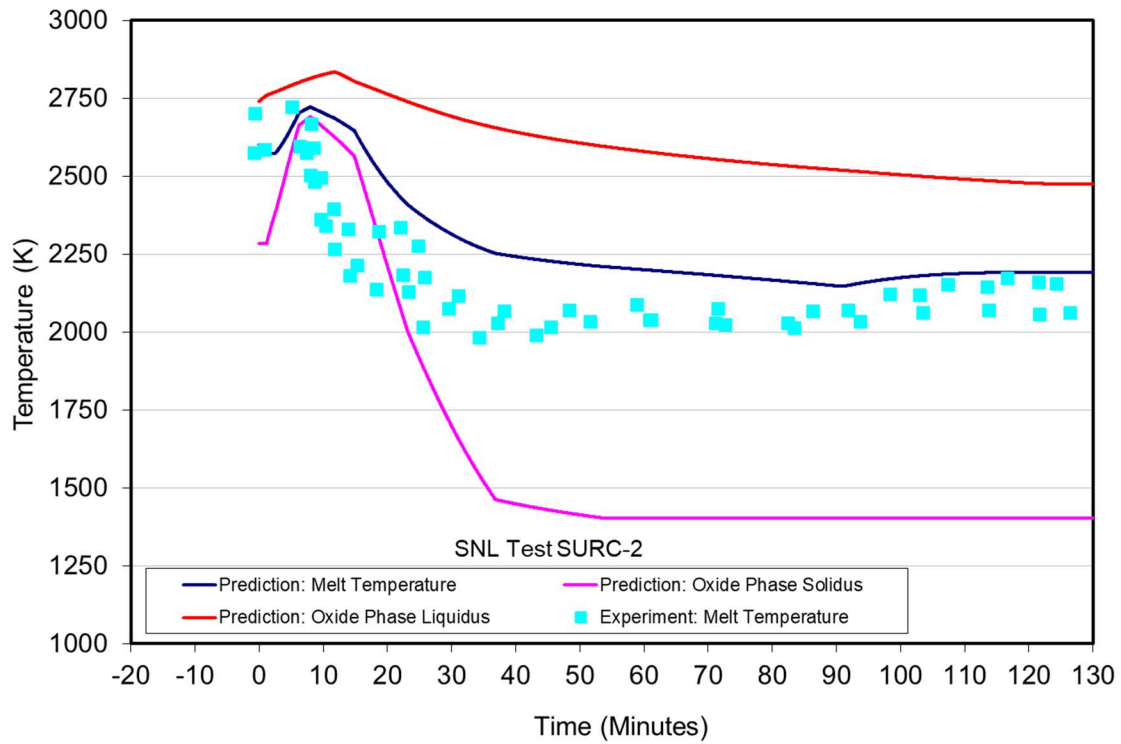


Figure C-27. Melt Temperature Prediction for SNL SURC-2 Test.

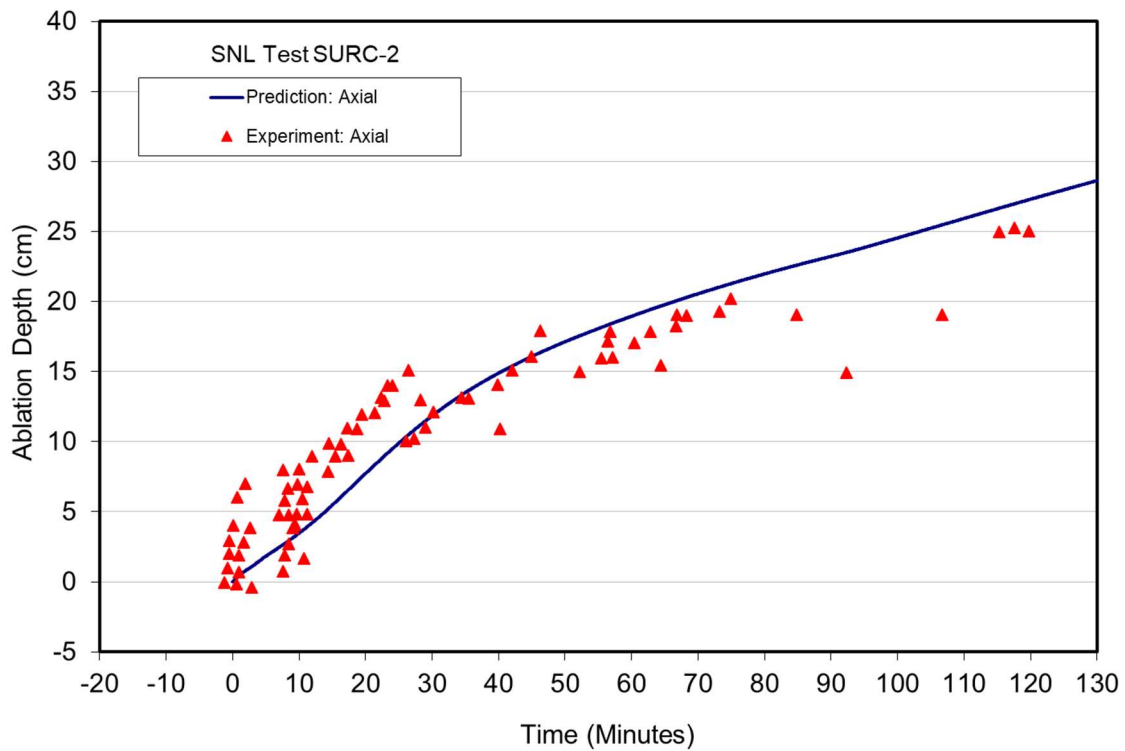


Figure C-28. Ablation Front Location Prediction for SNL SURC-2 Test.

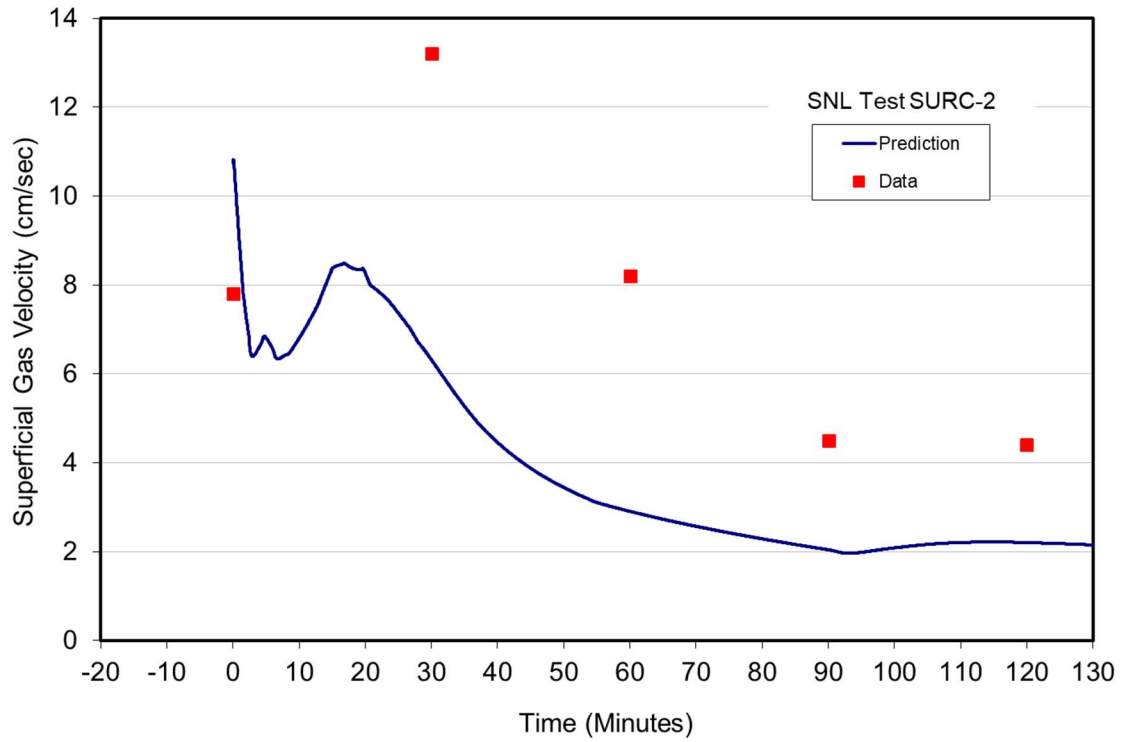


Figure C-29. Superficial Gas Velocity Prediction for SNL SURC-2 Test.

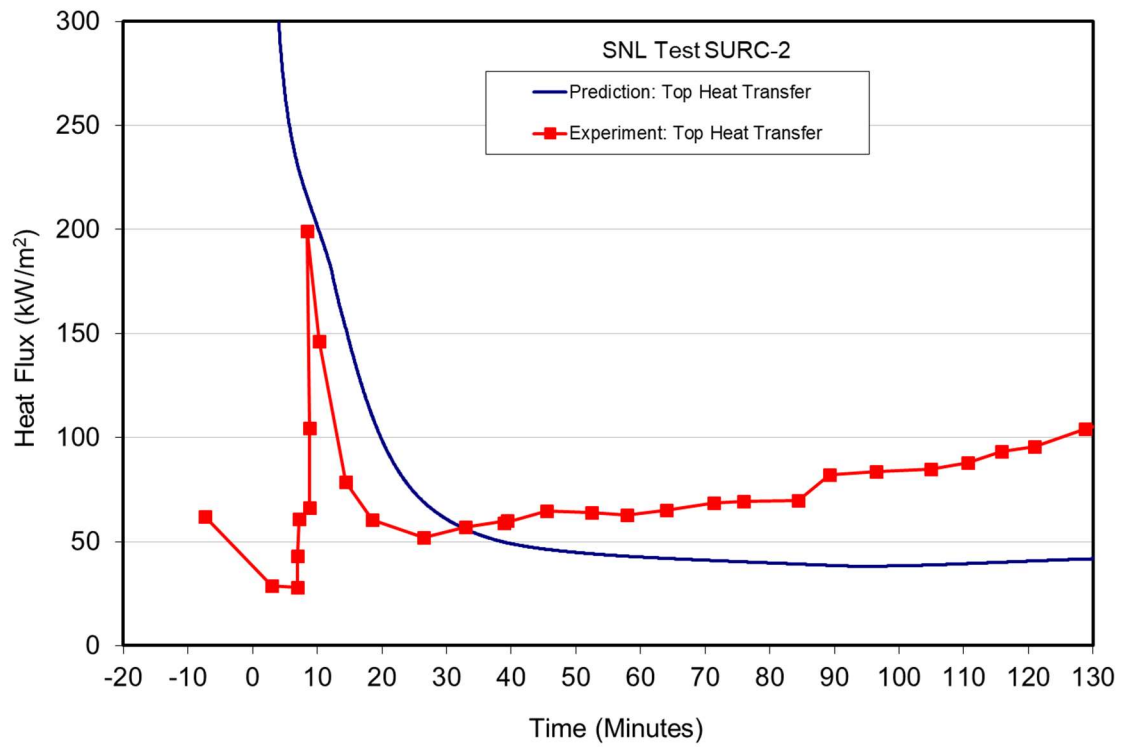


Figure C-30. Melt- Atmosphere Heat Flux Prediction for SNL SURC-2 Test.

C.3.3 Dry OECD/MCCI Tests

The OECD/MCCI Tests^[17-19] shown in Table C-1 were carried out with the overall objectives of providing data on: i) the axial/lateral power split during long term 2-D core concrete interaction and ii) the nature and extent of debris quenching following late phase cavity flooding. Tests CCI-4 and CCI-5 in the matrix were carried out under dry cavity conditions. The two walls between the tungsten electrodes were fabricated from concrete to allow the ablation to proceed laterally as well as axially. For CCI-4, the test was modeled using the 2-D notch geometry option with two ablating sidewalls (N2DCALCC=3). The width between the two adiabatic sidewalls was 0.5 m (i.e., distance between tungsten electrodes), while the width between the two ablating concrete walls was 0.4 m. Thus, the initial basemat surface area was 0.20 m². Since CCI-5 had only one ablating sidewall, it was modeled with the 2-D notch geometry option with one ablating wall (N2DCALCC=4). The width between the two adiabatic sidewalls was also 0.5 m for this test, but the length between the third adiabatic wall and the concrete was 0.79 m, so that the initial basemat surface area was 0.395 m².

For CCI-5, thermite was used to produce the melt, and so the transient surface crust formation model was used on both horizontal and vertical concrete surfaces (i.e., NABBL=2 with NABLB/NABLS=1). However, in CCI-4 a concrete/metal insert was used in order to incorporate unoxidized metal into the melt prior to onset of axial ablation. Thus, this test was calculated using the fully developed concrete dryout model (NABBL=1) since significant heatup of the underlying concrete occurred during the insert ablation phase. Both tests remained dry, and so the simulations were run assuming a floating crust boundary condition.

The concrete compositions for all five CCI tests are shown in Table C-13. For the dry cavity tests, CCI-4 utilized limestone/common sand concrete, while CCI-5 used siliceous. The concrete solidus and liquidus temperatures for these two concrete types are shown in Table C-14, along with the ablation temperatures that were assumed as part of this study. They are the same as those used for the ACE/MCCI test analyses provided previously. The CCI test section was designed to be relatively leaktight up to 70 kPa test section differential pressure; as a result, all gases arising from concrete decomposition traveled up through the melt.

The initial melt compositions for all the CCI tests are shown in Table C-15. For CCI-4, the initial composition includes the incorporation of the decomposition byproducts from the erosion of the concrete/metal inserts after accounting for the oxidation of Zr from H₂O and CO₂ present in the inserts.^[47] Initial melt temperatures for the tests are provided in Table C-16. This table also provides the upper structure temperatures that were used in the upward radiation heat transfer calculation. The structure temperatures are based on readings taken on the sidewalls of the apparatuses above the melt surface prior. The assumed emissivity was 0.30 for all cases, which is indicative of oxide materials such as cast MgO and concrete. Finally, the input power curves for all tests are shown in Figure C-31. Time t=0 in the figure and all others related to this test series corresponds to the time of melt contact with the basemat.

Table C-13. Concrete Compositions for OECD/MCCI Tests.

Constituent	Wt % for Test:				
	CCI-2	CCI-3	CCI-4	CCI-5	CCI-6
CO ₂	30.42	10.0	24.02	9.50	8.80
H ₂ O	4.46	3.78	7.06	4.78	6.53
K ₂ O	0.56	0.83	0.54	0.80	0.98
Na ₂ O	0.32	0.68	0.39	0.49	0.67
TiO ₂	0.14	0.16	0.17	0.15	0.15
SiO ₂	22.01	61.32	26.23	58.30	54.02
CaO	26.42	17.21	28.07	20.21	22.58
MgO	11.71	0.87	9.29	0.92	0.91
Al ₂ O ₃	2.54	3.61	2.81	3.51	4.06
Fe ₂ O ₃	1.42	1.53	1.41	1.33	1.31

Table C-14. Assumed Properties of Concretes for OECD/MCCI CCI Tests.

Property	CCI-2	CCI-3	CCI-4	CCI-5	CCI-6
T _{solidus} (K)	1393	1403	1393	1403	1403
T _{liquidus} (K)	1568	1523	1568	1523	1523
T _{ablation} (K)	1500	1450	1500	1450	1450
Fraction H ₂ O liberated	1.00	1.00	1.00	1.00	1.00
Fraction CO ₂ liberated	1.00	1.00	1.00	1.00	1.00

Table C-15. Initial Corium Compositions for OECD/MCCI CCI Tests.

Constituent	Mass (kg) for Test:				
	CCI-2	CCI-3	CCI-4	CCI-5	CCI-6
UO ₂	242.48	211.41	169.36	332.29	562.50
ZrO ₂	99.60	86.82	64.51	136.47	231.03
SiO ₂	13.56	41.92	12.15	65.90	40.41
Al ₂ O ₃	1.64	2.40	1.47	3.78	2.43
MgO	4.56	0.45	4.08	0.70	0.36
CaO	12.52	8.31	11.23	13.04	8.01
Zr	0.00	0.00	13.82	0.00	0.00
Cr	25.64	24.06	14.08	37.82	55.26
Fe	0.00	0.00	8.97	0.00	0.00
Total	400.00	375.37	299.67	590.00	900.00

Table C-16. Assumed Initial Melt and Boundary Temperatures for OECD/MCCI Tests.

Test	Initial Melt Temperature (K)	Upper Structure Temperature (K)
CCI-2	2150	750
CCI-3	2220	750
CCI-4	2250	750
CCI-5	2200	750
CCI-6	2320	750

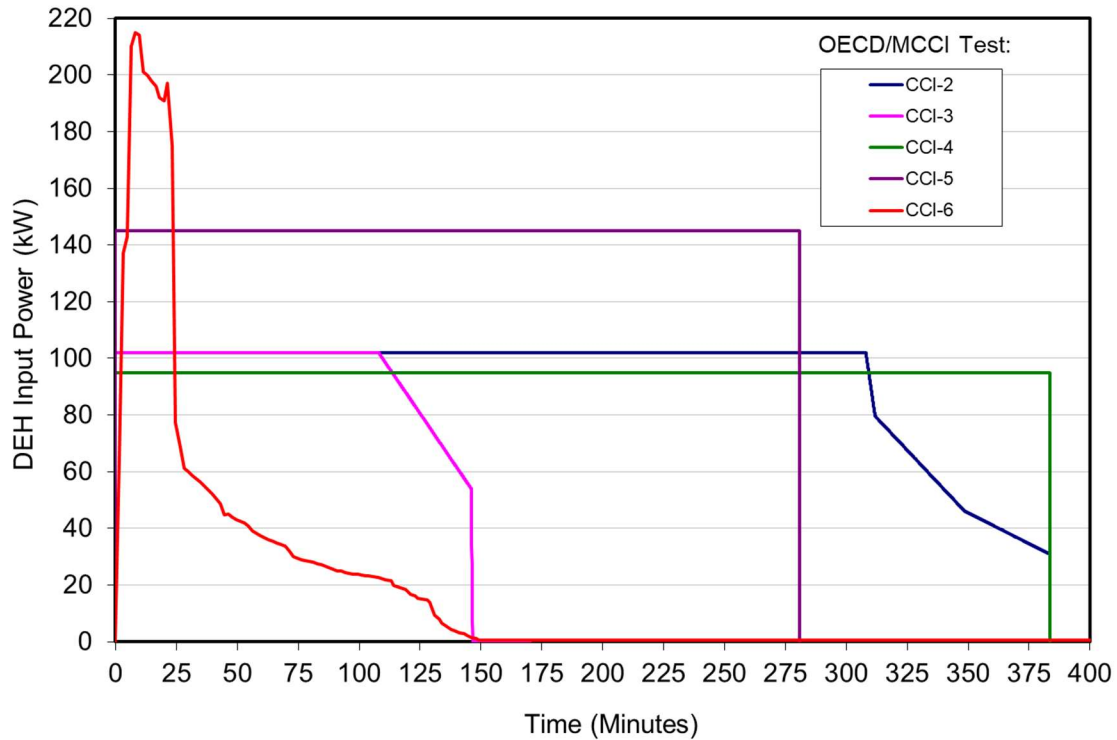


Figure C-31. Input Power for OECD/MCCI CCI Tests.

C.3.3.1 OECD/MCCI CCI-4 Test

As shown in Table C-1, CCI-4 was conducted with a 78 % oxidized BWR core melt interacting with a limestone/common sand concrete crucible. The melt temperature and ablation front predictions are compared with the test data in Figures C-32 and C-33, respectively. For this test, the melt temperature is reasonably predicted while the cavity ablation is slightly over-predicted. As noted earlier, these cases were run using the Bradley slag film heat transfer model^[39] on both the lateral and axial concrete surfaces. Thus, the lateral and axial ablation progression is identical on both surfaces. As discussed in the data report,^[47] this test experienced extensive melt foaming and so heat losses to the non-ablating sidewalls were higher than planned. Thus, the effective input power to the melt may have been reduced by as much as 33% relative to that shown in Figure C-31. This may partially explain the over-prediction of cavity ablation that is evident in Figure C-33.

C.3.3.2 OECD/MCCI CCI-5 Test

As shown in Table C-1, CCI-5 was conducted with a fully oxidized BWR core melt interacting with a siliceous concrete crucible. The melt temperature and ablation front predictions are compared with the test data in Figures C-34 and C-35, respectively. For this test, the melt temperature and axial erosion depth are reasonably predicted, but the radial ablation is extensively over-predicted. In this experiment, onset of sidewall erosion was delayed until ~ 150 minutes in the experiment sequence, and this was attributed to the presence of a resilient crust that protected the wall up until this time.^[66] The code does not capture this effect. However, after sidewall ablation commences, the radial erosion rate prediction seems to match the data fairly well.

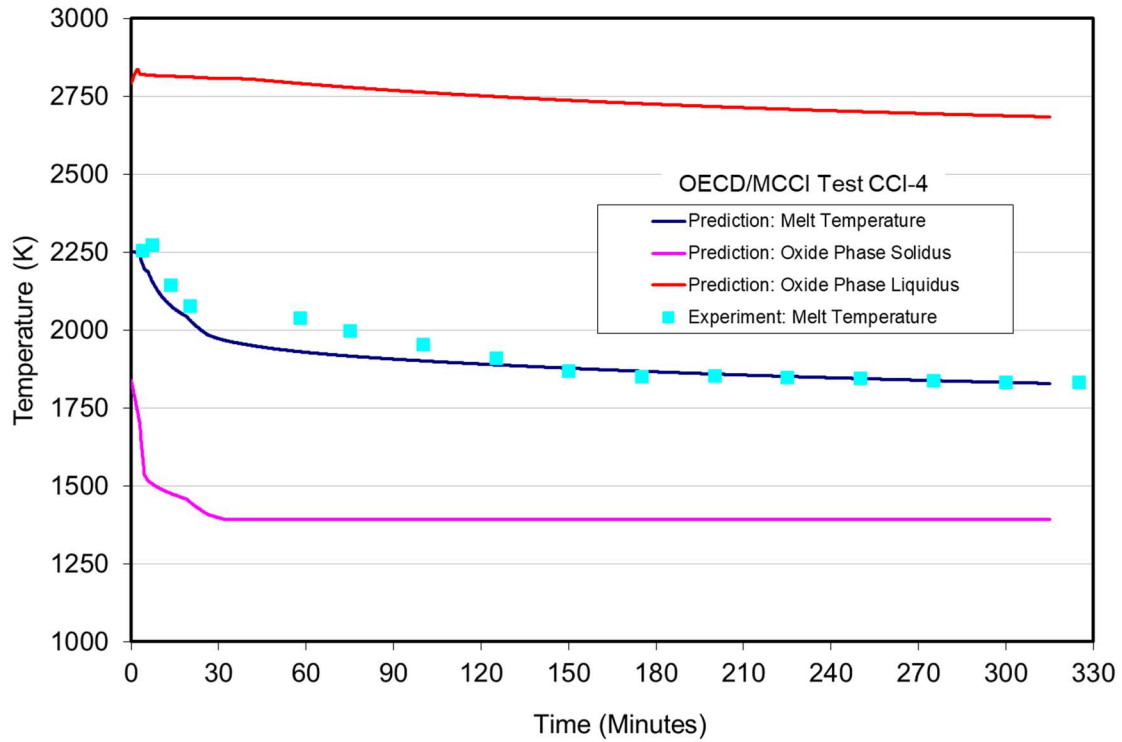


Figure C-32. Melt Temperature Prediction for OECD/MCCI CCI-4 Test.

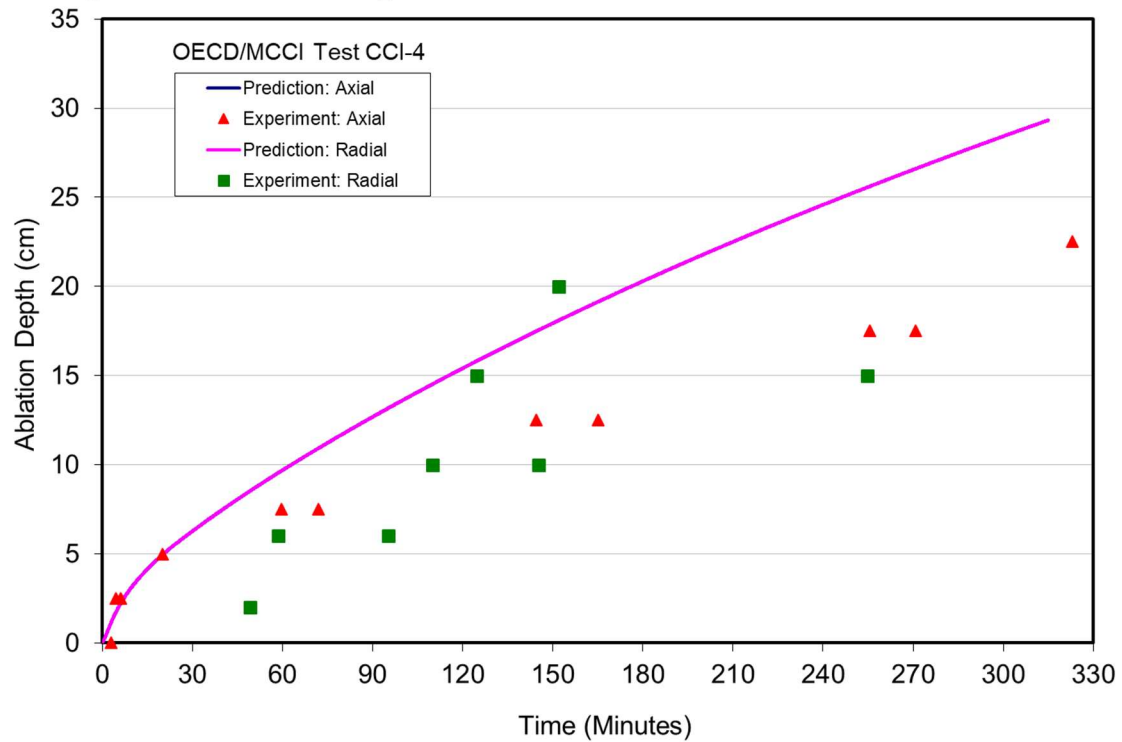


Figure C-33. Ablation Front Location Prediction for OECD/MCCI CCI-4 Test.

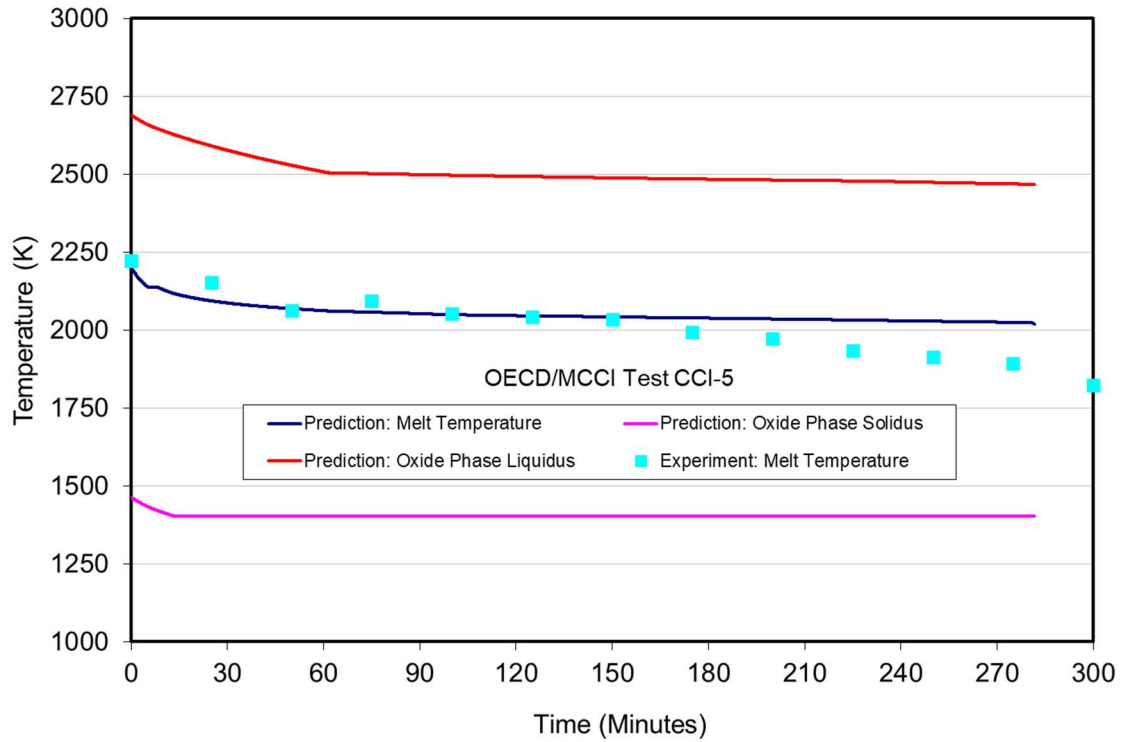


Figure C-34. Melt Temperature Prediction for OECD/MCCI CCI-5 Test.

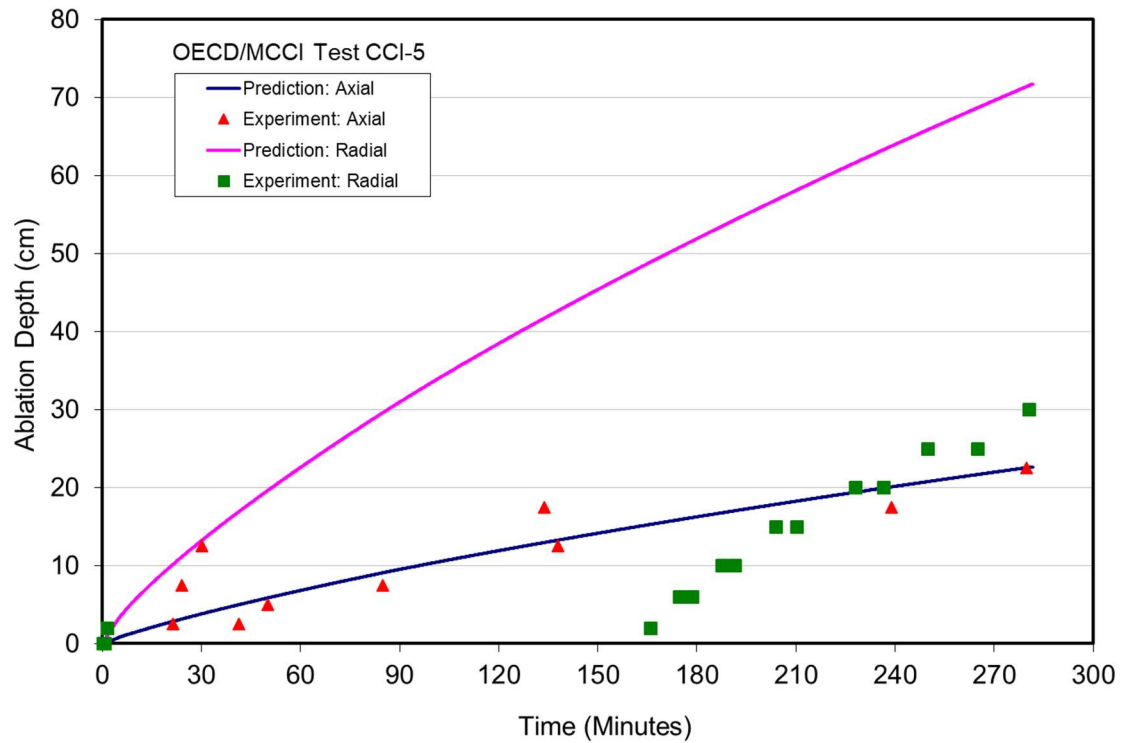


Figure C-35. Ablation Front Location Prediction for OECD/MCCI CCI-5 Test.

C.4 Wet Cavity Experiment Results

C.4.1 Wet OECD/MCCI Tests

The flooded cavity OECD/MCCI Tests^[17-19,128] provided data on the nature and extent of debris quenching under both early- and late-phase cavity flooding conditions. These tests also utilized a concrete cavity that was in the shape of a 2-D notch. As shown in Table C-1, Tests CCI-2 and CCI-3 were constructed such that the initial concrete basemat cross-sectional area was 50 cm x 50 cm, while CCI-6 was an increased scale experiment featuring a 70 cm x 70 cm basemat. The two walls between the tungsten electrodes were fabricated from concrete to allow the ablation to proceed laterally as well as axially. Thus, these tests were modeled using the 2-D notch geometry option (N2DCALCC=3) with the width between the two adiabatic sidewalls set at 0.5 m for CCI-2 and CCI-3. The width was increased to 0.7 m for CCI-6. All three tests used thermite to produce the melt, and so the transient surface crust formation model was used on both horizontal and vertical concrete surfaces (i.e., NABBL=2 with NABLB/NABLS=1). Since no large continuous voids formed between the crust and solidified debris zones for these tests, all three cases were run assuming a floating crust boundary condition after water addition.

The concrete compositions for the three tests are shown in Table C-13. CCI-2 was conducted with limestone/common sand concrete, while CCI-3 and CCI-6 used siliceous. The concrete solidus and liquidus temperatures for these two concrete types are shown in Table C-14, along with the ablation temperatures that were assumed as part of this study. They are the same as those used for the ACE/MCCI and MACE test analyses provided previously. The CCI test section was designed to be relatively leaktight up to 70 kPa test section differential pressure; as a result, all gases arising from concrete decomposition traveled up through the melt.

The initial melt compositions for the two tests are shown Table C-15, while initial melt temperatures are shown in Table C-16. The latter table also provides the overlying structure temperatures that were used in the upward radiation heat transfer calculation during the dry period of core-concrete interaction prior to water addition to the test section. Structure temperatures are based on readings taken on the sidewalls of the apparatuses above the melt surface prior to cavity flooding. The assumed emissivity was 0.30 for both cases, which is indicative of oxide materials such as cast MgO and concrete. Finally, the input power curves for the three tests are shown graphically in Figure C-31. Time $t=0$ in this figure and all others related to this test series corresponds to the time of melt contact with the basemat.

C.4.1.1 OECD/MCCI CCI-2 Test

As shown in Table C-1, CCI-2 utilized limestone/common sand concrete.^[128] The test ran dry for 300 minutes and was then flooded. The calculation was run in the same manner.

The melt temperature, ablation front location, and upwards heat flux predictions are compared with the test data in Figures C-36 through C-38, respectively, while the evolution of the various surface elevations is shown in Figure C-39. For this test, the melt temperature trend is reasonably predicted during the dry phase; after flooding, the temperatures are under-predicted. As noted earlier, these cases were run using the Bradley heat transfer model^[39] on both lateral and axial concrete surfaces. Thus, the lateral and axial ablation predictions identical. As shown in Figure C-37, the model slightly under-predicts the overall cavity ablation observed in the test.

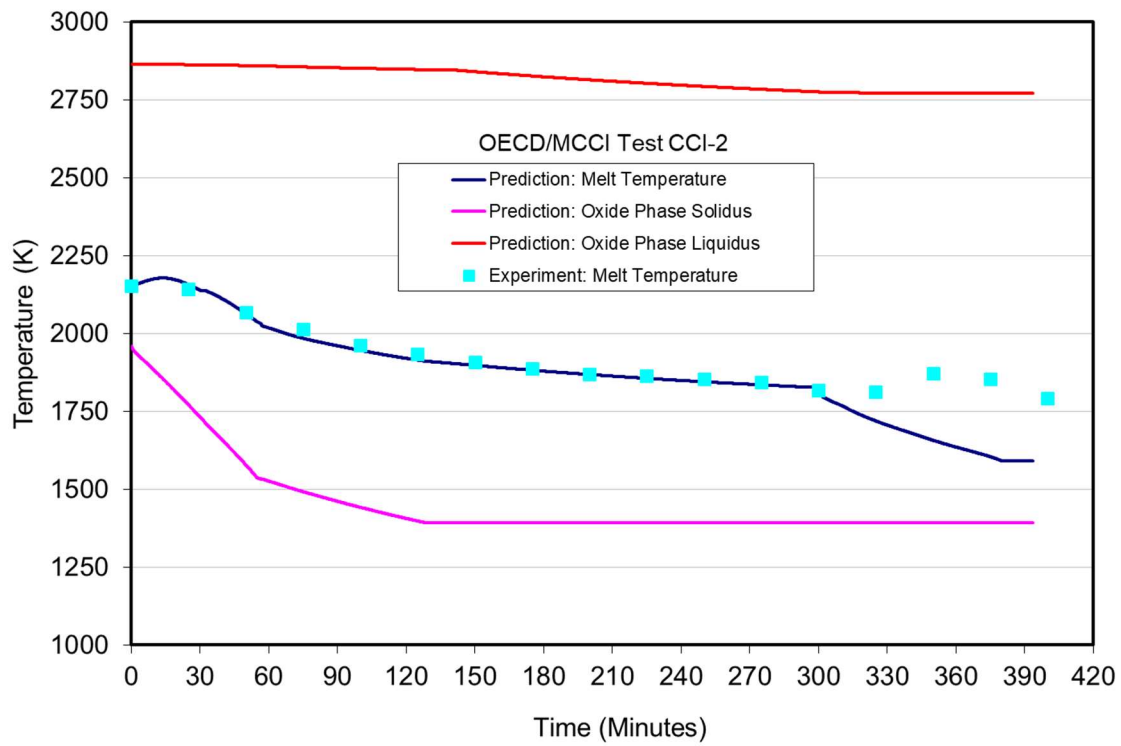


Figure C-36. Melt Temperature Prediction for OECD/MCCI CCI-2 Test.

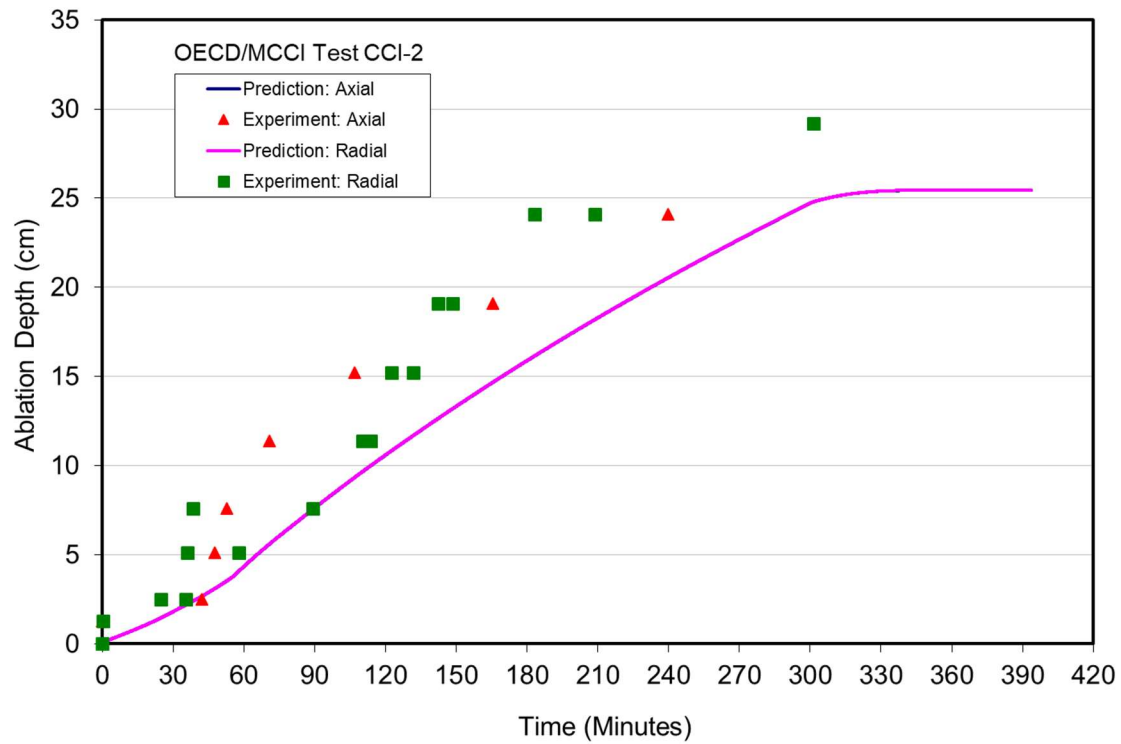


Figure C-37. Ablation Front Location Prediction for OECD/MCCI CCI-2 Test.

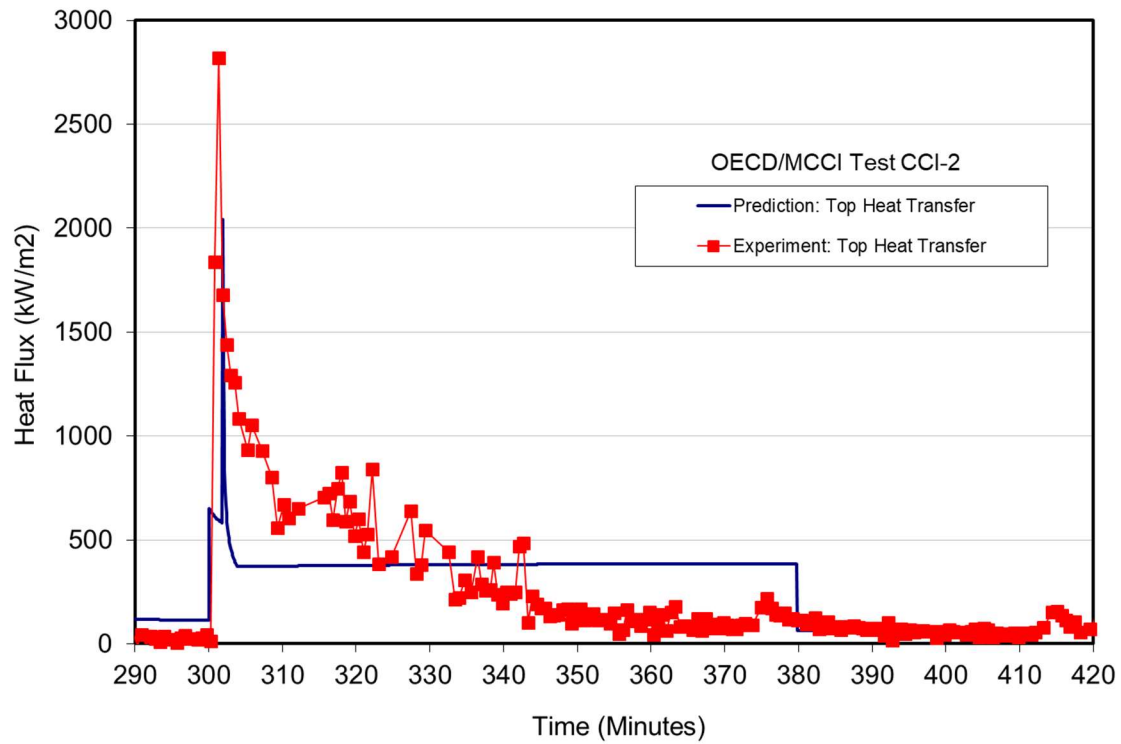


Figure C-38. Melt-Atmosphere Heat Flux Prediction for OECD/MCCI CCI-2 Test.

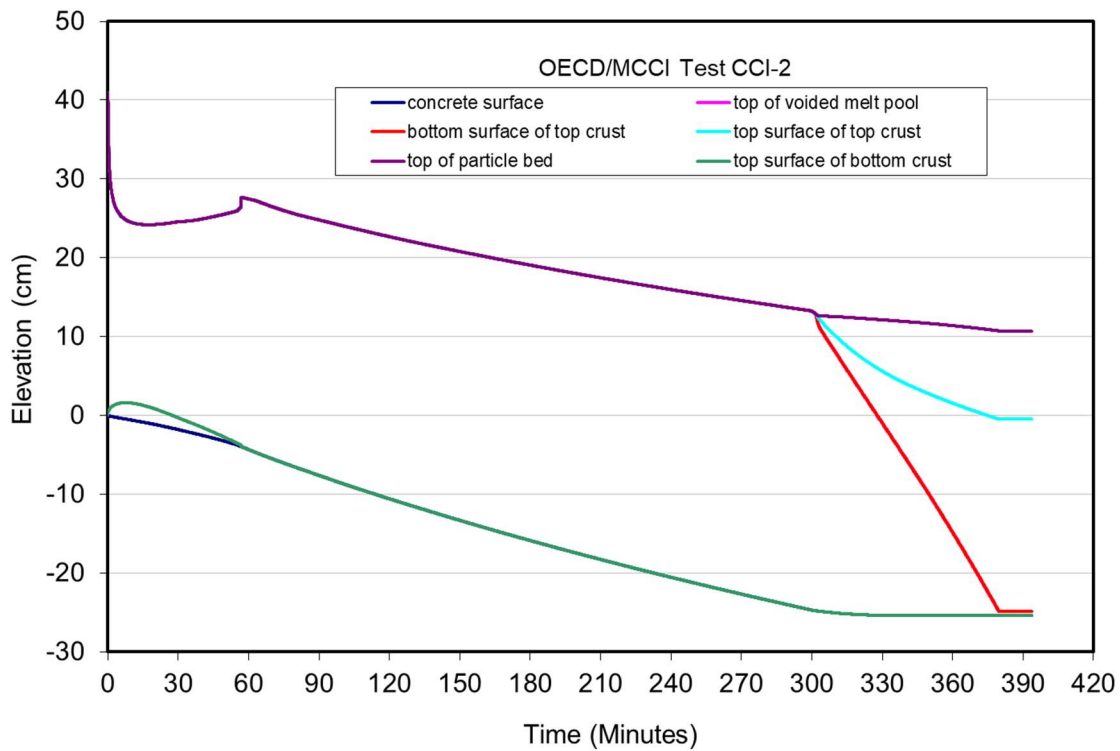


Figure C-39. Surface Elevation Predictions for OECD/MCCI CCI-2 Test.

In terms of the debris-water heat flux, the model seems under-predict the data over the first 10 minutes of the interaction. In the middle phase of the transient from 10 to 30 minutes, the agreement is reasonable, whereas over the balance of the test the heat flux is over-predicted. The results of the calculation indicate that there was a brief bulk cooling period lasting ~ 1 minute, followed by crust formation with water ingress into the crust beginning a few minutes later (i.e., at 304 minutes). Past this point, the crust steadily grows by ingress until the melt is completely quenched at 380 minutes. Melt eruptions contribute to debris cooling during this phase

The model thus predicts a posttest debris configuration that consists of a ~ 24 cm deep debris bed layer that was effectively cooled by water ingress. The crust is covered by a debris bed formed by eruptions that weighs ~ 149 kg. The depth of the cooled crust layer remaining over the basemat is less than the ~ 30 cm layer observed in the test. Conversely, the volume of erupted material in the experiment was ~ 44 liters with ~ 50 % porosity, or ~ 22 liters with void absent. The solidified debris theoretical density was ~ 3700 kg/m³, and so the actual mass of the particle bed was ~ 82 kg. Thus, the model over-predicts the particle bed mass by ~80%.

C.4.1.2 OECD/MCCI CCI-3 Test

As shown in Table C-1, the CCI-3 experiment utilized siliceous concrete. Dry cavity operations were maintained for 108 minutes, at which time the cavity was flooded. Water was added in the calculation at the same time.

The melt temperature, ablation front location, and upwards heat flux predictions are compared with the test data in Figures C-40 through C-42, respectively, while the evolution of the various surface elevations is shown in Figure C-43. For this test, the melt temperature is reasonably predicted. In terms of ablation, the axial erosion is slightly over-predicted, whereas radial erosion is over-predicted.

In terms of the debris-water heat flux, the model under-predicts the data over virtually all of the interaction. The model indicates that the melt sparging rate is initially not high enough to preclude stable crust formation, and so crust growth begins immediately. The model predicts a crust at the debris upper surface that is 5.3 cm deep, and this agrees well with the posttest examination finding up an upper porous crust layer that was ~ 5 cm deep. This crust overlaid some intervening void pockets and a second 5-10 cm thick porous layer that sat on the balance of the solidified monolithic layer over the basemat. Thus, the model underestimates the amount of material that was solidified as porous structure in this experiment, which is consistent with the under-prediction of the debris cooling rate.

C.4.1.3 OECD/MCCI CCI-6 Test

As shown in Table C-1, the CCI-6 experiment was a large scale integral test conducted with siliceous concrete. As opposed to the earlier tests, water was added quite soon after initial melt contact with the concrete surface; i.e., at 0.7 minutes. Water was added in the calculation at this time also. Unlike other tests with siliceous concrete, substantial melt eruptions occurred during CCI-6, and so eruptions were calculated using the Rico-Spalding correlation (NENTR=2) with the proportionality constant set at E=0.08. This is the same value used for the calculation of the limestone/common sand concrete debris coolability experiments.

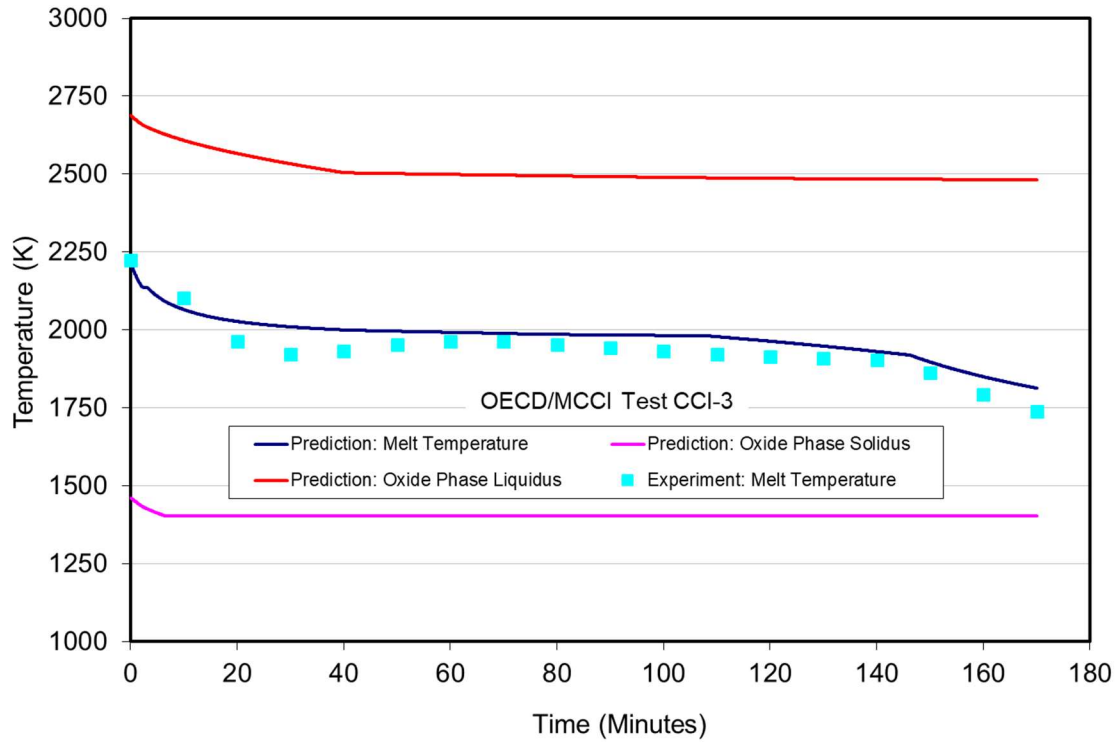


Figure C-40. Melt Temperature Prediction for OECD/MCCI CCI-3 Test.

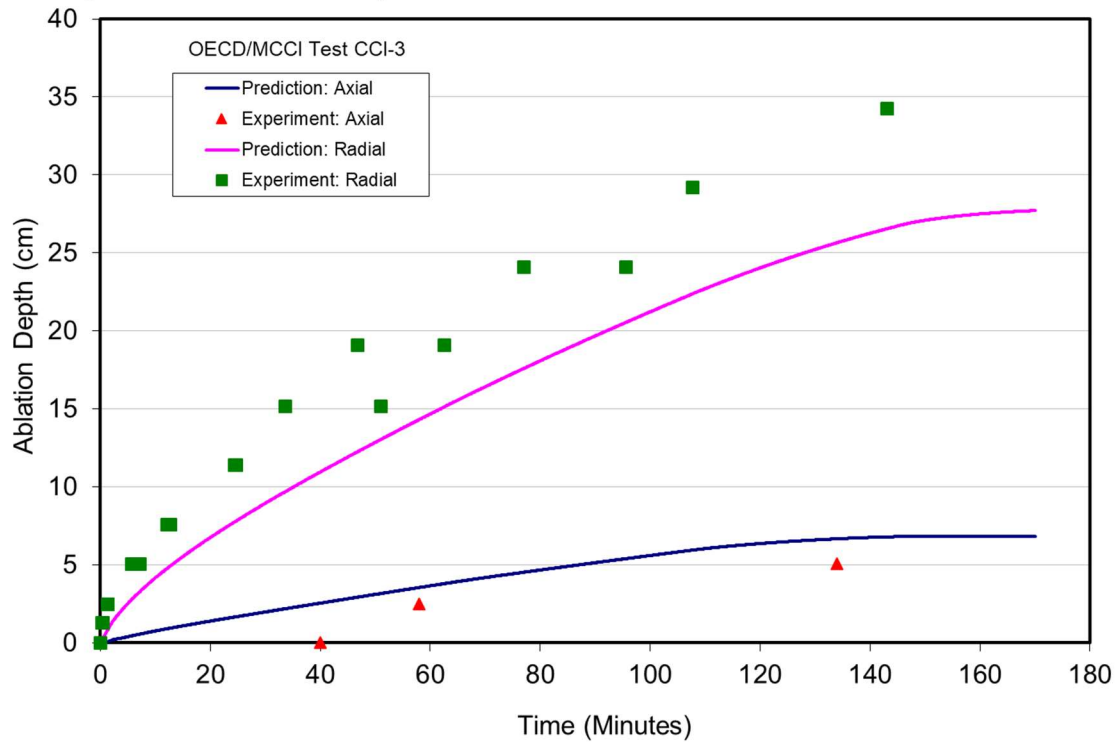


Figure C-41. Ablation Front Location Prediction for OECD/MCCI CCI-3 Test.

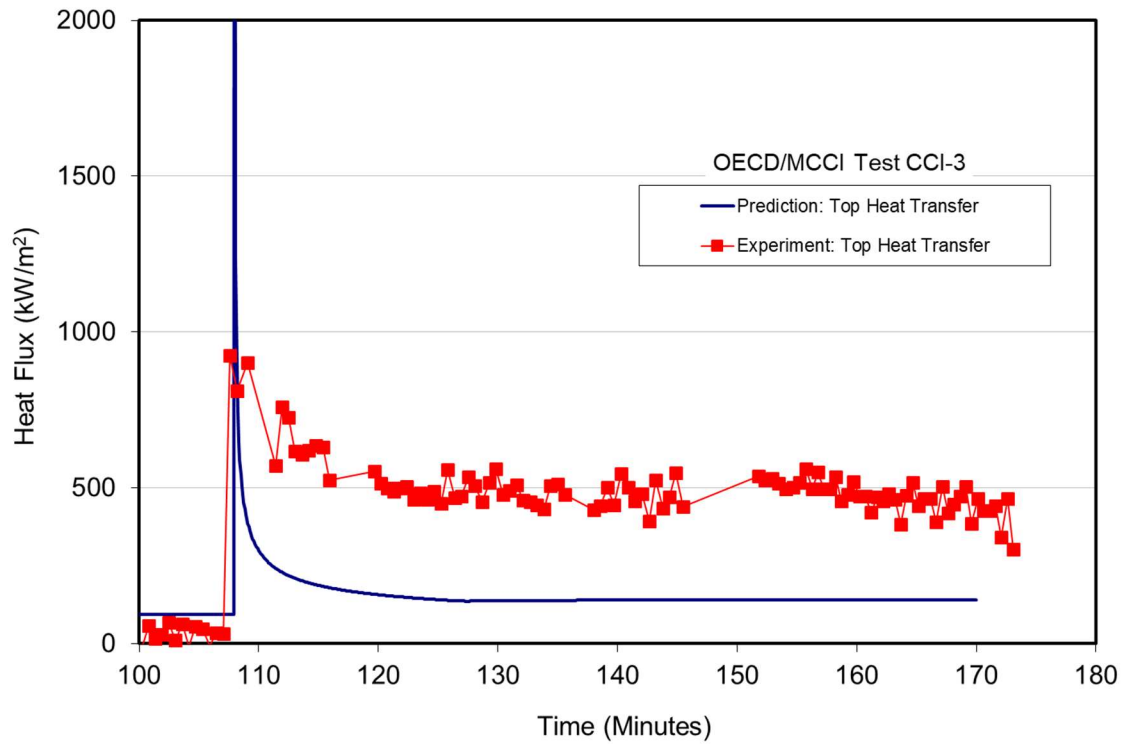


Figure C-42. Melt- Atmosphere Heat Flux Prediction for OECD/MCCI CCI-3 Test.

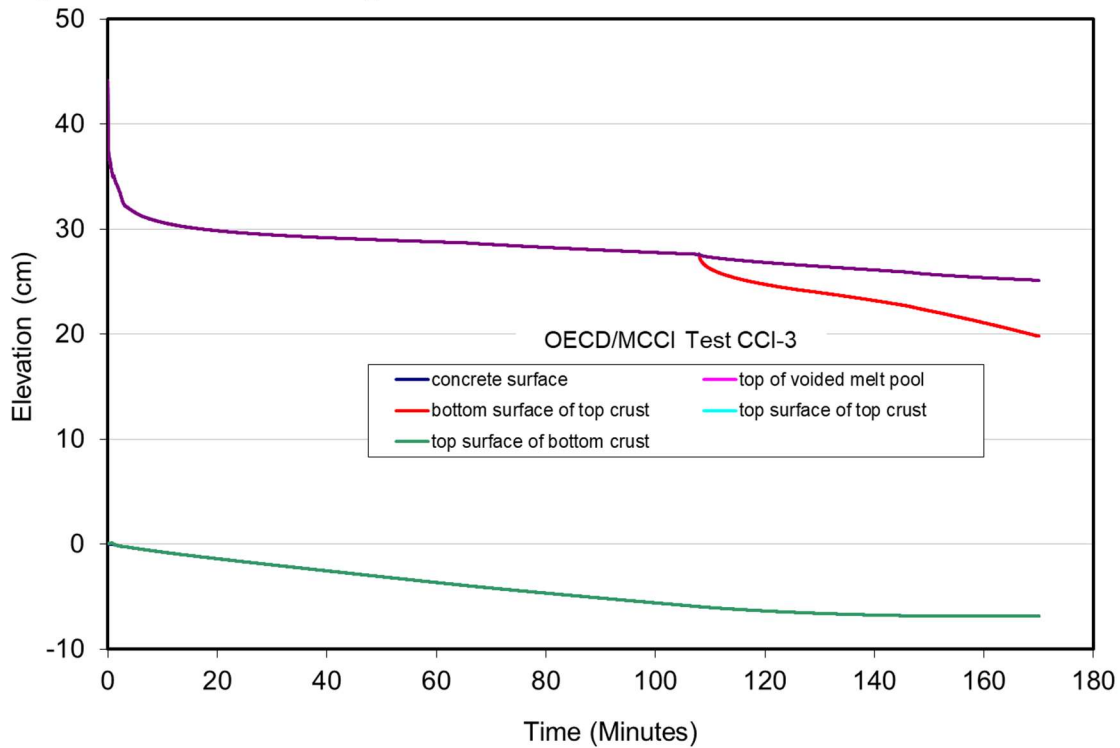


Figure C-43. Surface Elevation Predictions for OECD/MCCI CCI-3 Test.

The melt temperature, ablation front location, and upwards heat flux predictions for CCI-6 are compared with the test data in Figures C-44 through C-46, respectively, while the evolution of the various surface elevations is shown in Figure C-47. For this test, the melt temperature trend shows an increase following the initial bulk cooling transient. This is due to the fact that the calculated melt solid fraction (and corresponding viscosity) was quite high during the initial phase of the experiment (i.e., 0.9 to 0.95), and so the corium heated to the point where input power could be dissipated by convection to the pool boundaries.

In this experiment, onset of sidewall erosion was delayed until ~ 22 minutes in the sequence. Like CCI-5, this was attributed to the presence of a crust that protected the wall up until this time.^[66] After sidewall ablation commenced, the radial erosion rate was significantly larger than the axial rate. The model over-predicts the radial ablation, and under-predicts the axial.

In terms of the debris-water heat flux, the model under-predicts the first few minutes of the interaction. Thereafter, a sustained heat flux in the range of 500-700 kW/m² is predicted, which includes the combined effects of water ingression and melt eruption cooling mechanisms. In reality, eruptions occurred over the time intervals from 4 to 7 minutes and from 21 to 26 minutes. Complete debris quench is predicted to occur by 61 minutes.

The posttest debris configuration is predicted to consist of a ~ 6 cm deep particle bed formed by melt eruptions that overlies a porous crust layer that is ~ 18 cm deep. The particle bed formed by melt eruptions weighs 134 kg, which can be compared to the experimentally measured value of 186 kg. Posttest examinations revealed the presence of large region of fractured crust material beneath this bed, which is qualitatively similar to the model prediction.

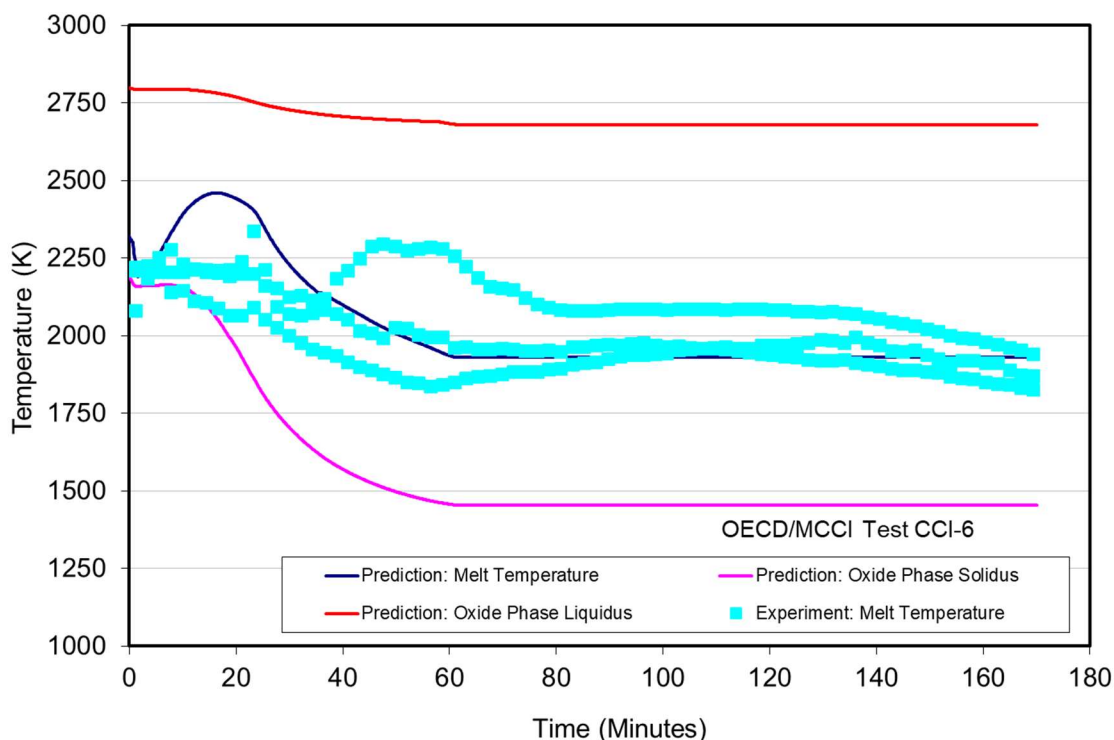


Figure C-44. Melt Temperature Prediction for OECD/MCCI CCI-6 Test.

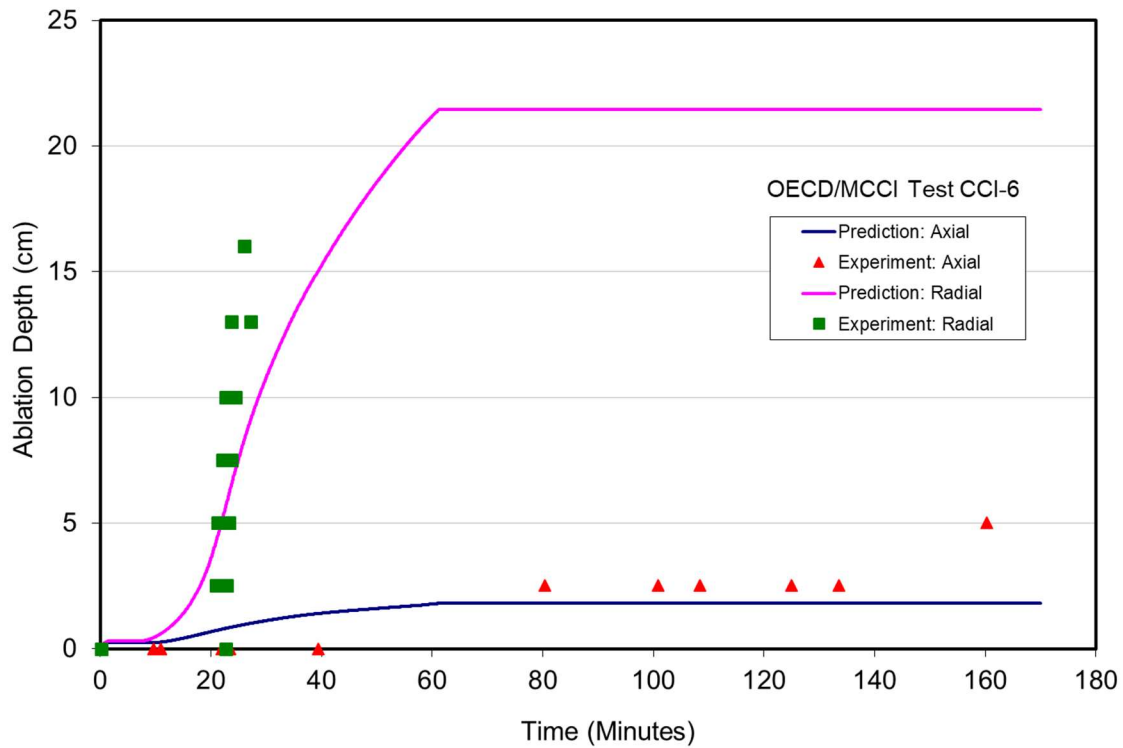


Figure C-45. Ablation Front Location Prediction for OECD/MCCI CCI-6 Test.

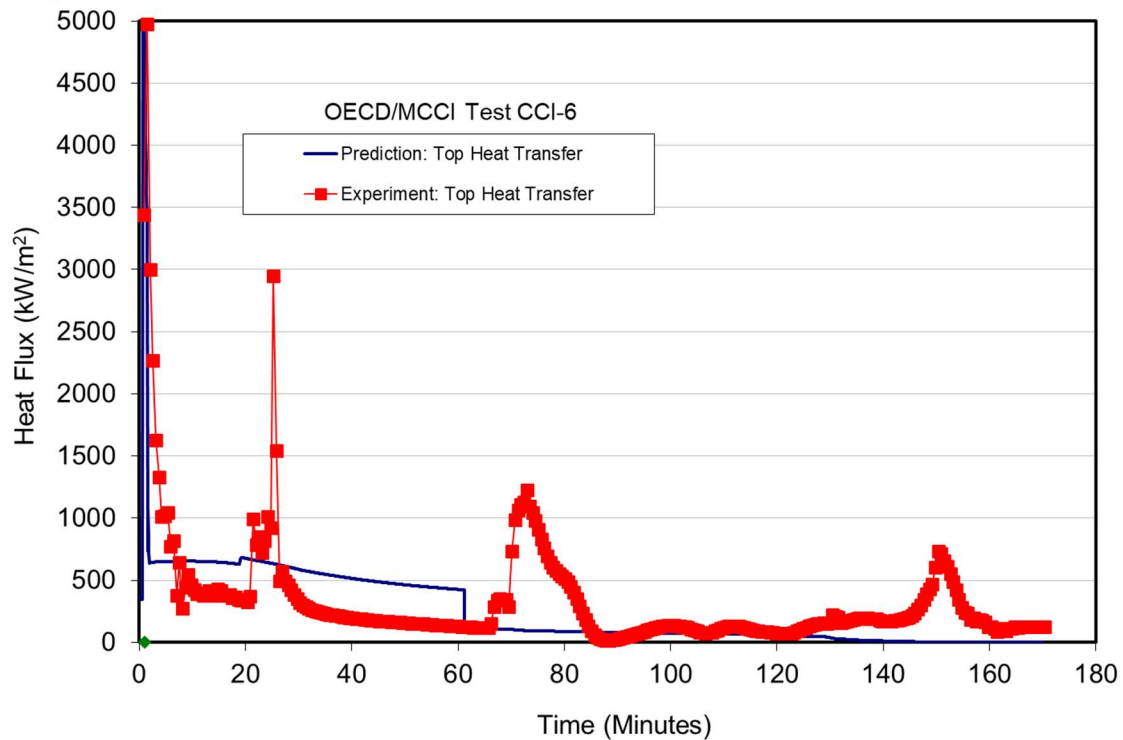


Figure C-46. Melt-Atmosphere Heat Flux Prediction for OECD/MCCI CCI-6 Test.

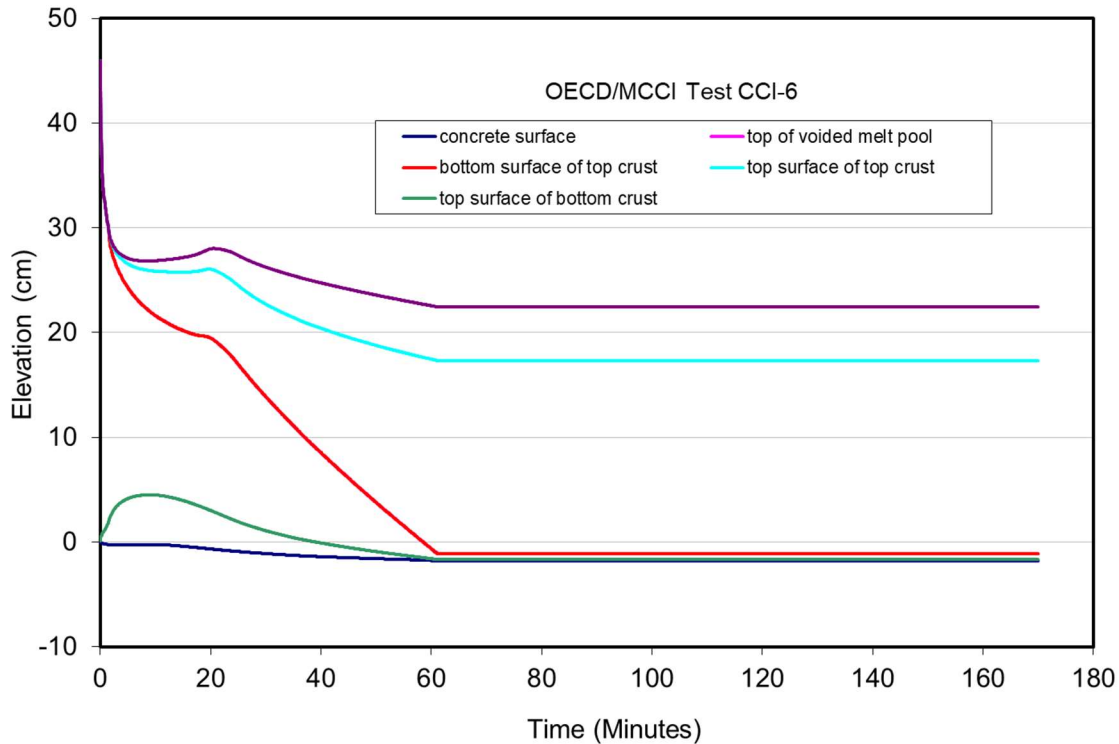


Figure C-47. Surface Elevation Predictions for OECD/MCCI CCI-6 Test.

C.5 Summary

A series of single-node validation calculations have been carried out with CORQUENCH4.1 to provide an indication of the predictive capability. The matrix includes nine dry cavity experiments and seven tests in which the cavity was flooded at some point in the experiment sequence. For the dry 1-D cavity tests, an attempt has been made to provide an assessment of the modeling uncertainties by comparing the end-of-test ablation depth and melt temperatures with the code predictions. This comparison is provided in Table C-17. Errors in ablation depth predictions range from -22 to +30 %. Similarly, variations in melt temperature predictions range from -11 to +16 %.

A similar type of comparison is not as practical for the wet cavity tests since there are large variations in cavity design (i.e., 1-D vs. 2-D) and timing of cavity flooding. Furthermore, many tests experienced crust anchoring and so the test progression deviated substantially from that expected at plant scale. However, the general observation can be made that the melt-water heat transfer models incorporated in the code provide the opportunity to predict the posttest debris morphology which in most cases agreed at least qualitatively with that observed in the tests. Furthermore, in many cases the magnitude of the heat transfer to overlying water was under-predicted. Improvements in heat transfer and posttest morphology predictions could be achieved by fine tuning code input related to melt eruption and water ingression cooling mechanisms, but this type of activity lies beyond the current scope of work.

Table C-17. Summary of CORQUENCH4.1 Validation Results Against 1-D Dry Cavity Tests.

Test	Corium/ Concrete	End-of-Test Ablation Depth, cm			End-of-Test Melt Temperature, K		
		Actual ¹	Calc.	% Deviation	Actual	Calc.	% Deviation
L2	70 % Oxidized PWR/Siliceous	14	13.9	-0.7	2400	2400	0
L4	50 % Oxidized BWR/Serpentine Over Siliceous	19	21.6	+13.7	2250	2000	-11
L5	100 % Oxidized PWR/LCS	10	13	+30.0	1880	1950	+3.7
L6	30 % Oxidized PWR/Siliceous	18	14.1	-21.7	2140	2210	-1.9
L8	70 % Oxidized PWR/L-L	15	17.8	+15.6	2090	2060	-1.4
SURC-1	70 % Oxidized PWR/L-L	27	28.1	+4.1	1880	2280	+16.0
SURC-2	70 % Oxidized PWR/Basalt	25	31.3	+25.2	2120	2180	+2.8

¹Includes depth of concrete-metal inserts for ACE-MCCI tests; ²at 100 minutes.



NSE Division

Argonne National Laboratory
9700 South Cass Avenue, Bldg. #208
Argonne, IL 60439

www.anl.gov



Argonne National Laboratory is a U.S. Department of Energy
laboratory managed by UChicago Argonne, LLC